Integration of satellite interferometry and geological methods for landslide research

Cristina Reyes Carmona

Ph.D. Thesis 2023

Supervised by Jorge Pedro Galve and Rosa María Mateos

Programa Doctorado Ciencias de la Tierra

UNIVERSIDAD DE GRANADA

CSIC Consejo Superior de Investigaciones Científicas | IGME Instituto Geológico y Minero de España

Editor: Universidad de Granada. Tesis Doctorales
Autor: Cristina Reyes Carmona
ISBN: 978-84-1117-900-3
URI: https://hdl.handle.net/10481/82578

A las mujeres geólogas y científicas.

“Ignoramos nuestra verdadera estatura

hasta que nos ponemos de pie”

Emily Dickinson

Acknowledgments

Me gustaría aprovechar este espacio para agradecer a varias personas que me han acompañado durante este tiempo de tesis. Voy a permitirme un poco de romanticismo y diré algunas cosas que en persona no digo porque me pondría roja.

Quiero comenzar agradeciendo a mi director Jorge Pedro Galve y mi directora Rosa María Mateos, a los que admiro mucho y de los que es muy difícil tener alguna queja. JP y Rosa, deciros que he tenido una suerte enorme de haber estado bajo vuestra dirección. No solo por todo lo que me habéis enseñado en lo profesional, si no también por el trato personal que me habéis dado durante este tiempo. Si he llevado bien este viaje doctoral es indudablemente gracias a vuestra guía y vuestro trato. A ti, JP, siempre pendiente de cómo podía ir enlazando contratos para hacer la tesis: gracias por apostar por mí desde el primer momento allá por 2017. La oportunidad que he tenido de hacer la tesis ha sido gracias a ti. Gracias también por inspirarme y aconsejarme tan sabia y calmadamente cuando lo he necesitado. Sin duda, me quedo con tu frase en tono tranquilo: “tu no te agobies”. Para mí eres y serás siempre un ejemplo a seguir, tanto en lo científico como en lo personal. A ti, Rosa, siempre con un sabio proverbio consejero y una divertida enseñanza: gracias por regalarme esa positividad y tranquilidad que tanto te caracteriza. Me quedo con esta frase tuya: “Cristina, tienes que ser práctica”. Qué gusto aprender de ti. Además de tan buena científica, espero algún día ser tan buena artista y divulgadora como eres tú. Eres toda una jefaza y referente.

A los miembros del Departamento de Geodinámica, donde me he sentido como en casa durante estos años. Sobre todo, gracias a los miembros del grupo de investigación ARPA, en el que tanta suerte he tenido de estar: a Vicente Pérez, José Miguel Azañón, Patricia Ruano y Guillermo Booth. Echaré de menos esas reuniones informales y divertidas con un buen plato de arroz por delante. Mención especial a Antonio Jabaloy, al que tengo mucho cariño por comenzar con él esta aventura de la investigación con el TFG. Antonio, gracias por la simpatía y amabilidad recibida desde entonces hasta hoy.

Cómo no, el agradecimiento más especial a mis compis de la becaría de Geodinámica. Comienzo por la generación que tan bien me acogió cuando comencé la tesis: Ángela, Cristina, Víctor y Álex. Gracias por la gran cantidad de buenos momentos que siempre recordaré con infinito cariño, como la hora de comer creando nuestro pequeño rincón de la ofensa, o aquellas tardes de juegos de mesa y cervezas que casualmente había en la nevera. Os voy a echar (y ya os echo) mucho de menos. Mención especial a Lourdes y Mayte, por lo bien que me han cuidado a base de chocolate y pistachos, y a Asier, con quien además he tenido la suerte de compartir estancia (y muchas canecas). Continuo con “las nuevas generaciones”: Marcos, Dani, David, Roberto y Paula. Echaré de menos esos cafés de camarero y azucarillos machistas, aunque creáis que no. Gracias por hacer tan amena y divertida esta última etapa de tesis.

A varias personas de distintas universidades y centros por los que he tenido la suerte de pasar. A Oriol Monserrat y Anna Barra, del CTTC, por haberme metido en este fregao del InSAR. Uri y Anna: gracias por aquella paciente acogida frente a la pantalla negra y por

la buena relación personal que hemos podido mantener hasta hoy. Siempre os tendré mucho cariño. A Pedro Pinto, Susana Pereira y José Luis Zêzere, del IGOT: gracias por el tiempo dedicado y por vuestra cálida acogida durante mi estancia. Agradecer también a Roberto Sarro y Mónica Martínez, compis del IGME, con los que he compartido curro y viajes muy gozosos a Baleares.

A mis compis de la carrera, por haber compartido una de las etapas más bonitas y únicas de la vida. Trotamontes, espero que ahora que soy doctora dejéis de llamarme delegada. Mención especial a Javi, con quien he tenido la suerte de compartir más tiempo desde entonces hasta hoy, incluyendo penurias tésicas y cuidados gatunos. Mención especial también a María, por lo fuerte que ha demostrado ser a pesar de las circunstancias. Javi y María, os deseo mucha suerte con vuestras tesis y lo mejor juntos (estoy deseando la geo-boda). También agradecer a Noe, porque sigue siendo mi amiga a pesar de que nunca voy a verla a Córdoba (vaya paciencia). A Iñigo y Vito, dos compañeros del máster que son muy especiales para mí. Iñigo, gracias por el apoyo y ánimo constante durante la tesis. Sobre todo, gracias por creer tan incondicionalmente que soy la mejor geóloga del mundo (que sepas que es recíproco). A ti, Vito, gracias por el tiempo compartido, aunque se me ha hecho muy corto. Nos acabaremos encontrando allá donde estés. A Sara, compañera del máster, por el cariño que me ha enviado desde la distancia. Sarilla, nos quedan muchos cafés que tomar próximamente en Alicante. También agradecer a las compis de doctorado (amadas precarias) que conocí en Lisboa y que hicieron de mi estancia, contra todo pronóstico, una experiencia muy disfrutada. Mención especial a Antía y Juan: ya sabéis que os adoro.

A mis amigas, las del pueblo, las que son para toda la vida. Blanca, Pili, María, Clara y Almu: gracias por estar siempre ahí, os quiero un montón. A mi amigo Jorge, con quien he compartido muchos momentos durante la tesis que le han llevado a ser el mejor alumno no-geólogo que tengo.

A Jesús, por lo compartido y vivido, que no ha sido poco si incluimos un rescate en helicóptero. Jesús, gracias por el amor y el sostén recibido durante este tiempo. Gracias también por la paciencia durante estos últimos meses, y por la compañía hasta en los findes en los que ha tocado currar.

A mi familia (abuela, tita, titos, prima, primo, hermanos y sobris), a la que he sentido muy cerca aun con distancia de por medio. En especial, a mi madre y a mi padre, por animarme desde pequeña a hacer lo que verdaderamente me gustase, por muy raro que sonase aquello de la geología y por muy difícil que pareciese aquello de la investigación. Mamá, papá: si hoy soy geóloga y doctora, es gracias a vosotros.

Abstract

Properly assessing the hazard of landslides begins with mapping and characterising them from a geological perspective. Although landslides have demonstrated a worldwide impact and are the second most damaging geohazard in Spain (after floods), there is still little social awareness about them. This fact evidences the necessity of additional efforts for the study of these natural phenomena. The integration of an innovative remote sensing technique, like satellite radar interferometry, with geomorphological and geological methods has demonstrated to be an effective multi-technique approach for landslide research. The present Ph.D. Thesis is developed in this framework and improves the knowledge of landslides by applying such combination of methodologies. Two critical and interesting areas in the Province of Granada (Southern Spain) have been selected for study: the Sierra Nevada Range and the Rules Reservoir.

The Sierra Nevada is a high-elevation mountain range where some landslides have been unreported or unnoticed, despite being susceptible to slope movements. In this case, Differential Synthetic Aperture Radar (DInSAR) and Landscape Analysis techniques were integrated to optimise landslide mapping and provide an updated landslide inventory map of the range. The Landscape Analysis was based on the identification of river anomalies by the double normalised channel steepness (k_{snn}) index, a novel derivation from the conventional normalised steepness index (k_{sn}) that reduced the active tectonics signal of the area. The visual exploration of k_{snn} anomalies and the unstable ground areas obtained from DInSAR velocity maps evidenced 28 new landslides. This mapping reveals a significant increase of the area affected by landslides (33.5%) compared with the previous inventory from the Geological and Mining Institute of Spain (IGME-CSIC) (14.5%). A relevant finding of this study is the identification, for the first time, in the Sierra Nevada, of two landslide typologies: Deep-Seated Gravitational Slope Deformations (DGSDs) and rockslides. Their diffuse boundaries, homogeneous lithology (schists), and previous glacial morphologies made delimiting these landslides difficult, but the utilised techniques greatly facilitated the process. The geomorphological observations made in the field and the exploration of maps (e.g. slope, hillshade, aspect, rugosity) derived from high-resolution Digital Elevation Models (DEMs) were fundamental procedures for accurately defining the landslides' boundaries, as well as to describe landslide-related morphologies. Due to the large size and typology of these landslides, attempts were made to provide a first insight about their hazard and potential impacts in the region.

The Rules Reservoir is one of the most strategic infrastructures in the Province of Granada, with well-known slope instability problems during and after its construction. In this case, DInSAR techniques were applied in the reservoir's slopes to derive ground velocity maps that revealed three active landslides. The thorough geomorphological investigation, based on field observations and photo-interpretation of historical aerial images, allowed to distinguish between rotational (Lorenzo-1 and Rules Viaduct landslides) and translational (El Arrecife Landslide) landslide typologies, as well as to identify surficial damages related to their activity. The DInSAR-derived times series of

accumulated displacement (TSs) revealed a correlation between the acceleration of the rotational landslides' movement and drawdowns of the reservoir water level. Due to their dimensions, rotational character and minor accelerations, a rapid slope failure and sudden collapse into the reservoir is not expected from the Lorenzo-1 and Rules Viaduct landslides. However, they pose a risk to nearby infrastructures due to the retrogressive evolution of these landslides: the Lorenzo-1 Landslide is already affecting the N-323 National Road, while the Rules Viaduct Landslide may be provoking deformation on the southern sector of the Rules Viaduct (A-44 Highway). Regarding the El Arrecife Landslide, its translational character implies a greater potential hazard and further efforts were made to characterise this landslide.

The El Arrecife Landslide is located in the western slope of the Rules Reservoir and it was identified by using DInSAR data, as the poorly defined boundaries of the landslide made its recognition in the landscape challenging. This landslide was analysed by a multi-technique approach to provide a rapid characterisation and comprehensive understanding of its structure, volume and historical activity. The structural field surveys enabled the identification of many foliation orientations of the rocks (phyllites) and a kinematic analysis revealed the most probable orientation to cause a planar slope failure. The estimated location of the surface of rupture allowed determining the extremely large volume of the landslide (14.7 million m^3). The short-term activity of the landslide (last 5 years) was evidenced by DInSAR, while geophysical data based on Ground Penetrating Radar (GPR) data revealed its medium-term activity (last 22 years). Both techniques evidenced a vertical movement of the landslide around 2 cm/yr. Photogrammetric techniques based on the Structure-for-Motion (SfM) method were also applied, but no rapid shallow movements were detected during the analysed period (14 years). Besides having an overall translational movement, the landslide's foot is composed by smaller-size rotational landslides. The DInSAR TSs indicated that variations in the reservoir water level do not affect the overall landslide body, but drawdowns of the water level do accelerate the movement of these rotational slides. Therefore, the most significant hazard of the El Arrecife Landslide is related to such rotational slides, that have been causing damage to the N-323 National Road for several decades and are expected to persist. Although improbable, the possibility of a rapid and sudden acceleration of the entire landslide and subsequent collapse into the reservoir cannot be underestimated, given its translational kinematics and large size. It is therefore crucial to consider the response of this landslide to possible hazardous scenarios derived from extraordinary events, such as drastic reservoir water level drawdowns, intense precipitation, or an earthquake.

Resumen

La cartografía y caracterización geológica de los movimientos de ladera son el primer paso para la evaluación de su peligrosidad. A pesar del impacto que generan a nivel mundial y de ser el segundo peligro geológico más dañino en España (después de las inundaciones), todavía existe poca concienciación social sobre los movimientos de ladera. Este hecho evidencia la necesidad de realizar esfuerzos adicionales para el estudio de estos fenómenos naturales. La aplicación de un enfoque multi-técnica que combine métodos innovadores de teledetección, como la interferometría de satélite radar, con métodos geomorfológicos y geológicos ya ha demostrado ser muy eficaz para la investigación de movimientos de ladera. La presente Tesis Doctoral se desarrolla en este marco y mejora el conocimiento de los movimientos de ladera aplicando dicha combinación de técnicas. El estudio de esta tesis se ha focalizado en zonas críticas y de interés de la Provincia de Granada (Sur de España): Sierra Nevada y el Embalse de Rules.

Sierra Nevada es una cadena montañosa de gran altitud, en la que algunos movimientos de ladera no han sido identificados, a pesar de ser susceptible a ellos. En este caso, se integraron técnicas de Interferometría Diferencial de Radar de Apertura Sintética (DInSAR) y de Análisis del Relieve para optimizar la cartografía de movimientos de ladera y proporcionar un inventario actualizado de estos. El Análisis del Relieve se basó en la identificación de anomalías en ríos, utilizando el índice de pendiente doble normalizada (k_{snn}), una novedosa derivación del índice de pendiente normalizada convencional (k_{sn}), mediante el cual se redujo la influencia de la tectónica activa de la zona. Así, se detectaron 28 nuevos movimientos de ladera mediante la visualización de anomalías del índice k_{snn} y de las zonas inestables del terreno obtenidas de los mapas de velocidad DInSAR. La nueva cartografía revela un aumento significativo de la superficie afectada por movimientos de ladera (33.5%) en comparación con el inventario anterior del Instituto Geológico y Minero de España (IGME-CSIC) (14.5%). Otro hallazgo importante ha sido la identificación, por primera vez en Sierra Nevada, de dos tipos de movimientos de ladera: Deformaciones Gravitacionales Profundas de Ladera (DGSDs) y deslizamientos en roca. Los límites difusos, la litología homogénea (esquistos) y las morfologías glaciares dificultaron la delimitación de estos movimientos, pero las técnicas utilizadas facilitaron enormemente el proceso. Las observaciones geomorfológicas realizadas en campo y la exploración de mapas (p. ej. pendiente, sombreado, orientación, rugosidad) derivados de Modelos Digitales de Elevación (DEMs) de alta resolución fueron fundamentales para definir con precisión los límites de los movimientos de ladera, así como para describir sus morfologías. Debido al gran tamaño y a la tipología de estos movimientos, se ha proporcionado una visión preliminar sobre su peligrosidad y posible impacto en la región.

El Embalse de Rules es una de las infraestructuras más estratégicas de la Provincia de Granada y bien conocido por los problemas de inestabilidad del terreno que ocurrieron durante y después de su construcción. En este caso, se aplicaron técnicas DInSAR en las laderas del embalse para obtener mapas de velocidad del terreno, que revelaron la existencia de tres deslizamientos activos. La exhaustiva investigación geomorfológica,

basada en observaciones de campo y fotointerpretación de imágenes aéreas históricas, permitió distinguir entre dos tipologías de deslizamientos: rotacionales (Lorenzo-1 y Viaducto de Rules) y traslacionales (El Arrecife), así como identificar daños superficiales relacionados con la actividad de estos. Las series temporales de desplazamiento acumulado (TSs) derivadas de DInSAR revelaron una correlación entre la aceleración del movimiento de los deslizamientos rotacionales y los descensos del nivel de agua del embalse. Las dimensiones, el carácter rotacional y las leves aceleraciones de estos deslizamientos, hacen que sea poco probable que se produzca un colapso repentino y rápido de las laderas en el embalse. Sin embargo, estos suponen un riesgo para las infraestructuras cercanas por su evolución retrogresiva: el Deslizamiento Lorenzo-1 ya está afectando a la Carretera Nacional N-323, mientras que el Deslizamiento del Viaducto de Rules puede estar deformando el tramo sur del Viaducto de Rules (Autovía A-44). En cuanto al Deslizamiento de El Arrecife, su carácter traslacional lo hace potencialmente más peligroso, lo cual ha motivado realizar una caracterización más detallada del mismo.

El Deslizamiento de El Arrecife está situado en la ladera occidental del Embalse de Rules y se identificó gracias a los datos DInSAR, ya que sus límites poco definidos dificultaron su reconocimiento en el paisaje. Este deslizamiento ha sido analizado mediante un enfoque multi-técnica para elaborar una caracterización rápida y una comprensión exhaustiva de su estructura, volumen y actividad histórica. Mediante el trabajo de campo estructural, se pudieron identificar varias orientaciones de la foliación de las rocas (filitas), y se obtuvo la orientación más probable para generar una rotura planar de la ladera mediante un análisis cinemático. También se estimó la estimación de la superficie de rotura, determinando así el volumen extremadamente grande del deslizamiento (14.7 millones de m^3). Los datos DInSAR mostraron la actividad a corto plazo del deslizamiento (5 años), mientras que los datos geofísicos obtenidos de Radar de Penetración Terrestre (GPR) revelaron su actividad a medio plazo (últimos 22 años). Con ambas técnicas se obtuvo un movimiento vertical del deslizamiento de alrededor de 2 cm/año. También se aplicaron técnicas fotogramétricas basadas en el método 'Structure-for-Motion' (SfM), pero no se detectaron movimientos rápidos superficiales durante el periodo analizado (14 años). Además de su movimiento traslacional general, el pie del deslizamiento está formado por deslizamientos rotacionales de menor tamaño. Las series temporales (TS) derivadas de DInSAR indican que las variaciones en el nivel de agua del embalse no afectan a todo el cuerpo del deslizamiento, pero los descensos del nivel del embalse sí que aceleran el movimiento de los movimientos rotacionales del pie. Por lo tanto, el peligro más significativo del deslizamiento de El Arrecife está relacionado con estos deslizamientos rotacionales, que ya han estado generando daños en la Carretera Nacional N-323 durante varias décadas y se espera que persistan. Aunque es improbable, la posibilidad de una aceleración rápida y repentina de todo el deslizamiento y su posterior colapso en el embalse no debe descartarse, debido a su cinemática traslacional y tamaño. Por lo tanto, es de vital importancia considerar la respuesta de este deslizamiento ante posibles escenarios peligrosos derivados de acontecimientos extraordinarios, tales como una reducción drástica del nivel de agua del embalse, precipitaciones intensas o un terremoto.

Index

Chapter I

Introduction

1. Background

The hazard and risk threatened by landslides are widely recognised throughout the world. A recent publication from the Geological Surveys of Europe (Mateos et al. 2020) reports 4000 damaging landslides events in Europe from 2015 to 2017, that resulted in 39 fatalities, 155 injuries and severe destruction to housing, properties and infrastructures. According to this study, Spain is the second country in Europe (after Italy) with more population exposed to landslides: around 4 million people are living in areas with high and very high degree of landslide susceptibility. Moreover, landslides are the second most important geohazard in Spain (after floods) taking into account the significant damage caused to infrastructures (Mateos 2017) with reported annual economic losses of 160 million Euros (Corominas et al. 2017). Despite the demonstrated impact of landslides, the completeness of the Spanish landslide database is less than 5% (Herrera et al. 2018). This result indicates that these hazardous phenomena have not been given enough attention and importance in Spain. The elaboration of a proper landslide inventory is a fundamental task for risk management (Confuorto et al. 2023) and thus, further efforts have to be done in the inventory and study of landslides in Spain to know in detail their impact on society. Even in Spanish provinces where landslides have been specially studied such as Catalonia (Baeza and Corominas 2001; Abellán et al. 2010; Ortuño et al. 2017; Guinau et al. 2019; Palau et al. 2020), Asturias (Domínguez-Cuesta et al. 1999, Valenzuela et al. 2018; Cuervas-Mons et al. 2021), Balearic Islands (Bianchini et al. 2013; Sarro et al. 2014; Mateos et al. 2016, 2018) or Granada (Chacón and Soria 1992; Fernández et al. 1997; Irigaray et al. 2000; El Hamdouni et al. 2001; Palenzuela et al. 2016; Jiménez-Perálvarez et al. 2017), the use of up-to-date methods and technologies can bring to light new useful information to manage landslide hazard, as it will show in this Ph.D. Thesis.

The present thesis is framed in several areas of the Province of Granada. As mentioned above, this province is one of the regions in Spain where landslides have been studied in-depth and for which an inventory of slope movements has existed for years (Chacón et al. 2007). The existence of this inventory is not casual: the recent geological and geomorphological evolution of the region has determined the abundance of landslide-prone areas, which have been object of continuous research since the last decades. Those studies carried out in the 1980s, 1990s and 2000s (e.g. Chacón 1988, 1992; Fernández et al. 1997, 2003; Irigaray et al. 2000; El Hamdouni 2001) were aimed on the systematic mapping of landslides to generate inventories through conventional methods (i.e. photointerpretation and fieldwork). It was not until the 2010s when remote sensing techniques started to be applied in the Province of Granada for landslide investigation. These techniques mainly include photogrammetry (Fernández et al. 2011), Terrestrial Laser Scanner (TLS) (Palenzuela et al. 2013), Light Detection and Ranging (LiDAR)

(Palenzuela et al. 2015; Fernández et al. 2017) and Differential Interferometric Synthetic Aperture Radar (DInSAR) (Fernández et al. 2009; Notti et al. 2015; Mateos et al. 2017; Galve et al. 2017; Barra et al. 2022). The mentioned works demonstrate the effectiveness of these techniques, not only to monitor the activity of previously known landslides but also to discover new ones and to further understand their temporal evolution and kinematics. However, there is still research to be done in landslide-susceptible areas where the existing landslide inventories may be outdated our uncomplete. An example is the Sierra Nevada Range, where multiple slopes have been estimated to have a medium/high degree of landslide susceptibility (Jiménez-Perálvarez et al. 2017) but the mapped landslides are scarce in this area (see Chacón et al. 2007). Moreover, other areas with multiple mapped landslides have not been yet the subject of detailed studies despite being located in strategic places. An example is the Rules Reservoir, one of the most critical infrastructures of the Province of Granada, that was constructed on slopes affected by landslides (see Fernández et al. 1997). However, neither a monitoring activity nor a detailed geological analysis have been carried out in any of the reservoir slopes' landslides. To enhance landslide research, recent works have already evidenced that a multi-technique approach based on remote sensing, geological, geomorphological and geophysical techniques is a good choice (e.g. Gullà et al. 2017; Tomás et al. 2018; Peduto et al. 2021).

2. Objectives

Given the interest of the topic but the lack of information, this Ph.D. Thesis aims to improve the knowledge of landslides by the data-fusion derived from differential satellite radar interferometry (DInSAR) and geological methods. This thesis also aims to underline the importance of analysing landslides from a geological and geomorphological perspective to perform a more complete interpretation of DInSAR data. To reach these objectives, two study zones are selected in the Province of Granada, Southern Spain: the Sierra Nevada Range and the Rules Reservoir. As explained in the previous section, both areas have the potential to be of interest for landslide research.

The specific objectives proposed in these study areas are the following:

- Identify active landslides by generating ground displacement maps derived from DInSAR techniques.
- Characterise the detected active landslides by producing detailed geomorphological and geological maps.
- Perform a more precise detection and characterisation of landslides by applying other geological methods that complement the DInSAR data.
- Update and improve the existing landslide inventories.
- Propose a preliminary perspective of the landslide hazard that may guide and optimise a proper risk assessment at future.

3. Structure of the Ph.D. Thesis

This Ph.D. Thesis is presented as a group of publications, that constitute independent but thematically related chapters. Preceded by an abstract, this manuscript is organised in five chapters. The present introductory chapter (Chapter I) describes the background and objectives of this thesis. A geographical, geological and geomorphological overview of the study areas is also provided, together with a description of the used methods and procedures to carry out the research.

Chapters II, III and IV correspond to the scientific publications, through which the main results and discussions of the thesis are exposed. For being a compendium of articles, repetitions of content are expected in these three chapters, especially in the introduction and methodology sections. These chapters are organised according to the scale of study, ranging from regional to local. Chapter II (Reyes-Carmona et al. in press) provides a landslide inventory of the southwestern sector of Sierra Nevada, where two landslide types are firstly recognised in this mountain range. Chapter III (Reyes-Carmona et al. 2020) offers the discovery of several active landslides in the Rules Reservoir's slopes. Chapter IV (Reyes-Carmona et al. 2021) is focused on the comprehensive characterisation of the most relevant active landslide detected in the Rules Reservoir area: the El Arrecife Landslide. In this way, two areas were analysed, but three different study cases are presented independently in each chapter: the southwestern sector of Sierra Nevada, the Rules Reservoir and the El Arrecife Landslide.

Finally, Chapter V provides an integrated discussion of the main topics addressed in Chapters II, III and IV, followed by the conclusions of the thesis. This chapter also outlines some open issues that are suitable for future research in the region.

4. Setting of the study areas

As mentioned in the previous sections, the research of this Ph.D. Thesis has been carried out in two locations: the Sierra Nevada Range and the Rules Reservoir. Their geographic, geological and geomorphological settings are described in Chapters II, III and IV. For avoiding excessive repetitions of content, this section intends to offer geological and geomorphological information of the study areas that was not extensively covered in these three chapters.

4.1. Geographic location and climate

The study areas are located in the southern part of the Spanish Province of Granada (Figure 1). They are settled within the hydrological basin of the Guadalfeo River, that runs into the Mediterranean Sea. The Guadalfeo River Basin has a drainage area of 1285 km^2 and collects water from several surrounding mountain ranges of the Betic Cordillera: Sierra de Albuñuelas, Sierra de los Guájares and Sierra del Chaparral (eastern divide), Sierra de Lújar and Sierra de la Contraviesa (western divide) and Sierra Nevada (northern divide) (Figure 1). The study area described in Chapter II (378.5 km^2) contains the headwaters of the Guadalfeo River Basin, that drain the southwestern side of Sierra Nevada (the highest peaks of the Iberian Peninsula, ~3400 m.a.s.l.) (Figure 1). Thus, the

Guadalfeo River Basin is characterised by high topographic gradients, as the distance from the Sierra Nevada to the coastline is just 35 km. Along the southern side of Sierra Nevada, there are several small singular villages that form the historical region of 'La Alpujarra', of around 25000 inhabitants (Figure 1). The analysed area in Chapter III (53 km^2) comprises the slopes of the Rules Reservoir, which is located half-way through the Guadalfeo River (Figure 1). In Chapter IV, the research is focused only on the western slope of the Rules Reservoir, covering a smaller area of 2.5 km^2 (Figure 1).

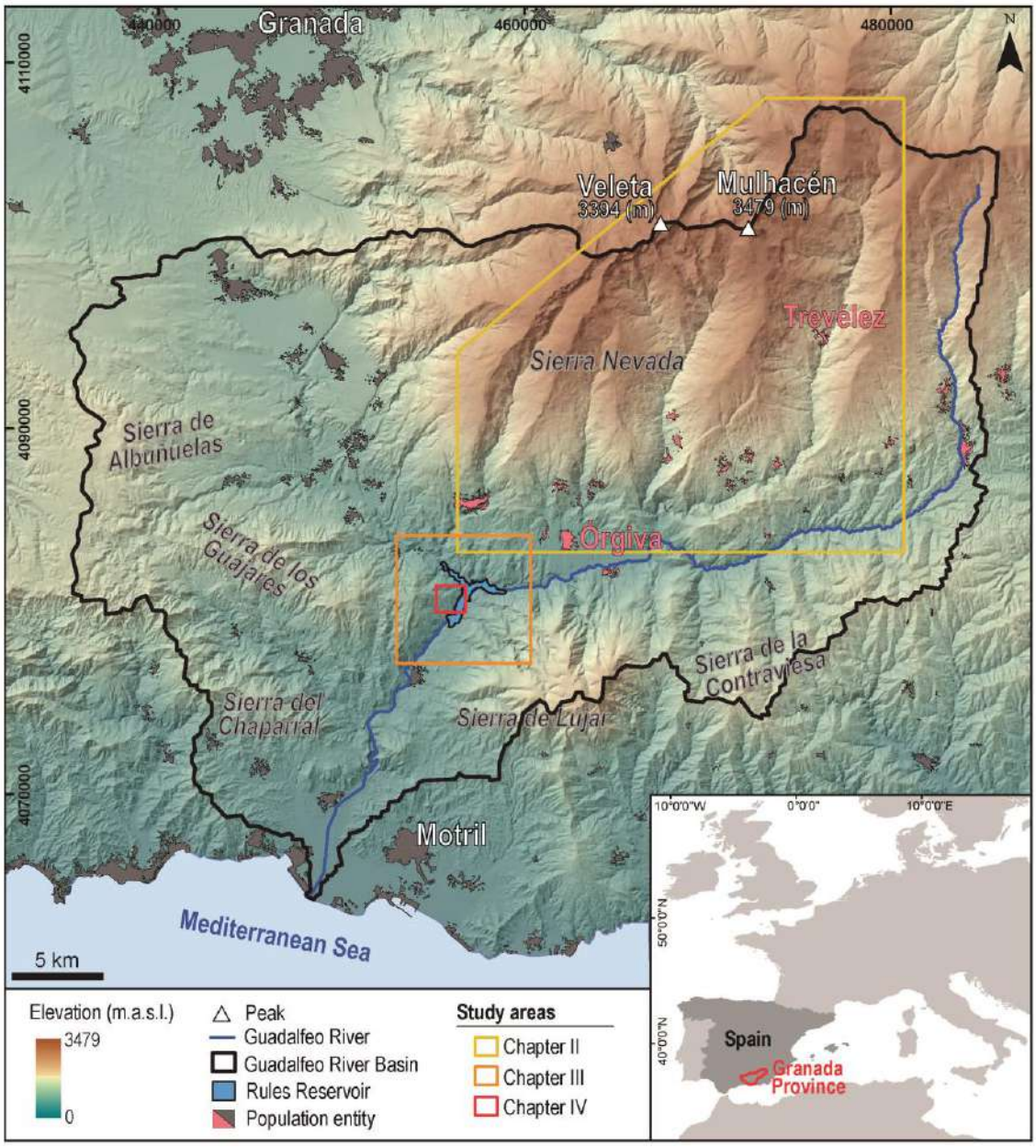

Figure 1. Location of the study areas in the Guadalfeo River Basin (Province of Granada, Southern Spain). Some geographical elements of interest are indicated: the main mountain ranges of the basin, the highest peaks, the Rules Reservoir, and population entities. The villages that comprise the region of 'La Alpujarra' are highlighted in pink polygons. The study areas of Chapters II, III and IV are also pointed out.

The change in elevation is wide enough to imply different climatic scenarios in the analysed zones. According to the Köppen classification, the climate varies from hot-

summer Mediterranean (Csa) in the Rules Reservoir area (150 m.a.s.l.) to Mediterranean-influenced subarctic climate (Dsc) in the Sierra Nevada (up to 3479 m.a.s.l. in the Mulhacén Peak) (Figure 1). Thus, the average temperature is 12ºC but it decreases around 0ºC in the Sierra Nevada's summits. The majority of the rainfall occurs from October to April, with annual mean precipitation ranging from 340 mm in the reservoir area to 750 mm in higher elevations, where snow is registered from 2100 m.a.s.l. Despite of this, the regional altitude gradients can cause the climate to change and generate erratic and strong rainfall events (Palenzuela et al. 2016). It is worth to mention two historical rainfall periods that affected the study areas, in 1996-1997 and 2009-2010, when the average annual precipitation was more than doubled (Irigaray et al. 2000; Chacón et al. 2007). In the case of the 1996-1997 event, the registered precipitation was more than 900 mm in just 4 months (Jiménez-Perálvarez et al. 2017).

4.2. Geology

The Betic Cordillera is a mountain range located in the south-southeast of the Iberian Peninsula, and it corresponds to the westernmost segment of the Alpine orogenic belt. It resulted from the Eurasia-Africa convergence and the progressive collision of the Alboran Domain (or microplate) with the southern Iberian paleomargin since the Eocene (DeMets 1994). Traditionally, the Betic Cordillera has been divided into the External Zones, the Internal Zones and the Campo de Gibraltar Complex. The Internal Zones are also referred as the Alboran Domain (Bouillin et al. 1986) and they are constituted by three main superposed tectono-metamorphic units that are, from lower to higher position: the Nevado-Filábride, Alpujárride and Maláguide complexes. At present, the Alpujárride and Maláguide complexes are firmly considered to be allochthonous tectonic units due to their westward migration across the western Mediterranean (Comas et al. 1992; Gutscher et al. 2012). However, recent investigations exclude the Nevado-Filábride Complex from the Alboran Domain and they support it being a subducted part of the south Iberian Paleomargin (Platt et al. 2006; Gómez-Pugnaire et al. 2012). The Maláguide Complex includes Paleozoic to Tertiary marine rocks that are not metamorphosed or barely metamorphosed, resulting mainly from the Variscan orogeny (Lonergan 1993). On the contrary, the Alpujárride and Nevado-Filábride complexes' rocks are intensely deformed and metamorphosed, that resulted from the Variscan and Alpine orogenies (Monié et al. 1991; Zeck et al. 1992). The study areas of this thesis are settled in the Internal Zones of the Betic Cordillera: the Rules Reservoir is placed within the Alpujárride Complex (mainly on phyllites), while the Nevado-Filábride Complex is the main outcropping geological unit in the Sierra Nevada (Figure 2).

The lithostratigraphic sequence of the Alpujárride consists on, from bottom to top (Azañón and Crespo-Blanc 2000): i) Paleozoic dark schists; ii) Paleozoic light schists and quartz-schists; iii) Permo-Triassic phyllites and quartzites; and iv) Triassic dolomitic marbles (Figure 2). A succession of Alpine deformational events, compiled by Simancas (2018), generated several structures at both small and large scale (i.e. foliations, lineations, folds and faults) that are observable in the Permo-Triassic phyllites and marbles. These deformational events (D) and the resultant structures are, from older to

younger: i) D_{1A}: defined by a foliation exceptionally preserved at microscopic scale in phyllites (Azañón and Goffé 1997); ii) D_{2A}: defined by a very penetrative foliation (S_{2A}) and an associated stretching lineation (L_{S2A}) with subparallel minor folds (F_{2A}) (Simancas and Campos 1993; Balanyá et al. 1997); iii) D_{3A}: defined by kilometre-scale, overturned, NW-vergent folds trending NNE-SSW (F_{3A}) with an axial planar foliation (S_{3A}) (Simancas and Campos 1993); iv) D_{4A}: constituted by low-angle faults (Galindo-Zaldívar et al. 1997); and v) D_N: linked to recent structures (from Serravallian to present) that include low-angle normal faults, large-scale upright folds and a perpendicular system of conjugate lateral faults (Jabaloy et al. 1993; Martínez-Martínez et al. 2002).

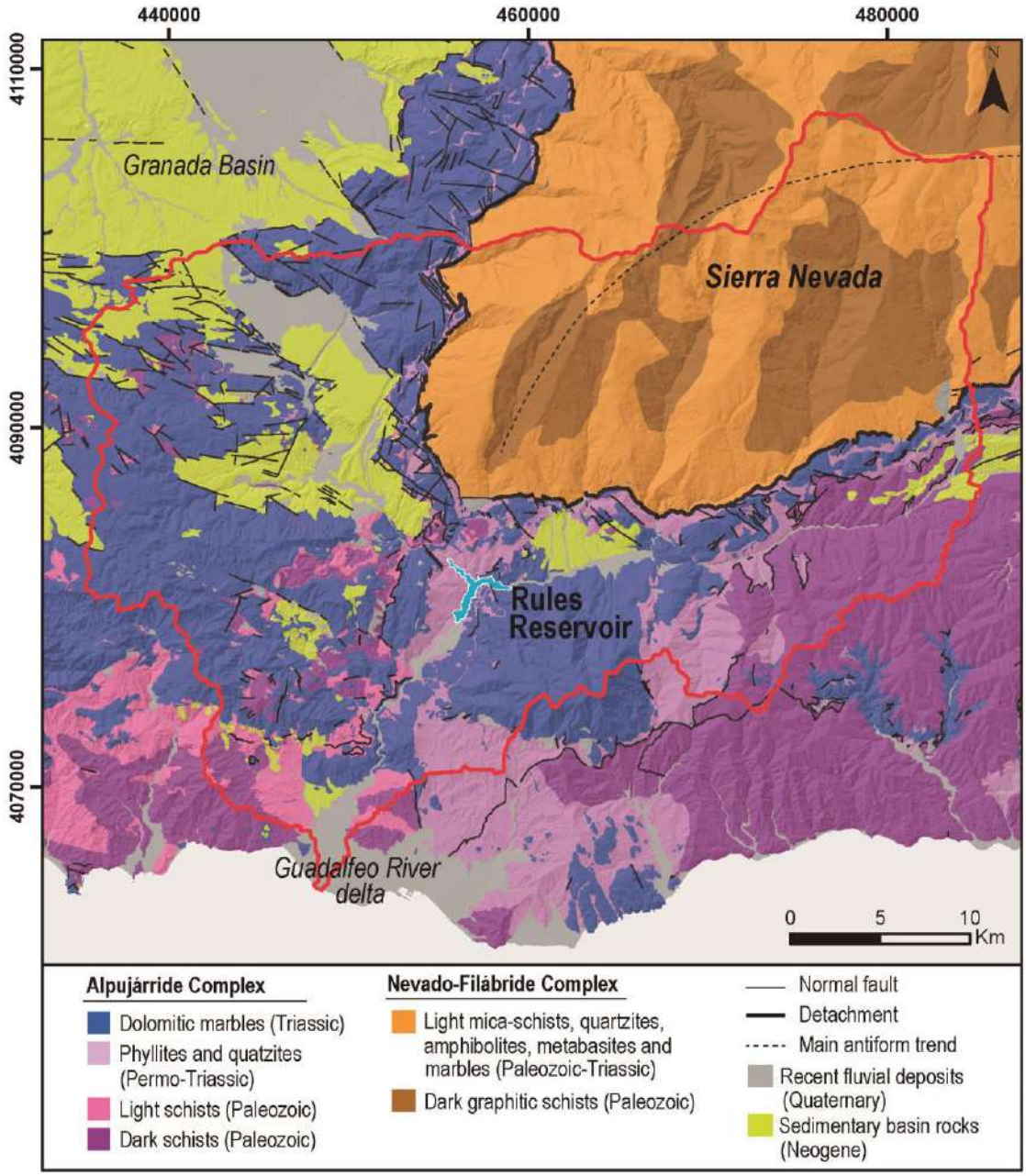

Figure 2. Simplified lithological map of the Guadalfeo River Basin, which is indicated by a continuous red line (modified from the Geological Map of Andalucía, https://www.ideandalucia.es/portal/). Some of the main tectonic structures, as well as the location of the Rules Reservoir and Sierra Nevada are also indicated.

The internal subdivision of the Nevado-Filábride Complex into different lithologic and/or tectonic units has been under discussion since the first investigations up to present. Several authors distinguish internal thrusts to define different tectonic units (García-Dueñas et al. 1988; Martínez-Martínez et al. 2002; Puga et al. 2002, 2011; Ruiz-Fuentes et al. 2018; Poulaki et al. 2023), while other authors propose a stratigraphically continuous sequence (Jabaloy et al. 1993, 2018; Gómez-Pugnaire et al. 2004, 2012; Sanz de Galdeano and Santamaría-López 2019). Compiling from the previous works, the lithostratigraphic sequence of the complex can be summarised, from bottom to top, as following: i) Paleozoic dark graphitic schists; ii) Paleozoic graphitic mica-schists with quartzites; iii) Permo-Triassic light schists with amphibolites and marbles; and iv) Triassic-Jurassic marbles, serpentinites and metabasites (Figure 2). The recognised sequence of deformational events and their nomenclature also differ depending on the authors. Compiled by Ruiz-Fuentes et al. (2018), these deformational events (D) and the resulting structures recognised in the schists are, from older to younger: i) D_1: defined by a relic foliation preserved in garnets (S_1) (Aerden and Sayab 2008); D_2: defined by a penetrative schistosity parallel to the bedding with metric/kilometric-scale isoclinal folds (Jabaloy et al. 1993, 2015); iii) D_3: resulting in upright folds trending NW to WNW, that deformed S_2 and generated a sub-vertical crenulation cleavage (S_3) (Aerden et al. 2013); iv) D_4: linked to the Nevado-Filábride-Alpujárride contact (i.e. a detachment fault) that is defined by a sub-horizontal shear band cleavage of several hundred meter-thick (S_4) (Aerden and Sayab 2008); and v) D_5: associated with the late- and post- Miocene folds trending NE-SW to E-W and related strike-slip faults that deform S_4 (Martínez-Martínez et al. 2002; Martínez-Martínez 2006).

The Eurasia-Africa slow convergence (4 mm/yr, according to DeMets et al. 2010) in combination with subduction processes have made the geodynamic evolution of the western Mediterranean and the Betic Cordillera complex (e.g. Royden 1993; Calvert et al. 2000; Brun and Faccena 2008; de Lis Mancilla et al. 2013; Williams and Platt 2018; Gómez de la Peña et al. 2021). As a result, compressive structures were formed coeval with extensional structures, that affected the Alboran Domain during its westward emplacement on the Iberian paleomargin during Miocene. This compression-extension coexistence has generated the main reliefs and the recent tectonic structures of the Betic Cordillera since Last Tortonian (Sanz de Galdeano and Alfaro 2004). The highest reliefs are related to large-scale NE-SW/E-W oriented antiforms, such as the Sierra Nevada (Figure 2) or Sierra de Lújar ranges, that have resulted from a NW-SE compression (Galindo-Zaldívar et al. 2003). An orthogonal extension has generated large NW-SE/E-W oriented extensional systems that have favoured the exhumation of the Internal Zones through low-angle detachment faults (Jabaloy et al. 1992; Sánchez-Vizcaino et al. 2001; Behr and Platt 2012) (Figure 2). These systems are also compounded by strike-slip and high-angle normal faults that have formed Neogene intra-mountain basins, like the Granada Basin (Figure 2) or de Alpujarran Corridor (Galindo-Zaldivar et al. 2003; Martínez-Martos et al. 2017; Madarieta-Txurruka et al. 2021). Overall, the sedimentary filling of these basins is characterised by a succession of Miocene marls, sandstones,

calcarenites and evaporites, followed by Plio-Quaternary fluvial-alluvial conglomerates (Fernández et al. 1993; Braga et al. 1990, 2003) (Figure 2).

Some of these extensional systems have evidenced recent activity, such as the Granada Basin's faults (Figure 2). The faults of the northern border of this basin are linked to the recent 'Granada 2021 seismic swarm', that reached a maximum intensity of V and a maximum moment magnitude (M_w) of 4.5 (Madarieta-Txurruka et al. 2022). This seismic sequence was felt in the metropolitan area of the city of Granada, but no damages were reported. Other significant seismic event occurred in the same basin border in 1956, with a M_w of 4.9 and a maximum intensity of VIII (Vidal 1986), that caused severe damages, dozens of injuries and 20 deaths (Chacón et al. 2007). Another important earthquake had its epicenter in the southwestern border of the Granada Basin in 1884, known as 'the earthquake of Andalucía'. The estimated M_w was 6.5 and the maximum intensity was X (Mezcua et al. 2004). More than 800 casualties and several destroyed villages were reported, being considered one of the most destructive earthquakes in the Iberian Peninsula during the past 200 years. This seismicity can also induce or reactivate landslides in the region, as it will be explained in Section 4.3.

4.3. Geomorphology

The Guadalfeo River has a typical concave-shaped longitudinal profile, with a steep upper reach (6º) that corresponds to the crestlines of Sierra Nevada, and a moderate average slope (~1º) in the middle and lower areas (Jabaloy et al. 2014). The high topographic gradients of the river and its basin have led to abundant bed load contributions generating fluvial deposits of gravels, cobbles and blocks up to tens of metres thick along the Guadalfeo River, as well as a deltaic system at its present-day outlet (Bergillos et al. 2016) (Figure 2). The construction of two reservoirs (Béznar in 1986 and Rules in 2004) regulate the 85% of the total runoff and they have also modified the hydrological regime of the basin, hindering the sediment transport into the coastal system (Avilés et al. 2006). Other anthropic activities such as channelisation and damming of the Guadalfeo River have contributed to the delta and coastline retreat (Bergillos and Ortega 2017).

The geomorphology of the Guadalfeo River Basin and the study areas is the result of the interaction of both endogenic (tectonics) and exogenic (fluvial, glacial and gravitational) processes. Active tectonics have conducted to the uplift and exhumation of the relief in the region, as explained in Section 4.2. The most recent estimated uplift rate was given by Azañón et al. (2015) in the Sierra Nevada Range: 0.3-0.4 mm/year in the western sector and 0.1-0.2 mm/year in the eastern sector. The resultant fluvial incision of the Guadalfeo River and its tributaries have generated erosional fluvial landforms, such as excavated rocky bed V-shaped valleys. Some examples are the Lanjarón, Chico, Poqueira and Trevélez tributary rivers that have generated incised valleys of ~1000 m depth in the southwestern sector of Sierra Nevada (Figure 1). Similarly, the Guadalfeo River has carved an incised valley along its upper sector as well as in the lower sector, where it has excavated a meandering gorge of 200 m height ('Garganta del Escalate'). The river incision rates were estimated by dating of travertine, ranging from 0.3 mm/year near the village of Vélez de Benaudalla (3 km downstream the Rules Reservoir) to 5.9 mm/year

near the village of Lanjarón (southwestern of the Sierra Nevada) (Chacón et al. 2001) (Figure 1). The geometry and steepness of the fluvial valleys have also conditioned the generation of glacial and gravitational landforms in the region.

The glacial development occurred in the Sierra Nevada range during the Last Glacial Maximum (30 ka ago) above 2500 m (Gómez-Ortiz et al. 2012). According to these authors, glaciers were adapted to the pre-existing morphostructure of the main valleys by filling their higher sections. The glaciarism history of the Sierra Nevada left a relevant imprint on the landscape of this range, and also in one of the study areas of this thesis (Chapter II). The glaciers were of small cirque type that formed classical U-shaped valleys, delimited by steep walls with sharp crests and including horn-shaped peaks such as the Veleta Peak (3394 m) (Gómez-Ortiz et al. 2022) (Figure 1). Lateral moraines are the most abundant depositional glacial landforms, being very well preserved in the headwaters of the Poqueira River (Gómez-Ortiz et al. 2002, 2012). Glacial retreat started after 19 ka with some readvances until the Holocene (Palacios et al. 2016), but the deglaciation of most of the range occurred around 15-14 ka ago, favoring the development of rock glaciers under a permafrost regime (Palma et al. 2017). Rock glaciers are very characteristic deposits of the Sierra Nevada (Gómez-Ortiz et al. 2002, 2012). They are located on the cirque walls at minimum elevations of 2500 and despite of being relict, they are extraordinarily well preserved. Glaciers finally disappeared 10-9 ka ago, with the beginning of the present interglacial period (Gómez-Ortiz et al. 2012). Afterwards, periglacial processes were intense until 7 ka ago and just a small glaciar persisted (the Corral del Veleta; 3150 m) in colder periods such as the Little Ace Age (14^{th}-19^{th} Centuries) (Oliva et al. 2016). This glacier was the southernmost one of Europe and it definitively disappeared in the mid-20^{th} Century (Gómez-Ortiz et al. 2018). At present, there is still one active rock glacier related to the degradation of such glacier (Gómez-Ortiz et al. 2012).

Gravitational landforms have been the main object of geomorphological studies in the Guadalfeo River Basin, as well as in the whole Province of Granada, since the 1980s. The first research initiative was a provincial-scale landslide inventory (Macau 1962) with the associated report (Macau 1963), where the Alpujárride Complex was pointed out as the most affected by ground instabilities. Two decades after, the Map of Slope Movements of the Province of Granada at 1:10000-scale was published (MOPU 1987), in which incidences related to slope movements are estimated to affect most of the province (30-60% of its total area). Most of the following research has been carried out by the group of Engineering Geology and Risks from the University of Granada, that has been developing its studies since 1985 (e.g. Chacón 1988; Chacón 1995; Irigaray 1995; Fernández et al. 1997; El Hamdouni 2001). The aforementioned mapping efforts were then included in the landslide inventory from the Natural Risks Atlas of the Province of Granada at 1:200000-scale (Chacón et al. 2007) (Figure 3a). This inventory was lately compiled and integrated in the Spanish Land Movements Database (BD-MOVES, http://info.igme.es/catalogo/), that was firstly published by the Spanish Geological and Mining Institute (IGME-CSIC) in 2016. The Guadalfeo River Basin has been one of the most analysed areas of the Province of Granada until nowadays. More recently, the

detection and study of landslides in this basin have been performed mainly through remote sensing techniques (Fernández et al. 2009; Palenzuela et al. 2016; Fernández et al. 2017) and GIS-based analysis (El Hamdouni et al. 2010; Jiménez-Perálvarez et al. 2011, 2017). The most common landslide types distinguished in the mentioned works are slides and flows, followed by complex landslides and rockfalls (Figure 3b). Many of these studies have conducted to similar conclusions: lithology and slope angle are the most important conditioning factors for landslide generation. A higher landslide occurrence is documented on steep slopes of around 16-22º, that are the result of the high river incision of the region (Chacón et al. 2007). Similarly, Jiménez-Perálvarez et al. (2017) estimated a predominance of translational slides produced on slopes with an average angle of 24º. Regarding the lithology influence, the Alpujárride phyllites and marbles are the most susceptible rocks to landslides, followed by the Nevado-Filábride schists (El Hamdouni et al. 2010; Jiménez-Perálvarez et al. 2011, 2017). Slides are prevalent on the Alpujárride phyllites and marbles, while flows and complex landslides are frequently developed on weathered Alpujárride phyllites, as well as in the Nevado-Filábride schists. Rockfalls are recorded mainly where the Alpujárride marbles outcrop (Jiménez-Perálvarez et al. 2011).

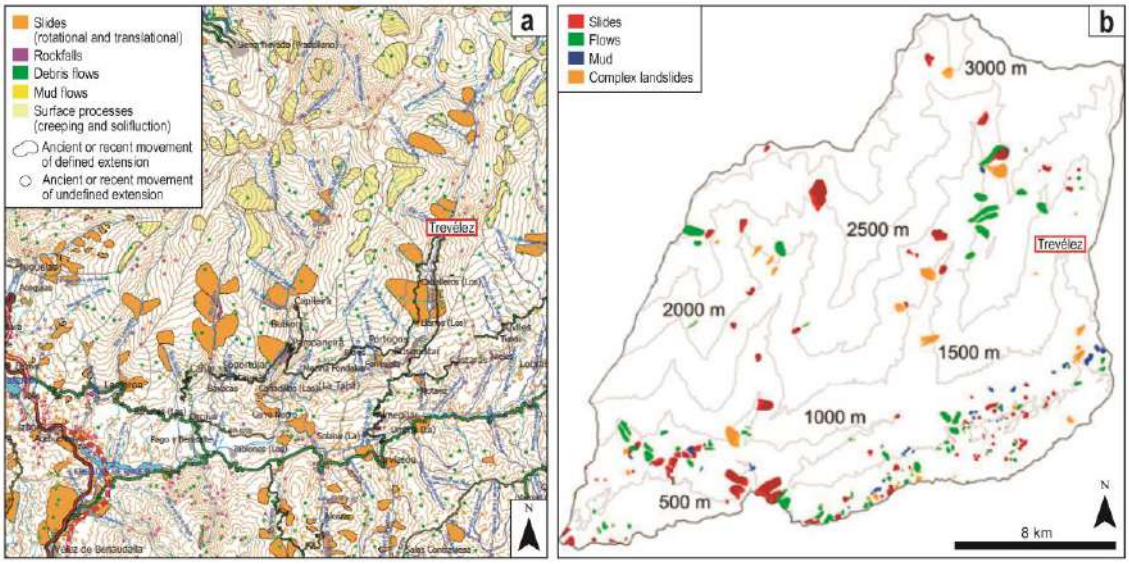

Figure 3. Landslide inventory maps of the southwestern sector of Sierra Nevada, modified from **(a)** Chacón et al. (2007), and **(b)** Jiménez-Perálvarez et al. (2011). The village of Trevélez is marked in a red rectangle as a reference with Figure 1.

Landslides can be triggered by extraordinary rainfall events (Varnes 1984), what is well-evidenced in the Province of Granada by historical events, previously mentioned in Section 4.1. For example, the 1997-1998 and 2009-2010 heavy rainfall periods generated landslides that seriously affected several villages of La Alpujarra (Irigaray et al. 2000; Jiménez-Perálvarez 2012). A recent probabilistic study of the Guadalfeo River Basin and the Granada Coast (Palenzuela et al. 2016) determined a return period of 13.2 years for anomalous rainfall periods that can trigger landslides, like the 1997-1998 and 2009-2010 ones.

As explained in Section 4.2, the regional geodynamic context makes the Granada Basin to be the most seismically active area in Spain, and earthquakes of a certain magnitude

are also a well-known triggering factor of landsdides (Varnes 1984). It is reported that the 1884 Andalucía earthquake triggered multiple rockfalls and rock avalanches, causing serious damages and injuries in several villages of the province (Chacón et al. 2007). As an example, the Güevéjar Landslide (located in the eastern border of the Granada Basin) was reactivated by the 1884 earthquake, as well as by the prior 1755 Lisbon earthquake (Rodríguez-Peces et al. 2011). These authors also establish that a reactivation of this landslide could be expected in the case of a moderate M_w earthquake (4.7-5.6), which is likely to occur related to the Granada Basin's faults. Similarly, the 1959 Atarfe earthquake generated some landslides and collapses that caused eight deaths in the epicenter's populations (Chacón et al. 2007). Some recent investigations are focused on predicting landslide reactivations under many possible earthquake magnitudes, not only in the Granada Basin (Rodríguez-Peces et al. 2014, Delgado et al. 2015) but also in the whole Betic Cordillera (Delgado et al. 2011).

5. Methodology

A multi-technique approach has been followed in this Ph.D. Thesis to obtain the necessary data for improving the previous knowledge of landslides in the selected study areas. This approach consists mainly on the application of Differential Interferometric Synthetic Aperture Radar (DInSAR) together with a variety of other geological methods. DInSAR is the principal method applied in this thesis, as it was the first step to develop the landslide research in the study zones. This technique allowed to detect new landslides for then, being analysed and described through the other complementary geological methods. In this section, further details of each used methodology, that are not included in Chapters II, III and IV, will be provided for a better understanding of the results and derived conclusions.

5.1. Satellite interferometry

Interferometry is a key technology in radar remote sensing that allows measuring ground displacement occurring between two or more satellite radar images in different times over the same area. This technique was first applied by Massonnet et al. (1993) to capture ground movement produced by the 1992 earthquake in California. Therefore, it is possible to identify unstable areas of the ground surface for then, relating them to natural or anthropic processes such as mining activities (López-Vinielles et al. 2020), glacier dynamics (Leinss et al. 2021), subsidence (Ezquerro et al. 2021), earthquakes (Béjar-Pizarro et al. 2018) or landslides (Barra et al. 2016). The aim of this section is to explain the main characteristics of the images acquisition and processing methods of DInSAR.

5.1.1. Radar imaging geometry

The Synthetic Aperture Radar (SAR) is an active sensor that emit microwaves pulses towards an area and then collects the signal that returns back to the sensor after reaching the ground surface (ESA 2007). This sensor is an imaging system of the Earth when it is carried by a satellite, usually at an altitude ranging from 500 to 800 km above the Earth's surface. The radar systems can operate in both dark and cloudy conditions, as the wavelength (λ) of microwaves ranges from one millimetre to one metre. Currently,

satellite SAR systems work in one of the following microwave bands, from higher to lower spacial resolution: X-band (λ = 3 cm), C-band (λ = 5.6 ~ 5.8 cm), and L-band (λ = 23 cm).

Starting with SeaSat (L-band) in the late 1970s, numerous satellite missions have been continuously launched, especially during the 1990s and 2000s, and they have provided large amounts of data to scientists, commercial users and public authorities. Other L-band satellites, launched by the Japan Aerospace Exploration Agency (JAXA), were JERS-1 (1992-1998), ALOS-1 (2006-2011) and ALOS-2 (2014-present). The first C-band satellites were ERS-1 (1991-2000) and ERS-2 (1995-2011), launched by the European Space Agency (ESA) and followed by ENVISAT (2002-2012). Other two C-band satellites were launched by the Canadian Space Agency (CSA): RADARSAT-1 (1995-2013) and RADARSAT-2 (2007-present). In the last decade, the ESA's Sentinel-1 constellation (C-band) was launched, that consists on the Sentinel-1A (2014-present), Sentinel-1B (2016-2021) and Sentinel-1C that will be launch in 2023. Regarding the high-resolution satellites (X-band), the first one was COSMO-SkyMed (2007-2021), from the Italian Space Agency (ASI), followed by TerraSAR-X (2007-present) and TanDEM-X (2010-present), both from the German Aerospace Center (DLR). Lastly, the Spanish satellite PAZ was launched in 2018 by a commercial company (Hisdesat) together with the Ministry of Defence of Spain.

For understanding the interferometry technique, it is necessary to describe how the radar satellite orbits work and how the acquisition geometry of the radar images is. The radar sensor adopts a side-looking geometry and emits the microwaves pulses to the ground surface in an oblique direction with a specific 'incidence angle', that is the angle defined by the incident pulse and the vertical to the intercepting surface (ESA 2007) (Figure 4). This angle usually ranges from 20º to 50º, depending on the satellite platform. The area of the ground that is covered by the radar signal (i.e. the illuminated area) is referred as 'swath'. The flight direction of the satellite is called 'azimuth' or 'line of flight' (Figure 4). Each flight direction is referred with a specific 'track' number and thus, all the images registered along that direction have the same track. The 'range direction' is the distance between the radar and the illuminated target of an image perpendicular to the azimuth. Therefore, azimuth and range are the reference directions of a radar image (Figure 4). The obliquity of the sensor implies that it can only look along the 'Line-of-Sight (LoS)' or 'slant range', which is the line that connects the sensor and the ground surface (Figure 4). A consequence of this obliquity is a geometric distortion in a radar image, that results in three effects: foreshortening, layover and shallowing (ESA 2007). These distortions usually affect topographic features like steep mountains or artificial targets like tall buildings, that are displaced from their desired orthographic position in an image. Foreshortening occurs when the relief or target have a compressed appearance, and layover is an extreme form of foreshortening when the relief or target appears to have fallen towards the radar. Shallowing is the absence of radar signal because of intervening reflecting or absorbing objects, that usually are concave or convex relief features. These geometric limitations must be considered and corrected for further processing of the images.

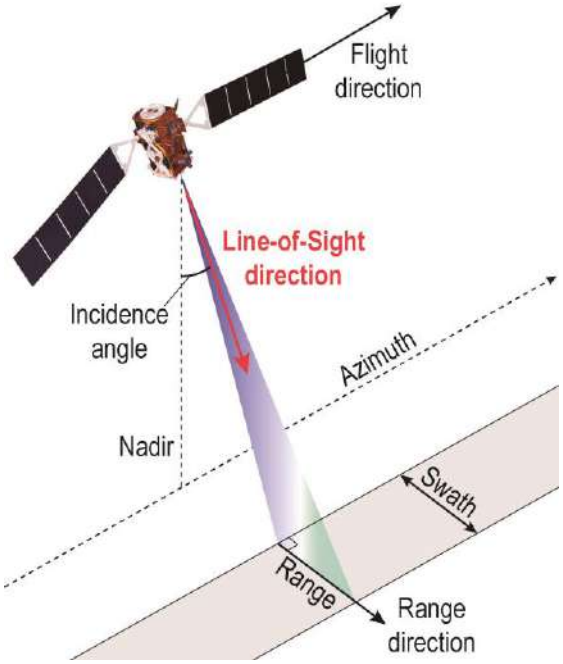

Figure 4. Geometry of a Synthetic Aperture Radar (SAR) system on board a satellite.

All the satellites equipped with SAR sensors travels around the Earth on a near-polar orbit and radar images are collected in two possible geometries of acquisition (or orbits): ascending and descending (Figure 5). Therefore, the same area is registered by images through both orbits. Along the ascending orbit, the satellite travels from the south pole to the north pole with a side-look to the east (Figure 5). Conversely, the satellite travels from the north pole to the south pole with a side-look to the west along the descending orbit (Figure 5). The existence of two orbits, together with the obliquity of the sensor, condition the nature of the SAR images-derived products and are key for their proper interpretation.

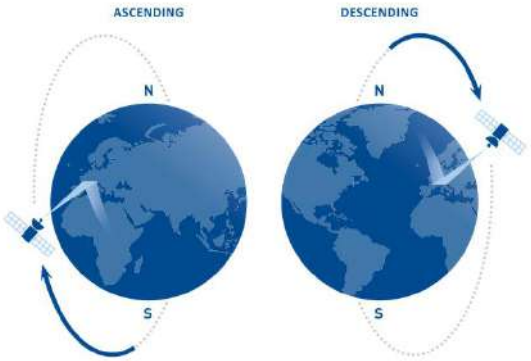

Figure 5. Acquisition geometries or orbits of a radar satellite (retrieved from TRE-Altamira 2023).

Sentinel-1 satellite

The images of the Sentinel-1 (S1) satellite have been used in this thesis. Therefore, some of its particular characteristics regarding the image acquisition needs to be clarified. Barra (2022) compiled the following peculiarities:

- **Wide area coverage**. The S1 operates in four exclusive acquisition modes, that depends on the dimensions of the illuminated surface area (i.e. swath). These modes are Stripmap (SM), Extra-Wide swath (EW), Wave (WV) and Interferometric Wide Swath (IW). The latter mode (IW) provides acquisitions over wide areas (250x250 km^2), what is possible through the use of the 'Terrain Observation with Progressive Scanning SAR' (TOPSAR) imaging technique. Due to its application, the image is subdivided in three sub-swaths, and each one is divided in nine fragments that are called 'bursts'. This characteristic allows to select and analyse independent bursts from a sub-swath of the image, what can optimise and accelerate the images processing.
- **Medium spatial resolution (C-band).** The S1 provides several product types that includes raw SAR data (Level-0), geo-referenced images (Level-1) and geophysical products derived from images (Level-2). The 'Single Look Complex' (SLC) is one of the Level-1 products, that consists on an image with a full resolution of ~4 m in range and ~14 m in azimuth. This resolution improves the applicability of the images for regional-scale analysis, and it also allows monitoring faster ground displacement than higher resolution bands (X-band) (Crosetto et al. 2010).
- **Reliable acquisitions.** The S1 IW acquisition mode is programmed to work in a conflict-free operational mode, what allows the creation of a consistent long-term image archive (Snoeij et al. 2008). This characteristic makes the Sentinel-1 a promising satellite for applications that require a long-term analysis or monitoring.
- **High temporal sampling.** The S1 acquires an image over the same area with a revisit period of 6 days or 12 days, having been improved in comparison with the previous C-band satellites. This characteristic is key to its application in interferometry, as the high temporal sampling allows measuring faster ground displacement and improves the S1 potential for a near-real-time monitoring application (Barra et al. 2016). Moreover, a shorter revisit time reduces the processing noise and increases the quality of the ground displacement measurements.
- **Free and easy download.** Finally, it is important to remark that S1 images can be freely and easily downloaded from the Copernicus Open Access Hub web portal (https://scihub.copernicus.eu/).

5.1.2. Fundamentals of the technique

The SAR image contains a measurement of two parameters of the radar signal in each image pixel: amplitude and phase. The amplitude is the strength or intensity of the backscattered signal towards the sensor that comes from the ground surface objects, referred as 'scatterers'. This amplitude mainly depends on the roughness of the scatterers. For example, exposed rocks and urban areas show strong amplitudes (i.e. strong backscattering), while smooth flat surfaces or water bodies show low amplitudes, as the signal is almost mirrored away from the sensor. Similarly, intermediate amplitudes are usually registered in vegetated areas, where a part of the signal is backscattered towards

the sensor and another is dispersed in opposite directions. The SAR amplitude image is generally visualised in grey scale colours, where bright pixels correspond to a strong backscattered signal and dark pixels correspond to low backscattering.

The phase of the SAR image is the fraction of one complete sine wave cycle (a single SAR wavelength). This phase is determined primarily by the distance between the sensor and the ground targets during the transmission-reception ('two-way travel') of the wave. Specifically, the phase is a measure of just the last fraction of this two-way travel distance. The phase change from one pixel to another within a single SAR image looks random and has practical no utility. Nevertheless, the phase component of two or more SAR images can be useful, as it is the basis of the SAR Interferometry (InSAR) techniques.

The InSAR techniques are based on the generation and exploitation of interferograms. An interferogram is the result of comparing two SAR images at different times (t_1 and t_2) by subtracting the phase of one image (Φ_{t_1}) from the phase of the other one (Φ_{t_2}) for each pixel of the images from the same location. This phase difference is the interferometric phase of the interferogram ($\Delta_{\Phi \mathrm{Int}}$), that includes other components (Equation 1):

$$\Delta\Phi_{\mathrm{Int}} = \Phi_{t_2} - \Phi_{t_1} = \Phi_{\mathrm{Topo}} + \Phi_{\mathrm{Disp}} + \Phi_{\mathrm{Atm}} + \Phi_{\mathrm{Noise}} + \mathrm{k} \cdot 2 \cdot \pi$$

(**Equation 1**)

Where Φ_{Topo} is the topographic contribution; Φ_{Disp} is the contribution due to ground surface displacement; Φ_{Atm} is the component of atmospheric perturbations due to propagation of the microwaves through the ionosphere and troposphere; Φ_{Noise} is the noise component related to other factors such as changes in the ground; and $\mathrm{k} \cdot 2 \cdot \pi$ is related to the phase ambiguity (k) in terms of the unknown number of 2π cycles.

The topographic component can be simulated ($\Phi_{\mathrm{Topo-simu}}$) by deriving it from a Digital Elevation Model (DEM) of the area covered by the SAR images. It can be subtracted from the interferometric phase to obtain the differential interferometric phase ($\Delta\Phi_{\mathrm{D-Int}}$). In this way, the topographic component is eliminated and just a residual component ($\Phi_{\mathrm{Topo-res}}$) remains (Equation 2):

$$\Delta\Phi_{\mathrm{D-Int}} = \Delta\Phi_{\mathrm{Int}} - \Phi_{\mathrm{Topo-simu}} = \Phi_{\mathrm{Disp}} + \Phi_{\mathrm{Atm}} + \Phi_{\mathrm{Topo-res}} + \Phi_{\mathrm{Noise}} + 2 \cdot k \cdot \pi$$

(**Equation 2**)

The calculation of the differential interferometric phase allows obtaining differential interferograms, which are the base of the so-called Differential Synthetic Aperture Radar Interferometry (DInSAR) techniques. When the residual topographic ($\Phi_{\mathrm{Topo-res}}$) and atmospheric contributions (Φ_{Atm}) are small, the noise level (Φ_{Noise}) is low, and the phase ambiguity (k) is zero, the main component that determines the value of the differential interferometric phase ($\Delta\Phi_{\mathrm{D-Int}}$) is Φ_{Disp}: the contribution due to ground displacement (Φ_{Disp}) during the time period between the acquisition dates of the two SAR images. Note that the residual topography can be easily minimised thanks to the current high-resolution DEMs, but the atmospheric contribution treatment is usually more challenging (Ding et

al. 2008). Therefore, a differential interferogram can be used to calculate the ground displacement between two images (d) (Equation 3):

$$d = \frac{\lambda}{4\pi} \cdot \Phi_{\text{Disp}} \qquad \textbf{(Equation 3)}$$

As DInSAR phases range from -π to π radians, the maximum differential interferometric phase that can be measured without ambiguity between two SAR images is $\pm\pi$. Therefore, if a ground displacement occurred, it can be detected by the phase difference between both images, as the phase of microwaves are very sensitive to ground surface changes. This fact constitutes the basis of the DInSAR technique (Figure 6).

The information of interferograms is used for punctual events with high displacement components, through single pairs of images acquired before and after the movements. A typical example of its application is co-seismic movements (e.g. Atzori et al. 2009; Béjar-Pizarro et al. 2018). To measure slower movements, it is necessary to make periodic observations over the same area, through multiple images at consecutive acquisition times. Therefore, a stack of images is compiled for then generating a network of interferograms, from which a progressive ground displacement can be registered. The techniques based on a stack of images and interferograms are generally called as Multi Temporal InSAR (MT-InSAR), which are also called as Advanced DInSAR (A-DInSAR).

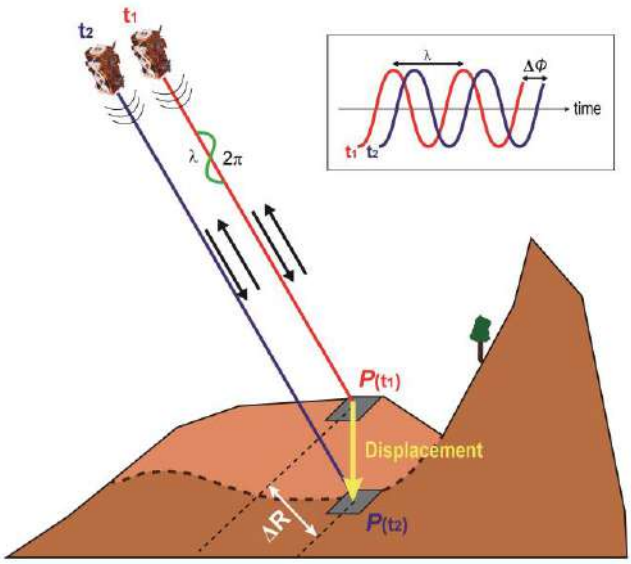

Figure 6. DInSAR basis concept (modified from Sousa and Bastos 2013). The ground displacement (ΔR) at the point *P* occurred between two radar images acquisition at different times (t_1 and t_2) results in a phase shift ($\Delta\Phi$) of the microwaves.

The output of a MT-InSAR processing is the estimation of the mean annual displacement (or velocity) and the accumulated displacement times series (TS) over a set of Measurement Points (MPs), that are spatially distributed on the ground. Not all the pixels of the images stack can be used (i.e. be selected as a MP) to estimate the ground displacement. For example, it can be measured only over the image pixels where the noise component (ϕ_{Noise}, Equation 2) is low. Similarly, ground displacement (ϕ_{Disp}, Equation 2) cannot be measured when it is too fast and higher than π between neighboring pixels. The

mean velocity and the TSs are the most relevant SAR-derived products for the study of ground movements during long periods of time (i.e. years).

5.1.3. Processing methods

In this thesis, the used data was derived from A-DInSAR methods but they are referred as DInSAR (Chapters II, III and IV) just to simplify the acronym. Several MT-InSAR or A-DInSAR processing approaches have been developed during the last decades. The two most common methods are the Persistent Scatterer Interferometry (PSI) and the Small Baseline Subset (SBAS). The main difference between both procedures is the criterium to select the Measurements Points (MPs) within the SAR images stack. Overall, a pixel is good enough (low noise) and appropriate to be selected as a MP if it maintains a strong and stable backscattered radar signal during the measured period of time. The temporal coherence (γ_t) is a quality index of each MP in terms of phase noise (ϕ_{Noise}, Equation 2). It varies between 0 and 1: high coherence means that ϕ_{Noise} is zero (i.e. a favourable MP) while low coherence indicates a noisy and unsuitable MP.

Persistent Scatterers Interferometry (PSI)

The PSI method is based on detecting Persistent Scatterers (PSs), which are ground targets or surfaces that generate a strong backscattering of the radar signal. These targets are typically anthropic structures (e.g. buildings or roads) or exposed rocks outcrops (Figure 7). A PS corresponds most often to one dominant or single scatterer in a ground pixel that maintain a high radar signal over the time (i.e. low noise) (Figure 7). Therefore, the PSI technique makes it possible to calculate displacement with a high precision and resolution, being particularly suitable for studies in urban areas. However, its effectiveness in rural environments (e.g. agricultural or forested areas) is more limited. Some examples of the developed PSI processing chains, that usually exploits images of X and C bands are: Permanent Scatterers (PSInSAR) (Ferretti et al. 2001), Interferometric Point Target Analysis (IPTA) (Werner et al. 2003), Spatio Stable Point Network (SPN) (Crosetto et al. 2008) or the Persistent Scatterer Interferometry of the Geomatic Division (PSIG) (Devánthery et al. 2014, 2019).

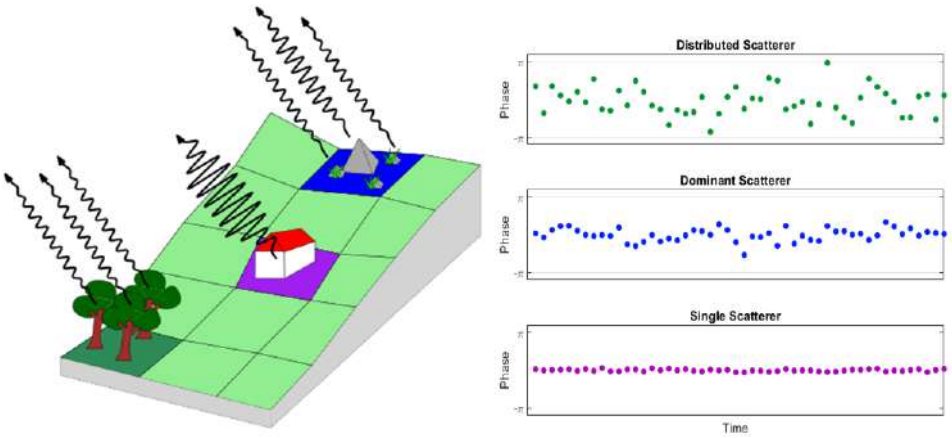

Figure 7. Schematic illustration of simulated SAR phases for distributed, dominant and single scatterers on the ground surface (retrieved from University of Stuttgart 2023).

The PSIG processing chain was developed by the Geomatic Division of the Centre Tecnològic de Telecomunicacions de Catalunya (CTTC), and it has been used in this thesis (Chapter III) during a 3-months stay (October-December 2018) in the CTTC under the supervision of Oriol Monserrat and Anna Barra. This chain is described in detail in Devánthery et al. (2014, 2019) and briefly explained in Section 3.1 of Chapter III. A general workflow of the PSIG chain was proposed by Barra (2022), which processing steps are summarised hereunder:

1 - Input data. The method requires an initial input of a stack of SAR images covering the same area, the precise orbit of each SAR image, and a DEM of the covered area.

2 - Image co-registration. The co-registration procedure consists on resampling all the SAR images with respect to a reference image, to ensure pixel-to-pixel alignment along the entire image stack.

3 - Interferogram and coherence generation. The interferogram network is generated through several combinations of pairs of images, being each image used for more than one interferogram generation (redundant procedure). The network is usually based on limits imposed to the temporal baseline, that is the time period between two successive acquisitions. The coherence of each interferogram is also calculated, that determines the similarity between pair of images and represent the level of noise of the interferogram. This coherence can be used to eliminate the noisiest interferograms and the related images. Afterwards, the topographic component ($\Phi_{\text{Topo–simu}}$, Equation 2) is simulated and subtracted from the interferometric phase ($\Delta\Phi_{\text{D–Int}}$, Equation 2) of each interferogram, by using the DEM and the precise orbits of each pair of images.

4 - Selection of Measurement Points (MPs) candidates. It is a fist selection of the pixels in the images stack that are potentially suitable (i.e. low noise) for the ground displacement calculation. Their real quality will be confirmed later during the processing (steps 6 and 7). The pixel selection is based on the Dispersion of Amplitude (DA) of the image stack (Ferretti et al. 2001), that measures the variability of the amplitude. A pixel is considered an appropriate MP if the DA is low, meaning that the backscattered signal (and amplitude) is strong and stable during the time covered by the image stack.

5 - Estimation of annual velocity and residual topography. The annual displacement or velocity and the topographic residuals ($\Phi_{\text{Topo–res}}$, Equation 2) are estimated for each MP, according to Biescas et al. (2007)'s methodology. The annual velocity represents the mean trend of the displacement in the period covered by the image stack, and it is approximated by a linear model. The topographic residuals are removed from the interferograms and they will be used for a precise 3D location (step 8). By using both the velocity and residual topography, the temporal coherence (γ_t) is estimated to select the MPs with lower noise.

6 - Phase unwrapping. This procedure is the most critical step of the processing, and it consists on estimating the phase ambiguity (k, Equation 2) in terms of space (2D) and time (1D).

- 2D-phase unwrapping. This process is performed for each interferogram. To correctly unwrap the phases, the difference between unwrapped phases of neighbouring MPs must be less than π. If the phase difference is higher than π, the ambiguity cannot be solved and spatial errors are then generated. Therefore, the actual capability to solve the ambiguity depends on other external factors, such as the density of MPs (the higher the density, the better the phase unwrapping is).
- 1D-phase unwrapping. This process is carried out for each MP to generate the displacement times series (TS). To correctly unwrap the phases, the sum of the interferometric components (Equation 2) for each interferogram must be smaller than π. Assuming that all the terms of Equation 2 except Φ_{Disp} are zero, the differential displacement of a MP occurred between the two images has to be less than $\lambda/4$ (Equation 3). If this condition is not achieved, temporal errors can be generated (e.g. underestimation of the displacement or displacement 'jumps' in the TSs). As explained in Devanthéry et al. (2014, 2019) the redundant observation for each image allows to iteratively check and eventually correct phase unwrapping errors. The final output of the 1D phase unwrapping is the temporal evolution of the phase, which is translated in displacement: one value per each acquisition date of the image stack, starting from the first image in which displacement is set as zero. The phases (and displacement) are referred to a selected MP that is considered as stable.

7 - Atmospheric component estimation. In this step, the atmospheric phase component (Φ_{Atm}, Equation 2) is estimated from the 1D and 2D phase unwrapping outputs. Its estimation is usually based on assumptions related to spatio-temporal characteristics of the data: Φ_{Atm} is spatially correlated but temporally uncorrelated, while Φ_{Disp} is correlated over time. Using the so-called low-pass and high-pass filters, Φ_{Atm} and Φ_{Disp} are separated for finally, removing Φ_{Atm} from the interferograms and performing again the steps 4, 5 and 6.

8 - Geocoding or geolocation. This final step allows to estimate the geographical or cartographic coordinates of the MPs, as they are settled in the radar geometry of the reference image by two coordinates: azimuth and range. This operation uses these coordinates of each MP, the orbit of the reference image, the residual topography and the DEM. This is the key step that enables the exploitation of the DInSAR products on a Geographic Information System (GIS) environment for their interpretation and further analysis. The output data consists on a set of points (maximum resolution of 14x4 m) that contains a value of mean annual displacement rate (in mm/yr) and a value of displacement (in mm) per each acquisition image date.

Small Baseline Subset (SBAS)

The SBAS method is based on detecting Distributed Scatterers (DSs), which are groups of small targets of similar size in a ground pixel that generate a lower backscattered radar signal, in comparison with PSs (Figure 7). These targets share a similar scattering response and they usually correspond to natural features, such as agriculture areas, open fields or bare soils (Figure 7). Despite that the SBAS methods imply a higher noise and a loss in resolution, they allow to analyse rural environments and arid areas with low vegetation and debris. The main SBAS processing chains, that usually exploits images of C and L bands, are: Small Baseline Subset (Berardino et al. 2002), Enhanced Spatial Differences (ESD) (Fornaro et al. 2007) and the Parallel Small Baseline Subset (P-SBAS) (Casu et al. 2014). It is worth to mention that other processing chains are able to combine PSs and DSs (hybrid methods) such as SqueeSAR (Ferretti et al. 2011).

The P-SBAS processing chain has been implemented within the European Space Agency (ESA)'s Geohazards Exploitation Platform (GEP), as detailed in De Luca et al. (2015). Its workflow is described in detail in Casu et al. (2014) and the processing steps are approximately similar to those of the PSIG chain, previously explained. Briefly, these steps are: (1) Input of SAR images, orbit information and DEM; (2) DEM conversion in SAR coordinates; (3) SAR image co-registration; (4) Interferograms generation; (5) Phase unwrapping; (6) Ground mean displacement calculation; and (7) TSs generation. This chain has been used in the present thesis (Chapters II and IV) in a fully automated and unsupervised manner through the GEP web portal (Figure 8), in the framework of the ESA Network of Resources (NoR) Initiative (Project ID: 63737, Project title: Monitoring ground instability in Southern Spain). The GEP access is free if an ESA NoR Project Sponsorship is conceded, that provides vouchers for a free-at-point-of-use consumption of the selected processing services for scientific research purposes. The GEP is an ESA initiative that provides satellite Earth Observation (EO) methods to support the needs of the geohazards community. It provides on-demand and systematic processing services for a specific user of both optical and SAR data, connecting to massive compute power on multi-tenant cloud computing resources. The P-SBAS processing chain is one of the multiple services (also called as 'thematic applications'), available at the GEP through a user-friendly web interface (Figure 8). For being an automated processing chain, the user only has to select the required input SAR images and decide on a few parameters through the app's web portal. The specific steps to request a processing and obtain DInSAR products are the following:

1 - Selection of the P-SBAS service. After the sign-in on the GEP Portal (https://geohazards-tep.eo.esa.int/), the 'CNR IREA SBAS Ground Motion Service' has to be selected from the available Thematic Applications (Apps). After opening the processing service, its specific window comes into view, which consists of three panels: selection, global map and service (Figure 8).

2 - Selection of the input images. Through the global map panel (Figure 8), an Area of Interest (AOI) can be selected by using the drawing tools. Then, the service shows the available images within this AOI. There is also a list of search parameters that helps in

filtering the images to find the required ones in an easier manner. The most useful parameters are:

- Start and end of the temporal interval of the images.
- Orbit direction. It is chosen between ascending or descending.
- Track. A number or interval to request the range of orbit tracks.
- Platform. It is chosen between Sentinel-1A or Sentinel-1B. If any of these are selected, the images of both satellites appear by default.

Once the images appear in the selection panel, according to the defined AOI and parameters, they have to be selected and dragged into the 'Sentinel-1 input SLCs' tab of the service panel (Figure 8).

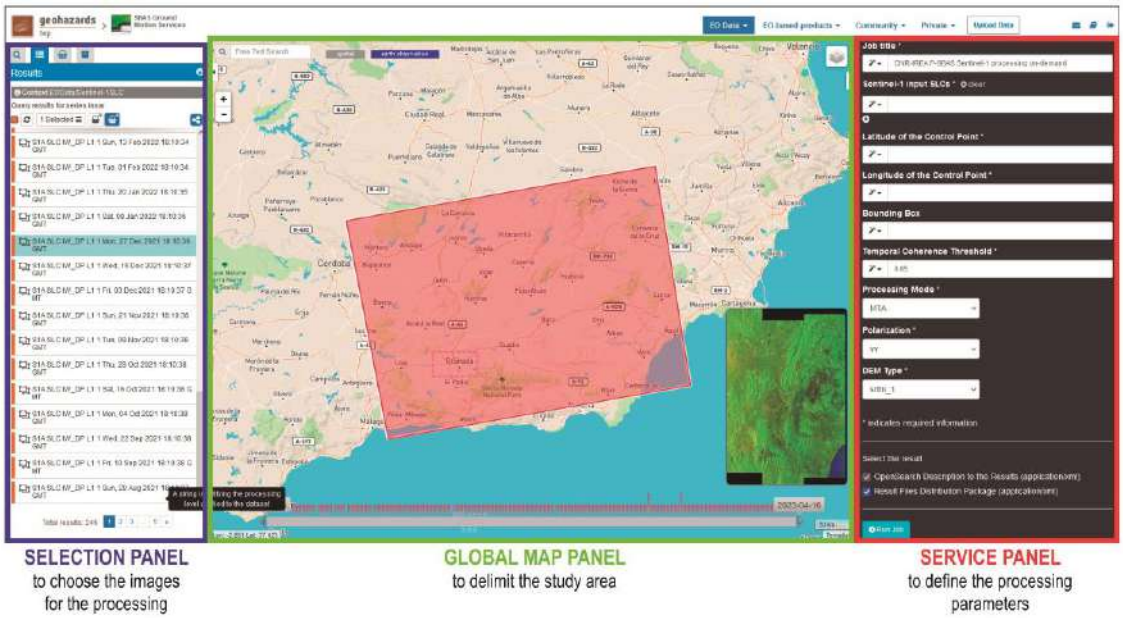

Figure 8. Web portal of the Parallel Small Baseline Subset (P-SBAS) processing service in the Geohazards Exploitation Platform (GEP). The selection, global map and service panels are also indicated.

3 - Selection of processing parameters. Just a few parameters have to be decided for the processing through many tabs within the service panel (Figure 8), that are the following:

- Latitude and longitude of the control point. This parameter is to introduce the coordinates (in decimal degrees) of a selected point that is considered as stable. This reference point is used for the phase unwrapping procedure and the ground displacement calculation. It should be located in a stable area or where the displacement behaviour is known and preferably, in expected coherent areas (e.g. urban areas).
- Bounding box. This parameter allows to perform the analysis in a restricted area that can be the previously defined AOI.
- Polarisation. Any of the four available polarisations (vv, vh, hh, hv) can be selected. The recommended value is vv, being the default Sentinel-1 images polarisation for data acquired over land.

- Processing Mode. One of the two processing modes has to be selected: Multi-Temporal Analysis (MTA) or Interferogram Generation (IFG). The IFG mode's output is an interferogram and requires just two input images. The outputs of the MTA mode (the one used in this thesis) are the mean displacement (or velocity) data and the corresponding time series of accumulated displacement (TSs).
- DEM Type. An input DEM of the Shuttle Radar Topography Mission (SRTM) is required and there are two available types with different spacial resolutions: SRTM-1 (30 m) and SRTM-3 (90 m).
- Temporal coherence threshold. A temporal coherence (γ_t) value ranging from 0.7 to 0.9 has to be introduced. This value discriminates the number of points to be obtained, where the displacement is calculated (MPs). For example, if the value is settled at 0.85 (default value), only points with a temporal coherence higher than 0.85 will be used for the processing. Note that the temporal coherence is related to the degree of noise: the lower coherence threshold is stablished, the noisier results will be obtained.

4 - Run the processing. After clicking the 'Run Job' button in the service panel (Figure 8), the processing will appear as successful or failed after about 48 hours. Meanwhile, the progress of the running job can be followed (in % completed). In case of obtaining a failed job, an error code appears (e.g. Error 20 - idl executables failed, processing aborted). To report the issue about the job execution and/or claim for assistance, the technical support can be contacted by clicking on the 'Contact Support' button on the service panel.

5 - Download and visualisation of results. Finally, the results of a successful job can be shown for a preliminary view. The mean ground displacement data appear on the global map panel and a TS viewer also appear after clicking on a displacement point. By clicking the 'Download' button, the DInSAR results are provided in .csv format for its later management in a GIS as a set of points. Each point (resolution of 90x90 m) has a value of mean annual displacement rate (in cm/yr) and one value of displacement (in cm) per each acquisition image date.

5.1.4. Interpretation and post-processing of the data

The ground displacement data, both mean and accumulated, is always calculated along the satellite LoS direction, what is an oblique view. This is an important characteristic of the DInSAR data that must be taken into account for its proper interpretation. Therefore, the detected displacement is registered as approaching or distancing from the satellite: negative values indicate that points move away from the satellite, while positive values refer to points moving toward the satellite (Figure 9). Note that displacement over the same unstable same area can be registered oppositely by both acquisition geometries (e.g. negative values in ascending geometry are positive values in descending geometry, or vice versa) (Figure 9). In some cases, the measurement sensitivity may be lower in one geometry than in other. Similarly, the sensitivity decreases when the ground movement occurs along the north-south direction, being parallel to the satellite azimuth or flight direction. The LoS acquisition also implies that the measured displacement may be an apparent component and not the true displacement. This fact is an intrinsic limitation of

the DInSAR technique, which may result in movements being undetected or underestimated (Schlögel et al. 2015).

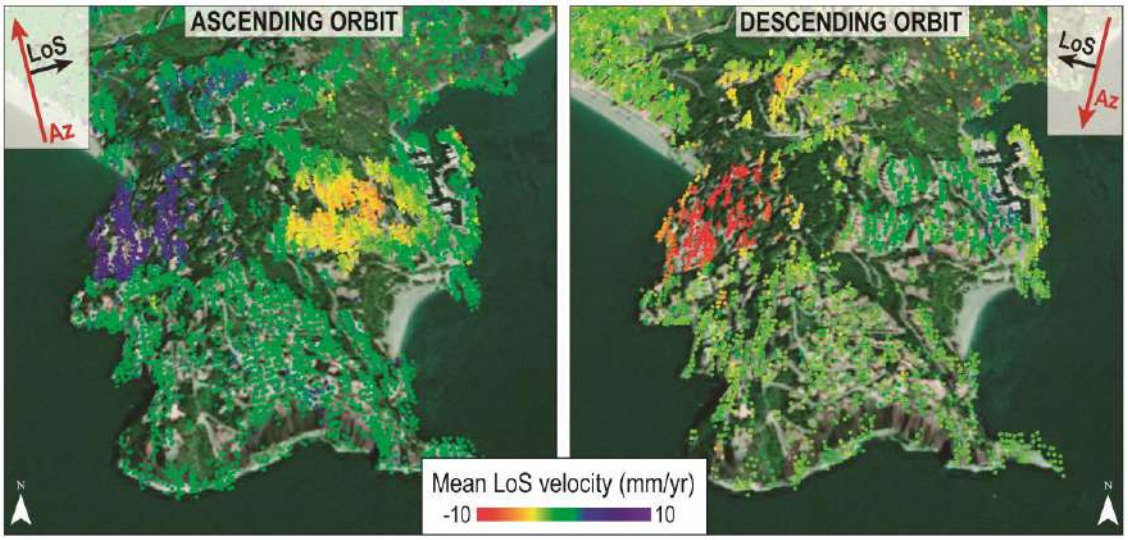

Figure 9. Maps of mean velocity or displacement rate of the ground surface, measured along the satellite Line-of-Sight (LoS) in two different acquisition geometries: ascending and descending orbits (retrieved from EGMS 2023).

In order to properly visualise the mean displacement or velocity data in a plan view map, a stability range has to be established to differentiate stable from unstable points. The most common procedure is to established a threshold according to the standard deviation (STD) of the mean velocity data, being typically established as two times STD (Barra et al. 2017). As an example, for a displacement data set with average velocity of 0 mm/yr and a STD of 2.5, the stability range would be settled between 5 and -5 mm/yr. The stability ranges for medium resolution processing (C-band satellites) typically are from [4, -4] to [6, -6] mm/yr, while X-band satellites can provide higher resolution results with stability ranges of [2, -2] mm/yr. This stability range can be reduced or increased depending on the quality of the measured points. As explained in Section 5.1.3, the temporal coherence value controls the number of measured points and it also influences on determining the stability range: if only the points with the highest temporal coherence (i.e. the most reliable) are taken into account, this range can be smaller (i.e. more precise results). On the contrary, by lowering the coherence threshold, the number of points is increased but the precision of the displacement measurement can be lost (i.e. the stable range is higher). It is important to remark that the stability range also represents the general noise of the results (i.e. the sensitivity of the technique). This fact implies that a displacement point classified as stable can be either 'truly stable' or 'unstable but non-detected'. According to the stability range, equal intervals are defined to classify the velocity points usually represented in different colours: green for stable points (values around zero), red for negative values, and blue for positive values (Figure 8). The visual inspection of the mean displacement or velocity maps have been carried out in all the study cases of this thesis (Chapters II, III and IV).

Additional post-processing operations can be carried out from the LoS displacement rate or velocity points. When data of both acquisition geometries is available, a 2-D

displacement field can be derived. This procedure has been carried out in this thesis (Chapter IV) for the case of the El Arrecife Landslide. Assuming that the north component is negligible, the eastward and vertical components of the displacement can be calculated is a GIS environment (see procedures in Notti et al. 2014; Béjar-Pizarro et al. 2017) (Equations 4 to 9) (Figure 10). The Inverse Distance Weighted (IDW) method (power 2, search radius 200 m, 1 point minimum) was used to interpolate the ascending ($vLoS_a$) and descending ($vLoS_d$) velocities (from points to rasters) for then, applying the following equations through the raster calculator:

$$V_{eastward} = \frac{\left(\left(\frac{vLoS_d}{H_d}\right) - \left(\frac{vLoS_a}{H_a}\right)\right)}{\left(\frac{E_d}{H_d} - \frac{E_a}{H_a}\right)} \quad \textbf{(Equation 4)}$$

$$V_{vertical} = \frac{\left(\left(\frac{vLoS_d}{E_d}\right) - \left(\frac{vLoS_a}{E_a}\right)\right)}{\left(\frac{H_d}{E_d} - \frac{H_a}{E_a}\right)} \quad \textbf{(Equation 5)}$$

Being:

$$H_a = \cos(\alpha_a) \quad \textbf{(Equation 6)}$$

$$H_d = \cos(\alpha_d) \quad \textbf{(Equation 7)}$$

$$E_a = \cos(90 - \alpha_a) \cdot \cos(270 - \gamma_a) \quad \textbf{(Equation 8)}$$

$$E_d = \cos(90 - \alpha_d) \cdot \cos(270 - \gamma_d) \quad \textbf{(Equation 9)}$$

Where H_a, H_d, E_a and E_d are the direction cosines of the ascending (a) and descending (d) LoS displacement vectors, that are estimated from the incidence angles (α_a and α_a) and the LoS azimuths (γ_a and γ_d) of ascending (a) and descending (d) geometries.

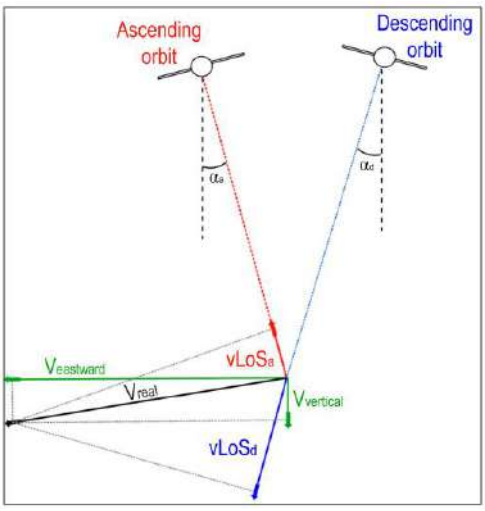

Figure 10. Geometrical relationships between the incidence angle of the two satellite geometries and their velocities ($vLoS_a$ and $vLoS_d$) with the actual velocity (V_{real}) and the east and vertical components of the displacement ($V_{eastward}$ and $V_{vertical}$) (modified from Béjar-Pizarro et al. 2017).

The accumulated displacement data (in mm) is usually represented versus the total temporal span (dates) in a graphic, which is referred as a 'time series' (TS). Each of the measured points has a record of such accumulated displacement, and a TS can be represented individually or as an average TS of a group of points. It is common that a TS presents anomalous and misleading trends as a result of residual atmospheric noise of the processing. To avoid misattributing this trend to actual ground movement patterns, a raw TS can be referenced to a stable neighbour point (or group of stable points) to reduce such noise (Figure 11a). This procedure is done just by removing the trend or background pattern of the stable point, thus obtaining a filtered TS that reflects more accurately the true ground movement (Figure 11b). The analysis of TSs has a great potential for a more detailed study of the displacement patterns and trends, especially focused on accelerations and decelerations of the movement. Moreover, it is a common practice to compare the temporal behavior of the displacement with typical triggering factors of ground movement or instabilities such as rainfall, groundwater or reservoir water level variations, earthquakes, etc. The TSs analysis has been carried out in Chapters III and IV of this thesis.

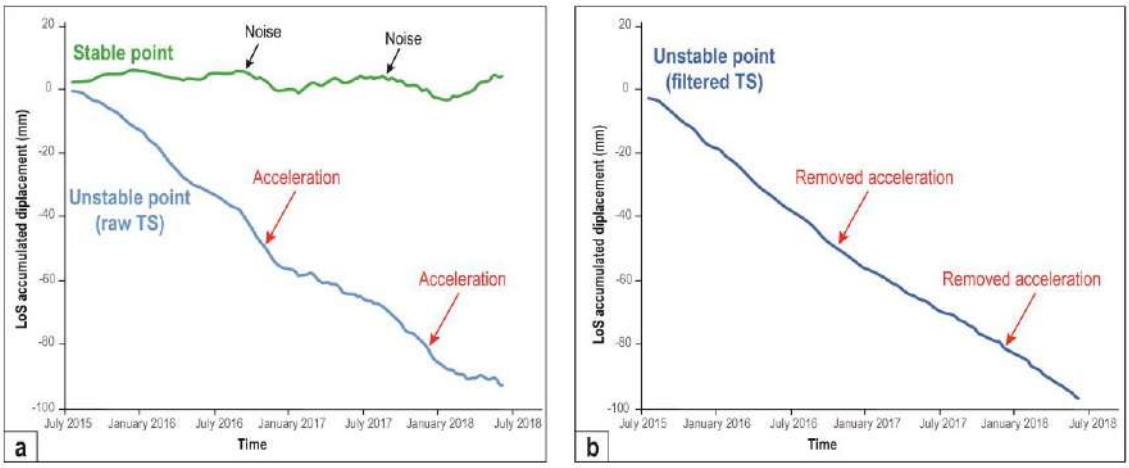

Figure 11. Procedure of noise filtering of the time series of accumulated displacement (TSs), illustrated by using the example of the El Arrecife Landslide (Chapter III). **(a)** Raw TSs of a stable and an unstable point. Notice the noise of the stable point TS, reflected as bounces of the line and indicated with black arrows. The accelerations of the unstable point raw TS are evidenced by increases in the slope of the line (indicated with red arrows), that generates a stepped trend of the TS. **(b)** Filtered TS of the unstable point of Figure 11a. Once referenced to the stable point, the noisy accelerations disappear and the trend of the TS becomes linear.

5.2. Geological methods

This section compiles the description of all the procedures and techniques that were used for the geological characterisation of landslides. These geological methods include methodologies from different geological disciplines such as geomorphology, structural geology and geophysics (Ground Penetrating Radar); together with photogrammetry (Structure-for-Motion); and geomatics techniques, that includes Landscape Analysis and other data analysis on a GIS environment (volume estimation). It is important to remark that some of these methods have been applied in a collaborative manner, and the people involved in the execution of each method and their specific work will be mentioned

during this section. DInSAR techniques were applied in the three study cases of this thesis, but notice that not all the geological methods were applied in all of them (Table 1). The aim of this section is to provide further descriptions of both the fundamentals and the analysis steps of each geological method, that are not as widely explained in Chapters II, III and IV.

Technique \ Study area		Sierra Nevada (Chapter II)	Rules Reservoir (Chapter III)	El Arrecife (Chapter IV)
Differential Synthetic Aperture Radar (DInSAR)		✓	✓	✓
Geological methods	Geomorphological investigation	✓	✓	
	Landscape Analysis	✓		
	Structural and kinematic analysis			✓
	Volume estimation			✓
	Ground Penetrating Radar (GPR)			✓
	Structure-for-Motion (SfM)			✓

Table 1. Summary of the techniques used in this thesis in each of the three study cases: the Sierra Nevada Range, the Rules Reservoir and the El Arrecife Landslide.

5.2.1. Geomorphological investigation

The geomorphological investigation mainly consisted on the recognition and delimitation of the landslides' boundaries to provide accurate landslide inventory maps at regional-scale. These inventory maps were produced for the southwestern sector of Sierra Nevada Range and the Rules Reservoir area (Chapter II and III, respectively). A more comprehensive inspection of landslide-related features was carried out at site-scale in some selected landslides of the Rules Reservoir's slopes (Chapter III) to provide detailed geomorphological maps. The recognised landforms of these maps include main and secondary scarps, benches, cracks and lateral boundaries of landslides, as well as other anthropic, fluvial and runoff features. To produce the geomorphological and inventory maps, the following procedures were applied:

- **Photo-interpretation**. By using stereoscopic pairs, the aerial images from the American Flight (1956-1957) and the PNOA project (2004 to 2017) were explored. These photos were freely downloaded from the Spanish Geographical Institute (https://fototeca.cnig.es/fototeca/).
- **Analysis of digital data.** Carried out in a GIS environment, this analysis was based on the exploration of 2-m and 5-m resolution DEMs (freely available at https://centrodedescargas.cnig.es/) and their derived products: hillshade, slope, aspect, rugosity, and topographic openness maps. These products of raster type were also exported to Google Earth for a 3-D visualisation by using the Global Mapper GIS (File > Export Raster > Export KMZ). Other digital information of

interest was also managed, such as the 1:50000-scale Geological Map of Spain (MAGNA) or the land movement database (BD-MOVES), both from the Geological Institute of Spain (IGME-CSIC) and available at https://info.igme.es/catalogo/.

- **Field survey**. This step was necessary to perform an in situ visual identification of landslide morphologies and deposits to elaborate the geomorphological and inventory maps as accurate as possible. The observations made in the field were also essential to validate those made by photo-interpretation and digital analysis, as well as to validate the ground displacement detected by DInSAR techniques. Moreover, a comprehensive inspection of damages in infrastructures (e.g. roads) or cracks within the landslides' bodies was also carried out (Chapters III and IV). Around thirty days of fieldwork were performed to achieve the objectives of this thesis.

The main types of landslides identified in this thesis, as it will be shown in Chapters II, III and IV, were Deep-Seated Gravitational Slope Deformations (DGSDs), rockslides, rotational slides and translational slides. Information about their general morphological characteristics were not provided in these chapters. For this reason, a summarised description of the main attributes of these landslides is presented below.

Deep-Seated Gravitational Slope Deformations

These slope movements were referred as DGSDs by Dramis and Sorriso-Valvo (1994) but also as DSGSD, according to Agliardi et al. (2001). DGSDs involve large to extremely large areas and volumes of rock with a very low displacement rate (mm/yr to cm/yr) over long periods of time. They are usually developed in mountainous areas, affecting the entire length of high-relief valley flanks. DGSDs are characterised by discontinuous or poorly defined boundaries and it is common to find them contiguously, sharing the same boundary that can coincide with a tributary stream (Crosta et al. 2013). These movements do not have a well-defined sliding surface (Figure 12), where a visco-plastic deformation occurs at depth of slopes (Bisci et al. 1996). Their typical morpho-structural features are doubled ridges, ridge top depressions, scarps and counterscarps, trenches, open tension cracks and bulging of the slope toe with multiple secondary movements (Figure 12). DGSDs can be related to active tectonics (Moro et al. 2009) but typically, DGSDs are prehistoric landslides that may have been predisposed and triggered by numerous and different processes such as glaciation, de-glaciation, exceptional rainfall events, seismic activity or valley incision (Crosta et al. 2013). DGSDs are widespread in alpine regions (Agliardi et al. 2013; Jarman et al. 2014; Del Rio et al. 2021; Crippa et al. 2021) under tectonic exhumation contexts (Agliardi et al. 2013), where the constant relief uplift has produced a high fluvial downcutting of slopes and incision of valleys (Tolomei et al. 2013; Tsou et al. 2015). DGSDs have been recognised to affect different lithologies at many worldwide locations, but foliated metamorphic rocks are more prone to their occurrence (see Crosta et al. 2013 and references therein). Secondary medium-scale slope movements, such as rotational slides or rockfalls, are usual within the lower sectors of DGSDs. For this reason, they imply a usual non-considered hazard due to the potential

high velocity of these secondary movements that may generate risky situations (Soldati 2013). This means that the presence of DGSDs may help to identify large slopes that may be susceptible to catastrophic landslides in the future.

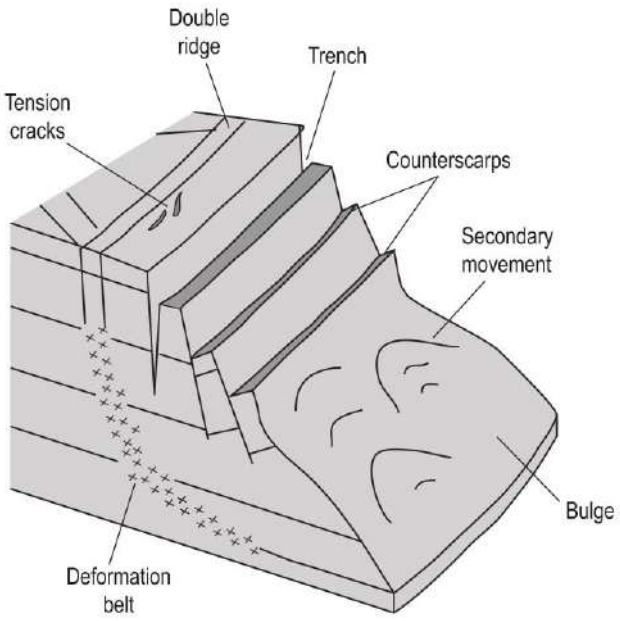

Figure 12. Schematic illustration of the typical morpho-structures of a DGSD (modified from Soldati 2013).

Rockslides

There are many discussions on which slope movements should be included in this category (Sorriso-Valvo and Gullà 1996). In this thesis, the slope movements identified as rockslides are based on the descriptions of 'rockslide' in Crosta et al. (2014) and 'deep-seated rock slides' (DSRSs) in Borrelli and Gullà (2017). In these works, rockslides are defined as complex phenomena that includes rotational, planar and compound deep slides that result from the combination of long-term predisposing factors to slope failure (e.g. geological structure, tectonics, slope morphology), and short-term triggering causes (e.g. snowmelt, fluvial erosion of the toe of slopes, rainfall, seismicity). Rockslides can occur in high-relief valley flanks and can reach very large volumes, often related to DGDSs (Dramis and Sorriso-Valvo 1994; Ambrosi and Crosta 2006). They may be easily identified through clear morphologies on the slope, such as (1) well-defined main scarp and flanks; (2) a scar with debris; or (3) a chaotic mass of rocky debris, especially at the toe of the slide. These slope movements are characterised by velocities on the order of few cm/yr, showing correlation with seasonal and annual changes of external factors such as rainfall, snowmelt or temperature and groundwater level oscillations. This long-lasting displacement progressively worsen the geomechanical properties of the involved rocks and can damage infrastructures. Moreover, they can result in unexpected and catastrophic failures (rock avalanches) under certain external conditions, such as strong rainfall or earthquakes (Chigira 2009).

Rotational slides

These slope movements consist of displacement of a mass body along a relatively narrow surface of rupture that is curved concavely upward (spoon-shaped) (Varnes 1978). The shape of this surface is often influenced by the pre-existing discontinuities of the rocks, such as faults, joints, bedding or lithological contacts. The morphology of the rotational slides is characterised by (1) a prominent main scarp of amphitheatre-shaped; (2) a system of secondary scarps with related benches, that forms many different minor internal mass bodies; and (3) limited internal deformation, evidenced as back-tilted blocks (Hungr et al. 2014). These slides tend to move in a ductile manner at slow or moderately slow velocities (mm/year) as the rotational mechanism is self-stabilising, what means that driving forces decrease with increasing displacement over time. Rotational slides typically occur in very weak rock mass that are subjected to the overburden pressure of stronger rocks. As this type of slides are very frequent, their incidence among anthropic infrastructures (e.g. embankments, dams, highways) is high relative to other types of landslides, for which they have been more actively studied to face instability problems (Varnes 1978). These landslides imply a particular hazard due to the possible occurrence of extremely large rock avalanches, related to the destabilisation of the more cohesive rocks (e.g. D'Alessandro et al. 2002).

Translational slides

These slope movements consist of displacement of a mass body along a more or less planar or gently wavy surface or rupture (Varnes 1978). Translational or planar slides occur at all scales mainly in layered, folded sedimentary and metamorphic rocks, which fail along the bedding, schistosity and faults planes (Hungr et al. 2014). Planar slides reach velocities higher than rotational slides, because the mass movement along a planar surface of rupture does not reach a new equilibrium condition until the bottom of the slope (i.e. the movement is not self-stabilising). If the mass initiates the movement under conditions favourable to the low dissipation of energy by friction, the movement may accelerate rapidly (Sorriso-Valvo and Gullà 1996). This fact means that the slide mass may continue to move indefinitely and reach extremely high velocities (m/s) in the case of failures, especially when they occur on very flat-dipping discontinuity planes and/or very weak rocks. Therefore, the destructive power of a rapid translational slide can be enormous in case of rapid slide. Many of the largest and most damaging landslides on the Earth were translational slides, as in some cases, they can be initiated as slides and rapidity disintegrated and transformed into rock avalanches (Roberts and Evans 2013).

5.2.2. Structural and kinematics analysis

This method was exclusively applied to the El Arrecife Landslide (Chapter IV) and it consisted on (1) a field-based structural study of the landslide's slope, followed by (2) a kinematic analysis to obtain its instability conditions. A summary of the analysis' steps with some additional information, not present in Chapter IV, is provided as follows:

1 - Structural study. It consisted on carrying out a field survey to make measurements of the main deformation structure of the rocks, that in this case, were phyllites of the

Alpujárride Complex. The attention was focused on the most penetrative structure of the phyllites (i.e. S_{2A} foliation), which was assumed to have the greatest influence on the stability of the landslide's slope. Therefore, all possible S_{2A} foliation planes were measured within the landslide and surrounding areas. A higher number of measurements were taken in five specific locations, named as 'Measurement Stations' (MSs), that were required for the next step.

2 - Kinematic analysis. For this analysis, the measured S_{2A} foliation planes in the five MSs were considered as possible discontinuities through which a slope failure could occur. The potential for failure of these discontinuities was graphically evaluated by applying the 'planar sliding analysis' of the software DIPS™ (Rocscience Inc 2004). This method tests for the combined frictional and kinematics possibility of planar sliding along a slope through the following steps:

- Introducing the measurements of the foliation planes and plotting their poles. Therefore, the poles have to be arranged in different groups or sets and a mean plane is then defined for each set.
- Adding the plane of the average slope. A daylight enveloped is automatically generated for the introduced plane, and it represents the zone in which all poles belong to planes that are potentially unstable. The introduced value is the angle of the average slope (in this case, 23º).
- Adding a friction cone, that represents the poles of planes that may form unstable blocks on an inclined slope of a determined type of rock. The introduced values are the minimum and maximum internal friction angles of the specific type of rock. In the case of phyllites, these angles were 20º and 25º, respectively.
- Defining the area of rupture. This area is defined outside of the friction cone when intersecting with the daylight envelope of the average slope. Any pole plotted inside this area represents a plane that is susceptible to generate a planar failure of the slope.

Complementary, we used the 'WEDGEFAIL' tool from the SAGA-GIS to determine the areas where slope failure on geological discontinuities is kinematically possible. Several failure scenarios were simulated for different discontinuities planes (i.e. S_{2A} foliation planes of different orientations), for which the tool also requires introducing a DEM of the slope, and the maximum and minimum internal friction angles of the rock. The final output is a map, for each discontinuity orientation, that show areas of possible slope failure.

5.2.3. Volume estimation

This operation was based on the previous kinematic analysis results and it was carried out in a GIS environment through the detailed steps bellow. Figure 13 illustrates an example of the proposed method by using the case of the El Arrecife Landslide (Chapter IV).

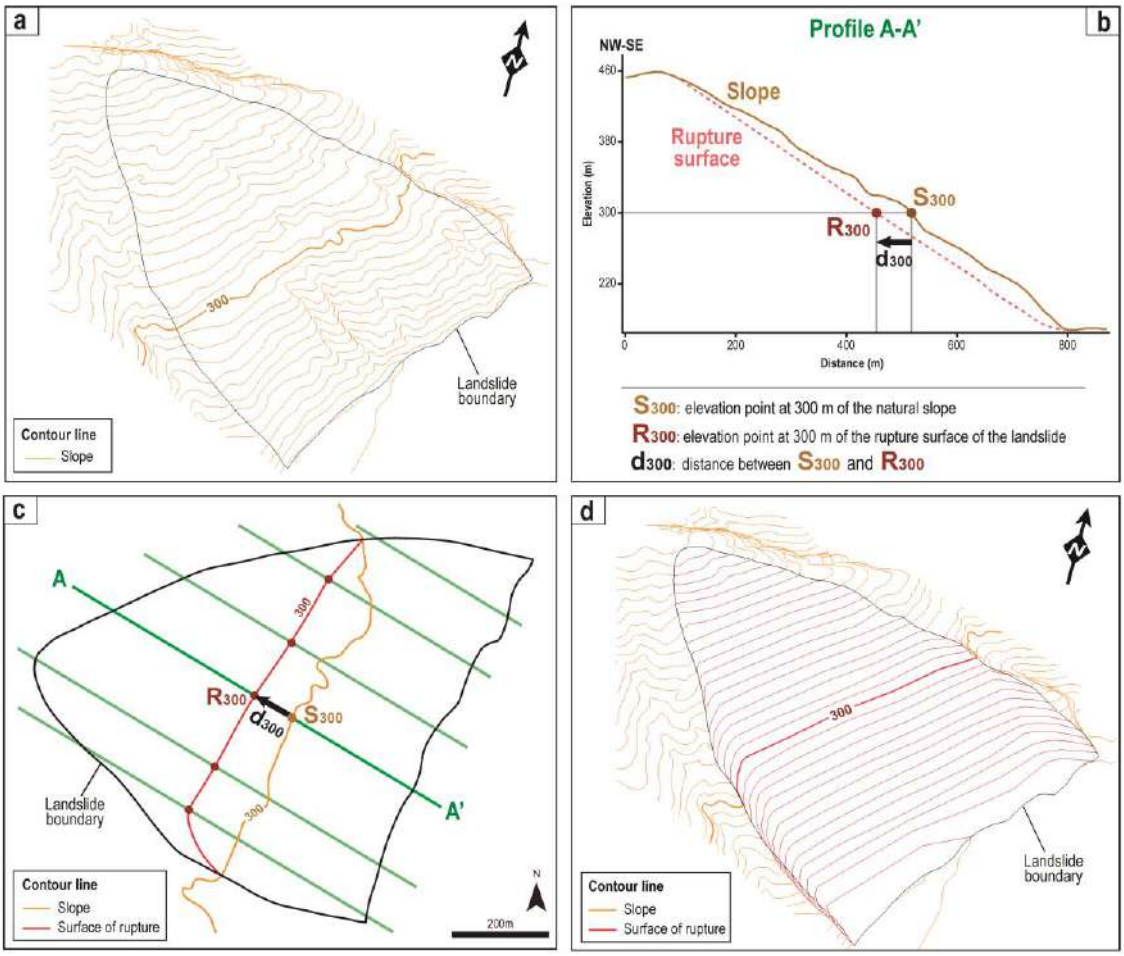

Figure 13. Method for volume estimation of a landslide. **(a)** Three-dimensional view of the contour lines of the slope. The contour at an elevation of 300 m is bolded for reference. **(b)** Extrapolation procedure in a cross section (profile A-A') using elevation points at 300 m. The elevation point of the slope (S_{300}) was horizontally extrapolated to intercept the surface of rupture of the landslide (R_{300}), generating the distance d_{300} between both points. **(c)** Top view map of the landslide that illustrate the procedure of projecting the rupture surface's points. Starting from the slope point S_{300}, the distance d_{300} define the location of R_{300} in the profile A-A'. This operation was repeated in the remaining cross sections to define the corresponding points for then, drawing the 300 m contour line. The contours of the slope and the rupture surface are illustrated with orange and red lines, respectively. **(d)** Three-dimensional view of the contour lines of the rupture surface of the landslide, illustrated with red lines. The contour at an elevation of 300 m is bolded for reference.

- Deriving a DEM of the slope, before being anthropically modified by the reservoir construction (Figure 13a). This DEM was derived by digitalising the contours of a 1999 topographic map, obtained from the digital historical catalogue of the Andalusian Cartographic Institute (https://www.ideandalucia.es/portal/).
- Tracing six parallel cross sections along the landslide's slope. The direction of these cross sections was drawn according to a preferential direction obtained by the kinematic analysis (i.e. the plane more likely to generate failure).
- Drawing the surface of rupture of the landslide in each cross section (Figure 13b). The surface of rupture was manually drawn according to the morphological

features of the slope and also considering the preferential inclination obtained by the kinematic analysis (i.e. the plane more likely to generate failure) (Figure 13b).

- Extrapolating elevations from the slope profile to the surface of rupture. This process was carried out in each cross section at intervals of 10 m of elevation. Figures 13b, c illustrates an example with points elevation at 300 m. The distance (d_{300}) between each elevation point of the slope (S_{300}) and the corresponding elevation point of the rupture surface (R_{300}) was measured in the profile A-A' (Figure 13b). This distance was then projected back onto the map along each cross section to define the elevation points of the rupture surface, what actually estimates its depth (Figure 13c).
- Deriving a DEM of the surface of rupture. This DEM was generated by connecting the elevation points from the six cross sections (Figure 13c) to generate contour lines at each corresponding elevation of the rupture surface (Figure 13d).
- Calculating the thickness of the landslide. This estimation was performed by subtracting the DEM of the natural slope from the DEM of the rupture surface through the GIS raster calculator.
- Calculating the volume of the landslide. The final step involved multiplying the average thickness value by the landslide area.

5.2.4. Landscape Analysis

Landscape Analysis has become a useful tool to investigate natural processes and landforms such as tectonics, bedrock lithology, fluvial captures or landslides. This technique employs a DEM to derive many geomorphic indexes from the drainage network, which allows to identify topographic footprints of these phenomena on rivers (e.g. Pérez-Peña et al. 2010; Troiani et al. 2014; Camafort et al. 2020). In this thesis, the analysis was focused just on one geomorphic index: the normalised channel steepness (k_{sn}), that has already been effectively used for landslide detection (Walsh et al. 2012; De Palézieux et al. 2018; Gu et al. 2021). A new index derived from the k_{sn} is firstly propose in this thesis: the double normalised channel steepness (k_{snn}). The k_{sn} and k_{snn} indexes were calculated for the Sierra Nevada Range (Chapter II) with the aim of mapping landslides. The present sub-section summarises the fundamentals of Landscape Analysis techniques focused on the derivation procedure of the k_{sn} index.

5.2.4.1. Fundamentals of the technique

The drainage network can be easily disturbed by the bedrock lithology, tectonic context, erosional processes or landslides, between other natural phenomena. These processes deviate river channels from equilibrium and rivers, in turn, respond with changes in gradient. A classical analysis of bedrock river profiles uses a stream-power model, that relates the local channel slope (dz/dx) and the contributing drainage area upstream (A) (Perron and Royden 2013) (Equation 10):

$$\frac{dx}{dz} = \left(\frac{U}{K}\right)^{\frac{1}{n}} A(x)^{\frac{-m}{n}} \qquad \textbf{(Equation 10)}$$

Where z is elevation, x is horizontal upstream distance, U is the rate of rock uplift, K is an erodibility coefficient, A is drainage area, and m and n are constants. The m/n ratio is also referred as 'concavity index' (θ) and $(U/K)^{1/n}$ as 'channel steepness' (k_s). The concavity index typically varies from 0.35 to 0.65 in natural river channels, and it is relatively insensitive to differences in rock uplift rates or bedrock lithology (Kirby and Whipple 2012). Small variations in the concavity index can lead to large variations in the k_s index, what complicates the interpretation of the profiles (Wobus et al. 2006). Therefore, a solution is to account for a normalised steepness index (k_{sn}), that is calculated with a fixed concavity named as 'reference concavity' (θ_{ref}). A value of 0.45 usually is considered as a suitable θ_{ref} for the analysis or large drainage basins (Bellin et al. 2014).

One of the most popular approaches to estimate the k_{sn} index is proposed by Perron and Royden (2013) through integrating both sides of Equation 10 to obtain:

$$z(x) = k_{sn} \int_0^x A(x)^{-\theta_{ref}} dx \equiv k_{sn} \cdot \chi \qquad \textbf{(Equation 11)}$$

Equation 11 has the form of a line in which the dependent variable is z and the independent variable is χ, in units of distance. The integral quantity χ ('chi') is also refereed as 'chi index'. The plot of z versus χ for a river profile is defined as 'chi plot'. Therefore, the k_{sn} index is obtained by a linear regression of the Chi index and elevation (i.e. the slope of the Chi-elevation plot).

In practice, a k_{sn} value is usually obtained for equally-spaced segments of river channels within a basin. In this thesis, the k_{sn} index was calculated, as well as a variant from the k_{sn} index named as 'double normalised channel steepness' (k_{snn}) index. For its generation, the obtained k_{sn} values of each channel segment of the basin were normalised by the mean k_{sn} of the whole basin. In other words, the k_{snn} index was simply calculated by subtracting the k_{sn} index of the whole basin from the k_{sn} index of each channel segment.

5.2.4.2. Processing methods

The topographic analysis and extraction of indexes can be performed through some independent softwares. One of the most popular ones is TopoToolbox (Schwanghart and Kuhn 2010; Schwanghart and Scherler 2014; https://topotoolbox.wordpress.com/), that is developed in MATLAB computing environment. This software is free and open source, and the only required input data is a DEM.

A similar tool has been recently and freely developed in Python programming language by José Vicente Pérez-Peña: landspy (https://github.com/geolovic/landspy), that was used in this thesis. The landspy library provides some useful Python functions for landscape analysis and the extraction of geomorphic indexes. It follows the approach defined by Perron and Royden (2013) (Equation 12) to calculate the Chi and k_{sn} indexes. The only necessary input data to perform this analysis is a DEM. Landspy can be also installed and managed in the Python QGIS environment through a very user-friendly interface, especially aimed at those who do not have deep programming skills but have the potential to interpretate the derived results for geological analyses. For the case of Sierra Nevada

(Chapter II), the calculation of the k_{sn} and k_{snn} indexes was carried out by José Vicente Pérez Peña and Marcos Moreno-Sánchez.

5.2.4.3. Interpretation of the data

As previously mentioned, the data obtained from river longitudinal profiles and their steepness allows extracting information such as landslides, between other natural processes and landforms. These phenomena can generate abrupt slope changes along river profiles, that are commonly known as ‘knickpoints'. When slope changes affect a longer transect of a river channel, they are referred as ‘knickzones’. Both knickpoints and knickzones separate a part of the river profile that remains unaffected by the influence of the phenomenon, while the other part is still being adjusted to the new imposed conditions. In the case of landslides, there are two possible scenarios depending on the position of the landslide with respect to the river (Figure 14). When a river flows across a landslide, knickpoints can result from the slope breaks of the main scarp and the bulging of the landslide’s toe. Contrarily, if the landslide downslope force is perpendicular to the river flow direction, knickzones can be generated as a result of stream stretches and deviations (Figure 14).

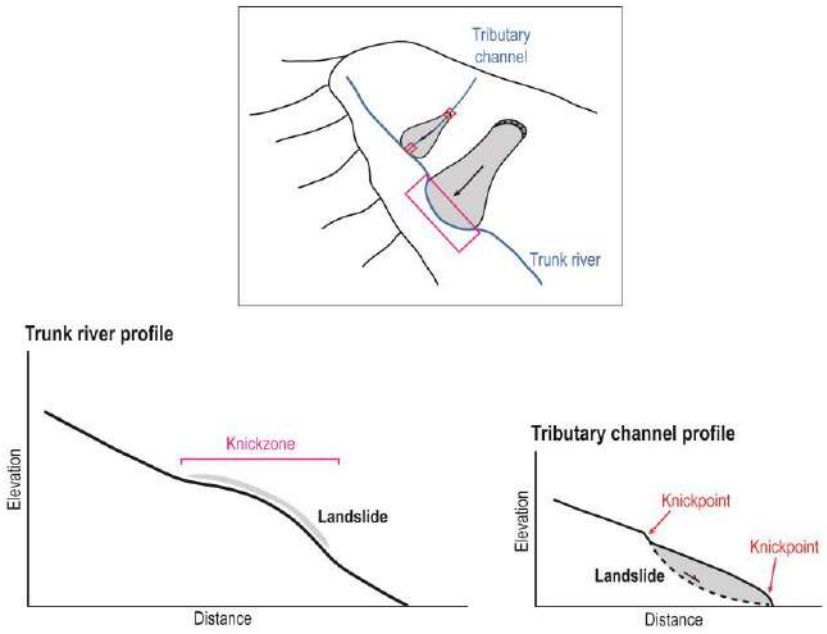

Figure 14. Schematic illustration of a drainage basin and longitudinal profiles of a trunk river and a tributary channel, which are affected by landslides. The trunk river flows perpendicularly to the landslides’ force, while the tributary channel flows parallel to the landslide’s force. In the case of the tributary channels, knickpoints (in red rectangles) are generated by the main scarp and toe of the landslide. In the case of the trunk river, a knickzone (in a pink rectangle) is caused by a stream deviation resultant from the landslide impact.

Knickzones are reflected as anomalous values of gradient-related geomorphic indexes, such as the k_{sn}, which are clearly higher than the rest of the values along the profile. The criteria to establish a threshold for considering or not a k_{sn} value as anomalous (i.e. knickzone or anomaly) is relative and dependent of the study case. At any case, several

intervals must be defined coherently to visualise the distribution of anomalies in a plan view map. In such way, it is possible to identify and associate knickzones to landforms and/or processes. For example, in an active tectonic setting with a considerable relief uplift, higher steepness (anomalous) values are expected in the higher uplift area (Azañón et al. 2015). In this way, anomalies can be very useful to delineate tectonic boundaries such as faults or shear zones (Wobus et al. 2006).

The challenge of interpreting the geomorphic indexes data is attributing an anomaly to a dominant processes or landform (Walsh et al. 2012). Frequently, many processes contribute to an anomaly generation and a predominant one may mask other processes of our interest. This is the study case presented in Chapter II, where the active tectonics resulted in entire river channels with k_{sn} anomalous values. By developing the k_{snn} index, the active tectonics could be minimised and the spatial distribution of the anomalies revealed other different phenomena such as large landslides and glaciar landforms. The latter cause significant slope breaks that result in prominent anomalies, while large landslides generate knickzones associated with river channel stretches and/or deviations due to the downslope force of the landslide.

5.2.5. Structure-from-Motion

The Structure-from-Motion (SfM) is a relatively new photogrammetric method that emerged in the late 1970s (Ullman 1979). This technique allows generating 3D models of the ground surface by exploiting digital aerial images to derive a DEM over an area. The SfM method has been applied to create terrain reconstructions and monitor the evolution of landforms and vegetation (Gómez et al. 2014), volcanoes (Gómez et al. 2015), glaciers (Barrand et al. 2009) or river erosion (Cook 2017). Once a DEM is derived through the SfM method, it is possible to compare different DEMs with the aim of quantifying vertical changes of the ground surface. In this thesis, the innovative procedure of Riquelme et al. (2019) was used, that employs the SfM technique through managing archived historical aerial images. The application of the SfM and further calculations of DEMs were applied for the El Arrecife Landslide study case (Chapter IV). This sub-section aims to explain the fundamentals of the SfM and its processing methods for a better understanding of the derived results.

5.2.5.1. Fundamentals of the technique

An aerial image is any photograph of the Earth's ground surface that is captured from the air. Normally, these images are taken vertically and use a high-quality camera that is carried by Unmanned Aerial Vehicles (UAVs), aircrafts or satellites. For photogrammetric purposes, the image acquisition strategy has to be organised in a series of passes along different flight lines. Throughout each pass, the taken images must have a common area with the neighbouring images. The overlap is the amount (in %) by which one image includes the area covered by another image. The forward or frontal overlap (i.e. between images along the same flight line) is usually settled at 60%, while the lateral or side overlap (i.e. between images on adjacent flight lines) ranges from 20% to 40%. Two

overlapping images are called as ‘stereo pair’, that when combined, they provide a three-dimensional view.

The main satellite systems used to produce stereo pairs are Ikonos, WorldView, SPOT and Pléiades, all of which are commercial. On the contrary, images taken from light aircrafts can often be downloaded free-of-charge from public repositories. These repositories are usually managed by the national geographic services of the country, as the case of the Spanish National Centre for Geographic Information (CNIG) (https://www.ign.es/web/qsm-cnig). In this thesis (Chapter IV), historical aerial images of the year 2000 from the ‘Quinquennial Flight’ were obtained through the CNIG Download Portal. These digital images were then exploited to generate a DEM by means of the SfM technique.

The SfM is based on the generation and treatment of 3D Points Cloud (3DPC), which are a set of vertices where the position of each vertex is known and based on a three-dimensional coordinate system. These 3DPCs are generated from a set of digital aerial photos through the application of ‘Multi-View Stereo’ (MVS) algorithms (Hartley and Zisserman 2003). In this way, it is performed an automatic 3D reconstruction of the ground surface for a DEM generation. This reconstruction requires information about the geometry of the scene and the camera position and orientation, that are automatically solved by introducing Ground Control Points (GCPs). A GCP is an object-space within the scene of known coordinates that enables the projection of a photogrammetric product to an absolute coordinate system. The GCPs should be easily identifiable targets in the images (e.g. road signs, concrete structures or powerlines). At least 10 CGPs are recommended for a proper georeferencing, and they should be well-distributed within the area of interest.

5.2.5.2. Processing methods

The SfM processing is usually carried out by digital photogrammetry commercial softwares. Currently, the most widely known are Pix4Dmapper (Pix4D SA 2017) and PhotoScan (Agisoft LLC 2016), the latter used in the present thesis. Both softwares allow the production of 3DPCs and the photogrammetric reconstruction of 3D ground models. The software PhotoScan stands out for its powerful processing capacity and extensive configuration possibilities during all the processing steps. Firstly, after the input on the images, the software estimates the orientation parameters of the camera for then, correlating and aligning all the images in a local coordinate system (or relative position). After introducing the CGPs, the camera parameters are optimised and the photogrammetric reconstruction is georeferenced. The software also calculates the error of the GCPs in meters and those points with unacceptable errors (e.g. 10 m, according to Riquelme et al. 2019) can be revised and removed. In this sense, the insertion of CGPs is usually an iterative process that requires many visual inspections and corrections to finally provide an optimal dense cloud of the ground surface (i.e. DEM).

It is essential to consider the spatial resolution and the model error to properly interpret the derived products. The spatial resolution of the aerial images is mainly conditioned by

the camera and the flight height. Both factors determine the ground sampling distance (GSD), that represents the distance between two consecutive pixel centres measured on the ground. The higher the flight height, the higher the GSD value and the lower the spatial resolution of the image and thus, of the resultant DEM (e.g. a GSD of 5 cm means that one pixel in the image represents an area of 25 cm^2). Frequently, different images acquired in photogrammetric flights have different GSDs, even when the flight altitude of the aircraft is constant. This fact is due to differences in terrain elevation and consequent changes in the camera's angle while taking the images. The quality of the model is based on the error between the coordinates of the GCPs and the coordinates of the corresponding 3DPC vertices. This error is usually measured through the Root Mean Square Error (RMSE). Generally, the accuracy of SfM models obtained from aircraft's images is of metric or sub-metric order.

Once a DEM is obtained through the SfM method, other products can be derived from them to carry out geomorphological analysis of landforms and their evolution. As previously mentioned, it is possible to monitor vertical changes or displacement of the ground surface by comparing different DEMs. This operation can be performed through the software CloudCompare (GPL 2019), that allows aligning different DEMs on the same reference system. The method followed in this thesis is the one proposed by Riquelme et al. (2019), that consists on the rasterization of the DEM into a 2.5D model for then, comparing height elevations. This method decimates de 3DPC, what reduces the resolution of the results. Despite of this, the advantage of the method is the simplicity and high speed of the computation process. The application of the SfM technique and the DEMs subtraction operations were carried out by Adrián Riquelme and Roberto Sarro.

5.2.5.3. Interpretation of the data

The result of the DEMs difference is a raster that shows the vertical changes or displacement (in m) of the ground surface, together with a histogram of the derived data. In this histogram, a Gaussian or normal distribution (i.e. bell curve-shaped) can be fitted, which are symmetric about the mean of the data. Negative values indicate subsidence of the ground, while positive values indicate uplift of the ground. To properly quantify the changes, the technique error must be considered, which is typically around 5 m (Riquelme et al. 2019). This value can be also derived from the migration of the mean value from 0 (e.g. a mean of 5 indicates an error of 5). As an example, if a subsidence value of -10 m is obtained, it actually refers to a displacement of -5 m after subtracting the error value.

5.2.6. Ground Penetrating Radar

The Ground Penetrating Radar (GPR) is a geophysical method that use the propagation of Electromagnetic Waves (EM) through the ground sub-surface to investigate its structure. Apart from the classical applications for archaeology (Conyers 2015), the GPR has been applied for geomorphological investigations of many phenomena such as glacial deposits (Sadura et al. 2006), coastal dunes (Girardi and Davis 2010), sinkholes (Gutiérrez et al. 2011) or landslides (Bichler et al. 2004), as well as for imaging roads and railways (Rasol et al. 2022). An active landslide can cause deformation of a road

pavement, which can be seen through GPR data and used to induce the vertical ground displacement of both the road and the landslide (Lissak et al. 2015). Such procedure was applied for the El Arrecife Landslide study case (Chapter IV). The aim of this sub-section is to explain the basic principles and processing methods of the GPR technique for a more comprehensive interpretation of the derived data.

5.2.6.1. Fundamentals of the technique

The GPR equipment consists on an antenna that is typically composed of a transmitter and a receiver of radio waves, with typical frequencies from 1 to 1000 MHz (Cassidy and Jol 2009). The transmitter sends pulses of radio waves at defined time intervals to the sub-surface, through which they are propagated at a specific speed depending of the medium properties. The receiver records the signal that is reflected back when it intercepts with objects or when the medium properties change, that are named as 'reflectors'. Specifically, the receiver records the amplitude of the wave and time taken by the wave to travel from the transmitter to the reflector, and back to the receiver (i.e. 'two-way travel time'). The antenna has to be moved along a survey line on the ground surface to construct a 'GPR profile'. During this process, the wave pulses are emitted and then registered back with the required information (i.e. amplitude and two-way travel time) that has to be processed by specific softwares for the GPR data interpretation.

The fundamental of the GPR technique is based on some Maxwell's equations that relate an electromagnetic field with the material behavior (Equations 12 to 14):

$$D = \varepsilon \cdot E \qquad \textbf{(Equation 12)}$$

$$J = \sigma \cdot E \qquad \textbf{(Equation 13)}$$

$$B = \mu \cdot B \qquad \textbf{(Equation 14)}$$

Where D is the electric displacement, J is the electric current intensity, B is magnetic induction, ε is the dielectric permittivity, σ is the electrical conductivity and μ is the magnetic permeability.

These electrical properties of the materials have an important role in the performance of the GPR, as they control the propagation and attenuation of the waves through the ground sub-surface (Lalagüe 2015). These properties are the following:

- Dielectric permittivity (ε) (Equation 12). It refers to the ability of the material to store charge when an electric field is applied. Actually, the measured parameter is the relative dielectric permittivity (ε_r), that is the ratio between the absolute permittivity (ε) and the vacuum permittivity (ε_0). This parameter is often named as 'dielectric constant' and it is related to the composition, moisture and void content of the material.
- Electrical conductivity or resistivity (σ) (Equation 13). It refers to the ability of a material to conduct an electric current. Overall, the higher the conductivity of a material is, the greater the attenuation of the EM is expected.

- Magnetic permeability (μ) (Equation 14). It refers to the ability of the material to become magnetised when an electromagnetic field is applied. As well as the electrical conductivity, the higher the magnetic permeability is, the higher the attenuation of the EM is. For most of the materials and soils, this parameter is assumed to be negligible (μ=1).

The operating frequency of the GPR antenna is also an essential aspect to consider for the application of the method. Equation 15 defines an EW as:

$$\lambda = \frac{c}{f} \qquad \textbf{(Equation 15)}$$

Where λ is wavelength (m), c is the velocity of the EW propagation in free space (i.e. $3x10^8$ m/s) and f is frequency.

Therefore, low frequencies produce longer wavelengths while high frequency generate shorter wavelengths (Equation 15). The wavelength is related to the depth of penetration of the wave through the ground sub-surface, what it turns, define de resolution of the GPR profile (the higher the frequency, the better the resolution). For example, the high-frequency GPR antennas (1600-1900 MHz) could penetrate up to 1 m, middle frequencies (500-200 MHz) could penetrate up to 7 m and lower frequencies (bellow 100 MHz) could reach depths of 50 m. In this thesis, the used antenna had a frequency of 400 MHz (middle-frequency antenna), which allowed a wave penetration up to 2 m depth and a resolution of 10 cm. The antenna and the GPR equipment were all rendered by Agustín Millares.

Standard GPR systems consist on three main elements: the control unit (pulse generator, computer and associated software), the display unit (computer screen) and the antenna (Conyers 2015). There are two GPR systems categories: frequency radar and impulse radar. The latter is the most common and the one used in this thesis, which collects data in the time domain (two-way travel time), while the frequency radar register the data in frequency domain for then converting it to time-domain (Lalagüe 2015). The main component of the GPR is the antenna, that emit and receive the radio waves. Antennas can be can be suspended above the ground (air-coupled) or can be in direct contact with the ground surface (ground-coupled), providing the latter more accurate images of the sub-surface. In the case of ground-coupled antennas, they are usually carried by small trolleys or small platforms with wheels to be dragged along the ground surface (Figure 15a). Therefore, the GPR is a non-destructive geophysical method, as excavations and alterations of the ground are not required for the equipment installation and data acquisition.

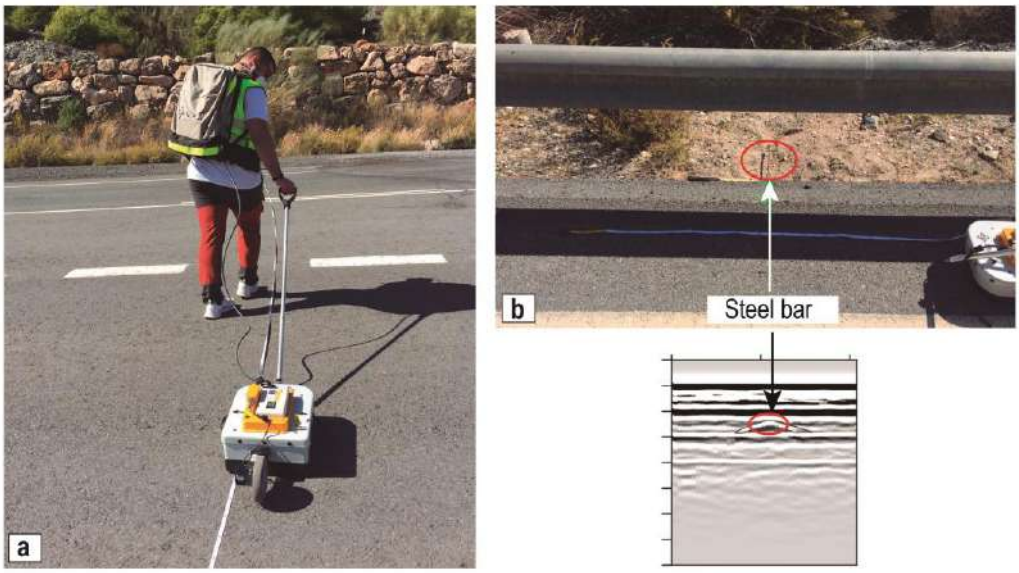

Figure 15. **(a)** Photograph of a Ground Penetrating Radar (GPR) antenna carried on a wheeled platform while obtaining a profile along a road. **(b)** Photograph of the steel bar used to estimate the ground velocity through the reflected-wave method. The resultant hyperbola in the GRP profile is also shown, where the steel bar and the hyperbola are indicated with red circles (modified from Moreno-Sánchez 2020).

The recent GPR systems adjustments are often automatically programmed by the acquisition software, but some manual adjustments have to be carried out prior to conducting a survey. The most important parameter to be chosen is the 'time window': the time period over which reflection data is recorded (i.e. the amount of two-way travel times that the receiving antenna registers), that is measured in nanoseconds (Conyers 2015). This window starts just before the radar pulse is emitted and it is finishes when the reflections of interest are recorded. It is also essential to know the velocity of the ground material to ensure that the amount of time selected is enough to register the desired features (reflections). There are two general techniques to determine this velocity: the direct-wave method and the reflected-wave method. Direct methods transmit waves through the ground from one antenna to another along a measured distance, while reflected methods require the wave to be reflected from buried objects or interfaces at depth (Conyers and Lucius 1996). The analysis of the geometry of reflection hyperbolas generated from these objects allow to obtain the velocity. Metallic objects are exceptional signal reflectors, and they generate distinct hyperbolas that are very easily identifiable on most GPR profiles. In this thesis (Chapter IV), a steel bar was inserted and buried below the sub-surface (Figure 15b). The antenna was then slowly pulled over the bar and reflections were recorded in a GPR profile, that generate a well-defined hyperbola (Figure 15b). As the reflection profiles are immediately visible on the system computer screen, the velocity (time and depth) (Equation 16a) can be rapidly calculated and the time window can be decided to perform the required profiles. Therefore, the calculated ground velocity (v) is related with the two-way travel time of the reflected pulses (Δt), with depth (z) and with the relative dielectric permittivity of waves (ε_r) (Equations 16 and 17):

$$z = v \cdot \frac{\Delta t}{2} \qquad \textbf{(Equation 16a)}$$

Where v is defined as:

$$v = \frac{c}{\sqrt{\varepsilon_r}} \qquad \textbf{(Equation 16b)}$$

And therefore:

$$z = \frac{\mathrm{c} \cdot \Delta t}{2\sqrt{\varepsilon_r}} \qquad \textbf{(Equation 17)}$$

Where z is ground sub-surface depth, v is the velocity of the propagating wave in the ground material, Δt is the two-way travel time, c is the velocity of the propagating wave in free space ($3x10^8$ m/s) and ε_r is the relative dielectric permittivity of waves.

5.2.6.2. Processing methods

The acquired raw data has to be treated by a specialised software to generate the final product of the GPR technique: a radargram. A radargram is a sequential stack of traces or layers that graphically represent the amplitude data from the registered reflected waves. It is an image visualised in grey-scale colours, where bright traces correspond to high amplitudes received by the antenna (i.e. high amount of reflection), while dark traces correspond to low amplitudes (i.e. low amount of reflection).

There are several private and open softwares that allow obtaining radargrams. Reflex® (Sandmeier 1997) is one of the most popular commercial softwares for GPR and seismic data processing. Another well-known software is RADAN 7 (GSSI 2012), that has been used in this thesis. The processing of the GPR data to derive radargrams was carried out by Teresa Teixidó and Marcos Moreno-Sánchez. The raw data processing was very laborious, and it can be summarised in the following steps, as described in Marcos-Moreno 2020:

1 - Adjust to time zero. This first step corrects the air and ground layer effect, which is translated as a temporal shift (in ns).

2 - Background elimination. The effect of the coupled wave (air-ground contact) is then eliminated. In radargrams, this category of noise appears as horizontal periodic layers that can often be so strong that they may mask layers of interest (Rashed 2015).

3 - Gaining. This step allows to enhance the radargram by increasing amplitudes for those reflections that have a weak signal, but are of interest. This is commonly applied to the shallowest layers of the radargram.

4 - Migration. The effect of diffraction and flattening of some reflectors are eliminated and some reflections are moved from an apparent to their true location. This step can be done by applying different geometrical approaches and algorithms. In this case, the Kirschhoff migration method was the one used (Moran et al. 2000).

5 - Deconvolution. This step allows eliminating the multiple reflections that can mask other reflections of interest for being recorded at the same time. The radargram is considerably cleaned and looks clearer after this correction.

6 - Application of band-pass filters. These filters allow discriminating some specific frequencies to display only the frequency of interest. For the used 400-MHz antenna, the frequencies are emitted to the ground in a broader band, from 200 to 800 MHz. Therefore, a high-pass filter of 250 MHz (displays frequencies higher than 250 MHz) combined with a low-pass filter of 750 MHz (displays frequencies lower than 750 MHz) was applied.

5.2.6.3. Interpretation of the data

If a road runs along an active landslide, the continuous subsidence of the upper part of the landslide often causes deformation and damages (e.g. potholes, cracks) of the road pavement (Figure 16). In these cases, frequent asphalt resurfacing activities are usually carried out to level the road and compensate the tilting of the damaged sectors (Figure 16). This situation conducts to the generation of a sub-surface horizontal sequence of asphalt layers, that can be clearly visualised in a radargram obtained along the road. The asphalt sequence is shown as a successive sequence of high-amplitude horizontal reflectors (i.e. bright traces). These reflectors can be interpreted as a significant contrast between two asphalt layers, probably related to differences in the composition of the road structure, or to the presence of groundwater (Lissak et al. 2015). The asphalt sequence can be easily differentiated from the natural ground that correspond to the slide mass of the landslide, where there is absence of reflectors. Moreover, the landslide's lateral boundaries are commonly revealed by an increase of asphalt thickness on the damaged road sector compared to the intact road. If the period of time of the resurfacing works is known, an indirect measurement of the vertical displacement rate of road can be obtained (e.g. in cm/yr). Therefore, the estimated road subsidence rate can be correlated with the vertical ground motion of the landslide. In the case of the El Arrecife Landslide (Chapter IV), yearly repairs have been performed since the inauguration of the road in 1997. This information was provided by the employees of the Road State Demarcation in Granada, as a personal communication in a scheduled meeting.

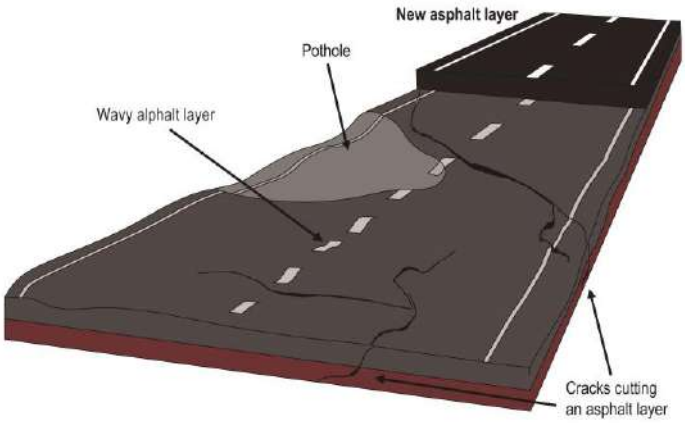

Figure 16. Schematic illustration showing the typical damages of a deformed road pavement and the resurfacing process (modified from Moreno-Sánchez 2020).

Other sub-surface structures such as vertical cracks with air-filled voids or water infiltrations are easily detectable in a radargram as vertical cuts in the continuity of the horizontal reflectors. Moreover, the internal structure of the ground can reveal the landslide's lateral boundary in the radargram: there are no reflectors in the slide mass, as the internal structure of a landslide deposit is chaotic, while high-amplitude dipping reflectors correspond to the in situ rock bedding. Lastly, if a radargram is obtained across the road and transversally to the landslide, other geometries of the asphalt layers can be identified. The associated reflectors may be tilted as a consequence of the landslide movement, what is known as a 'cumulative wedge-out' (Gutiérrez et al. 2011). These structures record progressive deformation, and they also reveal the rotational displacement regime of a landslide.

References

Abellán A, Calvet J, Vilaplana JM, Blanchard J (2010) Detection and spatial prediction of rockfalls by means of terrestrial laser scanner monitoring. Geomorphology 119: 162-171. https://doi.org/10.1016/j.geomorph.2010.03.016

Aerden D, Sayab M (2008) From Adria-to Africa-driven orogenesis: evidence from porphyroblasts in the Betic Cordillera, Spain. J of Struct Geol 30: 1272-1287. https://doi.org/10.1016/j.jsg.2008.06.009

Aerden DGAM, Bell TH, Puga E, Sayab M, Lozano JA, Diaz de Federico AD (2013) Multi-stage mountain building vs. relative plate motions in the Betic Cordillera deduced from integrated microstructural and petrological analysis of porphyroblast inclusion trails. Tectonophysics 587: 188-206. https://doi.org/10.1016/j.tecto.2012.11.025

Agisoft LLC (2016) PhotoScan Professional Edition (Software)

Agliardi F, Crosta G, Zanchi A (2001) Structural constraints on deep-seated slope deformation kinematics. Eng Geol 59: 83-102. https://doi.org/10.1016/S0013-7952(00)00066-1

Agliardi F, Crosta GB, Frattini P, Malusà MG (2013) Giant non-catastrophic landslides and the long-term exhumation of the European Alps. Earth Planet Sci Lett 365: 263-274. https://doi.org/10.1016/j.epsl.2013.01.030

Ambrosi C, Crosta GB (2006) Large sackung along major tectonic features in the Central Italian Alps. Eng Geol 83: 183-200. https://doi.org/10.1016/j.enggeo.2005.06.031

Atzori S, Hunstad I, Chini M, Salvi S, Tolomei C, Bignami C, Stramondo S, Trasatti E, Antonioli A, Boschi E (2009) Finite fault inversion of DInSAR coseismic displacement of the 2009 L'Aquila earthquake (central Italy). Geophys Res Lett 36: L15305. https://doi.org/10.1029/2009GL039293

Avilés A, Rodero J, Amores V, De Vicente I, Rodríguez MI, Niell FX (2006) Factors controlling phosphorus speciation in a Mediterranean basin (River Guadalfeo, Spain). J Hydrol 331: 396-408. https://doi.org/10.1016/j.jhydrol.2006.05.024

Azañón JM, Goffé B (1997) Ferro- and magnesiocarpholite assemblages as record of high-P, low-T metamorphism in the central Alpujárrides, Betic Cordillera (SE Spain). Eur J Mineral 9: 1035–1051

Azañón JM, Crespo-Blanc A (2000) Exhumation during a continental collision inferred from the tectonometamorphic evolution of the Alpujarride Complex in the central Betics (Alboran Domain, SE Spain). Tectonics 19: 549-565. https://doi.org/10.1029/2000TC900005

Azañón JM, Galve JP, Pérez-Peña JV, Giaconia F, Carvajal R, Booth-Rea G, Jabaloy A, Vázquez M, Azor A, Roldán FJ (2015) Relief and drainage evolution during the exhumation of the Sierra Nevada (SE Spain): Is denudation keeping pace with uplift? Tectonophysics 663: 19-32. https://doi.org/10.1016/j.tecto.2015.06.015

Baeza C, Corominas J (2001) Assessment of shallow landslide susceptibility by means of multivariate statistical techniques. Earth Surf Process Landf 26: 1251-1263. https://doi.org/10.1002/esp.263

Balanyá JC, García-Dueñas V, Azañón JM, Sánchez-Gómez M (1997) Alternating contractional and extensional events in the Alpujarride nappes of the Alboran Domain (Betics, Gibraltar Arc). Tectonics 16: 226-238. https://doi.org/10.1029/96TC03871

Barra A, Monserrat O, Mazzanti P, Esposito C, Crosetto M, Scarascia-Mugnozza G (2016) First insights on the potential of Sentinel-1 for landslides detection. Geomatics, Nat Hazards Risk 7: 1874-1883. https://doi.org/10.1080/19475705.2016.1171258

Barra A, Solari L, Béjar-Pizarro M, Monserrat O, Bianchini S, Herrera G, Crosetto M, Sarro R, González-Alonso E, Mateos RM, Ligüerzana S, López C, Moretti S (2017) A methodology to detect and update active deformation areas based on sentinel-1 SAR images. Remote Sens 9: 1002. https://doi.org/10.3390/rs9101002

Barra A (2022) Advanced exploitation of Sentinel-1 data for supporting landslide risk analysis. Doctoral Thesis, Universitat Politècnica de Catalunya

Barra A, Reyes-Carmona C, Herrera G, Galve JP, Solari L, Mateos RM, Azañón JM, Béjar-Pizarro M, López-Vinielles J, Palamà R, Crosetto M, Sarro R, Cuervas-Mons J, Monserrat O (2022) From satellite interferometry displacements to potential damage maps: A tool for risk reduction and urban planning. Remote Sens Environ 282: 113294. https://doi.org/10.1016/j.rse.2022.113294

Barrand NE, Murray T, James TD, Barr SL, Mills JP (2009) Optimizing photogrammetric DEMs for glacier volume change assessment using laser-scanning derived ground-control points. J. Glaciol 55: 106–116. https://doi.org/10.3189/002214309788609001.

Behr WM, Platt JP (2012) Kinematic and thermal evolution during two-stage exhumation of a Mediterranean subduction complex. Tectonics 31: TC4025 https://doi.org/10.1029/2012TC003121

Béjar-Pizarro M, Notti D, Mateos RM, Ezquerro P, Centolanza G, Herrera G, Sanabria M, Solari L, Duro J, Fernández J (2017) Mapping vulnerable urban areas affected by slow-moving landslides using Sentinel-1 InSAR data. Remote Sens 9: 876. https://doi.org/10.3390/rs9090876

Béjar-Pizarro M, Álvarez Gómez JA, Staller A, Luna MP, Pérez-López R, Monserrat O, Chunga K, Lima A, Galve JP, Martínez-Díaz J, Mateos RM, Herrera G (2018) InSAR-based mapping to support decision-making after an earthquake. Remote Sens 10: 899. https://doi.org/10.3390/rs10060899

Bellin N, Vanacker V, Kubik PW (2014) Denudation rates and tectonic geomorphology of the Spanish Betic Cordillera. Earth Planet Sci Lett 390: 19-30. https://doi.org/10.1016/j.epsl.2013.12.045

Berardino, P., Fornaro, G., Lanari, R., & Sansosti, E. (2002). A new algorithm for surface deformation monitoring based on small baseline differential SAR interferograms. IEEE Trans Geosci Remote Sens 40: 2375-2383. https://doi.org/10.1109/TGRS.2002.803792

Bergillos RJ, López-Ruiz A, Ortega-Sánchez M, Masselink G, Losada MA (2016) Implications of delta retreat on wave propagation and longshore sediment transport-Guadalfeo case study (southern Spain) Mar Geol 382: 1-16. https://doi.org/10.1016/j.margeo.2016.09.011

Bergillos RJ, Ortega-Sánchez M (2017) Assessing and mitigating the landscape effects of river damming on the Guadalfeo River delta, southern Spain. Landsc Urban Plan 165: 117-129. https://doi.org/10.1016/j.landurbplan.2017.05.002

Bianchini S, Herrera G, Mateos RM, Notti D, Garcia I, Mora O, Moretti S (2013) Landslide activity maps generation by means of persistent scatterer interferometry. Remote Sens 5: 6198-6222. https://doi.org/10.3390/rs5126198

Bichler A, Bobrowsky P, Best M, Douma M, Hunter J, Calvert T, Burns R (2004) Three-dimensional mapping of a landslide using a multi-geophysical approach: the Quesnel Forks landslide. Landslides 1: 29-40. https://doi.org/10.1007/s10346-003-0008-7

Biescas E, Crosetto M, Agudo M, Monserrat O, Crippa B (2007) Two radar interferometric approaches to monitor slow and fast land deformation. J Surv Eng 133: 66-71. https://doi.org/10.1061/(ASCE)0733-9453(2007)133:2(66)

Bisci C, Dramis F, Sorriso-Valvo, M (1996) Rock flow (sackung). In: Dikau R, Brunsden D, Schrott L, Ibsen ML (eds) Landslide Recognition, Identification, Movement and Causes. John Wiley and Sons, pp 150-160

Borrelli L, Gullà G (2017) Tectonic constraints on a deep-seated rock slide in weathered crystalline rocks. Geomorphology 290: 288-316. https://doi.org/10.1016/j.geomorph.2017.04.025

Bouillin JP, Durand-Delga M, Olivier P (1986) Betic-Rifian and Tyrrhenian arcs: distinctive features, genesis and development stages. In: Wezel F (ed) The Origin of Arcs. Elsevier, pp 281-304. https://doi.org/10.1016/B978-0-444-42688-8.50017-5

Braga JC, Martin JM, Alcala B (1990) Coral reefs in coarse-terrigenous sedimentary environments (Upper Tortonian, Granada Basin, southern Spain). Sediment Geol 66: 135-150. https://doi.org/10.1016/0037-0738(90)90011-H

Braga JC, Martín JM, Quesada C (2003) Patterns and average rates of late Neogene–Recent uplift of the Betic Cordillera, SE Spain. Geomorphology 50: 3-26. https://doi.org/10.1016/S0169-555X(02)00205-2

Brun JP, Faccenna C (2008) Exhumation of high-pressure rocks driven by slab rollback. Earth Planet Sci Lett 272: 1-7. https://doi.org/10.1016/j.epsl.2008.02.038

Calvert A, Sandvol E, Seber D, Barazangi M, Roecker S, Mourabit T, Vidal F, Alguacil G, Jabour N (2000) Geodynamic evolution of the lithosphere and upper mantle beneath the Alboran region of the western Mediterranean: Constraints from travel time tomography. J Geophys Res Solid Earth 105: 10871-10898. https://doi.org/10.1029/2000JB900024

Camafort M, Pérez-Peña JV, Booth-Rea G, Melki F, Gràcia E, Azañón JM, Galve JP, Marzougui W, Gaidi S, Ranero CR (2020) Active tectonics and drainage evolution in the Tunisian Atlas driven by interaction between crustal shortening and mantle dynamics. Geomorphology 351: 106954. https://doi.org/10.1016/j.geomorph.2019.106954

Cassidy NJ (2009) Ground Penetrating Radar Data Processing, Modelling and Analysis. In: Jol HM (ed) Ground Penetrating Radar Theory and Applications. Elsevier, pp 141-176

Casu F, Elefante E, Imperatore P, Zinno I, Manunta M, De Luca C, Lanari R (2014) SBAS-DInSAR parallel processing for deformation time series computation. IEEE J Sel Top Appl Earth Obs Remote Sen 7: 3285–3296. https://doi.org/10.1109/JSTARS.2014.2322671

Chacón J (1988) Riesgos Geológicos en el sector de Olivares (Moclín, Granada). Proceedings of the II Simposio Nacional de Taludes y Laderas Inestables, Andorra la Vella, Andorra, pp 705-722

Chacón J, Soria FJ (1992) Inventario y caracterización de movimientos de ladera en la vertiente septentrional de Sierra Nevada. Proceedings of the III Simposio Nacional sobre Taludes y Laderas Inestables, La Coruña, Spain, pp 149-160

Chacón J (1995) Landslides in the Central Betic Cordillera (Southern Spain). Proceedings of the 3th Workshop of Meteorological Factors influencing Slope Stability and Slope Movements Types: Evaluation of Hazard Prone Areas (MeFISSt), Granada, Spain, pp 1-24

Chacón J, El Hamdouni E, Irigaray C, Delgado A, Reyes E, Fernández T, García AF, Juliá R, Sanz de Galdeano C, Keller EA (2001) Valores de encajamiento de la red fluvial deducidos a partir del estudio de travertinos del Valle de Lecrín y curso bajo del Guadalfeo (SO de Sierra Nevada, Granada). In: Sanz de Galdeano C, López-Garrido A, Peláez J (eds) La Cuenca de Granada: Estructura, Tectónica Activa, Sismicidad, Geomorfología y dataciones existentes. University of Granada-National Reseach Council, Granada, pp 29-39

Chacón J, Irigaray T, Fernández T (2007) Los movimientos de ladera de la provincia de Granada. In: Ferrer M (ed) Atlas Riesgos Naturales en la Provincia de Granada, 1st edn. Diputación de Granada-Geological Survey of Spain, Madrid, pp 45-82

Chigira M (2009) September 2005 rain-induced catastrophic rockslides on slopes affected by deep-seated gravitational deformations, Kyushu, southern Japan. Eng Geol 108: 1-15. https://doi.org/10.1016/j.enggeo.2009.03.005

Comas MC, García-Dueñas V, Jurado MJ (1992) Neogene tectonic evolution of the Alboran Sea from MCS data. Geo-Mar Lett 12: 157-164. https://doi.org/10.1007/BF02084927

Confuorto P, Casagli N, Casu F, De Luca C, Del Soldato M, Festa D, Lanari R, Manzo M, Onorato G, Raspini F (2023) Sentinel-1 P-SBAS data for the update of the state of activity of national landslide inventory maps. Landslides: 1-15. https://doi.org/10.1007/s10346-022-02024-0

Conyers LB, Lucius JE (1996) Velocity analysis in archaeological ground-penetrating radar studies. Archaeol Prospect 3: 25-38. https://doi.org/10.1002/(SICI)1099-0763(199603)3:1<25::AID-ARP39>3.0.CO;2-U

Conyers LB (2015) Analysis and interpretation of GPR datasets for integrated archaeological mapping. Near Surf Geophys 13: 645–651. https://doi.org/10.3997/1873-0604.2015018

Cook KL (2017) An evaluation of the effectiveness of low-cost UAVs and structure from motion for geomorphic change detection. Geomorphology 278: 195–208. https://doi.org/10.1016/j.geomorph.2016.11.009

Corominas J, Mateos M, Remondo J (2017) Review of landslide occurrence in Spain and its relation to climate. In: Ho K, Lacasse S, Picarelli L (eds) Slope Safety Preparedness for Impact of Climate Change. CRC Press, pp 351-377. https://doi.org/10.1201/9781315387789

Crippa C, Valbuzzi E, Frattini P, Crosta GB, Spreafico MC, Agliardi F (2021) Semi-automated regional classification of the style of activity of slow rock-slope deformations using PS InSAR and SqueeSAR velocity data. Landslides 18: 2445-2463. https://doi.org/10.1007/s10346-021-01654-0

Crosetto M, Biescas E, Duro J, Closa J, Arnaud A (2008) Generation of advanced ERS and Envisat interferometric SAR products using the stable point network technique. Photogramm Eng Remote Sensing 74: 443-450.

Crosetto M, Solari L, Mróz M, Balasis-Levinsen J, Casagli N, Frei M, Oyen A, Moldestad DA, Bateson L, Guerrieri L, Comerci V, Andersen, HS (2020) The evolution of wide-area DInSAR: From regional and national services to the European Ground Motion Service. Remote Sens 12: 2043. https://doi.org/10.3390/rs12122043

Crosta GB, Frattini P, Agliardi F (2013) Deep seated gravitational slope deformations in the European Alps. Tectonophysics 605: 13-33. https://doi.org/10.1016/j.tecto.2013.04.028

Crosta GB, Di Prisco C, Frattini P, Frigerio G, Castellanza R, Agliardi F (2014) Chasing a complete understanding of the triggering mechanisms of a large rapidly evolving rockslide. Landslides 11: 747-764. https://doi.org/10.1007/s10346-013-0433-1

Cuervas-Mons J, Domínguez-Cuesta MJ, Mateos Redondo F, Barra A, Monserrat O, Valenzuela P, Jiménez-Sánchez M (2021) Sentinel-1 data processing for detecting and monitoring of ground instabilities in the rocky coast of central Asturias (N Spain). Remote Sens 13: 3076. https://doi.org/10.3390/rs13163076

Domínguez-Cuesta MJ, Jiménez-Sánchez, M, García AR (1999) Press archives as temporal records of landslides in the North of Spain: relationships between rainfall and instability slope events. Geomorphology 30: 125-132. https://doi.org/10.1016/S0169-555X(99)00049-5

D'Alessandro GR, Berti M, Urbani A, Tecca PR (2002) Geomorphology, stability analyses and the stabilization works on the Montepiano travertinous cliff (Central Italy). In: Allison RJ (ed) Applied geomorphology-theory and practice. Wiley, pp 21-38

de Lis Mancilla F, Stich D, Berrocoso M, Martín R, Morales J, Fernandez-Ros A, Páez R, Pérez-Peña A (2013) Delamination in the Betic Range: Deep structure, seismicity, and GPS motion. Geology 41: 307-310. https://doi.org/10.1130/G33733.1

De Luca C, Cuccu R, Elefante S, Zinno I, Manunta M, Casola V, Rivolta G, Lanari R, Casu F (2015) An on-demand Web tool for the unsupervised retrieval of earth's surface deformation from SAR Data: the P-SBAS Service within the ESA G-POD Environment. Remote Sens 7:15630–15650. https://doi.org/10.3390/rs71115630

De Palézieux L, Leith K, Loew S (2018) Assessing the predictive capacity of hillslope projected channel steepness for rockslope instability in the High Himalaya of Bhutan. Proceedings of the 16th Swiss Geoscience Meeting, Bern, Switzerland, pp 12

Del Rio L, Moro M, Fondriest M, Saroli M, Gori S, Falcucci E, Cavallo A, Doumaz F, Di Toro G (2021) Active Faulting and Deep-Seated Gravitational Slope Deformation in Carbonate Rocks (Central Apennines, Italy): A New "Close-Up" View. Tectonics 40: e2021TC006698. https://doi.org/10.1029/2021TC006698

Delgado J, Peláez JA, Tomás R, García-Tortosa FJ, Alfaro P, Casado CL (2011) Seismically-induced landslides in the Betic Cordillera (S Spain). Soil Dyn Earthq Eng 31: 1203-1211. https://doi.org/10.1016/j.soildyn.2011.04.008

Delgado J, Garrido J, Lenti L, Lopez-Casado C, Martino S, Sierra FJ (2015) Unconventional pseudostatic stability analysis of the Diezma landslide (Granada, Spain) based on a high-resolution engineering-geological model. Eng Geol 184: 81-95. https://doi.org/10.1016/j.enggeo.2014.11.002

DeMets C, Gordon RG, Argus DF, Stein S (1994) Effect of recent revisions to the geomagnetic reversal time scale on estimates of current plate motions. Geophys Res Lett 21:2191-2194. https://doi.org/10.1029/94GL02118

DeMets C, Gordon RG, Argus DF (2010) Geologically current plate motions. Geophys Journal Int 181: 1-80. https://doi.org/10.1111/j.1365-246X.2009.04491.x

Devanthéry N, Crosetto M, Monserrat O, Cuevas-González M, Crippa B (2014) An approach to persistent scatterer interferometry. Remote Sens 6: 6662-6679. https://doi.org/10.3390/rs6076662

Devanthéry N, Crosetto M, Monserrat O, Crippa B, Mróz M (2019) Data analysis tools for persistent scatterer interferometry based on Sentinel-1 data. European Journal of Remote Sens 52: 15-25. https://doi.org/10.1080/22797254.2018.1554981

Ding XL, Li ZW, Zhu JJ, Feng GC, Long JP (2008) Atmospheric effects on InSAR measurements and their mitigation. Sensors 8: 5426-5448. https://doi.org/10.3390/s8095426

Dramis F, Sorriso-Valvo M (1994) Deep-seated gravitational slope deformations, related landslides and tectonics. Eng Geol 38:231-243. https://doi.org/10.1016/0013-7952(94)90040-X

EGMS (2023) European Ground Motion Service Explorer. Webpage. Retrieved from https://egms.land.copernicus.eu/

El Hamdouni R (2001) Estudio de Movimientos de Ladera en la Cuenca del Río Ízbor mediante un SIG: Contribución al Conocimiento de la Relación entre Tectónica Activa e Inestabilidad de Vertientes. Doctoral Thesis, University of Granada

El Hamdouni R, Irigaray C, Jiménez-Perálvarez JD, Chacón J (2010) Correlations analysis between landslides and stream length-gradient (SL) index in the southern slopes of Sierra Nevada (Granada, Spain). In: Williams AL, Pinches GM, Chin CY, McMorran TJ, Massey CY (eds) Geologically Active. Taylor and Francis, pp 141-149

ESA (2007) InSAR Principles: Guidelines for SAR Interferometry Processing and Interpretation. ESA Publications

Fernandez J, Bluck BJ, Viseras C (1993) The effects of fluctuating base level on the structure of alluvial fan and associated fan delta deposits: an example from the Tertiary of the Betic Cordillera, Spain. Sedimentology 40: 879-893

Fernández T, Brabb E, Delgado F Martin-Algarra A, Irigaray C, Estévez A, Chacón-Montero J (1997) Rasgos geológicos y movimientos de ladera en el sector Ízbor-Vélez Benaudalla de la cuenca del río Guadalfeo (Granada). Proceedings of the IV Simposio Nacional Sobre Taludes y Laderas Inestables, Granada, Spain, pp 795–808

Fernández T, Irigaray C, El Hamdouni R, Chacón J (2003) Methodology for landslide susceptibility mapping by means of a GIS. Application to the Contraviesa area (Granada, Spain). Nat Hazards 30: 297-308. https://doi.org/10.1023/B:NHAZ.0000007092.51910.3f

Fernandez P, Irigaray C, Jimenez J, El Hamdouni R, Crosetto M, Monserrat O, Chacón J (2009) First delimitation of areas affected by ground deformations in the Guadalfeo River Valley and Granada metropolitan area (Spain) using the DInSAR technique. Eng Geol 105: 84-101. https://doi.org/10.1016/j.enggeo.2008.12.005

Fernández T, Pérez JL, Delgado J, Cardenal J, Irigaray C, Chacón J (2011) Evolution of a diachronic landslide by comparison between different DEMs obtained from Digital Photogrammetry Techniques in Las Alpujarras (Granada, Southern Spain). Proceedings of the Conference of Geoinformation for Disaster Management (GI4DM), Antalya, Turkey, pp 1-6

Fernández T, Pérez JL, Colomo C, Cardenal J, Delgado J, Palenzuela JA, Irigaray C, Chacón J (2017) Assessment of the evolution of a landslide using digital photogrammetry and LiDAR techniques in the Alpujarras region (Granada, southeastern Spain). Geosciences 7: 32. https://doi.org/10.3390/geosciences7020032

Fernández-Merodo JA, Ezquerro P, Manzanal D, Béjar-Pizarro M, Mateos RM, Guardiola-Albert C, García-Davalillo JC, López-Vinielles J, Sarro R, Bru G, Mulas J, Aragón R, Reyes-Carmona C, Mira P, Pastor M, Herrera G (2021) Modeling historical subsidence due to groundwater withdrawal in the Alto Guadalentín aquifer-system (Spain). Eng Geol 283: 105998. https://doi.org/10.1016/j.enggeo.2021.105998

Ferretti A, Prati C, Rocca F (2001) Permanent scatterers in SAR interferometry. IEEE Trans Geosci Remote Sens 39: 8-20. https://doi.org/10.1109/36.898661

Ferretti A, Fumagalli A, Novali F, Prati C, Rocca F, Rucci A (2011) A new algorithm for processing interferometric data-stacks: SqueeSAR. IEEE Trans Geosci Remote Sens 49: 3460-3470. https://doi.org/10.1109/TGRS.2011.2124465

Fornaro G, Pauciullo A, Serafino F (2007) Multipass SAR processing for urbanized areas imaging and deformation monitoring at small and large scales. Proceedings of the IEEE Urban Remote Sensing Joint Event, Paris, France, pp 1-7. https://doi.org/10.1109/URS.2007.371879

Galindo-Zaldívar J, Jabaloy A, González-Lodeiro F, Aldaya F (1997) Crustal structure of the central sector of the Betic Cordillera (SE Spain). Tectonics 16: 18-37. https://doi.org/10.1029/96TC02359

Galindo-Zaldívar J, Gil AJ, Borque MJ, González-Lodeiro F, Jabaloy A, Marín-Lechado C, Ruano P, Sanz de Galdeano C (2003) Active faulting in the internal zones of the central Betic Cordilleras (SE, Spain). J Geodyn 36: 239-250. https://doi.org/10.1016/S0264-3707(03)00049-8

Galve JP, Pérez-Peña JV, Azañón JM, Closson D, Caló F, Reyes-Carmona C, Jabaloy A, Ruano P, Mateos RM, Notti D, Herrera G, Béjar-Pizarro M, Monserrat O, Bally P (2017) Evaluation of the SBAS InSAR Service of the European Space Agency's Geohazard Exploitation Platform (GEP) Remote Sens 9 1291. https://doi.org/10.3390/rs9121291

García-Dueñas V, Martínez-Martínez JM, Soto JI (1988) Los Nevado-Filábrides, una pila de pliegues-mantos separados por zonas de cizalla. Proceedings of the II Congreso Geológico de España, Granada, Spain, pp 17-26

Girardi JD, Davis DM (2010) Parabolic dune reactivation and migration at Napeague, NY, USA: Insights from aerial and GPR imagery. Geomorphology 114: 530-541. https://doi.org/10.1016/j.geomorph.2009.08.011

Gomez C (2014) Digital photogrammetry and GIS-based analysis of the biogeomorphological evolution of Sakurajima Volcano, diachronic analysis from 1947 to 2006. J Volcanol Geotherm Res 280: 1–13. https://doi.org/10.1016/j.jvolgeores.2014.04.015

Gomez C, Hayakawa Y, Obanawa H (2015) A study of Japanese landscapes using structure from motion derived DSMs and DEMs based on historical aerial photographs: new opportunities for vegetation monitoring and diachronic geomorphology. Geomorphology 242: 11–20. https://doi.org/10.1016/j.geomorph.2015.02.021

Gómez de la Peña L, Ranero CR, Gràcia E, Booth-Rea G (2021) The evolution of the westernmost Mediterranean basins. Earth-Sci Rev 214: 103445. https://doi.org/10.1016/j.earscirev.2020.103445

Gómez-Ortiz A, Schulte L, Salvador-Franch F, Sánchez-Gómer S, Simón-Torres M (2002) Map of Glacial and Periglacial Geomorphology of Sierra Nevada. Consejería de Medio Ambiente, Junta de Andalucía

Gómez-Ortiz A, Palacios D, Palade B, Vázquez-Selem L, Salvador-Franch F (2012) The deglaciation of the Sierra Nevada (Southern Spain). Geomorphology 159: 93-105. https://doi.org/10.1016/j.geomorph.2012.03.008

Gómez-Ortiz A, Oliva M, Salvador-Franch F, Salvà i Catarineu M, Plana i Castellví JA (2018) El interés geográfico de los documentos históricos en la explicación científica del foco glaciar del Corral del Veleta (Sierra Nevada, España) durante la Pequeña Edad del Hielo. Cuad Invest Geogr 44: 267-292. https://doi.org/10.18172/cig.3415

Gómez-Ortiz A, Oliva M, Palacios D, Franch FS, Fernández-Fernández JM (2022) The Impact of Glacial Development on the Landscape of the Sierra Nevada. In Zamora R, Oliva M (eds) The Landscape of the Sierra Nevada: A Unique Laboratory of Global Processes in Spain, Springer, pp 83-93. https://doi.org/10.1007/978-3-030-94219-9_6

Gomez-Pugnaire MT, Galindo-Zaldívar J, Rubatto D, González-Lodeiro F, Lopez Sanchez-Vizcaino V, Jabaloy A (2004) A reinterpretation of the Nevado-Filábride and Alpujárride complexes (Betic Cordillera): field, petrography and U-Pb ages from orthogneisses (western Sierra Nevada, S Spain). Schweiz Miner Petrogr Mitt 84: 303-322.

Gómez-Pugnaire MT, Rubatto D, Fernández-Soler JM, Jabaloy A, López-Sánchez-Vizcaíno V, González-Lodeiro F, Galindo-Zaldívar J, Padrón-Navarta JA (2012) Late Variscan magmatism in the Nevado-Filábride Complex: U-Pb geochronologic evidence for the pre-Mesozoic nature of the deepest Betic complex (SE Spain) Lithos 146: 93-111. https://doi.org/10.1016/j.lithos.2012.03.027

GPL (2016) CloudCompare (Software)

Gu ZK, Yao X, Yao CC, Li CG (2021) Mapping of geomorphic dynamic parameters for analysis of landslide hazards: A case of Yangbi river basin on the upper Lancang-Mekong of China. J Mt Sci 18: 2402-2411. https://doi.org/10.1007/s11629-021-6795-2

Guinau M, Tapia M, Pérez-Guillén C, Suriñach E, Roig P, Khazaradze G, Torné M, Royán MJ, Echeverria A. (2019). Remote sensing and seismic data integration for the characterization of a rock slide and an artificially triggered rock fall. Eng Geol 257: 105113. https://doi.org/10.1016/j.enggeo.2019.04.010

Gullà G, Peduto D, Borrelli L, Antronico L, Fornaro G (2017) Geometric and kinematic characterization of landslides affecting urban areas: the Lungro case study (Calabria, Southern Italy). Landslides 14: 171-188. https://doi.org/10.1007/s10346-015-0676-0

Gutiérrez F, Galve JP, Lucha P, Castañeda C, Bonachea J, Guerrero J (2011) Integrating geomorphological mapping, trenching, InSAR and GPR for the identification and characterization of sinkholes: A review and application in the mantled evaporite karst of the Ebro Valley (NE Spain). Geomorphology 134: 144-156. https://doi.org/10.1016/j.geomorph.2011.01.018

Gutscher MA, Dominguez S, Westbrook GK, Le Roy P, Rosas F, Duarte JC, Terrinha P, Miranda JM, Graindorge D, Gailler A, Sallares V, Bartolome R (2012) The Gibraltar subduction: A decade of new geophysical data. Tectonophysics 574: 72-91. https://doi.org/10.1016/j.tecto.2012.08.038

Hartley R, Zisserman A (2003) Multiple View Geometry in Computer Vision. Cambridge University Press

Herrera G, Mateos RM, García-Davalillo JC, Grandjean G, Poyiadji E, Maftei R, Filipciuc T-C, Jemec Auflič M, Jež J, Podolszki L, Trigila A, Iadanza C, Raetzo H, Kociu A, Przyłucka M, Kułak M, Sheehy M, Pellicer XM, McKeown C, Ryan G, Kopačková V, Frei M, Kuhn D, Hermanns RL, Koulermou N, Smith CA, Engdahl M, Buxó P, Gonzalez M, Dashwood C, Reeves H, Cigna F, Liščák P, Pauditš P, Mikulėnas V, Demir V, Raha M, Quental L, Sandić C, Fusi B, Jensen OD (2018) Landslide databases in the

Geological Surveys of Europe. Landslides 15: 359-379. https://doi.org/10.1007/s10346-017-0902-z

Hungr O, Leroueil S, Picarelli L (2014) The Varnes classification of landslide types, an update. Landslides 11: 167-194. https://doi.org/10.1007/s10346-013-0436-y

Irigaray C, Lamas F, El Hamdouni R, Fernández T, Chacón J (2000) The importance of the precipitation and the susceptibility of the slopes for the triggering of landslides along the roads. Nat. Hazards 21: 65–81. https://doi.org/10.1023/A:1008126113789

Jabaloy A, Galindo-Zaldívar J, González-Lodeiro F (1992) The Mecina Extensional System: its relation with the post-Aquitanian piggy-back basins and the paleostresses evolution (Betic Cordilleras, Spain). Geo-Marine Lett 12: 96-103. https://doi.org/10.1007/BF02084918

Jabaloy A, Galindo-Zaldívar J, González-Lodeiro F (1993) The Alpujárride-Nevado-Fibábride extensional shear zone, Betic Cordillera, SE Spain. J Struct Geol 15: 555-569. https://doi.org/10.1016/0191-8141(93)90148-4

Jabaloy-Sánchez A, Lobo FJ, Azor A, Martín-Rosales W, Pérez-Peña JV, Bárcenas P, Macías J, Fernández-Salas LM, Vázquez-Vílchez M (2014) Six thousand years of coastline evolution in the Guadalfeo deltaic system (southern Iberian Peninsula). Geomorphology 206: 374-391. https://doi.org/10.1016/j.geomorph.2013.08.037

Jabaloy-Sánchez A, Gómez-Pugnaire MT, Padrón-Navarta JA, Sánchez-Vizcaíno VL, Garrido CJ (2015) Subduction-and exhumation-related structures preserved in metaserpentinites and associated metasediments from the Nevado–Filábride Complex (Betic Cordillera, SE Spain). Tectonophysics 644: 40-57. https://doi.org/10.1016/j.tecto.2014.12.022

Jabaloy-Sánchez A, Talavera C, Gómez-Pugnaire MT, López-Sánchez-Vizcaíno V, Vázquez-Vílchez M, Rodríguez-Peces MJ, Evans NJ (2018) U-Pb ages of detrital zircons from the Internal Betics: A key to deciphering paleogeographic provenance and tectono-stratigraphic evolution. Lithos 318: 244-266. https://doi.org/10.1016/j.lithos.2018.07.026

Jarman D, Calvet M, Corominas J, Delmas M, Gunnell Y (2014) Large-scale rock slope failures in the eastern pyrenees: identifying a sparse but significant population in paraglacial and parafluvial contexts. Geogr Ann A 96: 357-391. https://doi.org/10.1111/geoa.12060

Jiménez-Perálvarez JD, Irigaray C, El Hamdouni R, Chacón J (2011) Landslide-susceptibility mapping in a semi-arid mountain environment: an example from the southern slopes of Sierra Nevada (Granada, Spain). Bull Eng Geol Environ 70: 265-277. https://doi.org/10.1007/s10064-010-0332-9

Jiménez-Perálvarez JD (2012) Movimientos de ladera en la vertiente meridional de Sierra Nevada (Granada, España): identificación, análisis y cartografía de susceptibilidad y peligrosidad mediante SIG. Doctoral Thesis, University of Granada

Jiménez-Perálvarez JD, El Hamdouni R, Palenzuela JA, Irigaray C, Chacón J (2017) Landslide-hazard mapping through multi-technique activity assessment: an example from the Betic Cordillera (southern Spain). Landslides 14: 1975-1991. https://doi.org/10.1007/s10346-017-0851-6

Kirby E, Whipple KX (2012) Expression of active tectonics in erosional landscapes. J Struct Geol 44:54-75. https://doi.org/10.1016/j.jsg.2012.07.009

Lalagüe A (2015) Use of ground penetrating radar for transportation infrastructure maintenance. Doctoral Thesis, Norwegian University of Science and Technology

Leinss S, Bernhard P (2021) TanDEM-X: Deriving InSAR height changes and velocity dynamics of great aletsch glacier. IEEE J Sel Top Appl Earth Obs Remote Sens 14: 4798-4815. https://doi.org/10.1109/JSTARS.2021.3078084

Lissak C, Maquaire O, Malet JP, Lavigne F, Virmoux C, Gomez C, Davidson R (2015) Ground-penetrating radar observations for estimating the vertical displacement of rotational landslides. Nat Hazards Earth Syst Sci 15: 1399–1406. https://doi.org/10.5194/nhess-15-1399-2015

Lonergan L (1993). Timing and kinematics of deformation in the Malaguide Complex, Internal Zone of the Betic Cordillera, southeast Spain. Tectonics 12: 460-476. https://doi.org/10.1029/92TC02507

López-Vinielles J, Ezquerro P, Fernández-Merodo JA, Béjar-Pizarro M, Monserrat O, Barra A, Blanco P, García-Robles J, Filatov A, García-Davalillo JC, Sarro R, Mulas J, Mateos RM, Azañón JM, Galve JP, Herrera G (2020) Remote analysis of an open-pit slope failure: Las Cruces case study, Spain. Landslides 17: 2173-2188. https://doi.org/10.1007/s10346-020-01413-7

Macau F 1962 Mapa de los movimientos del terreno de la provincia de Granada 1:200,000. Servicio Geológico de Obras Públicas. Barcelona

Macau F 1963. Previsión de los movimientos del terreno. Informaciones y estudios. Servicio Geológico de Obras Públicas del MOP, boletín nº 16, 83 pp.

Madarieta-Txurruka A, Galindo-Zaldívar J, González-Castillo L, Peláez JA, Ruiz-Armenteros AM, Henares J, Garrido-Carretero MS, Avilés M, Gil AJ (2021) High-and Low-Angle Normal Fault Activity in a Collisional Orogen: The Northeastern Granada Basin (Betic Cordillera). Tectonics 40: e2021TC006715. https://doi.org/10.1029/2021TC006715

Madarieta-Txurruka A, González-Castillo L, Peláez JA, Catalán M, Henares J, Gil AJ, Lamas-Fernández F, Galindo-Zaldívar J (2022) The role of faults as barriers in confined seismic sequences: 2021 seismicity in the Granada Basin (Betic Cordillera). Tectonics 41: e2022TC007481. https://doi.org/10.1029/2022TC007481

Martínez-Martínez JM, Soto JI, Balanyá JC (2002) Orthogonal folding of extensional detachments: structure and origin of the Sierra Nevada Elongated Dome (Betics, SE Spain). Tectonics 21: 1–3. https://doi.org/10.1029/2001TC001283

Martínez-Martínez JM (2006) Lateral interaction between metamorphic core complexes and less-extended, tilt-block domains: the Alpujarras strike-slip transfer fault zone (Betics, SE Spain) J Struct Geol 28: 602-620. https://doi.org/10.1016/j.jsg.2006.01.0124

Martínez-Martos M, Galindo-Zaldívar J, Sanz de Galdeano C, García-Tortosa FJ, Martínez-Moreno FJ, Ruano P, González-Castillo L, Azañón JM (2017) Latest extension of the Laujar fault in a convergence setting (Sierra Nevada, Betic Cordillera) J Geodyn 104: 15-26. https://doi.org/10.1016/j.jog.2016.12.002

Massonnet D, Rossi M, Carmona C, Adragna F, Peltzer G, Feigl K, Rabaute T (1993) The displacement field of the Landers earthquake mapped by radar interferometry. Nature 364: 138-142. https://doi.org/10.1038/364138a0

Mateos RM, García-Moreno I, Reichenbach P, Herrera G, Sarro R, Rius J, Aguió R, Fiorucci F (2016) Calibration and validation of rockfall modelling at regional scale: application along a roadway in Mallorca (Spain) and organization of its management. Landslides 13: 751-763. https://doi.org/10.1007/s10346-015-0602-5

Mateos RM, Azañón JM, Roldán FJ, Notti D, Pérez-Peña V, Galve JP, Pérez-García JL, Colomo CM, Gómez-López JM, Montserrat O, Devantèry N, Lamas-Fernández F, Fernández-Chacón F (2017) The combined use of PSInSAR and UAV photogrammetry techniques for the analysis of the kinematics of a coastal landslide affecting an urban area (SE Spain). Landslides 14: 743-754. https://doi.org/10.1007/s10346-016-0723-5

Mateos RM, Ezquerro P, Azañón JM, Gelabert B, Herrera G, Fernández-Merodo JA, Spizzichino D, Sarro R, García-Moreno I, Béjar-Pizarro M (2018) Coastal lateral spreading in the world heritage site of the Tramuntana Range (Majorca, Spain). The use of PSInSAR monitoring to identify vulnerability. Landslides 15: 797-809. https://doi.org/10.1007/s10346-018-0949-5

Mateos RM, López-Vinielles J, Poyiadji E, Tsagkas D, Sheehy M, Hadjicharalambous K, Liscák P, Podolski L, Laskowicz I, Iadanza C, Gauert C, Todorović S, Auflič MJ, Maftei R, Hermanns RL, Kociu A, Sandić C, Mauter R, Sarro R, Béjar M, Herrera G (2020) Integration of landslide hazard into urban planning across Europe. Landsc Urban Plan 196: 103740. https://doi.org/10.1016/j.landurbplan.2019.103740

Mezcua J, Rueda J, García Blanco RM (2004) Reevaluation of historic earthquakes in Spain. Seismol Res Lett 75: 75-81. https://doi.org/10.1785/gssrl.75.1.75

Monié P, Galindo-Zaldivar J, Lodeiro FG, Goffe B, Jabaloy A (1991) 40Ar/39Ar geochronology of Alpine tectonism in the Betic Cordilleras (southern Spain). J Geol Soc 148: 289-297. https://doi.org/10.1144/gsjgs.148.2.0289

MOPU 1987. Mapa de movimientos del Terreno de la provincia de Granada a escala 1:100,000

Moran ML, Greenfield RJ, Arcone SA, Delaney AJ (2000) Multidimensional GPR array processing using Kirchhoff migration. J Appl Geophy 43: 281-295. https://doi.org/10.1016/S0926-9851(99)00065-8

Moreno-Sánchez M (2020) Comparing subsidence rates estimated from GPR profiles with InSAR measurements at National Road N-323 (Granada, Spain). Master's Thesis, University of Cardiff

Moro M, Saroli M, Tolomei C, Salvi S (2009) Insights on the kinematics of deep-seated gravitational slope deformations along the 1915 Avezzano earthquake fault (Central Italy), from time-series DInSAR. Geomorphology 112: 261-276. https://doi.org/10.1016/j.geomorph.2009.06.011

Notti D, Herrera G, Bianchini S, Meisina C, García-Davalillo JC, Zucca F (2014) A methodology for improving landslide PSI data analysis. Int J Remote Sens 35: 2186-2214. https://doi.org/10.1080/01431161.2014.889864

Notti D, Galve JP, Mateos RM, Monserrat O, Lamas-Fernández F, Fernández-Chacón F, Roldán-García FJ, Pérez-Peña JV, Crosetto M, Azañón JM (2015) Human-induced coastal landslide reactivation. Monitoring by PSInSAR techniques and urban damage survey (SE Spain). Landslides 12: 1007-1014. https://doi.org/10.1007/s10346-015-0612-3

Oliva M, Gómez-Ortiz A, Salvador-Franch F, Salvà-Catarineu M, Palacios D, Tanarro L, Ramos M, Pereira P, Ruiz-Fernández J (2016) Inexistence of permafrost at the top of the Veleta peak (Sierra Nevada, Spain). Sci Total Environ 550: 484-494. https://doi.org/10.1016/j.scitotenv.2016.01.150

Ortuño M, Guinau M, Calvet J, Furdada G, Bordonau J, Ruiz A, Camafort M (2017). Potential of airborne LiDAR data analysis to detect subtle landforms of slope failure: Portainé, Central Pyrenees. Geomorphology 295: 364-382. https://doi.org/10.1016/j.geomorph.2017.07.015

Palacios D, Gómez-Ortiz A, Andrés N, Salvador F, Oliva M (2016) Timing and new geomorphologic evidence of the last deglaciation stages in Sierra Nevada (southern Spain). Quat Sci Rev 150: 110-129. https://doi.org/10.1016/j.quascirev.2016.08.012

Palau RM, Hürlimann M, Berenguer M, Sempere-Torres D (2020). Influence of the mapping unit for regional landslide early warning systems: comparison between pixels and polygons in Catalonia (NE Spain). Landslides 17: 2067-2083. https://doi.org/10.1007/s10346-020-01425-3

Palenzuela JA, Irigaray C, Jiménez-Perálvarez JD, Chacón J (2013) Application of terrestrial laser scanner to the assessment of the evolution of diachronic landslides. In: Margottini C, Canuti P, Sassa K (eds) Landslide Science and Practice, vol 2: Early Warning, Instrumentation and Monitoring. Springer, pp. 517-523

Palenzuela JA, Marsella M, Nardinocchi C, Pérez JL, Fernández T, Chacón J, Irigaray C (2015) Landslide detection and inventory by integrating LiDAR data in a GIS environment. Landslides 12: 1035-1050. https://doi.org/10.1007/s10346-014-0534-5

Palenzuela JA, Jiménez-Perálvarez JD, Chacón J, Irigaray C (2016) Assessing critical rainfall thresholds for landslide triggering by generating additional information from a reduced database: an approach with examples from the Betic Cordillera (Spain) Nat Hazards 84: 185-212. https://doi.org/10.1007/s11069-016-2416-8

Palma P, Oliva M, García-Hernández C, Ortiz AG, Ruiz-Fernández J, Salvador-Franch F, Catarineu M (2017) Spatial characterization of glacial and periglacial landforms in the highlands of Sierra Nevada (Spain). Sci. Total Environ 584: 1256-1267. https://doi.org/10.1016/j.scitotenv.2017.01.196

Peduto D, Santoro M, Aceto L, Borrelli L, Gullà G (2021) Full integration of geomorphological, geotechnical, A-DInSAR and damage data for detailed geometric-kinematic features of a slow-moving landslide in urban area. Landslides 18: 807-825. https://doi.org/10.1007/s10346-020-01541-0

Pérez-Peña JV, Azor A, Azañón JM, Keller EA (2010) Active tectonics in the Sierra Nevada (Betic Cordillera, SE Spain): Insights from geomorphic indexes and drainage pattern analysis. Geomorphology 119: 74-87. https://doi.org/10.1016/j.geomorph.2010.02.020

Perron JT, Royden L (2013) An integral approach to bedrock river profile analysis. Earth Surf Process Landf 38: 570-576. https://doi.org/10.1002/esp.3302

Pix4D SA (2017) Pix4D Mapper (Software)

Platt JP, Anczkiewicz R, Soto JI, Kelley SP, Thirlwall M (2006) Early Miocene continental subduction and rapid exhumation in the western Mediterranean. Geology 34: 981-984. https://doi.org/10.1130/G22801A.1

Poulaki EM, Stockli DF, Shuck BD (2023) Pre-Subduction Architecture Controls Coherent Underplating During Subduction and Exhumation (Nevado-Filábride Complex, Southern Spain) Geochem Geophys Geosystems 24: e2022GC010802. https://doi.org/10.1029/2022GC010802

Puga E, Díaz de Federico A, Nieto JM (2002) Tectonostratigraphic subdivision and petrological characterisation of the deepest complexes of the Betic zone: a review. Geodin Acta 15: 23-43. https://doi.org/10.1080/09853111.2002.10510737

Puga E, Fanning M, Díaz de Federico A, Nieto JM, Beccaluva L, Bianchini G, Díaz-Puga MA (2011) Petrology, geochemistry and U–Pb geochronology of the Betic Ophiolites: inferences for Pangaea break-up and birth of the westernmost Tethys Ocean. Lithos 124: 255-272. https://doi.org/10.1016/j.lithos.2011.01.002

GSSI (2012) RADAN 7 (Software)

Rashed EA (2015) GPR background removal using a directional total variation minimisation approach. J Geophys Eng 12: 897-908. https://doi.org/10.1088/1742-2132/12/6/897

Rasol M, Pais JC, Pérez-Gracia V, Solla M, Fernandes FM, Fontul S, Ayala-Cabrera D, Schmidt F, Assadollahi H (2022) GPR monitoring for road transport infrastructure: A systematic review and machine learning insights. Constr Build Mater 324: 126686. https://doi.org/10.1016/j.conbuildmat.2022.126686

Reyes-Carmona C, Barra A, Galve JP, Monserrat O, Pérez-Peña JV, Mateos RM, Notti D, Ruano P, Millares A, López-Vinielles J, Azañón JM (2020) Sentinel-1 DInSAR for monitoring active landslides in critical infrastructures: the case of the Rules Reservoir (Southern Spain). Remote Sens 12: 809. https://doi.org/10.3390/rs12050809

Reyes-Carmona C, Galve JP, Moreno-Sánchez M, Riquelme A, Ruano P, Millares A, Teixidó, Sarro R, Pérez-Peña V, Barra A, Ezquerro, López-Vinielles J, Béjar-Pizarro M, Azañón JM, Monserrat O Mateos RM (2021) Rapid characterisation of the extremely large landslide threatening the Rules Reservoir (Southern Spain). Landslides 18: 3781-3798. https://doi.org/10.1007/s10346-021-01728-z

Reyes-Carmona C, Galve JP, Pérez-Peña JV, Moreno-Sánchez M, Alfonso-Jorde D, Ballesteros D, Torre D, Azañón JM, Mateos RM (in press) Improving landslide inventories by combining satellite interferometry and landscape analysis: the case of Sierra Nevada (Southern Spain). Landslides

Riquelme A, Del Soldato M, Tomás R, Cano M, Bordehore LJ, Moretti S (2019) Digital landform reconstruction using old and recent open access digital aerial photos. Geomorphology 329: 206-223. https://doi.org/10.1016/j.geomorph.2019.01.003

Roberts NJ, Evans SG (2013) The gigantic Seymareh (Saidmarreh) rock avalanche, Zagros Fold–Thrust Belt, Iran. J Geol Soc London 170: 685-700. https://doi.org/10.1144/jgs2012-090

Rocscience Inc (2004) DIPS (Software)

Rodríguez-Peces MJ, García-Mayordomo J, Azañón JM, Insua-Arévalo JM, Jiménez-Pintor J (2011) Constraining pre-instrumental earthquake parameters from slope stability back-analysis: Palaeoseismic reconstruction of the Güevéjar landslide during the 1st November 1755 Lisbon and 25th December 1884 Arenas del Rey earthquakes. Quat Int 242: 76-89. https://doi.org/10.1016/j.quaint.2010.11.027

Rodríguez-Peces MJ, García-Mayordomo J, Martínez-Díaz JJ (2014) Slope instabilities triggered by the 11th May 2011 Lorca earthquake (Murcia, Spain): comparison to previous hazard assessments and proposition of a new hazard map and probability of failure equation. Bull Earthq Eng 12: 1961-1976. https://doi.org/10.1007/s10518-013-9509-5

Royden LH (1993) Evolution of retreating subduction boundaries formed during continental collision. Tectonics 12: 629-638. https://doi.org/10.1029/92TC02641

Ruiz-Fuentes A, Aerden DG (2018) Transposition of foliations and superposition of lineations during polyphase deformation in the Nevado-Filabride complex: tectonic implications. Int J Earth Sci 107: 1975-1988. https://doi.org/10.1007/s00531-017-1582-6

Sadura S, Martini IP, Endres AL, Wolf K (2006) Morphology and GPR stratigraphy of a frontal part of an end moraine of the Laurentide Ice Sheet: Paris Moraine near Guelph, ON, Canada. Geomorphology 75: 212-225. https://doi.org/10.1016/j.geomorph.2005.01.014

Sánchez-Vizcaíno VL, Rubatto D, Gómez-Pugnaire MT, Trommsdorff V, Müntener O (2001) Middle Miocene high-pressure metamorphism and fast exhumation of the Nevado-Filábride Complex, SE Spain. Terra Nova 13: 327-332. https://doi.org/10.1046/j.1365-3121.2001.00354.x

Sandmeier (1997) Reflex (Software)

Santamaría-López Á, Lanari P, Sanz de Galdeano C (2019) Deciphering the tectono-metamorphic evolution of the Nevado-Filábride complex (Betic Cordillera, Spain)–A petrochronological study. Tectonophysics 767: 128158. https://doi.org/10.1016/j.tecto.2019.06.028

Sanz de Galdeano C, Alfaro P (2004) Tectonic significance of the present relief of the Betic Cordillera. Geomorphology 63: 175-190. https://doi.org/10.1016/j.geomorph.2004.04.002

Sarro R, Mateos RM, García-Moreno I, Herrera G, Reichenbach P, Laín L, Paredes C (2014) The Son Poc rockfall (Mallorca, Spain) on the 6th of March 2013: 3D simulation. Landslides 11: 493-503. https://doi.org/10.1007/s10346-014-0487-8

Schlögel R, Doubre C, Malet JP, Masson F (2015) Landslide deformation monitoring with ALOS/PALSAR imagery: A D-InSAR geomorphological interpretation method. Geomorphology 231: 314-330. https://doi.org/10.1016/j.geomorph.2014.11.031

Schwanghart W, Kuhn NJ (2010) TopoToolbox: A set of Matlab functions for topographic analysis. Environ Model Softw 25: 770-781. https://doi.org/10.1016/j.envsoft.2009.12.002

Schwanghart W, Scherler D (2014) TopoToolbox 2–MATLAB-based software for topographic analysis and modeling in Earth surface sciences. Earth Surf Dyn 2: 1-7. https://doi.org/10.5194/esurf-2-1-2014

Simancas JF, Campos J (1993) Compresión NNW-SSE tardia postmetamórfica y extensión subordinada en el Complejo Alpujárride (Dominio de Alborán, Orógeno Bético). Rev Soc Geol España 6: 23-35

Simancas JF (2018) A reappraisal of the Alpine structure of the Alpujárride Complex in the Betic Cordillera: Interplay of shortening and extension in the westernmost Mediterranean. Journal Struct Geol 115: 231-242. https://doi.org/10.1016/j.jsg.2018.08.001

Snoeij P, Attema E, Davidson M, Floury N, Levrini G, Rosich B, Rommen B (2008) Sentinel-1, the GMES radar mission. Proceedings of the IEEE Radar Conference, Rome, Italy, pp 1-5. https://doi.org/10.1109/RADAR.2008.4720735

Soldati M (2013) Deep-seated gravitational slope deformation. In: Bobrowsky PT (ed) Encyclopedia of natural hazards. Springer, pp 151-155

Sorriso-Valvo M, Gullà G (1996) Rockslides. In: Dikau R, Brunsden D, Schrott L, Ibsen ML (eds) Landslide recognition: identification, movements and causes. John Wiley & Sons, pp 85-96

Sousa JJ, Bastos L (2013) Multi-temporal SAR interferometry reveals acceleration of bridge sinking before collapse. Nat Hazards Earth Syst Sc 13: 659-667. https://doi.org/10.5194/nhess-13-659-2013

Tolomei C, Taramelli A, Moro M, Saroli M, Aringoli D, Salvi S (2013) Analysis of the deep-seated gravitational slope deformations over Mt. Frascare (Central Italy) with geomorphological assessment and DInSAR approaches. Geomorphology 201: 281-292. https://doi.org/10.1016/j.geomorph.2013.07.002

Tomás R, Abellán A, Cano M, Riquelme A, Tenza-Abril AJ, Baeza-Brotons F, Saval JM, Jaboyedoff M (2018) A multidisciplinary approach for the investigation of a rock spreading on an urban slope. Landslides 15: 199-217. https://doi.org/10.1007/s10346-017-0865-0

TRE-Altamira (2023). Webpage. Retrieved from https://site.tre-altamira.com/insar/

Troiani F, Galve JP, Piacentini, Della Seta M, Guerrero J (2014) Spatial analysis of stream length-gradient (SL) index for detecting hillslope processes: a case of the Gállego River headwaters (Central Pyrenees, Spain). Geomorphology 214: 183-197. https://doi.org/10.1016/j.geomorph.2014.02.004

Tsou CY, Chigira M, Matsushi Y, Chen SC (2015) Deep-seated gravitational deformation of mountain slopes caused by river incision in the Central Range, Taiwan: Spatial distribution and geological characteristics. Eng Geol 196: 126-138. https://doi.org/10.1016/j.enggeo.2015.07.005

Ullman 1979 The interpretation of structure from motion. Proc. R. Soc. Lond. B. 203: 405-426. http://doi.org/10.1098/rspb.1979.0006

University of Stuttgart (2023). Webpage. Retrieved from https://www.f06.uni-stuttgart.de/studium/studium_gug/allgemein/fernerkundung/

Valenzuela P, Domínguez-Cuesta MJ, Mora García MA, Jiménez-Sánchez M (2018) Rainfall thresholds for the triggering of landslides considering previous soil moisture conditions (Asturias, NW Spain). Landslides 15: 273-282. https://doi.org/10.1007/s10346-017-0878-8

Varnes DJ (1978) Slope movement types and processes. In: Schuster RL, Krizek RJ (eds) Landslides: Analysis and Control. Transportation Research Board, National Academy of Sciences, pp 11-33

Varnes DJ (1984) Landslide hazard zonation: a review of principles and practice. United Nations Scientific and Cultural Organization (UNESCO), Paris, pp 1-63

Vidal (1986) Sismotectónica de la región Bética-Mar de Alborán. Doctoral Thesis, University of Granada

Walsh LS, Martin AJ, Ojha TP, Fedenczuk (2012) Correlations of fluvial knickzones with landslide dams, lithologic contacts, and faults in the southwestern Annapurna Range, central Nepalese Himalaya. J Geophys Res Earth Surf 117: F01012. https://doi.org/10.1029/2011JF001984

Werner C, Wegmuller U, Strozzi T, Wiesmann A (2003) Interferometric point target analysis for deformation mapping. Proceedings of the IEEE International Geoscience and Remote Sensing Symposium, Toulouse, France, pp 4362-4364. https://doi.org/10.1109/IGARSS.2003.1295516

Williams JR, Platt JP (2018) A new structural and kinematic framework for the Alborán Domain (Betic–Rif arc, western Mediterranean orogenic system). J Geol Soc 175: 465-496. https://doi.org/10.1144/jgs2017-086

Wobus C, Whipple KX, Kirby E, Snyder N, Johnson J, Spyropolou K, Crosby B, Sheenan D (2006) Tectonics from topography: Procedures, promise, and pitfalls. In: Willett SD, Hovius N, Brandon MT, Fisher DM (eds) Tectonics, Climate, and Landscape Evolution, Geological Society of America, vol 398, pp 55-74. https://doi.org/10.1130/2006.2398(04)

Zeck HP, Monié P, Villa IM, Hansen BT (1992) Very high rates of cooling and uplift in the Alpine belt of the Betic Cordilleras, southern Spain. Geology 20: 79-82. https://doi.org/10.1130/0091-7613(1992)020<0079:VHROCA>2.3.CO;2

Chapter II

Improving landslide inventories by combining satellite interferometry and landscape analysis: the case of Sierra Nevada (Southern Spain)

Accepted on:

Landslides

Article in press

(Received: 28 November 2022, Accepted: 12 April 2023)

Cristina Reyes-Carmona [1,2], Jorge Pedro Galve [1], José Vicente Pérez-Peña [1,3], Marcos Moreno-Sánchez [1], David Alfonso-Jorde [1], Daniel Ballesteros [1], Davide Torre [4], José Miguel Azañón [1,3,5], Rosa María Mateos [2]

[1] Departamento de Geodinámica, Universidad de Granada, Avenida del Hospicio s/n, 18010 Granada, Spain

[2] Geohazards InSAR laboratory and Modelling group (InSARlab), Geohazards and Climate Change Department, Geological and Mining Institute of Spain (IGME-CSIC), Calle de Ríos Rosas 23, 28003 Madrid, Spain

[3] Instituto Andaluz de Geofísica, Calle del Profesor Clavera 12, 18071 Granada, Spain

[4] Department of Applied and Pure Sciences, University of Urbino "Carlo Bo", Via Aurelio Saffi 2, 61029 Urbino, Italy

[5] Instituto Andaluz de Ciencias de la Tierra (IACT-CSIC), Avenida de las Palmeras 4, 18100 Armilla, Granada, Spain

Abstract

An updated and complete landslide inventory is the starting point for an appropriate hazard assessment. This paper presents an improvement for landslide mapping by integrating data from two well-consolidated techniques: Differential Synthetic Aperture Radar (DInSAR) and Landscape Analysis through the normalised channel steepness index (k_{sn}). The southwestern sector of the Sierra Nevada mountain range (Southern Spain) was selected as the case study. We first propose the double normalised steepness (k_{snn}) index, derived from the k_{sn} index, to remove the active tectonics signal. The obtained k_{snn} anomalies (or knickzones) along rivers and the unstable ground areas from the DInSAR analysis rapidly highlighted the slopes of interest. Thus, we provided a new inventory of 28 landslides that implies an increase in the area affected by landslides compared with the previous mapping: 33.5% in the present study vs. 14.5% in the Spanish Land Movements Database. The two main typologies of identified landslides are Deep-Seated Gravitational Slope Deformations (DGSDs) and rockslides, with the prevalence of large DGSDs in Sierra Nevada being first revealed in this work. We also demonstrate that the combination of DInSAR and Landscape Analysis could overcome the limitations of each method for landslide detection. They also supported us in dealing with difficulties in recognising this type of landslides due to their poorly defined boundaries, a homogeneous lithology and the imprint of glacial and periglacial processes. Finally, a preliminary hazard perspective of these landslides is outlined.

Keywords

DInSAR, k_{sn}, Landslide inventory, DGSD, Rockslide, Mountain range, Sierra Nevada, Southern Spain

1. Introduction

Landslides represent one of the main natural hazards with a strong socioeconomic impact on a global scale (e.g. Kirschbaum et al. 2015; Froude and Petley 2018; Mateos et al. 2020). A good-quality landslide inventory map is necessary for assessing landslide hazard (van Westen et al. 2008). There are some global databases that are actively maintained, such as the Global Landslide Catalogue (https://gpm.nasa.gov/landslides/index.html) and the Global Fatal Landslide Database (https://www.un-spider.org/links-and-resources/data-sources/global-fatal-landslide-database-gfld-university-sheffield). There are also inventories over a more specific spatial scale within a region or country that resulted mainly from the compilation of landslides after catastrophic triggering events (e.g. Hervás and Bobrowsky 2009; Mateos et al. 2012). In the case of Spain, there is a national non-official database of landslides (Land Movements Database, BD-MOVES, http://info.igme.es/catalogo/) published in 2016 by the Geological Survey of Spain (Instituto Geológico y Minero de España, IGME-CSIC). Traditionally, inventory maps have been produced through multi-temporal aerial photo-interpretation and field surveys. However, it remains difficult and time-consuming to produce and update landslide inventories in most regions of the world, especially in mountainous areas with high

extension and poor accessibility (Bekaert et al. 2020). Herrera et al. (2018) compared the European Landslide Susceptibility Map (ELSUS v1) (Günther et al. 2014) with the mapped landslides in each country to analyse where to expect more landslides than those already inventoried. For example, the completeness of the national landslide inventory in Spain (BD-MOVES) is less than 5% (Herrera et al. 2018). The inventoried landslides are usually the most morphologically visible on the landscape, while other typologies with more diffuse boundaries are often overlooked. Therefore, new technologies such as satellite remote sensing or advanced landscape analysis are gaining prominence to improve and optimise landslides' mapping at a regional scale.

Differential Synthetic Aperture Radar Interferometry (DInSAR) is a remote sensing technique that exploits radar satellite images to derive multitemporal displacement measurements of the ground surface. Among numerous applications, DInSAR is a powerful tool to map active landslides and produce inventory maps (e.g. Bekaert et al. 2020; Reyes-Carmona et al. 2020; Crippa et al. 2021). Thanks to the wide coverage (up to a 250 km swath width) and the high temporal resolution (up to 1 day) of the radar images, DInSAR makes analysing very large areas and constantly updating a landslide inventory possible. Some initiatives, such as the Geohazards Exploitation Platform (GEP), developed by the European Space Agency (ESA), aim to promote the use of DInSAR techniques in a user-friendly way. The GEP is a web-based platform (https://geohazards-tep.eu/#!) that allows users to perform automated and independent DInSAR analysis, offering quick results in just 24-48 h. The GEP services have already been successfully applied to discover new landslides, between other natural processes (e.g. Manunta et al. 2016; Galve et al. 2017; Tapete and Cigna 2017; Foumelis et al. 2019; Reyes-Carmona et al. 2021; Gaidi et al. 2021).

Landscape Analysis techniques can also be used to identify (1) recent geological processes, such as active tectonics, fluvial captures, or landslides; (2) local conditions, like lithological contrasts; and (3) the imprint of past geomorphic processes, such as glacial erosional features or high-elevation low-relief surfaces (e.g. Larue 2008; Pérez-Peña et al. 2010; Antón et al. 2014; Troiani et al. 2014; Subiela et al. 2019). These phenomena usually disturb the drainage network and express themselves topographically on rivers by creating knickpoints or knickzones (Walsh et al. 2012). A knickpoint or knickzone is an abnormal increase of the gradient in a specific segment of a river. Punctual changes in the gradient are commonly known as 'knickpoints' while 'knickzones' are referred to gradient changes that affect a longer transect of a river. Both knickpoints and knickzones can be assessed by indexes that analyse river gradient, such as the normalised steepness index (k_{sn}): the higher the gradient change, the higher the k_{sn} index value. Knickzones are reflected as clearly higher values than the rest of values along the river profile, that are considered as anomalous values or anomalies. The successful application of gradient-related indexes to detect landslides has already been proven in several studies (Panek et al. 2007; El Hamdouni et al. 2010; Walsh et al. 2012; Troiani et al. 2014, 2017; Penna et al. 2015; De Palézieux et al. 2018; Ahmed et al. 2019; Subiela et al. 2019; Piacentini et al. 2020; Gu et al. 2021; Liu et al. 2021). In recent years, Geographic Information Systems (GIS) platforms and high-resolution Digital Elevation

Models (DEMs) have facilitated the application of geomorphometric techniques in terms of time-consumption and cost-effectiveness (Troiani et al. 2014, 2017). These techniques also allow studying large areas accurately and efficiently to produce geomorphological maps (Weibel and Heller 1991; Pike 2000), including landslide inventories (e.g. Subiela et al. 2019).

In this study, we used a new combination of DInSAR and k_{sn} index data to explore its effectiveness for landslide detection and mapping in a mountainous area. The southwestern sector of the Sierra Nevada mountain range (Southern Spain) was selected as the case study. We consider this sector a complex mountainous area mainly due to its accessibility, the high local relief, the homogenous lithology, and the difficult recognition of landslides on its landscape. Through DInSAR techniques, we obtained the first ground displacement map of this sector of Sierra Nevada, where unstable areas were detected and related to active landslides. To perform the Landscape Analysis, we applied a new morphometric index: the double normalised steepness (k_{snn}) index. This index was derived from the conventional normalised steepness (k_{sn}) index. It enabled us to identify landslide anomalies by filtering the general tectonic signal observed in the Sierra Nevada from the k_{sn} values. Our results show that, despite their limitations, the combination of both techniques facilitated the identification and mapping of large landslides. The use of high-resolution DEM-derived products and field observations were also essential for the delimitation of landslides. With such a data combination, we provided an inventory with a higher degree of completeness than the previous one (the BD-MOVES). Our analysis also allowed us to identify, for the first time, the existence of Deep-seated Gravitational Slope Deformations (DGSDs) in the Sierra Nevada, as well as to contemplate their related hazard.

2. Study area

The study area contains the northeastern part of the Guadalfeo River Basin, located in the Province of Granada, Southern Spain (Figure 1). This area (378.5 km^2) includes the sub-basins of six tributaries of the Guadalfeo River that are, from west to east: the Lanjarón, Sucio, Chico, Seco, Poqueira, and Trevélez rivers (Figure 1). These rivers drain the southwestern side of Sierra Nevada mountain range, where they have excavated steep V-shaped valleys due to the high topographic gradients: 35 km from 3479 m.a.s.l. (Mulhacén Peak) to the coastline. The Sierra Nevada was declared a Biosphere Reserve by UNESCO in 1986, a Natural Park in 1989, and a National Park in 1999. It is a privileged and representative spot of the Mediterranean high mountain systems. This Alpine setting also has a rich cultural and historical heritage linked to several relict Berber villages known as ‘La Alpujarra’ (Figure 1). This region comprises 25 small picturesque villages with a total population of around 25000 people, being the municipalities of Órgiva (5420 inhabitants) and Lanjarón (3720 inhabitants) the most populated. Moreover, the Sierra Nevada is plenty of uncoated ditches excavated in the ground (locally known as ‘acequias de careo’), originally from the Middle Ages (Martín-Civantos 2010) with an important cultural and hydrological value. This irrigation system was designed to infiltrate the snow melt and runoff water in the wetter months to have spring water supply during the driest

months (Martos-Rosillo et al. 2019). Nowadays, more than 700 km of *acequias* are still working in the Sierra Nevada as a sustainable groundwater recharge system.

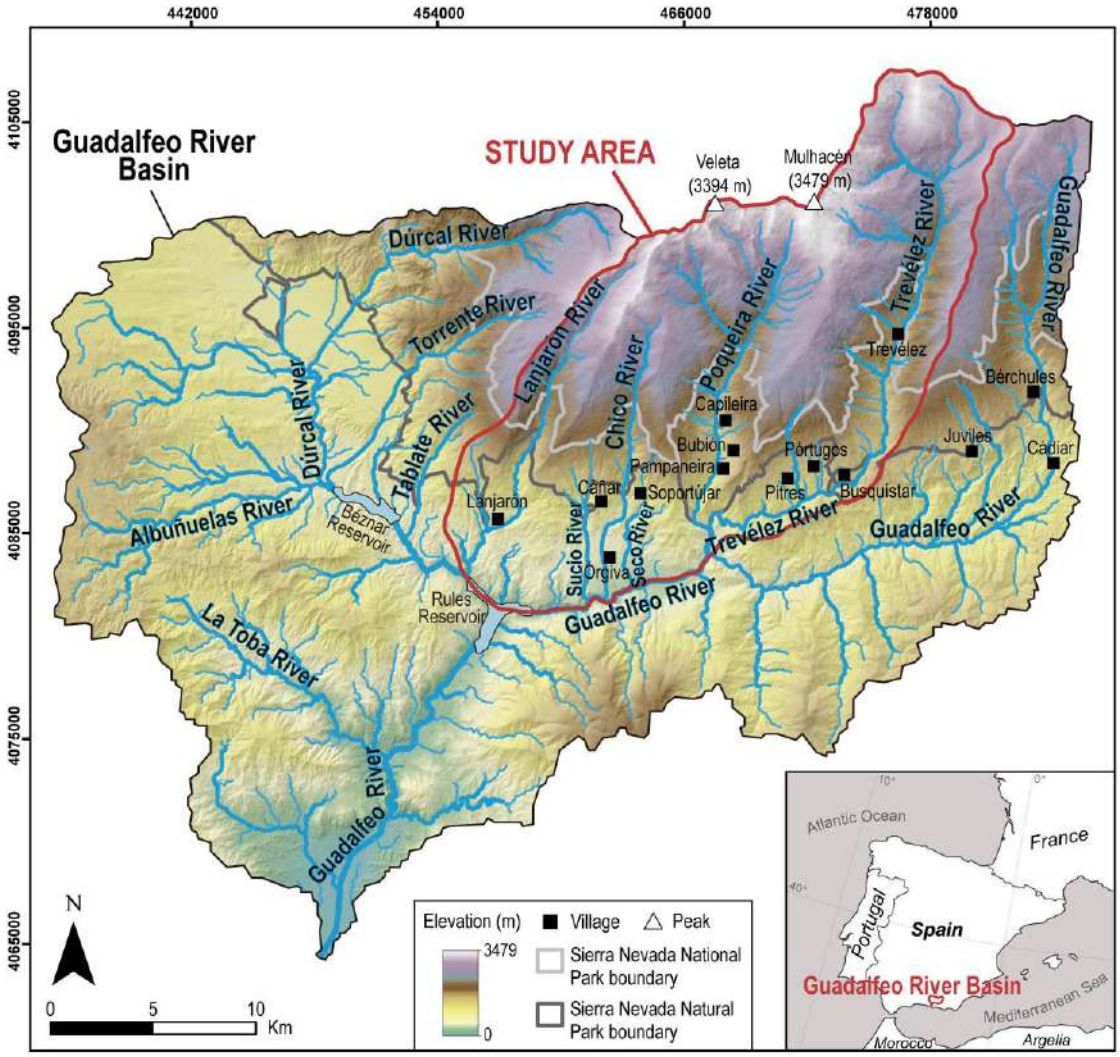

Figure 1. Location of the study area within the Guadalfeo River Basin in Southern Spain. The trunk rivers of the basin, the most famous villages of 'La Alpujarra' and the boundaries of the Sierra Nevada Natural and National Park are also indicated.

From a geological perspective, the Sierra Nevada is located in the central Betic Cordillera, that is the western termination of the Mediterranean Alpine orogen linked to the broad-scale collision between Africa and Iberia (DeMets 1994). The main outcropping geological units are the Nevado-Filábride Complex, the Alpujárride Complex, and the Neogene-Quaternary sedimentary rocks (Figure 2). The internal structure of the Nevado-Filábride Complex is very heterogeneous, characterised by multiple transposed foliations and lineations as the result of a complex polyphase deformation story (e.g. Jabaloy et al. 1993; Martínez-Martínez et al. 2002; Aerden et al. 2013; Puga et al. 2017; Ruiz-Fuentes et al. 2018). The subdivision of the Nevado-Filábride Complex is still under scientific discussion (e.g. Puga et al. 2002; Martínez- Martínez et al. 2002; Gómez-Pugnaire et al. 2012; Sanz de Galdeano et al. 2016; Santamaría-López et al. 2019) but in this study, we followed the classification proposed by Martínez-Martínez et al. (2002). According to these authors, there are two lithological units of metamorphic rocks (Figure 2): the Ragua

Unit and the Calar-Alto Unit. Black graphitic schists entirely form the Ragua Unit (Paleozoic). The Calar-Alto Unit is subdivided into two formations: the Montenegro Formation (Paleozoic), formed by graphitic mica-schists with alternation of quartzites, and the Tahal Formation (Permian-Triassic), formed by light schists with isolated amphibolites and marbles. These three lithologies outcrop in most of the study area (Figure 2), and we consider the lithological sequence relatively homogeneous from a mechanical point of view. The Alpujárride Complex is formed by Permian-Triassic metamorphic rocks that includes, from older to younger: graphitic schists, phyllites and quartzites, mica-schists and dolomitic marbles (Figure 2). The Neogene sedimentary rocks are related to fan deposits: conglomerates with intercalated sandstones (Aldaya et al. 1979). Quaternary deposits include fluvial deposits, travertines, and landslide bodies (Figure 2). The latter are those included in the Spanish Land Movements Database (BD-MOVES, http://info.igme.es/catalogo/). The contact within the Nevado-Filábride and Alpujárride complexes and the inferred limit between the two main units of the Nevado-Filábride Complex are inactive extensional detachments. These detachments and other high-angle normal faults have conducted an extension and consequent exhumation of the complexes since the Miocene (Galindo-Zaldívar et al. 1989; Martínez-Martínez et al. 2006). One of these normal faults (the 'Lanjarón Fault' in Figure 2) is considered to be probably active, although there are no clear signs of activity at present (Sanz de Galdeano et al. 2003). For this reason, this fault is catalogued as a debated fault in the Quaternary Active Faults Database of Iberia (QAFI, http://info.igme.es/qafi/). The overall structure of Sierra Nevada is a large-scale antiformal fold that coincides with the highest elevations of the mountain range. Despite the uplifting stated earlier, Pérez-Peña et al. (2010) inferred that the present-day drainage pattern started to develop in the Pleistocene. These authors analysed several geomorphic indexes to demonstrate that the Sierra Nevada is tectonically active nowadays, and that the recent uplift is concentrated within the southwestern sector, where our study area is located.

From a geomorphological perspective, the current morphology of the study area is highly influenced by the uplifting of the western part of Sierra Nevada, which has conditioned a strong river incision (e.g. incision rates of 5-5.9 mm/yr, according to Chacón et al. 2001; Reinhardt et al. 2007). Consequently, river incision produced over-steepened slopes prone to landslides (El Hamdouni et al. 2010). These landslides are mostly planar slides, earthflows, and rotational slides that occur mainly in the Alpujárride phyllites, the Nevado-Filábride schists, and the Neogene granular or slightly cohesive deposits (El Hamdouni et al. 2010). Chacón et al. (2007) carried out a landslide inventory of the whole Province of Granada in which they identified, just in our study area, a total of 67 landslides (Figure 2): 7 rockfalls, 36 slides and 24 surface processes such as creeping and solifluction. These landslides were later included in the BD-MOVES, in which the 24 surface processes were classified as flows. In the highest elevations of the range, glacial and periglacial morphologies are predominant, with magnificent examples within the upper part of the Poqueira and Trevélez valleys (Gómez-Ortiz et al. 2002). These are related to small valley and cirque glaciers that were the most southern in Europe during the Last Glacial Maximum (Gómez-Ortiz et al. 2012). Deglaciation took place around 14

ka ago, and rock glaciers were formed immediately after, affected by intense periglacial conditions until 7 ka ago (Palma et al. 2017). These authors also established an Equilibrium Line Altitude (ELA) for the last glaciation at 2650 m in the southern sector of Sierra Nevada.

The climate in the Sierra Nevada corresponds to a semiarid cold mountain climate (Dsc according to the Köppen climate classification). Mean annual temperatures are around 0ºC on the summit areas, and the average annual precipitation is around 710-750 mm. Snow is usually present from early December to the end of May, being the snowline settled at 2100 m.a.s.l.

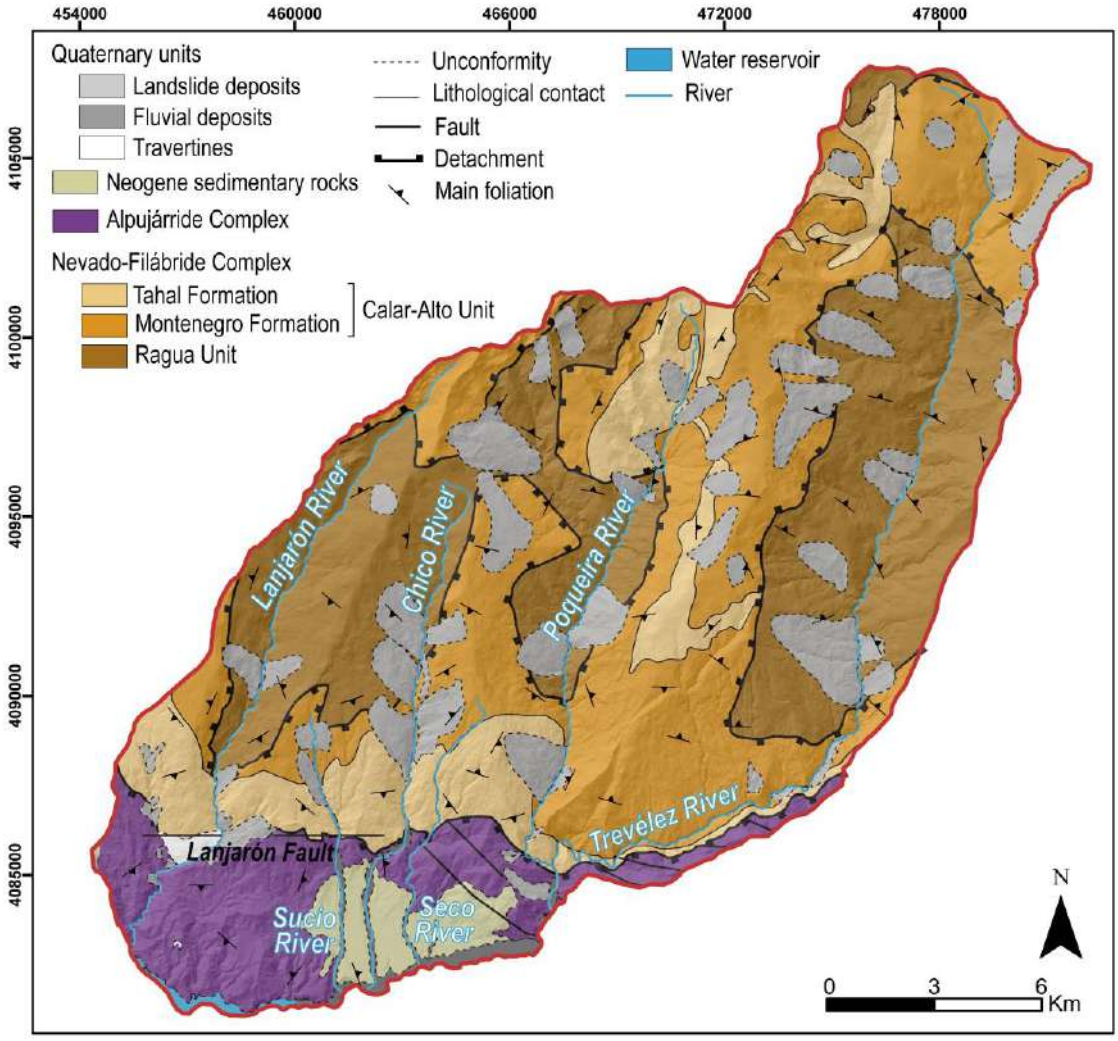

Figure 2. Geological map of the study area, modified from Azañón et al. (2015). The analysed rivers (from west to east) of Lanjarón, Sucio, Chico, Seco, Poqueira and Trevélez are also indicated. The slope movements are those included in the Spanish Land Movements Database (BD-MOVES). The 'Lanjarón Fault' is a probably active fault, according to Sanz de Galdeano et al. (2003), that is also included in the Quaternary Active Faults Database of Iberia (QAFI).

3. Methodology

The methodology of this work consists of the following main stages: (1) calculation of surface ground displacement, derived from DInSAR techniques through the Geohazard

Exploitation Platform; (2) calculation of the double normalised steepness (k_{snn}) index that we propose in this study for the first time; (3) examination of DInSAR results and identification of unstable areas; (4) interpretation of k_{snn} anomalies; and (5) creation of an updated landslide inventory map by combining the DInSAR and k_{snn} data with geomorphological observations. Essentially, our main interest was to evaluate the reliability of both techniques and their complementation to facilitate landslide mapping in a complex mountainous area such as the Sierra Nevada (Southern Spain).

3.1. Differential Synthetic Aperture Radar Interferometry (DInSAR)

To derive the DInSAR data, we used the Parallel Small Baseline Subset (P-SBAS) processing chain (Casu et al. 2014), which is based on measuring ground displacement in points that are Distributed Scatterers (DSs): small targets of similar radar signal that usually correspond to natural features (e.g. agriculture areas, open fields, bare soil, rock surfaces). For this reason, the SBAS methods are very suitable for analysing rural environments and arid areas with low vegetation and debris (Even and Schulz 2018), such as the Sierra Nevada Range. The P-SBAS processing chain has been implemented on the European Space Agency (ESA)'s Geohazards Exploitation Platform (GEP), as detailed in De Luca et al. (2015). It was possible to use the P-SBAS in a fully automated and unsupervised manner through the GEP web-portal thanks to a granted permission of access in the framework of the ESA Network of Resources (NoR) Initiative. For being an automated processing chain, we only had to select the desired input satellite images and decided on a few parameters that were: latitude and longitude of the reference point, polarisation, processing mode, DEM type and coherence threshold.

As radar images are acquired in two different geometries (i.e. ascending and descending orbits), we carried out a processing per each acquisition geometry. We used 101 Sentinel-1B images for the ascending orbit processing with a temporal sampling of 12 days from the 30th of September 2016 to the 13th of March 2020. For the descending orbit, we used 241 Sentinel-1A and Sentinel-1B images with a temporal sampling of 6 days and covering a period from the 22nd of December 2014 to the 19th of March 2020. For both processing jobs, the following parameters were established: vv polarisation, SRTM-1 DEM, coherence threshold of 0.85, and reference point in Lat 36.848/Long -3.497 (WGS84 projection). In the ascending orbit, the satellite travels along the NNW-SSE direction and looks to the east, while in the descending orbit, the satellite travels along the SSW-NNE direction and looks to the west. The direction to which the satellite looks is named Line-of-Sight (LoS) direction and the DInSAR velocity is always calculated along this direction. For this reason, the detected movement of the ground is registered as approaching or distancing from the satellite: negative values indicate that points move away from the satellite, while positive values refer to points moving toward the satellite. Therefore, the output of each processing was a set of points representing the LoS mean displacement or velocity in mm/yr. The pixel size of each point was 90 m.

The DInSAR surface ground displacement rate (or mean annual velocity) maps are represented in equal intervals by establishing a threshold for discriminating stable from unstable points as two times the standard deviation of all the measured velocity points

(Barra et al. 2017). Therefore, the stability range was set between 6 and -6 mm/year for the ascending orbit processing, and between 5 and -5 mm/year for the descending orbit. It is important to remark that the stability range also represents the general noise of the results (i.e. the sensitivity of the technique). This fact implies that a point classified as 'stable' can be either truly stable or unstable, but the displacement cannot be detectable by the technique.

3.2. Landscape Analysis

The morphometric analysis of rivers was computed through the Python library 'landspy', freely available at https://github.com/geolovic/landspy. This computing tool is based on the stream-power model, that relates the local channel slope and the contributing drainage area upstream (Perron and Royden 2013) (Equation 1):

$$S = k_s A^{\theta} \quad \text{(Equation 1)}$$

Where S is the slope of the channel, A is the up-stream drainage area, k_s is the steepness index and θ is the concavity index.

The traditional way to analyse k_s and θ is through linear regression in logarithmic area-slope river profiles. This procedure presents the problem of the high autocorrelation in both parameters, increased even by the logarithmic scale (Wobus et al. 2006; Kirby and Whipple 2012). As θ does not vary in high ranges, a solution to derive the steepness index is by using a fixed reference concavity (θ_{ref}) to obtain a normalised steepness index (k_{sn}). The most popular approach to derive the k_{sn} index from a fixed reference concavity was proposed by Perron and Royden (2013), through the integration of Equation 1 and the definition of the Chi index (χ). By applying this integration, the k_{sn} index is calculated by linear regression between the Chi index and elevation (i.e. the slope of a Chi-elevation plot is the k_{sn} index).

Even normalising the steepness index, the highest values still occur in high-relief areas. This fact makes it difficult to compare gradient changes in areas with prominent topographic differences. In these areas, compared to areas with low-to-moderate topography, Chi-elevation profiles are steeper, and thus, the k_{sn} values are higher. This is the case of the Sierra Nevada Range, where active tectonics have generated high topographic gradients and high k_{sn} values along the main rivers (Azañón et al. 2012, 2015), complicating the identification of knickpoints unrelated to tectonics. To discard these topographic gradient trends resulting from active tectonics, we proposed a double normalised steepness index (k_{snn}) by normalising the k_{sn} index with the mean slope of the Chi-elevation plot (mean k_{sn}). This normalisation eliminates these trends and highlights knickzones that were not evidenced through the k_{sn} index analysis.

To derive the k_{snn} index for the study area, the only input required by the tool 'landspy' was a 10-m resolution DEM, obtained from the Andalusian Environmental Information Network (REDIAM, https://www.juntadeandalucia.es/medioambiente/portal/acceso-rediam). Following, channel gradients and the Chi, k_{sn} and k_{snn} indexes were derived for the six selected sub-basins of the Lanjarón, Sucio, Chico, Seco, Poqueira and Trevélez

rivers. These indexes were calculated for rivers' segments of 700 m length, which was considered an appropriate value for the scale of our analysis. The Chi index was computed with a reference concavity of 0.45, which is a suitable value according to previous studies in the Betic Cordillera (Bellin et al. 2014; Azañón et al. 2015). Once obtained the K_{snn} index, we defined five intervals by a natural break classification for a proper data visualisation. The k_{snn} values higher than 7.4 were considered to be anomalous. This threshold is the cut value of the natural break intervals that is closest to one standard deviation of the data (7.6). Lastly, we focused on identifying anomalies (k_{snn} values higher than 7.4) with a length equal to or longer than two channel segments (1400 m) along the trunk rivers and their tributary channels.

3.3. Landslide detection and mapping

Once we obtained the raw DInSAR and k_{snn} results, we identified the unstable areas from the DInSAR ground displacement maps and the k_{snn} anomalous values (i.e. knickzones) from the k_{snn} map. Therefore, we inspected the spatial distribution of the unstable areas and knickzones in combination with the following existing data on a GIS environment: (1) lithological contrasts and faults from the 1:50000-scale National Geological Map of Spain (MAGNA), sheets 1027: Güejar-Sierra (Díaz de Federico et al. 1980) and 1042: Lanjarón (Aldaya et al. 1979); (2) lithological contrasts and faults from Martínez-Martínez et al. 2006; (3) active faults from the Quaternary Active Faults Database of Iberia (QAFI); (4) geomorphological features related to the glacial or periglacial landforms from the Glacial and Periglacial Geomorphological Map of Sierra Nevada (Gómez-Ortíz et al. 2002); and (5) the landslide inventory of the Spanish Land Movements Database (BD-MOVES). Crossing all of this information, we associated unstable areas and knickzones with landslides.

Our main aim was to delimit the landslides' boundaries as accurately as possible. For it, the exhaustive examination of products derived from high-resolution DEMs was essential. We used 2-m and 5-m DEMs, freely available at the Spanish National Geographic Institute (https://centrodedescargas.cnig.es/CentroDescargas/index.jsp) to derive the hillshade, slope, aspect, rugosity, and topographic openness maps. These products were also exported to Google Earth for a 3-D, more accurate visualisation of landslide-related features. The hillshade model combined with the slope, aspect and topographic openness maps allowed recognising the slope breaks related to the head and lateral scarps. The hillshade model was also useful to identify secondary scarps, benches and rock deposits within the landslides, as well to delimit the slide masses, that were expressed as an increase of rugosity and convexity of the ground surface. Moreover, we carried out field surveys for a further visual inspection of morphologies and rock deposits of the landslides, as well as for checking the observations made by the GIS analysis. All of this work conducted us to provide an updated landslide inventory of the SW sector of Sierra Nevada. We also made a classification of the mapped landslides into different typologies.

4. Results

4.1. DInSAR velocity maps

The mean displacement rate or velocity maps in ascending and descending orbits are shown in Figures 3a and 3b, respectively. A total number of 33 unstable areas were detected: 16 areas by the ascending orbit (polygons from 1 to 16 in Figure 3a) and 17 areas by the descending orbit (polygons from 17 to 33 in Figure 3b). Some of these areas are coincident in both geometries (1 and 19, 3 and 23, 4 and 24, 11 and 29, 15 and 31), what means that we detected 28 different unstable areas within the study area. The ascending orbit processing provides a better point coverage within the western slopes of the valleys, and the maximum LoS velocity recorded was -32 mm/yr along the Trevélez River's valley (area 13 in Figure 3a). On the contrary, the descending orbit provides the better point coverage within the eastern slopes, with a maximum LoS velocity recorded of -31 mm/yr along the Poqueira River's valley (area 26 in Figure 3b).

4.2. k_{sn} and k_{snn} maps

Figure 4a shows the k_{sn} map, where it is hard to identify anomalies (or knickzones) as values are consistently high. This fact is due to the strong river incision related to the active uplift of Sierra Nevada (Azañón et al. 2015). Such tectonic signal produces a steeper chi-elevation profile that can be described by its general slope (mean k_{sn}) (Figure 4b). By normalising the k_{sn} values (Figure 4c), this tectonic signal was reduced and we obtained the k_{snn} index (Figure 4d), that clearly evidence knickzones in the k_{snn} map (Figure 4e).

We detected 10 knickzones within the study area, named from number 1 to 10, that are distributed as follows (Figure 4e): knickzones 1 and 2 along the Lanjarón River, knickzone 3 along the Sucio River, knickzones 4 and 5 along the Chico River, knickzone 6 along the Seco River, knickzones 7 and 8 along the Poqueira River and knickzones 9 and 10 along the Trevélez River. We also detected other 15 k_{snn} anomalies, named with letters from 'a' to 'o' distributed along the tributary channels of the trunk rivers (Figure 4e). There is just one anomaly along the tributary channels of the Seco and Chico rivers (anomaly 'a' and 'b' respectively). Other seven anomalies (from 'c' to 'i') along the Poqueira River and six anomalies (from 'j' to 'o') along the Trevélez River were also identified (Figure 4e).

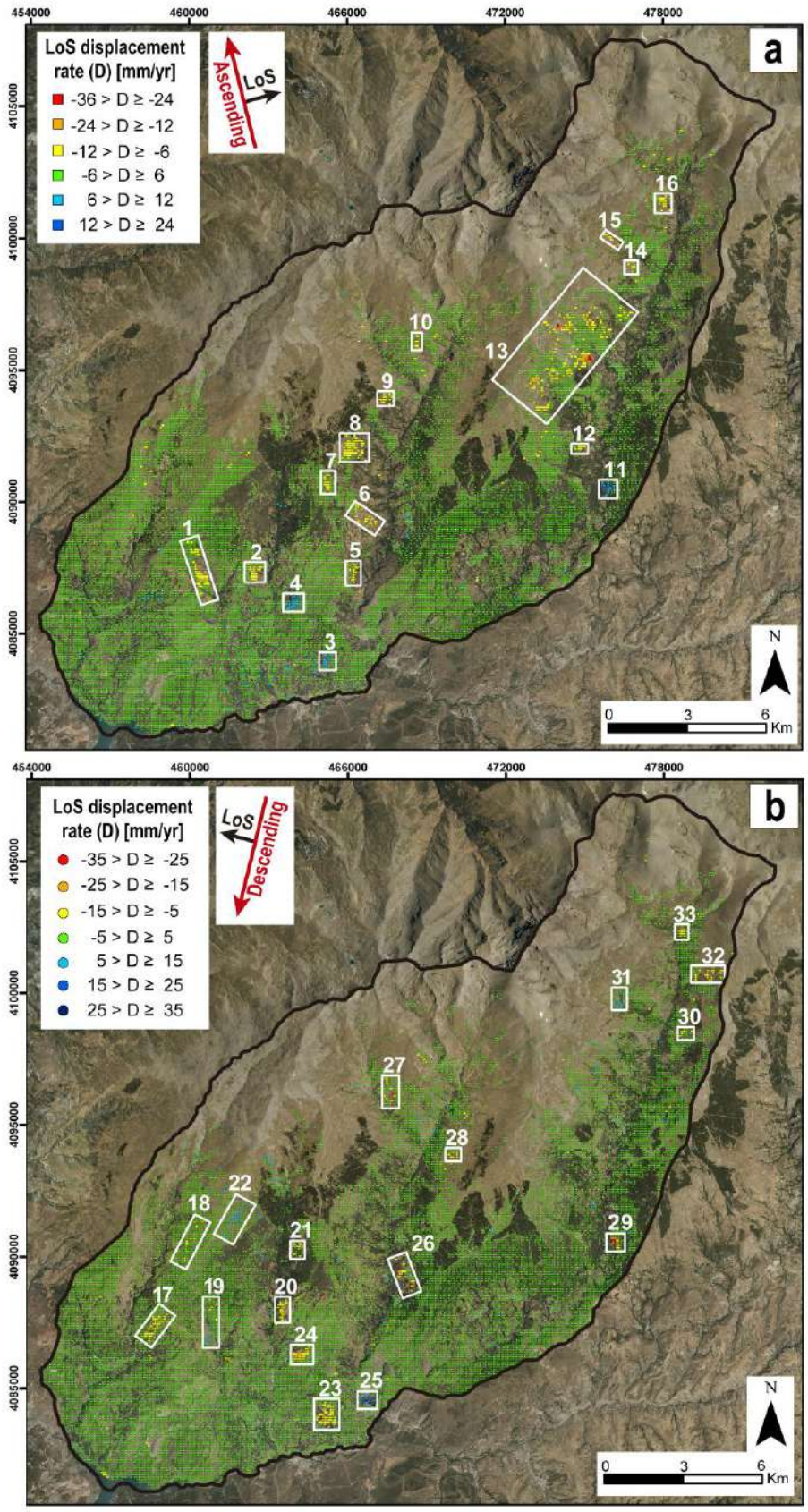

Figure 3. DInSAR displacement rate or velocity maps in **(a)** ascending and **(b)** descending orbit geometry. The detected unstable areas are highlighted within white polygons from numbers 1 to 33.

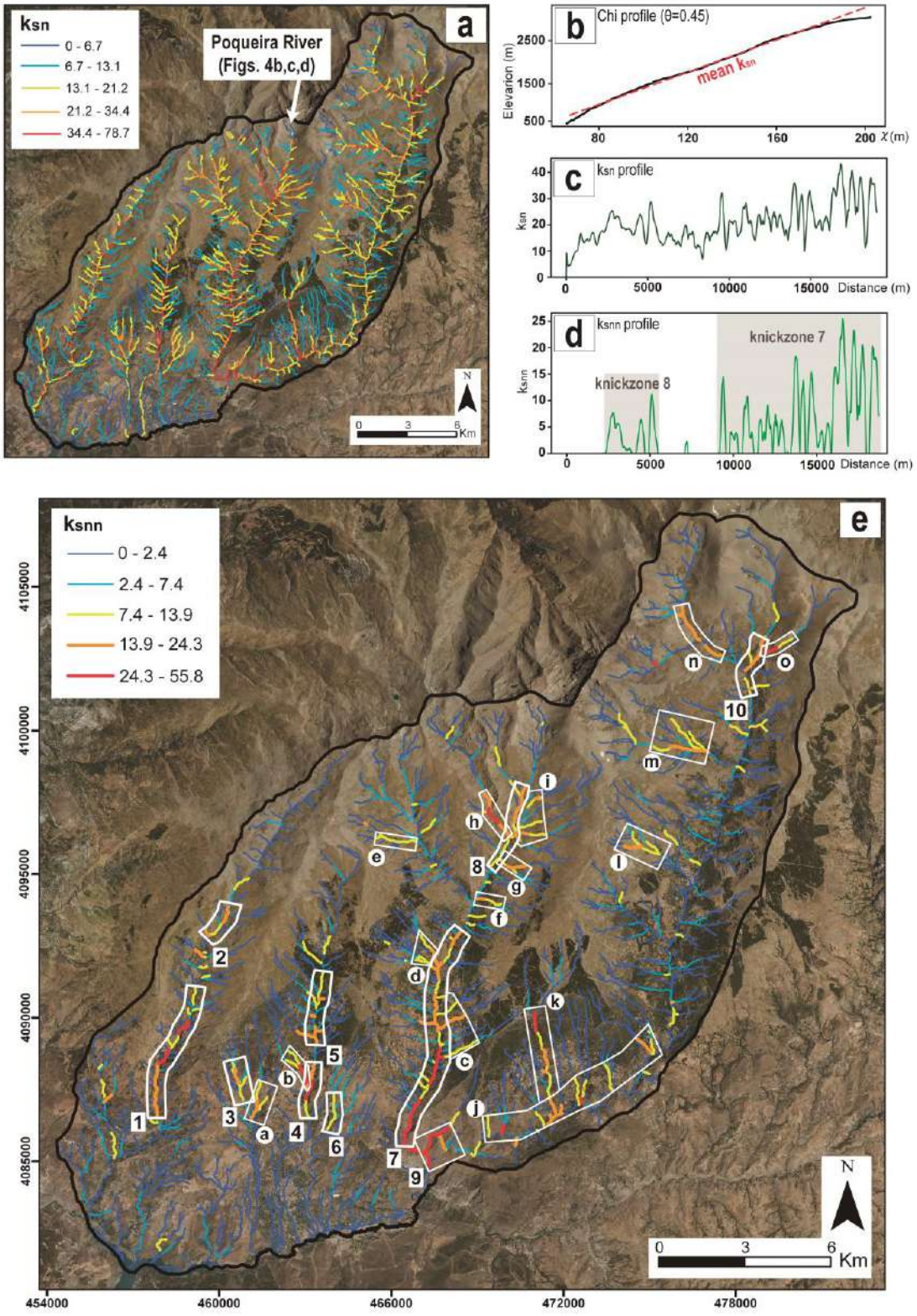

Figure 4. **(a)** k_{sn} map of the study area. **(b)** Chi-elevation plot of the Poqueira River. The mean k_{sn} is indicated with a red dashed line. **(c)** k_{sn} profile of the Poqueira River. **(d)** k_{snn} profile of the Poqueira River. The detected knickzones are also shown along the profile. **(e)** k_{snn} map of the study area. Anomalies located along the trunk rivers are indicated with numbers from 1 to 10 and anomalies along tributary channels are indicated with letters from 'a' to 'o'.

4.3. Landslide inventory map

The landslide inventory of the study area is shown in Figure 5. The k_{snn} values of the trunk rivers and tributaries (Figure 4e), as well as the unstable points from both DInSAR geometries (Figure 3) are also plotted to facilitate the correlation between these data and the mapped landslides. Through both DInSAR and k_{snn} anomalies data together with geomorphological observations, we could delimit a total of 28 landslides. Such a mapping implies that 126.8 km^2 of the study area is affected by landslides, which means 33.5% of its total extension. Table 1 details the associations of the DInSAR unstable areas and k_{snn} anomalies for each of these landslides. Their names and abbreviations were established according to the trunk river where they are located (Figure 5, Table 1): 'L' for Lanjarón, 'Su' for Sucio, 'C' for Chico, 'Se' for Seco, 'P' for Poqueira and 'T' for Trevélez (Figure 5). They are also numbered from lowest to highest towards the headwater for each river.

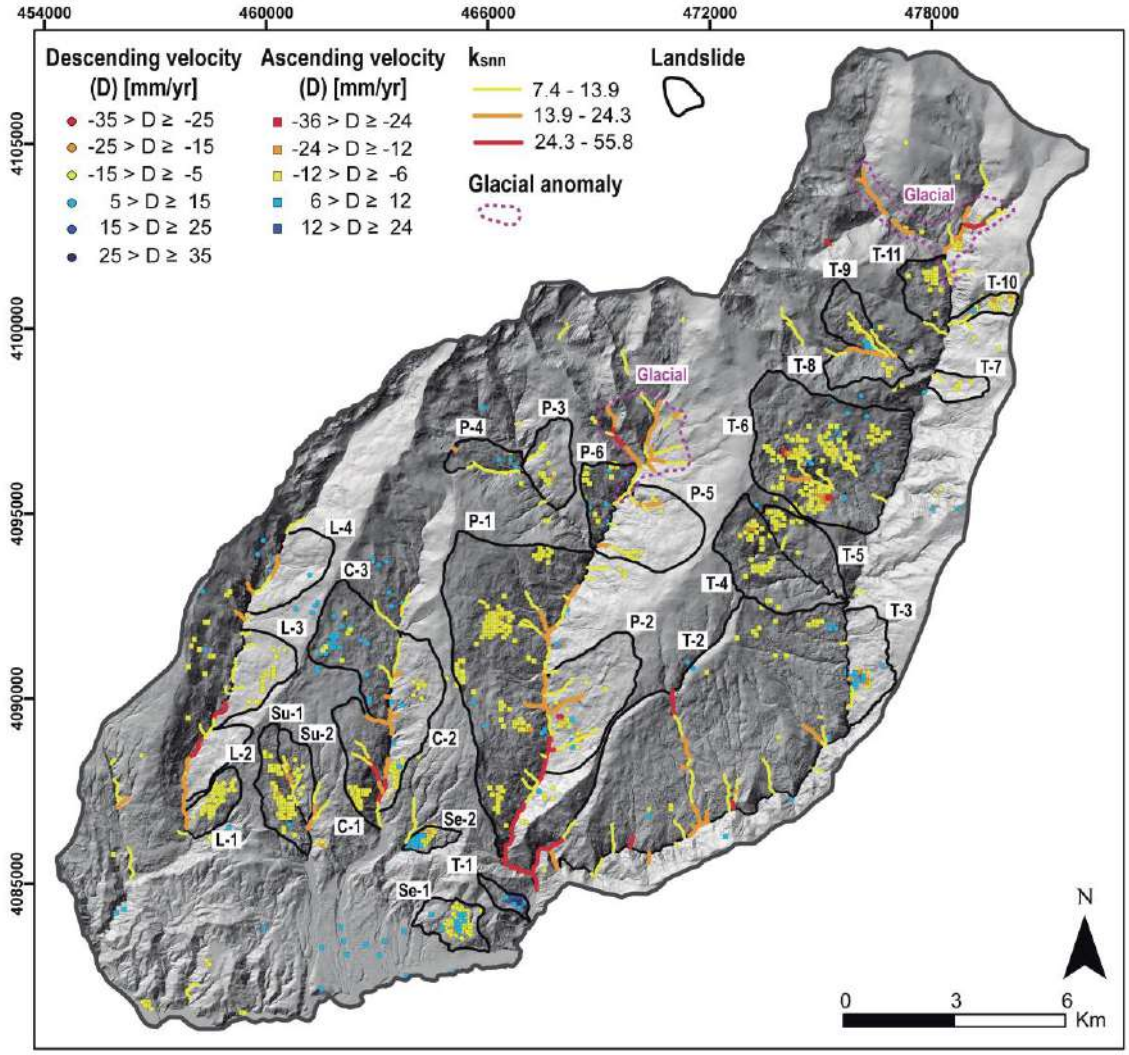

Figure 5. Landslide inventory of the SW sector of Sierra Nevada. The k_{snn} anomalous values of the trunk rivers and tributaries channels, as well as the unstable points from both DInSAR geometries (ascending and descending) are also shown to facilitate the correlation between these data and the mapped landslides. The k_{snn} anomalous values related to glacial and periglacial morphologies are indicated within dashed purple polygons.

Landslide name	Landslide abbreviation	DInSAR unstable area	k_{snn} anomaly		Landslide typology
			Trunk river	Tributary channel	
Lanjarón-1	L-1	17	1	-	DGSD
Lanjarón-2	L-2	-	1	-	DGSD
Lanjarón-3	L-3	18	1	-	DGSD
Lanjarón-4	L-4	-	2	-	DGSD
Sucio-1	Su-1	1	3	-	DGSD
Sucio-2	Su-2	19	3	a	DGSD
Chico-1	C-1	2	4	b	DGSD
Chico-2	C-2	20, 21	4, 5	-	DGSD
Chico-3	C-3	22	5	-	DGSD
Seco-1	Se-1	3, 23	-	-	Earthflow
Seco-2	Se-2	4, 24	-	-	Rock spreading
Poqueira-1	P-1	5, 6, 7, 8, 9	7	d	DGSD
Poqueira-2	P-2	26	7	c	DGSD
Poqueira-3	P-3	27	-	-	DGSD
Poqueira-4	P-4	-	-	e	Rockslide
Poqueira-5	P-5	28	-	f, g	DGSD
Poqueira-6	P-6	10	-	-	DGSD
Trevélez-1	T-1	25	-	-	Earthflow
Trevélez-2	T-2	12	9	j	DGSD
Trevélez-3	T-3	11, 29	-	-	DGSD
Trevélez-4	T-4	13	-	-	Rockslide
Trevélez-5	T-5	13	-		Rockslide
Trevélez-6	T-6	13	-	l	DGSD
Trevélez-7	T-7	30	-	-	Rockslide
Trevélez-8	T-8	14	-	m	Rockslide
Trevélez-9	T-9	15, 31	-	m	Rockslide
Trevélez-10	T-10	32	-	-	Rockslide
Trevélez-11	T-11	16	-	-	Rockslide

Table 1. Associations of the DInSAR unstable areas and k_{snn} anomalies (or knickzones) along the trunk rivers and the tributary channels for each of the mapped landslides of the study area. Landslide typologies are also included.

From DInSAR results, unstable areas from 1 to 32 (Figure 3) are associated with 25 different landslides (Figure 5, Table 1). Some of them are almost entirely active (e.g. the Lanjarón-1 or Sucio-1 landslides), while most show only active sectors within a larger landslide body (e.g. the Chico-1, the Poqueira-1 or the Trevélez-2 landslides). Regarding the k_{snn} anomalies, we could confidently assume a dominant role of landslides and glacial morphologies on the knickzones generation after dismissing the influence of other phenomena. Anomalies linked to lithological contrasts are not expected as the valleys' slopes are formed mainly by schists from the Nevado-Filábride Complex (Figure 2). Similarly, anomalies along the trunk rivers cannot be related to significant tectonic structures, such as clearly active faults. This is the case of the Lanjarón Fault (Figure 2), that is not spatially correlated with knickzones 1 and 3 (Figure 4e), what suggests that it

is an inactive fault. Therefore, six of the trunk rivers' anomalies could be spatially associated with landslides (numbers 1 to 5 and 7), and from the tributary channels' anomalies, ten were related to landslides (Figure 4e, Table 1). Out of the remaining anomalies, numbers 8 and 10 and letters h, i, n and o, are linked to glacial and periglacial morphologies (Figures 4e, 5), according to the mapping of Gómez-Ortíz et al. (2002). The origin of knickzone 6 is unknown, while knickzone 9 can be linked to either processes: the Trevélez-2 Landslide or active tectonics, according to the hypothesis from Azañón et al. (2015). Similarly, anomaly k results from a fluvial capture that cannot be certainly due to the Trevélez-2 Landslide (Figures 4e, 5).

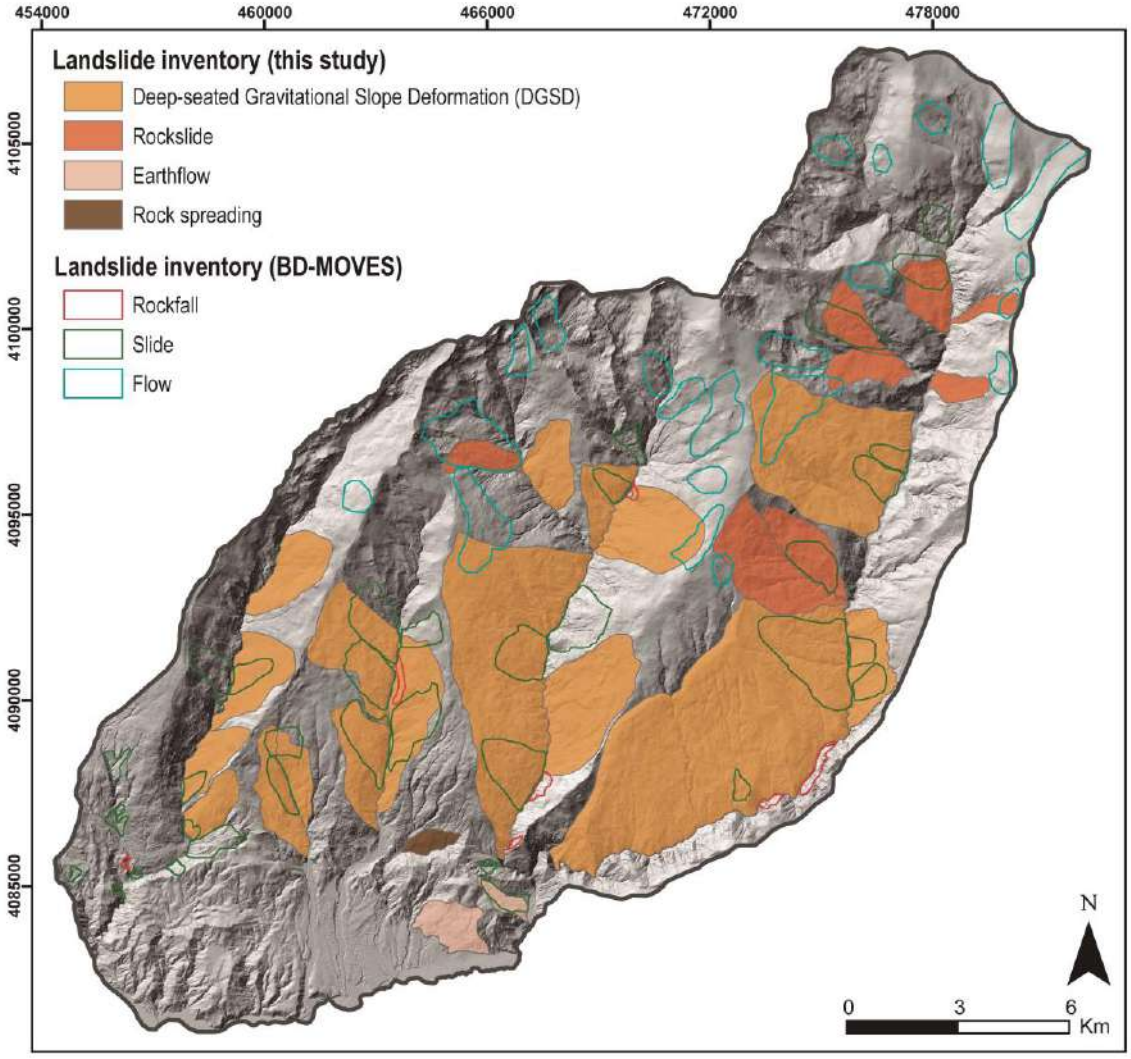

Figure 6. Landslide inventory of the SW sector of Sierra Nevada showing the four landslide typologies. The previous inventory of the Spanish Land Movements Database (BD-MOVES) is also illustrated with its three landslide typologies.

We also made a preliminary classification of the mapped landslides in four different typologies: (a) Deep-seated Gravitational Slope Deformation (DGSD), (b) rockslide, (c) earthflow, and (d) rock spreading. Figure 6 reclassifies the landslide inventory shown in Figure 5, taking into account these typologies, and Table 2 summarises the main characteristics of DGSDs and rockslides (i.e. the two most common typologies).

Landslide type	DGSD	Rockslide
Size (area in km²)	1.4 – 31.6	0.7 – 4.9
Number of mapped landslides	17	8
Covered area in km² (% of the total area)	107.5 (28.4%)	16.1 km² (4.3%)
Position along valley	Lower and medium	High
Lithology	Schists (Nevado-Filábride Complex)	Schists (Nevado-Filábride Complex)
Main geomorphological features	• Poorly-defined and irregular head scarps • Diffuse lateral boundaries • Affects entire slopes of valleys • Presence of nested secondary movements	• Well-defined curved head scarps covered by debris • Diffuse lateral boundaries • Partially affects slopes of valleys • Presence of debris from gelifraction and nival processes
Mean velocity (mm/yr)	9.8	10.5
Maximum velocity (mm/yr)	32	23
Affects trunk river	Yes (long anomalies)	No
Affects tributary channel	Yes (linked to nested movements)	Rarely (short anomalies)
Schematic illustration of the landslide		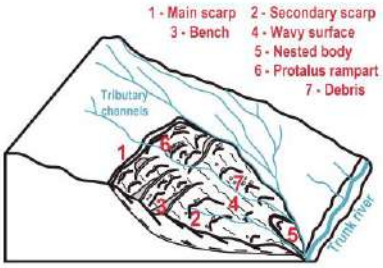

Table 2. Summary of the main characteristics of the two most common landslide typologies in the study area: DGSDs and rockslides.

Most of the mapped landslides are of DGSD type (17 landslides), developed within the Nevado-Filábride schists (Figure 2) and located along the lower and medium part of the valleys. They are large landslides of variable size, with areas from 1.4 to 31.6 km^2, that occupying 28.4% of the study area (Figure 6, Table 2). These DGSDs affect entire slopes of the trunk rivers' valleys and most of their head or main scarps reach the valley ridges. However, the DGSDs do not show well-defined head scarps and/or lateral boundaries, which made their delimitation an intricate task (Figure 7). Most of these DGSDs are compounded by smaller-size rotational slides or rockslides that generate multiple minor scarps and benches, that facilitated the delimitation of the slide masses, which were also well-evidenced by an increase of the slope rugosity in the hillshade model (Figure 7).

Active movements, with LoS velocities up to -32 mm/yr, are registered within punctual sectors of the larger landslides' bodies (Figures 3, 5). The longest knickzones (numbers 1 to 5 and 7 in Figure 4e) along the trunk rivers are associated with these DGSDs as their downslope force generates stream stretches and deviations, that disrupt the rivers equilibrium profile. In some cases, other anomalies along tributary channels are linked to slope breaks of nested movements located at the lower part of the larger DGSDs (e.g. anomalies b, c, and d in Figure 4e).

We also mapped eight other landslides that we classified as rockslides, according to the descriptions of Crosta et al. (2014) and Borrelli and Gullà (2017). They are mainly distributed in the upper part of the Trevélez valley, involving the Nevado-Filábride schists (Figure 2). The rockslides occupy 4.3% of the study area, and they have a smaller size than the DGSDs (areas up to 4.9 km^2). These slope movements are recognisable by well-defined curved main scarps that are covered by debris (Figure 8). They are characterised by multiple secondary movements, as well as by a very high ruggedness in the hillshade model (Figure 8a) and waviness of the ground surface (Figures 8b, c). These slope movements imply a deep sliding of the bedrock together with a shallow sliding of debris generated from thermal alterations (gelifraction). We also found some nival deposits like protalus ramparts that are accumulated in benches of the larger landslide body (Figure 8b). This fact proves the influence of gelifluction and gelifraction processes into the rockslides' kinematics, as well as the debris mobilisation by snow melting processes in a periglacial environment. These rockslides show LoS velocities up to -23 mm/yr (Figures 5, 6). Some of them can be related to k_{snn} knickzones of short length along the tributary channels (e.g. anomalies l and m in Figure 4e), while none of them generate anomalies along the trunk rivers.

Lastly, two earthflows (the Seco-1 and the Trevélez-1 landslides) and one rock spreading (the Seco-2 Landslide) (Figures 5, 6) were also identified within the Alpujárride Complex and Neogene sedimentary rocks (Figure 2). These three landslides entail the minority of the study area (0.9%). All of them are active landslides (maximum LoS velocities of -19 mm/yr) (Figure 3), and there are no k_{snn} anomalies related to them (Figure 4e).

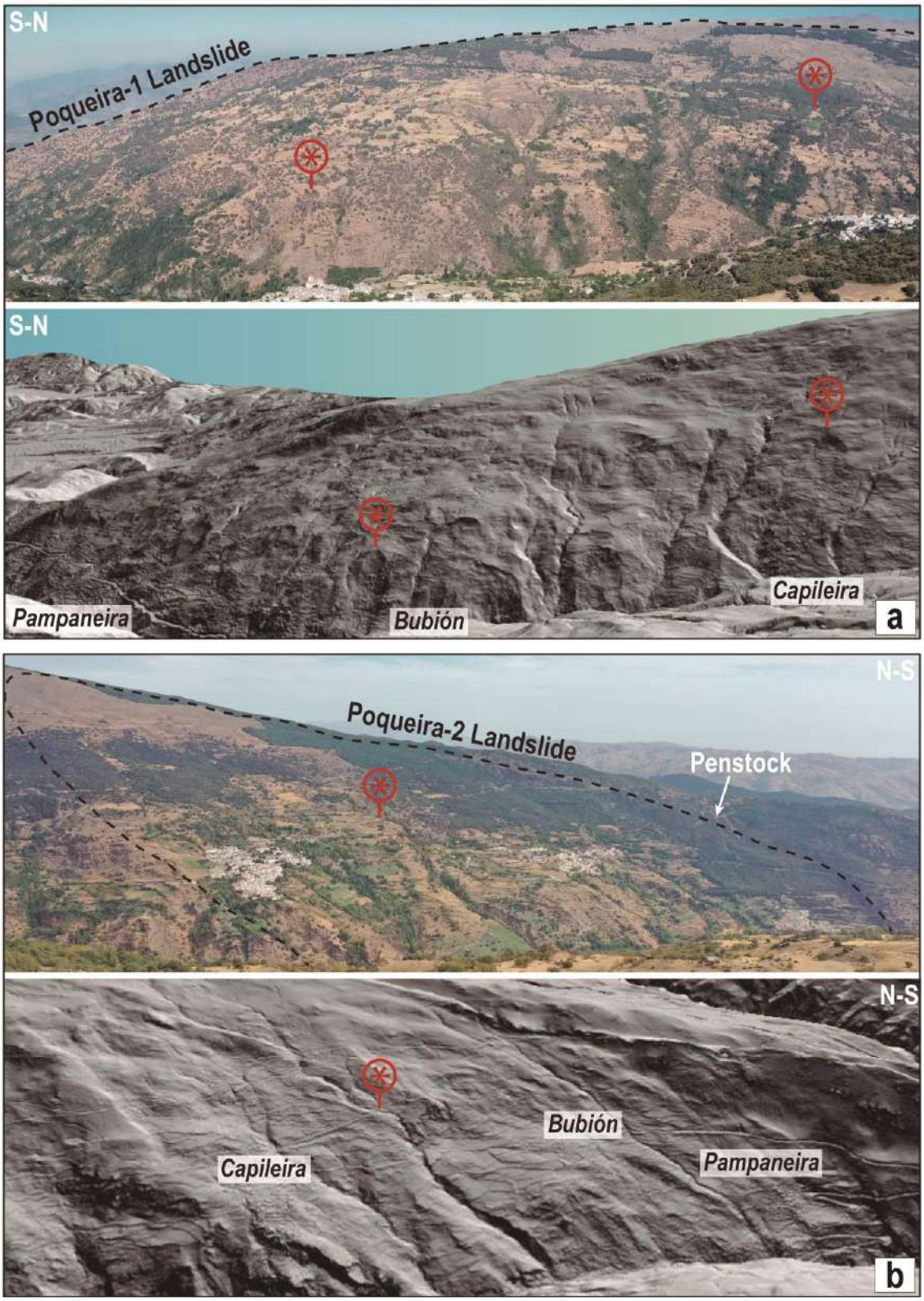

Figure 7. Panoramic photograph of **(a)** the Poqueira-1 and **(b)** Poqueira-2 landslides (DGSDs) and their approximate similar 3-D view on Google Earth of the 2-m resolution hillshade map. The villages of Pampaneira, Bubión and Capileira are also indicated. Red asterisks aim to facilitate the comparison between both images for each landslide.

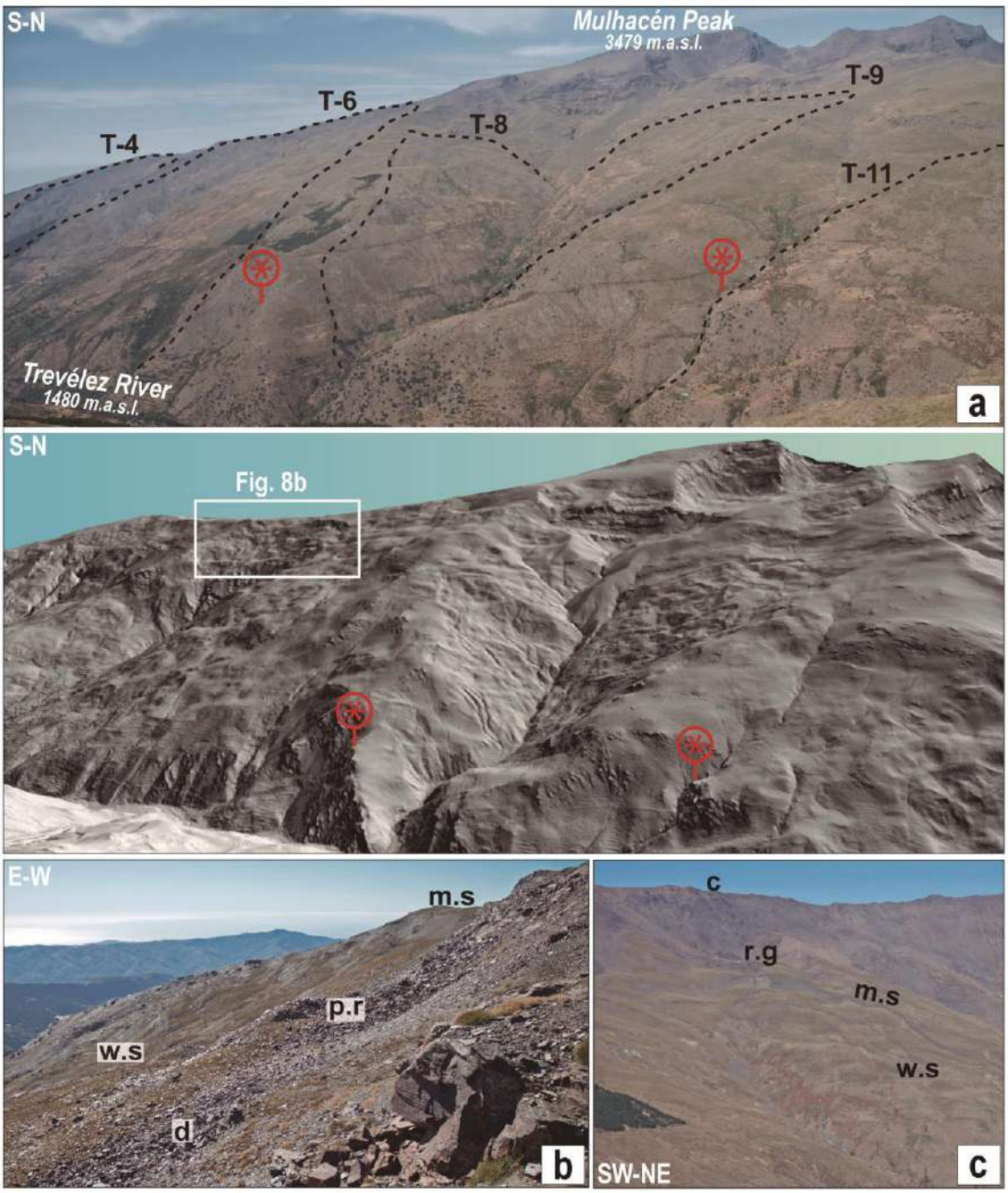

Figure 8. **(a)** Panoramic photograph of the western slope of the Trevélez River valley and its approximate similar 3-D view on Google Earth of the 2-m resolution hillshade map. The following landslides are also drawn: Trevélez-4 (T-4), Trevélez-6 (T-6), Trevélez-8 (T-8), Trevélez-9 (T-9) and Trevélez-11 (T-11). Red asterisks aim to facilitate the comparison between both images of the slope valley. **(b)** Lateral view of a rockslide within the Trevélez-6 Landslide and its related features: main scarp (m.s) covered by debris, wavy surface (w.s), protalus rampart (p.r) and debris from gelifraction processes (d) covering a large part of the slope. **(c)** Panoramic view of the Poqueira-4 Landslide (rockslide) and its main features: curved main scarp (m.s) covered by debris and a wavy ground surface (w.s). A glacial cirque (c) and a rock glacier (r.g) located above the landslide are also indicated.

5. Discussion

5.1. Strength of the combination of DInSAR and k_{snn} analysis for landslide detection

The DInSAR services of the Geohazards Exploitation Platform (GEP) have already been demonstrated to be effective tools for landslide detection (e.g. Galve et al. 2017; Reyes-Carmona et al. 2021; Gaidi et al. 2021; Cigna and Tapete, 2021), as well as the k_s and k_{sn} index analysis (e.g. Panek et al. 2007; Walsh et al. 2012; De Palézieux et al. 2018; Ahmed et al. 2019; Gu et al. 2021). Nevertheless, the advantages of combining both data sets have not been explored until the present study. From a quantitative point of view, 25 of the total 28 mapped landslides (89.3%) have been identified as active landslides through the DInSAR data, while 17 landslides (60.7%) have been attributed to k_{snn} anomalies along the trunk rivers and/or tributary channels. All the landslides were revealed at least by one of the methods, while 14 landslides (50%) were evidenced by both. These results are satisfactory enough as we provided a better landslide inventory than the previous one of the Spanish Database of Landslides (BD-MOVES). Our new inventory doubles the area affected by landslides (33.5%) in relation to the BD-MOVES (14.5%) (Figure 6). It is also remarkable that most of the landslides inventoried in this work have larger dimensions than those previously identified (e.g. landslides along the Lanjarón valley, the Poqueira-1 or the Trevélez-2 landslides in Figures 5, 6). Other large landslides were identified for the first time in this study, such as the Lanjarón-4 or the Poqueira-2 landslides (Figures 5, 6). We also dismissed several landslides at higher elevations due to the absence of ground motion, k_{snn} anomalies, and, most importantly, any recognisable landslide-related features. Instead, glacial and periglacial morphologies mask any other processes in these areas (Gómez-Ortiz et al. 2002; Palma et al. 2017).

The great potential of DInSAR is revealing the active landslides, which rapidly highlights the slopes that should be further investigated. However, in our study case, ground movements were generally detected only within some sectors and not in the whole landslides' bodies (Figure 3). This fact implies that the large size of the landslides may be underestimated if the attention is focused on mapping just the active zones, which usually correspond to smaller nested movements. In this sense, the identification of k_{snn} knickzones along trunk rivers was useful to reveal the complete extension of several large landslides, where unstable areas are restricted to isolated sectors (e.g. the Chico-3 or Poqueira-1 landslides in Figure 5) or even where there is not registered DInSAR points (e.g. the Lanjarón-2 or Lanjarón-4 landslides in Figure 5). The combination of these two datasets also provided two different temporal perspectives about the landslides: DInSAR shows a very short-term or recent activity, while k_{snn} anomalies point out a long-term activity that shows that a landslide has being perturbing fluvial channels at century or millennial timescale.

The scarcity of measurement points in some areas is due to some limitations that should be mentioned when applying DInSAR in mountainous areas. Some natural terrain properties usually scatter the radar signal of the satellite images, which introduces noise to the DInSAR processing and reduces the points coverage (Hanssen 2001). Some of these properties are steep slopes (e.g. the lower part of the valleys), dense vegetation (e.g.

the Chico River valley's landslides), terrace fields (e.g. the Poqueira-1 or Trevélez-2 landslides) and snow cover (e.g. highest elevations of the Sierra Nevada) (Figure 3). Other intrinsic limitation of DInSAR is the decrease of the radar sensitivity when true landslide displacement deviates from the satellite LoS (Schlögel et al. 2015), what makes slow movements to be not registered or underestimated. Typically, DGSDs have velocities of millimetre/year order, close to the usual stability range of DInSAR processing (around 5 mm/yr). This fact implies that unstable points may have not been registered in the cases of the Lanjarón-2, Lanjarón-4, or the Trevélez-2 landslides (Figure 6). Therefore, it is important to remark that these landslides could be either stable or unstable but not detected by our DInSAR processing. Combining ascending and descending data is usually helpful to deal with such limitations, as radar sensitivity varies in each geometry depending on the slope orientations. Some examples are the Poqueira-1 or the Trevélez-6 landslides, which unstable areas (5 to 9 and 13 in Figure 3a) were detected just by the ascending processing. On the contrary, the descending processing detected the Lanjarón-1 or the Poqueira-2 landslides' unstable areas (18 and 26 in Figure 3b, respectively). In this sense, the Geohazards Exploitation Platform (GEP) afforded us to obtain processing in both orbits in a very cost-effective way.

The great potential of the k_{snn} analysis is revealing the true extension of large landslides. In the study area, the longest knickzones along the Lanjarón, Sucio, Chico, and Poqueira rivers (numbers 1 to 5 and 7 in Figure 4b) correspond to large DGSDs (Figure 6). This type of landslides shows a relevant control on the evolution of drainage network along the valleys' bottom, where knickzones are commonly formed. The downslope force of DGSDs generate deviation and narrowing of the river channels, what may shift the focus of fluvial erosion (Korup 2006). It is also possible for a channel bed to be uplifted by the thrust of the landslide mass, if the failure plane extends below the channel (Bartarya and Sah 1995). These actions originate anomalous changes in the gradient of the river profiles when landslides are active and their gravitational force is able to counteract fluvial erosion. For this reason, rivers cannot reestablish their equilibrium or steady-state profile and knickzones are generated, what is reflected by anomalously high values of gradient-related geomorphic indexes. As the case of Sierra Nevada, other studies worldwide show the spatial coincidence of landslides, including DGSDs and other large rock-slope instabilities, with anomalous values of gradient-related indexes (Korup 2006; El Hamdouni et al. 2010; Walsh et al. 2012; Troiani et al. 2014, 2017; Penna 2015; Subiela et al. 2019).

The limitation of the k_{snn} analysis is that an anomaly does not necessarily have to be formed. According to Troiani et al. (2014), the formation of knickzones by landslides is dependent on several factors, such as the landslide size, the amount of sediment delivered by the landslide (landslide activity), or the river capacity to incise the landslide deposit (erosion power). For example, the large knickzones of the Lanjarón, Sucio, Chico and Poqueira rivers were generated as these four rivers' erosive power may be lower than the landslide activity. These cases are contrary to the case of the Trevélez River, where there are no long knickzones associated with large DGSDs, such as the Trevélez-2 or the Trevélez-6 landslides (Figure 5, 6). Nevertheless, shorter knickzones along tributary

channels and DInSAR data were essential to recognise some landslides such as the Trevélez-6 or the Trevélez-9 (Figure 5). As many natural processes can contribute to a knickzone generation, another challenge of the k_{snn} analysis is decoding which is the dominant process (Walsh et al. 2012). Frequently, a predominant process may mask other processes of our interest, such as landslides. Some examples are knickzones 8 and 10 (Figure 4e), where glacial and periglacial morphologies generate strong anomalies that cannot be certainly attributed to nearby landslides (e.g. the Poqueira-6 or the Trevélez-11 landslides). Another example is knickzone 9 (Figure 4e), which origin can be controversial. According to Azañón et al. (2015), it can be related to the water gap after the Guadalfeo River's migration that resulted from the recent uplifting of Sierra Nevada. Nevertheless, we consider that the Trevélez-2 Landslide could also contribute to this knickzone generation (Figure 5). To deal with these ambiguities, new tools need to be developed to unmask anomalous values related to a specific process. In this sense, the k_{snn} index calculation made it possible to eliminate a considerable influence of tectonic uplift and the consequent topographic gradients in the most active sector of Sierra Nevada. Thus, the visualization of knickzones related to landslides was greatly facilitated by the k_{snn} index (Figure 4e), in contrast with the conventional k_{sn} index (Figure 4b).

Despite their limitations, we conclude that both DInSAR techniques (e.g. Notti et al. 2010; Bianchini et al. 2013; Bekaert et al. 2020; Crippa et al. 2021; Kang et al. 2021) and the analysis of geomorphic indexes' anomalies (e.g. El Hamdouni et al. 2010; Walsh et al. 2012; Troiani et al. 2017; Liu et al. 2021) can optimise the landslide detection in mountainous areas. Our results demonstrate that both methods not only can be well-complemented but also limitations of each one can be compensated. In this sense, the visual inspection of k_{snn} anomalies and DInSAR data rapidly spotlight the slopes of interest on which to focus to recognise geomorphological features for landslides' delimitation. It should also be remarked that both the Geohazards Exploitation Platform (GEP) and the Python library 'landspy' are very user-friendly tools for obtaining quick results of DInSAR and geomorphic indexes, respectively. This makes both initiatives promising to improve and update landslide databases not only for the scientific community but also for public administrations.

5.2. Prevalence of DGSDs among the landslides affecting the SW of Sierra Nevada

Although the Province of Granada, including the Sierra Nevada, has been analysed thoroughly by different research teams for 30 years (see Chacón et al. 2007 and compiled references therein), DGSDs and their prevalence have not been pointed out until the present study. The main landslide research and inventories of the Sierra Nevada area were produced in the 1980s, 1990s and the early 2000s (e.g. Chacón et al. 1992; El Hamdouni 2001; Chacón et al. 2007) through photo-interpretation, fieldwork and basic GIS analysis, before the free availability of high-resolution DEMs such as those used in our research. Despite more recent studies (e.g. Azañón et al. 2008; Jiménez-Perálvarez et al. 2011, 2017; Jiménez-Perálvarez 2018) estimated a medium/high degree of landslide susceptibility in the SW sector of Sierra Nevada, the mapped landslides are scarce. Moreover, the attention and popularity of DGSDs in the landslide research community

have progressively increased since the 1990s (Chigira 1992; Dramis and Sorriso-Valvo 1994) and especially, during the last two decades (Agliardi et al. 2001; Korup 2005; Gutiérrez-Santolalla et al. 2005; Ambrosi and Crosta 2006; Agliardi et al. 2009; Crosta et al. 2013; Chigira et al. 2013; Agliardi et al. 2013; Tsou et al. 2015; Della Seta et al. 2017; Mariani and Zervoni 2020; Crippa et al. 2021). This type of landslide was already described before through different terms such as sackung (Zischinsky 1966), mass rock creep (Radbruch-Hall 1978), or rockflow (Varnes 1978). Therefore, it is not surprising that DGSDs in the Sierra Nevada were not mapped in previous inventories, as these slope movements can be difficult to identify if a surveyor is unfamiliar with them and/or due to the lack of high-quality topographic data.

In our study area, the DGSDs recognition and delimitation were supported by: (1) the knowledge acquired in other geological settings such as the Alps (e.g. Agliardi et al. 2001), Apennines (e.g. Di Luzio et al. 2004), Pyrenees (e.g. Gutiérrez-Santolalla et al. 2005) or the Carpathians (e.g. Pánek et al. 2011) that helped us in their identification by comparison with other known examples; (2) the high-resolution DEMs that offered us enough detail of the ground surface, even in forested areas, to identify morphological features of DGSDs; (3) a cutting-edge technology such as DInSAR that allowed to identify wide areas of ground motion along the slopes; and (4) landscape analysis techniques that provided information about how large landslides perturb rivers and where we had to look up the hillside. In this way, we could focus our geomorphological research directly on the slopes where these techniques provided us data for then, recognising scarps, benches, and slope convexities associated with DGSDs. Previously to this research, no one had ever had these resources to identify such large landslides. However, future research will for sure improve the mapping of DGSDs as they are always difficult to delimit accurately.

The challenges for DGSDs detection in the SW of Sierra Nevada should also be mentioned. As the Nevado-Filábride Complex is a homogeneous sequence of schists (Figure 2), there are no clear key layers or lithological contacts, which usually facilitates the recognition of slope ruptures (Crosta et al. 2013). In this context, only the surficial morphological features guided the recognition of these landslides and their boundaries, the latter being very diffuse and poorly defined. The general absence of well-developed DGSDs-related morphologies (e.g. double ridges, open trenches, or counterscarps) (Figure 7) also made mapping most of the DGSDs complex. Moreover, the presence of glacial and periglacial morphologies usually difficult the surficial mapping of landslides (Weidinger et al. 2014) due to the similarity of slope deposits with glacial moraines (Hewitt 1999) and between the scarps with glacial cirques (Turnbull and Davies 2006). Some examples are the Trevélez-4 and Trevélez-6 landslides (Figures 8a, b), which main scarps were mapped as glacial cirques by Gómez-Ortiz et al. (2002) and Palma et al. (2017). Similarly, we interpreted as protalus ramparts (Figure 8b) some deposits that were mapped as moraine segments by Gómez-Ortiz et al. (2002).

It is worth noting that it was expectable to find DGSDs in the Sierra Nevada as they are widespread in other Alpine mountain ranges (Jarman et al. 2014; Del Rio et al. 2021;

Crippa et al. 2021) where tectonic exhumation controls topography (Agliardi et al. 2013) and the constant relief uplift has produced a high fluvial incision of valleys (Korup et al. 2007; Tolomei et al. 2013; Tsou et al. 2015; Demurtas et al. 2021). DGSDs usually affect the entire length of high-relief valley flanks (Crosta et al. 2013), and we consider that the local relief of these valleys is high enough (0.8-1km) to cause the gravitational collapse of their slopes. Furthermore, the rocks that compose the Sierra Nevada are common materials (i.e. foliated metamorphic rocks) where DGSDs are prone to occur (Crosta et al. 2013). For this reason, this article is the first, but it should not be the last to investigate and map DGSDs in other sectors of the Sierra Nevada. Detailed morpho-structural studies about the internal segmentation of specific DGSDs as well as the research of their predisposing or causal factors (e.g. Agliardi et al. 2001; Ambrosi and Crosta 2006; Agliardi et al. 2013; Crosta et al. 2013; Crippa et al. 2021) could also be carried out for a comprehensive understanding of this phenomena and its integration into the relief evolution of the Betic Cordillera.

5.3. Human-slope interactions in the SW of Sierra Nevada: Implications of the new landslide inventory

The fact that the Sierra Nevada is a Natural and National Park implies a special commitment to its management and protection, what includes a better knowledge of natural processes such as landslides and their related hazard and risk (Mateos et al. 2018). Therefore, the newly inventoried landslides may have positive and negative implications on infrastructures and populations that should be taken into account.

Regarding the *acequias de careo*, landslides may positively affect their proper functioning. The fractured rocks of a slide mass may work better as a groundwater reservoir than an intact rock massif. However, the water infiltration from the *acequias* could be excessive and ineffective. Water infiltration could also trigger an acceleration of a landslide, and in turn, these accelerations could damage the *acequias*. As an example, we observed a transect of a waterproofed *acequia* (‘Acequia de Bérchules’) that runs across the Trevélez-10 Landslide (Figures 9a, b), probably to avoid excessive water infiltration or to prevent damage to the infrastructure. Further research has to be carried out to determine the positive and negative influence of landslides on water infiltration along the *acequias*.

The high local relief could have represented an important limitation for the human settlement in the SW sector of Sierra Nevada. However, the convex profiles of the slopes and the abundance of benches probably facilitated the creation of villages such as Pampaneira, Bubión, and Capileira (Figures 1, 7b), as well as terraced agriculture and livestock farming activities. These slope morphologies are related to DGDSs, and our inventory brings to light their importance in the historical human occupation of the area. Despite this, the well-known negative issues of landslides should also be considered in our study area. As an example, Pampaneira, Bubión, and Capileira (the three most touristic and famous villages of La Alpujarra region, Figure 1) are settled within a large DGSD: the Poqueira-2 Landslide (Figure 7b). Bubión is located just on top of a secondary or nested movement within this larger DGSD (Figure 9c). DInSAR data evidenced ground

displacement there, with LoS velocities up to -31 mm/yr (unstable area 26 in Figure 3b). Several damages, such as collapses of dry walls or piping phenomena were observed in some terraced fields (Figure 9d), what also prove the ground activity in this area. The ground movement has been generating damage during several decades in the penstock of the hydroelectric plant of Pampaneira (Alonso et al. 2021), that runs through the Poqueira-2 Landslide (Figure 7b). Other eight villages, such as Pitres, Pórtugos, and Busquístar (Figure 1), are settled within the largest DGSD of the study area: the Trevélez-2 Landslide (Figures 5, 6).

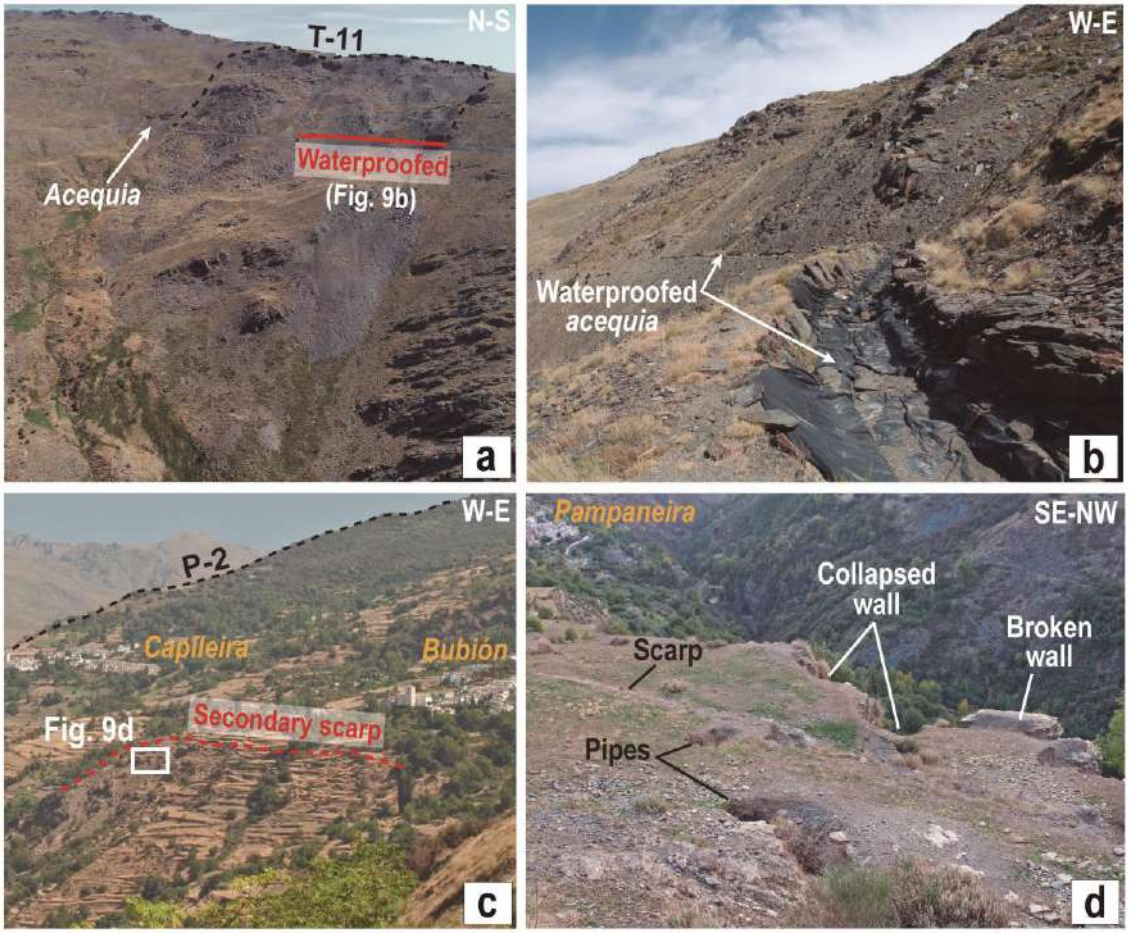

Figure 9. **(a)** Panoramic photograph of the Trevélez-11 (T-11) Landslide. Its main scarp is drawn by a black dashed line. An 'acequia de careo', that runs across the landslide, and its waterproofed transect are also indicated. **(b)** Detail of the waterproofed transect (black plastic) of the 'acequia de careo'. **(c)** Lateral view of a secondary (or nested) movement and its scarp within the Poqueira-2 (P-2) Landslide. The villages of Capileira and Bubión are also indicated. **(d)** Damages of terraced fields within the nested body of the Poqueira-2 Landslide. Piping phenomena, minor scarps and damaged dry walls are evidences of the active ground movement. The village of Pampaneira is also indicated.

Although DGSDs are slow slope movements, they are long-lived phenomena that can evolve into faster secondary movements, such as rotational slides or debris/rock avalanches, that are potentially destructive and may generate major risks to infrastructures and human lives (Soldati 2013). According to these authors, if monitoring and mitigation measures are focused on a single secondary movement within a larger DSGD, they may

result incomplete and noneffective. However, the presence of DGSDs helps to identify large slopes that may be susceptible to catastrophic landslides in the future (Tsou et al. 2015). That is why their recognition, research, and monitoring should be a priority in the Sierra Nevada.

Overall, detailed geological studies of these large landslides should be performed to understand better their internal structure and kinematics (Agliardi et al. 2013) and to model possible evolution scenarios for a correct hazard assessment (Soldati 2013; Spreafico et al. 2021). Similarly, in situ monitoring such as inclinometers or extensometers (Corominas et al. 2000), Global Positioning Systems (GPS) (Brunner et al. 2003) or the exploration drilling and geophysical techniques (Rogers and Chung 2017) should also be carried out for a precise sub-surface characterisation of the landslides. In this work, we produced an updated and more accurate landslide inventory that is the starting point to assess the landslide hazard over an area (van Westen et al. 2008). Our new research has important implications for such assessment in the SW of Sierra Nevada because a larger area than that initially mapped is potentially unstable. This fact also evidences that it is necessary to review and update the existing inventories by combining classical methods with innovative techniques to elaborate a landslide inventory as completely as possible.

6. Conclusions

Our work emerges the potential of integrating data from DInSAR techniques and Landscape Analysis to detect large landslides in a mountain range. Both are well-implemented tools that, when combined, considerably facilitated the mapping and understanding landslides in the SW part of Sierra Nevada. We provided an updated inventory of 28 landslides affecting 33.5% of the total area, compared with the area previously mapped in the Spanish Landslide Database (14.5%). Regarding the Landscape Analysis, we first proposed the k_{snn} index derived from the conventional k_{sn} index for reducing the effect of active tectonics in the Sierra Nevada. The visual inspection of DInSAR ground motion data (28 active areas) and k_{snn} anomalies along rivers (17 knickzones) rapidly spotlighted the slopes to focus for landslide research. We proved that the limitations of both techniques could be compensated (e.g. DInSAR data showed activity in punctual sectors of larger landslides' bodies, for what k_{snn} anomalies were useful to reveal such large sizes). High-resolution DEM-derived products were also essential for accurately delimitating the landslides' boundaries.

We distinguished two main typologies of landslides that have not been described in the area until the present work: rockslides and DGSDs, the latter being the prevailing ones. Overall, the recognition and delimitation of these landslides were challenging due to their large size and diffuse boundaries, what makes them usually difficult to envisage. The presence of glacial morphologies and the homogeneous lithology (schists) also hindered the recognition of landslides' features. Finally, we suggested the relevant role that DGSDs may have had in the landscape evolution of the Sierra Nevada, and we offered a preliminary vision of their potential hazard, as DGSDs are likely to evolve into faster secondary movements. Our new inventory has relevant implications as landslides are

larger and more abundant than previously considered, but further geological research and monitoring are still necessary for a proper landslide hazard assessment.

Acknowledges and funding

This work was mainly funded by the projects B-RNM-305-UGR18, A-RNM-508-UGR20, and P18-RT-3632 ('RADANDALUS') from the European Regional Development Fund (ERDF)/Junta de Andalucía-Consejería de Transformación Económica, Industria, Conocimiento y Universidades. This work was also supported by the ERDF through the project 'RISKCOAST' (SOE3/P4/E0868) of the Interreg SUDOE Programme and the project 'MORPHOMED' (PID2019-107138RB-I00) from the Spanish Ministry of Science (MCIN)/State Research Agency (SRA). The work of Jorge Pedro Galve was also funded by the 'Ramón y Cajal' Programme (RYC-2017-23335) of the Spanish Ministry of Science. Access to the Geohazard Exploitation Platform (GEP) of the European Space Agency (ESA) was provided by the NoR Projects Sponsorship (Project ID: 63737). The authors wish to thank to three anonymous reviewers that contributed to improve the manuscript.

References

Aerden DGAM, Bell TH, Puga E, Sayab M, Lozano JA, Diaz de Federico A (2013) Multi-stage mountain building vs. relative plate motions in the Betic Cordillera deduced from integrated microstructural and petrological analysis of porphyroblast inclusion trails. Tectonophysics 587: 188-206. https://doi.org/10.1016/j.tecto.2012.11.025

Agliardi F, Crosta G, Zanchi A (2001) Structural constraints on deep-seated slope deformation kinematics. Eng Geol 59: 83-102. https://doi.org/10.1016/S0013-7952(00)00066-1

Agliardi F, Crosta GB, Zanchi, A, Ravazzi C (2009) Onset and timing of deep-seated gravitational slope deformations in the eastern Alps, Italy. Geomorphology 103: 113-129. https://doi.org/10.1016/j.geomorph.2007.09.015

Agliardi F, Crosta GB, Frattini P, Malusà MG (2013) Giant non-catastrophic landslides and the long-term exhumation of the European Alps. Earth Planet Sci Lett 365:263-274. https://doi.org/10.1016/j.epsl.2013.01.030

Ahmed MF, Ali MZ, Rogers JD, Khan MS (2019) A study of knickpoint surveys and their likely association with landslides along the Hunza River longitudinal profile. Environ Earth Sci 78:1-15. https://doi.org/10.1007/s12665-019-8178-3

Aldaya F, Díaz de Federico A, García-Dueñas V, Martínez-García E, Navarro- Vilá F, Puga E (1979) Lanjarón-Geological Map of Spain 1:50000. Geological Survey of Spain, Madrid

Alonso EE, Sondon M, Alvarado M (2021) Landslides and hydraulic structures. Eng Geol 292:106264. https://doi.org/10.1016/j.enggeo.2021.106264

Ambrosi C, Crosta GB (2006) Large sackung along major tectonic features in the Central Italian Alps. Eng Geol 83:183-200. https://doi.org/10.1016/j.enggeo.2005.06.031

Antón L, De Vicente G, Muñoz-Martín A, Stokes M (2014) Using river long profiles and geomorphic indices to evaluate the geomorphological signature of continental scale drainage capture, Duero basin (NW Iberia). Geomorphology 206: 250-261. https://doi.org/10.1016/j.geomorph.2013.09.028

Azañón JM, Pérez-Peña J, Yesares J, Rodríguez-Peces M, Roldán F, Mateos R, Rodríguez-Fernández J, Delgado J, Pérez J, Azor A, Booth-Rea G, Martínez-Martínez JM. (2008) Metodología Para El Análisis de La Susceptibilidad Frente a Deslizamientos En El Parque Nacional de Sierra Nevada Mediante SIG. Proy. De Investig. En Parq. Nac. Convoc. 2008-2011: 7–24

Azañón JM, Pérez-Peña JV, Giaconia F, Booth-Rea G, Martínez-Martínez JM, Rodríguez-Peces MJ (2012) Active tectonics in the central and eastern Betic Cordillera through morphotectonic analysis: the case of Sierra Nevada and Sierra Alhamilla. J Iber Geol 38: 225-238. https://doi.org/10.5209/rev_JIGE.2012.v38.n1.39214

Azañón JM, Galve JP, Pérez-Peña JV, Giaconia F, Carvajal R, Booth-Rea G, Jabaloy A, Vázquez M, Azor A, Roldán FJ (2015) Relief and drainage evolution during the exhumation of the Sierra Nevada (SE Spain): Is denudation keeping pace with uplift? Tectonophysics 663:19-32. https://doi.org/10.1016/j.tecto.2015.06.015

Barra A, Solari L, Béjar-Pizarro M, Monserrat O, Bianchini S, Herrera G, Crosetto M, Sarro R, González-Alonso E, Mateos RM, Ligüerzana S, López C, Moretti S (2017) A methodology to detect and update active deformation areas based on Sentinel-1 SAR images. Remote Sens 9:1002. https://doi.org/10.3390/rs9101002

Barra A, Reyes-Carmona C, Herrera G, Galve JP, Solari L, Mateos RM, Azañón JM, Béjar-Pizarro M, López-Vinielles J, Palamà R, Crosetto M, Sarro R, Cuervas-Mons J. Monserrat O (2022) From satellite interferometry displacements to potential damage maps: A tool for risk reduction and urban planning. Remote Sens Environ 282:113294. https://doi.org/10.1016/j.rse.2022.113294

Bartarya SK, Sah MP (1995) Landslide induced river bed uplift in the Tal valley of Garhwal Himalaya, India. Geomorphology 12: 109-121. https://doi.org/10.1016/0169-555X(94)00085-6

Bekaert DP, Handwerger AL, Agram P, Kirschbaum DB (2020) InSAR-based detection method for mapping and monitoring slow-moving landslides in remote regions with steep and mountainous terrain: An application to Nepal. Remote Sens Environ 249:111983. https://doi.org/10.1016/j.rse.2020.111983

Bellin N, Vanacker V, Kubik PW (2014) Denudation rates and tectonic geomorphology of the Spanish Betic Cordillera. Earth Planet Sci Lett 390:19-30. https://doi.org/10.1016/j.epsl.2013.12.045

Bianchini S, Herrera G, Mateos RM, Notti D, Garcia I, Mora O, Moretti S (2013) Landslide activity maps generation by means of persistent scatterer interferometry. Remote Sens 5:6198-6222. https://doi.org/10.3390/rs5126198

Bisci C, Dramis F, Sorriso-Valvo, M (1996) Rock flow (sackung). In: Dikau R, Brunsden D, Schrott L, Ibsen ML (eds) Landslide Recognition, Identification, Movement and Causes. John Wiley and Sons, pp 150-160

Borrelli L, Gullà G (2017) Tectonic constraints on a deep-seated rock slide in weathered crystalline rocks. Geomorphology 290: 288-316. https://doi.org/10.1016/j.geomorph.2017.04.025

Brunner F, Zobl F, Gassner G (2003) On the capability of GPS for landslide monitoring. Felsbau 21:51–54

Casu F, Elefante E, Imperatore P, Zinno I, Manunta M, De Luca C, Lanari R (2014) SBAS-DInSAR parallel processing for deformation time series computation. IEEE J Sel Top Appl Earth Obs Remote Sen 7:3285–3296. https://doi.org/10.1109/JSTARS.2014.2322671

Chacón J, Soria FJ (1992) Inventario y caracterización de movimientos de ladera en la vertiente septentrional de Sierra Nevada. Proceedings of the II Simposio Nacional sobre Taludes y Laderas Inestables, Andorra la Vella, pp 723-739

Chacón J, El Hamdouni E, Irigaray C, Delgado A, Reyes E, Fernández T, García AF, Juliá R, Sanz de Galdeano C, Keller EA (2001) Valores de encajamiento de la red fluvial deducidos a partir del estudio de travertinos del Valle de Lecrín y curso bajo del Guadalfeo (SO de Sierra Nevada, Granada). In: Sanz de Galdeano C, López-Garrido A, Peláez J (eds) La Cuenca de Granada: Estructura, Tectónica Activa, Sismicidad, Geomorfología y dataciones existentes. University of Granada-National Reseach Council, Granada, pp 29-39

Chacón J, Irigaray T, Fernández T (2007) Los movimientos de ladera de la provincia de Granada. In: Ferrer M (ed) Atlas Riesgos Naturales en la Provincia de Granada, 1st edn. Diputación de Granada-Geological Survey of Spain, Madrid, pp 45-82

Chigira M (1992) Long-term gravitational deformation of rocks by mass rock creep. En Geol 32: 57-184. https://doi.org/10.1016/0013-7952(92)90043-X

Chigira M, Hariyama T, Yamasaki S (2013) Development of deep-seated gravitational slope deformation on a shale dip-slope: observations from high-quality drill cores. Tectonophysics, 605, 104-113. https://doi.org/10.1016/j.tecto.2013.04.019

Cigna F, Tapete D (2021) Sentinel-1 big data processing with P-SBAS InSAR in the geohazards exploitation platform: An experiment on coastal land subsidence and landslides in Italy. Remote Sens 13: 885. https://doi.org/10.3390/rs13050885

Corominas J, Moya J, Lloret A, Gili JA, Angeli MG, Pasuto A, Silvano S (2000) Measurement of landslide displacements using a wire extensometer. Eng Geol 55:149–166

Corominas J, Mateos M, Remondo J (2017) Review of landslide occurrence in Spain and its relation to climate. In: Ho K, Lacasse S, Picarelli L (eds) Slope Safety Preparedness for Impact of Climate Change. CRC Press, pp 351-377. https://doi.org/10.1201/9781315387789

Crippa C, Valbuzzi E, Frattini P, Crosta GB, Spreafico MC, Agliardi F (2021) Semi-automated regional classification of the style of activity of slow rock-slope deformations using PS InSAR and SqueeSAR velocity data. Landslides 18: 2445-2463. https://doi.org/10.1007/s10346-021-01654-0

Crosta GB, Frattini P, Agliardi F (2013) Deep seated gravitational slope deformations in the European Alps. Tectonophysics 605: 13-33. https://doi.org/10.1016/j.tecto.2013.04.028

Crosta GB, Di Prisco C, Frattini P, Frigerio G, Castellanza R, Agliardi F (2014) Chasing a complete understanding of the triggering mechanisms of a large rapidly evolving rockslide. Landslides 11: 747-764. https://doi.org/10.1007/s10346-013-0433-1

Della Seta M, Esposito C, Marmoni GM, Martin S., Mugnozza GS, Troiani F (2017) Morpho-structural evolution of the valley-slope systems and related implications on slope-scale gravitational processes: new results from the Mt. Genzana case history (Central Apennines, Italy). Geomorphology 289: 60-77. https://doi.org/10.1016/j.geomorph.2016.07.003

Del Rio L, Moro M, Fondriest M, Saroli M, Gori S, Falcucci E, Cavallo A, Doumaz F, Di Toro G (2021) Active Faulting and Deep-Seated Gravitational Slope Deformation in Carbonate Rocks (Central Apennines, Italy): A New “Close-Up” View. Tectonics 40: e2021TC006698. https://doi.org/10.1029/2021TC006698

Di Luzio E, Saroli M, Esposito C, Bianchi-Fasani G, Cavinato GP. Scarascia-Mugnozza G (2004) Influence of structural framework on mountain slope deformation in the Maiella anticline (Central Apennines, Italy). Geomorphology 60: 417-432. https://doi.org/10.1016/j.geomorph.2003.10.004

Chigira, M. (1992). Long-term gravitational deformation of rocks by mass rock creep. Engineering Geology, 32(3), 157-184. https://doi.org/10.1016/0013-7952(92)90043-X

Chigira M, Tsou CY, Matsushi Y, Hiraishi N, Matsuzawa M (2013). Topographic precursors and geological structures of deep-seated catastrophic landslides caused by Typhoon Talas. Geomorphology 201: 479-493. https://doi.org/10.1016/j.geomorph.2013.07.020

Del Rio L, Moro M, Fondriest M, Saroli M, Gori S, Falcucci E, Cavallo A, Doumaz F, Di Toro G (2021) Active Faulting and Deep-Seated Gravitational Slope Deformation in

Carbonate Rocks (Central Apennines, Italy): A New “Close-Up” View. Tectonics 40: e2021TC006698. https://doi.org/10.1029/2021TC006698

DeMets C, Gordon RG, Argus DF, Stein S (1994) Effect of recent revisions to the geomagnetic reversal time scale on estimates of current plate motions. Geophys Res Lett 21:2191-2194. https://doi.org/10.1029/94GL02118

Demurtas V, Orrù PE, Deiana G (2021) Evolution of deep-seated gravitational slope deformations in relation with uplift and fluvial capture processes in Central Eastern Sardinia (Italy). Land 10:1193. https://doi.org/10.3390/land10111193

De Luca C, Cuccu R, Elefante S, Zinno I, Manunta M, Casola V, Rivolta G, Lanari R, Casu F (2015) An on-demand web tool for the unsupervised retrieval of earth’s surface deformation from SAR data: The P-SBAS service within the ESA G-POD environment. Remote Sens 7:15630-15650. https://doi.org/10.3390/rs71115630

De Palézieux L, Leith K, Loew S (2018) Assessing the predictive capacity of hillslope projected channel steepness for rockslope instability in the High Himalaya of Bhutan. Proceedings of the 16th Swiss Geoscience Meeting, pp 12

Díaz de Federico A, Puga E, Burgos J, Gallegos JA, Sanz de Galdeano C, Crespo V, Reyes JL (1980) Güejar-Sierra-Geological Map of Spain 1:50000. Geological Survey of Spain, Madrid

Di Martire D, De Rosa M, Pesce V, Santangelo MA, Calcaterra D (2012) Landslide hazard and land management in high-density urban areas of Campania region, Italy. Nat Hazards Earth Syst Sci 12:905-926. https://doi.org/10.5194/nhess-12-905-2012

Dramis F, Sorriso-Valvo M (1994) Deep-seated gravitational slope deformations, related landslides and tectonics. Eng Geol 38:231-243. https://doi.org/10.1016/0013-7952(94)90040-X

El Hamdouni R (2001) Estudio de Movimientos de Ladera en la Cuenca del Río Ízbor mediante un SIG: Contribución al Conocimiento de la Relación entre Tectónica Activa e Inestabilidad de Vertientes. Doctoral dissertation, University of Granada

El Hamdouni R, Irigaray C, Jiménez-Perálvarez JD, Chacón J (2010) Correlations analysis between landslides and stream length-gradient (SL) index in the southern slopes of Sierra Nevada (Granada, Spain). In: Williams AL, Pinches GM, Chin CY, McMorran TJ, Massey CY (eds) Geologically Active. Taylor and Francis, pp 141-149

Even M, Schulz K (2018) InSAR deformation analysis with distributed scatterers: A review complemented by new advances. Remote Sens 10: 744. https://doi.org/10.3390/rs10050744

Ferrater M, Booth-Rea G, Pérez-Peña JV, Azañón JM, Giaconia F, Masana E (2015) From extension to transpression: Quaternary reorganization of an extensional-related drainage network by the Alhama de Murcia strike-slip fault (eastern Betics). Tectonophysics 663: 33-47. https://doi.org/10.1016/j.tecto.2015.06.011

Foumelis M, Papadopoulou T, Bally P, Pacini F, Provost F, Patruno J (2019) Monitoring geohazards using on-demand and systematic services on ESA's geohazards exploitation platform. IGARSS 2019–2019 IEEE International Geoscience and Remote Sensing Symposium, Yokohama, pp 5457–5460

Froude MJ, Petley DN (2018) Global fatal landslide occurrence from 2004 to 2016. Nat Hazards Earth Syst Sci 18: 2161-2181. https://doi.org/10.5194/nhess-18-2161-2018

Gaidi S, Galve, JP, Melki F, Ruano, Reyes-Carmona C, Marzougui W, Devoto S, Pérez-Peña JV, Azañón JM, Chouaieb H, Zargouni F Booth-Rea G (2021) Analysis of the geological controls and kinematics of the chgega landslide (Mateur, Tunisia) exploiting photogrammetry and InSAR technologies. Remote Sens 13: 4048. https://doi.org/10.3390/rs13204048

Galindo-Zaldivar J, Gonzalez-Lodeiro F, Jabaloy A (1989) Progressive extensional shear structures in a detachment contact in the Western Sierra Nevada (Betic Cordilleras, Spain). Geodin Acta 3: 73-85. https://doi.org/10.1080/09853111.1989.11105175

Galve JP, Pérez-Peña JV, Azañón JM, Closson D, Caló F, Reyes-Carmona C, Jabaloy A, Ruano P, Mateos RM, Notti D, Herrera G, Béjar-Pizarro M, Monserrat O, Bally P (2017) Evaluation of the SBAS InSAR Service of the European Space Agency's Geohazard Exploitation Platform (GEP) Remote Sens 9 1291. https://doi.org/10.3390/rs9121291

Gu ZK, Yao X, Yao CC, Li CG (2021) Mapping of geomorphic dynamic parameters for analysis of landslide hazards: A case of Yangbi river basin on the upper Lancang-Mekong of China. J Mt Sci 18:2402-2411. https://doi.org/10.1007/s11629-021-6795-2

Günther A, Hervás J, Van Den Eeckhaut M, Malet JP, Reichenbach P (2014) Synoptic Pan-European landslide susceptibility assessment: The ELSUS 1000 v1 map. In: Margottini C, Canuti P, Sassa K (eds) Landslides science and practice. Springer, pp 297–301. http://dx.doi.org/10.1007/978-3-319-04999-1_12

Gutiérrez-Santolalla F, Acosta E, Ríos S, Guerrero J, Lucha P (2005) Geomorphology and geochronology of sackung features (uphill-facing scarps) in the Central Spanish Pyrenees. Geomorphology 69:298-314. https://doi.org/10.1016/j.geomorph.2005.01.012

Guzzetti F (2000) Landslide fatalities and the evaluation of landslide risk in Italy. Eng Geol 58:89-107. https://doi.org/10.1016/S0013-7952(00)00047-8

Gómez-Ortiz A, Schulte L, Salvador-Franch F, Sánchez-Gómer S, Simón-Torres M (2002) Map of Glacial and Periglacial Geomorphology of Sierra Nevada. Consejería de Medio Ambiente, Junta de Andalucía.

Gómez-Ortiz A, Palacio, D, Palade B, Vázquez-Selem, Salvador-Franch F (2012) The deglaciation of the Sierra Nevada (Southern Spain) Geomorphology 159: 93-105. https://doi.org/10.1016/j.geomorph.2012.03.008

Gómez-Pugnaire MT, Rubatto D, Fernández-Soler JM, Jabaloy A, López-Sánchez-Vizcaíno V, González-Lodeiro F, Galindo-Zaldívar J, Padrón-Navarta JA (2012) Late

Variscan magmatism in the Nevado-Filábride Complex: U-Pb geochronologic evidence for the pre-Mesozoic nature of the deepest Betic complex (SE Spain). Lithos 146:93-111. https://doi.org/10.1016/j.lithos.2012.03.027

Hack JT (1973) Stream-profile analysis and stream-gradient index. J. Res. U. S. Geol. Surv. 1: 421-429.

Hanssen RF (2001) Radar interferometry: data interpretation and error analysis. Springer.

Herrera G, Mateos RM, García-Davalillo JC, Grandjean G, Poyiadji E, Maftei R, Filipciuc T-C, Jemec Auflič M, Jež J, Podolszki L, Trigila A, Iadanza C, Raetzo H, Kociu A, Przyłucka M, Kułak M, Sheehy M, Pellicer XM, McKeown C, Ryan G, Kopačková V, Frei M, Kuhn D, Hermanns RL, Koulermou N, Smith CA, Engdahl M, Buxó P, Gonzalez M, Dashwood C, Reeves H, Cigna F, Liščák P, Pauditš P, Mikulėnas V, Demir V, Raha M, Quental L, Sandić C, Fusi B, Jensen OD (2018) Landslide databases in the Geological Surveys of Europe. Landslides 15: 359-379. https://doi.org/10.1007/s10346-017-0902-z

Hervás J, Bobrowsky (2009) Mapping: inventories, susceptibility, hazard and risk. In: Sassa K, Canuti P (eds) Landslides disaster risk reduction. Springer, pp 321-349.

Hewitt K (1999) Quaternary moraines vs catastrophic rock avalanches in the Karakoram Himalaya, northern Pakistan. Quat Res 51: 220-237. https://doi.org/10.1006/qres.1999.2033

Hilley GE, Burgmann R, Ferretti A, Novali F, Rocca F (2004) Dynamics of slow-moving landslides from permanent scatterer analysis. Science 304: 1952-1955. https://doi.org/10.1126/science.1098821

Jabaloy A, Galindo-Zaldívar J, González-Lodeiro F (1993) The Alpujárride-Nevado-Fibábride extensional shear zone, Betic Cordillera, SE Spain. J Struct Geol 15: 555-569. https://doi.org/10.1016/0191-8141(93)90148-4

Jarman D, Calvet M, Corominas J, Delmas M, Gunnell Y (2014) Large-scale rock slope failures in the eastern pyrenees: identifying a sparse but significant population in paraglacial and parafluvial contexts. GEOGR ANN A 96: 357-391. https://doi.org/10.1111/geoa.12060

Jiménez-Perálvarez JD, Irigaray C, El Hamdouni R, Chacón J (2011) Landslide-susceptibility mapping in a semi-arid mountain environment: an example from the southern slopes of Sierra Nevada (Granada, Spain). Bull. Eng. Geol. 70: 265-277. https://doi.org/10.1007/s10064-010-0332-9

Jiménez-Perálvarez JD, El Hamdouni R, Palenzuela JA, Irigaray C, Chacón J (2017) Landslide-hazard mapping through multi-technique activity assessment: an example from the Betic Cordillera (southern Spain). Landslides 14: 1975-1991. https://doi.org/10.1007/s10346-017-0851-6

Jiménez-Perálvarez JD (2018) Landslide-risk mapping in a developing hilly area with limited information on landslide occurrence. Landslides 15: 741-752. https://doi.org/10.1007/s10346-017-0903-y

Kang Y, Lu Z, Zhao C, Xu Y, Kim JW, Gallegos AJ (2021) InSAR monitoring of creeping landslides in mountainous regions: A case study in Eldorado National Forest, California. Remote Sens Environ 258: 112400. https://doi.org/10.1016/j.rse.2021.112400

Kirby E, Whipple KX (2012) Expression of active tectonics in erosional landscapes. J Struct Geol 44: 54-75. https://doi.org/10.1016/j.jsg.2012.07.009

Kirschbaum D, Stanley T, Zhou Y (2015) Spatial and temporal analysis of a global landslide catalog. Geomorphology 249: 4-15. https://doi.org/10.1016/j.geomorph.2015.03.016

Korup O (2005). Large landslides and their effect on sediment flux in South Westland, New Zealand. Earth Surf Process Landf 30: 305-323. https://doi.org/10.1002/esp.1143

Korup O (2006) Rock-slope failure and the river long profile. Geology 34: 45-48. https://doi.org/10.1130/G21959.1

Korup O, Densmore AL, Schlunegger F (2010) The role of landslides in mountain range evolution. Geomorphology 120:77-90. https://doi.org/10.1016/j.geomorph.2009.09.017

Larue JP (2008) Effects of tectonics and lithology on long profiles of 16 rivers of the southern Central Massif border between the Aude and the Orb (France). Geomorphology 93: 343-367. https://doi.org/10.1016/j.geomorph.2007.03.003

Liu F, Yao X, Li L (2021) Applicability of geomorphic index for the potential slope instability in the Three River Region, Eastern Tibetan Plateau. Sensors 21:6505. https://doi.org/10.3390/s21196505

Mariani GS, Zerboni A (2020) Surface geomorphological features of deep-seated gravitational slope deformations: A look to the role of lithostructure (N Apennines, Italy). Geosciences 10:334. https://doi.org/10.3390/geosciences10090334

Martínez-Martínez JM, Soto JI, Balanyá JC (2002) Orthogonal folding of extensional detachments: structure and origin of the Sierra Nevada elongated dome (Betics, SE Spain). Tectonics 21:3-1. https://doi.org/10.1029/2001TC001283

Martín-Civantos JM (2010) Las aguas del río Alhama de Guadix y el sistema de careos de Sierra Nevada (Granada) en época medieval. In: Jiménez-Puertas M, Mattei L (eds) El paisaje y su dimensión arqueológica/Estudios sobre el Sur de la Península Ibérica en la Edad Media. Alhulia, pp 79-111

Martínez-Martínez JM (2006) Lateral interaction between metamorphic core complexes and less-extended, tilt-block domains: the Alpujarras strike-slip transfer fault zone (Betics, SE Spain). J Struct Geol 28:602-620. https://doi.org/10.1016/j.jsg.2006.01.012

Martos-Rosillo S, Ruiz-Constán A, González-Ramón A, Mediavilla R, Martín-Civantos J. M, Martínez-Moreno FJ, Jódar J, Marín-Lechado C, Madialdea A, Galindo-Zaldívar J, Pedrera A, Durán JJ (2019) The oldest managed aquifer recharge system in Europe: New insights from the Espino recharge channel (Sierra Nevada, southern Spain). J Hydrol 578:124047. https://doi.org/10.1016/j.jhydrol.2019.124047

Mateos RM, García-Moreno I, Azañón, JM (2012) Freeze–thaw cycles and rainfall as triggering factors of mass movements in a warm Mediterranean region: the case of the Tramuntana Range (Majorca, Spain). Landslides 9:417-432. https://doi.org/10.1007/s10346-011-0290-8

Mateos RM, Ezquerro P, Azañón JM, Gelabert B, Herrera G, Fernández-Merodo JA, Spizzichino D, Sarro R, García-Moreno I, Béjar-Pizarro M (2018) Coastal lateral spreading in the world heritage site of the Tramuntana Range (Majorca, Spain). The use of PSInSAR monitoring to identify vulnerability. Landslides 15:797-809. https://doi.org/10.1007/s10346-018-0949-5

Mateos RM, López-Vinielles J, Poyiadji E, Tsagkas D, Sheehy M, Hadjicharalambous K, Liscák P, Podolski L, Laskowicz I, Iadanza C, Gauert C, Todorović S, Auflič MJ, Maftei R, Hermanns RL, Kociu A, Sandić C, Mauter R, Sarro R, Béjar M, Herrera G (2020) Integration of landslide hazard into urban planning across Europe. Landsc Urban Plan 196:103740. https://doi.org/10.1016/j.landurbplan.2019.103740

Notti D, Davalillo JC, Herrera G, Mora O (2010) Assessment of the performance of X-band satellite radar data for landslide mapping and monitoring: Upper Tena Valley case study. Nat Hazards Earth Syst Sci 10:1865-1875. https://doi.org/10.5194/nhess-10-1865-2010

Palma P, Oliva M, García-Hernández C, Gómez-Ortiz A, Ruiz-Fernández J, Salvador-Franch F, Catarineu M (2017) Spatial characterization of glacial and periglacial landforms in the highlands of Sierra Nevada (Spain). Sci Total Environ 584: 1256-1267. https://doi.org/10.1016/j.scitotenv.2017.01.196

Pánek T, Smolková V, Hradecký J, Kirchner K (2007) Landslide dams in the northern part of Czech Flysch Carpathians: geomorphic evidence and imprints. Studia Geomorphologica Carpatho-Balcanica 41: 77-96

Penna IM, Hermanns RL, Daicz S, Suriano J, Tedesco AM (2015) Effects of tectonic deformation and landslides in the erosion of a mountain plateau in the transitional zone between the central and Patagonian Andes. Am J Sci 315: 257-274. https://doi.org/10.2475/03.2015.03

Pérez-Peña JV, Azor A, Azañón JM, Keller EA (2010) Active tectonics in the Sierra Nevada (Betic Cordillera, SE Spain): Insights from geomorphic indexes and drainage pattern analysis. Geomorphology 119: 74-87. https://doi.org/10.1016/j.geomorph.2010.02.020

Perron JT, Royden L (2013) An integral approach to bedrock river profile analysis. Earth Surf Process Landf 38: 570-576. https://doi.org/10.1002/esp.3302

Piacentini D, Troiani F, Servizi T, Nesci O, Veneri F. (2020). SLIX: A GIS toolbox to support along-stream knickzones detection through the computation and mapping of the stream length-gradient (SL) index. ISPRS Int. J. Geo-Inf 9: 69. https://doi.org/10.3390/ijgi9020069

Pike RJ (2000). Geomorphometry-diversity in quantitative surface analysis. Prog Phys Geogr 24: 1-20. https://doi.org/10.1177/030913330002400101

Puga E, Díaz de Federico A, Nieto JM (2002) Tectonostratigraphic subdivision and petrological characterisation of the deepest complexes of the Betic zone: a review. Geodin Act 15: 3-43. https://doi.org/10.1080/09853111.2002.10510737

Radbruch-Hall DH (1978). Gravitational creep of rock masses on slopes. In: Voight B (ed) Rockslides and avalanches: natural phenomena. Elsevier, pp 607-657

Reinhardt LJ, Bishop P, Hoey TB, Dempster TJ, Sanderson DCW (2007) Quantification of the transient response to base-level fall in a small mountain catchment: Sierra Nevada, southern Spain. J Geophys Res Earth Surf 112. https://doi.org/10.1029/2006JF000524

Reyes-Carmona C, Barra A, Galve JP, Monserrat O, Pérez-Peña JV, Mateos RM, Notti D, Ruano P, Millares A, López-Vinielles J, Azañón JM (2020) Sentinel-1 DInSAR for monitoring active landslides in critical infrastructures: the case of the Rules Reservoir (Southern Spain). Remote Sens 12: 809. https://doi.org/10.3390/rs12050809

Reyes-Carmona C, Galve JP, Moreno-Sánchez M, Riquelme A, Ruano P, Millares A, Teixidó, Sarro R, Pérez-Peña V, Barra A, Ezquerro, López-Vinielles J, Béjar-Pizarro M, Azañón JM, Monserrat O Mateos RM (2021) Rapid characterisation of the extremely large landslide threatening the Rules Reservoir (Southern Spain). Landslides 18: 3781-3798. https://doi.org/10.1007/s10346-021-01728-z

Rogers JD, Chung J (2017) A review of conventional techniques for subsurface characterization of landslides. Environ Earth Sci 76:1-13. https://doi.org/10.1007/s12665-016-6353-3

Ruiz-Fuentes A, Aerden DGAM (2018) Transposition of foliations and superposition of lineations during polyphase deformation in the Nevado-Filabride complex: tectonic implications. Int J Earth Sci 107: 1975-1988. https://doi.org/10.1007/s00531-017-1582-6

Santamaría-López Á, Lanari P, Sanz de Galdeano C (2019) Deciphering the tectono-metamorphic evolution of the Nevado-Filábride complex (Betic Cordillera, Spain) - A petrochronological study. Tectonophysics 767: 128158. https://doi.org/10.1016/j.tecto.2019.06.028

Sanz de Galdeano C, Peláez Montilla JA, López Casado C (2003) Seismic potential of the main active faults in the Granada Basin (southern Spain). Pure Appl Geophys 160: 1537-1556. https://doi.org/10.1007/s00024-003-2359-3

Sanz de Galdeano C, López-Garrido AC (2016). The nevado-filábride complex in the western part of Sierra de los Filabres (Betic Internal Zone), structure and lithologic succession. Bol Geol Min 127: 823-836. https://doi.org/10.21701/bolgeomin.127.4.005

Sassa K, Wang G, Fukuoka H, Wang F, Ochiai T, Sugiyama M, Sekiguchi T (2004) Landslide risk evaluation and hazard zoning for rapid and long-travel landslides in urban development areas. Landslides 1: 221-235. https://doi.org/10.1007/s10346-004-0028-y

Schlögel R, Doubre C, Malet JP, Masson F (2015) Landslide deformation monitoring with ALOS/PALSAR imagery: A D-InSAR geomorphological interpretation method. Geomorphology 231: 314-330. https://doi.org/10.1016/j.geomorph.2014.11.031

Singhroy V, Mattar KE, Gray A (1998) Landslide characterisation in Canada using interferometric SAR and combined SAR and TM images. Adv Space Res 21: 465-476. https://doi.org/10.1016/S0273-1177(97)00882-X

Soldati M (2013) Deep-seated gravitational slope deformation. In: Bobrowsky PT (ed) Encyclopedia of natural hazards. Springer, pp 151-155

Spreafico MC, Sternai P, Agliardi F (2021). Paraglacial rock-slope deformations: sudden or delayed response? Insights from an integrated numerical modelling approach. Landslides 18: 1311-1326. https://doi.org/10.1007/s10346-020-01560-x

Stevens MR, Berke PR, Song Y (2010) Creating disaster-resilient communities: Evaluating the promise and performance of new urbanism. Landsc Urban Plan 94: 105-115. https://doi.org/10.1016/j.landurbplan.2009.08.004

Subiela G, Guinau M, Galve JP (2019) Idoneidad del índice SL para la identificación semi-automática de movimientos en masa que afectan a la red de drenaje. Boletín Geológico y Minero 130: 465-487

Tapete D, Cigna F (2017) InSAR data for geohazard assessment in UNESCO World Heritage sites: state-of-the-art and perspectives in the Copernicus era. Int J Appl Earth Obs Geoinf 63:24–32. https://doi.org/10.1016/j.jag.2017.07.007

Tolomei C, Taramelli A, Moro M, Saroli M, Aringoli D, Salvi S (2013) Analysis of the deep-seated gravitational slope deformations over Mt. Frascare (Central Italy) with geomorphological assessment and DInSAR approaches. Geomorphology 201: 281-292. https://doi.org/10.1016/j.geomorph.2013.07.002

Troiani F, Galve JP, Piacentini, Della Seta M, Guerrero J (2014) Spatial analysis of stream length-gradient (SL) index for detecting hillslope processes: a case of the Gállego River headwaters (Central Pyrenees, Spain). Geomorphology, 214, 183-197. https://doi.org/10.1016/j.geomorph.2014.02.004

Troiani F, Piacentin, D, Della Seta M, Galve JP (2017) Stream Length-gradient Hotspot and Cluster Analysis (SL-HCA) to fine-tune the detection and interpretation of knickzones on longitudinal profiles. Catena 156:30-41. https://doi.org/10.1016/j.catena.2017.03.015

Tsou CY, Chigira M, Matsushi Y, Chen SC (2015) Deep-seated gravitational deformation of mountain slopes caused by river incision in the Central Range, Taiwan: Spatial distribution and geological characteristics. Eng Geol 196:126-138. https://doi.org/10.1016/j.enggeo.2015.07.005

Turnbull JM, Davies TR (2006) A mass movement origin for cirques. Earth Surf Process and Landf 31: 1129-1148. https://doi.org/10.1002/esp.1324

Van Westen CJ, Castellanos E, Kuriakose SL (2008) Spatial data for landslide susceptibility, hazard, and vulnerability assessment: An overview. Eng Geol 102:112-131. https://doi.org/10.1016/j.enggeo.2008.03.010

Varnes DJ (1978) Slope movement types and processes. In: Schuster RL, Krizek RJ (eds) Landslides, analysis and control. National Academy of Sciences, New York, pp. 11-33

Walsh LS, Martin AJ, Ojha TP, Fedenczuk (2012). Correlations of fluvial knickzones with landslide dams, lithologic contacts, and faults in the southwestern Annapurna Range, central Nepalese Himalaya. J Geophys Res Earth Surf 117. https://doi.org/10.1029/2011JF001984

Weidinger J T, Korup O, Munack H, Altenberger U, Dunning SA, Tippelt G, Lottermoser W (2014) Giant rockslides from the inside. Earth Planet Sci Lett 389: 62-73. https://doi.org/10.1016/j.epsl.2013.12.017

Weibel R, Heller M (1991) Digital terrain modelling. In: Longley PA, Goodchild MF, Maguire DJ, Rhind DW (eds) Geographical Information Systems: Principles and Applications. Longman, pp 269-297

Whipple KX (2004) Bedrock rivers and the geomorphology of active orogens. Annu. Rev. Earth Planet. Sci 32: 151-185. https://doi.org/10.1146/annurev.earth.32.101802.120356

Whipple KX, Dibiase RA, Crosby BT (2013) Bedrock rivers. In: Shroder JJ, Wohl E (eds) Fluvial Geomorphology. Elsevier, pp 550-573. https://doi.org/10.1016/B978-0-12-374739-6.00254-2

Wobus C, Whipple KX, Kirby E, Snyder N, Johnson J, Spyropolou K, Crosby B, Sheenan D (2006) Tectonics from topography: Procedures, promise, and pitfalls. In: Willett SD, Hovius N, Brandon MT, Fisher DM (eds) Tectonics, Climate, and Landscape Evolution, Geological Society of America Special Paper, vol 398, pp 55-74. https://doi.org/10.1130/2006.2398(04)

Zischinsky U (1969) Uber Sackungen. Rock Mechanics 1: 30–52

Chapter III

Sentinel-1 DInSAR for monitoring active landslides in critical infrastructures: the case of the Rules Reservoir (Southern Spain)

Published on:

Remote Sensing, 2020

Volume 12, Page 809

DOI: 10.3390/rs12050809

(Received: 17 February 2020, Accepted: 27 February 2020, Published: 3 March 2020)

Cristina Reyes-Carmona [1], Anna Barra [2], Jorge Pedro Galve [1], Oriol Monserrat [2], José Vicente Pérez-Peña [1,3], Rosa María Mateos [4], Davide Notti [5], Patricia Ruano [1,6], Agustín Millares [7], Juan López-Vinielles [4,8], José Miguel Azañón [1,6]

[1] Departamento de Geodinámica, Universidad de Granada, Avenida del Hospicio s/n, 18010 Granada, Spain
[2] Geomatics Division, Centre Tecnològic de Telecomunicacions de Catalunya (CTTC), Avinguda Carl Friedrich Gauss 7, 08860 Castelldefels, Spain
[3] Instituto Andaluz de Geofísica, Calle del Profesor Clavera 12, 18071 Granada, Spain
[4] Geohazards InSAR laboratory and Modelling group (InSARlab), Geoscience Research Department, Geological Survey of Spain (IGME), Calle de Ríos Rosas 23, 28003 Madrid, Spain
[5] Italian National Research Council, Research Institute for Geo-Hydrological Protection (CNR-IRPI), Strada delle Cacce 73, 10135 Torino, Italy
[6] Instituto Andaluz de Ciencias de la Tierra (IACT-CSIC), Avenida de las Palmeras 4, 18100 Armilla, Granada, Spain
[7] Instituto Interuniversitario de Investigación del Sistema Tierra en Andalucía (IISTA), Avenida del Mediterráneo s/n, 18006 Granada
[8] HEMAV SL, Carrer d'Esteve Terrades 1, 08860 Castelldefels, Spain

Abstract

Landslides in reservoir contexts are a well-recognised hazard that may lead to dangerous situations regarding infrastructures and people's safety. Satellite-based radar interferometry is proving to be a reliable method to monitor the activity of landslides in such contexts. Here, we present a DInSAR (Differential Interferometric Synthetic Aperture Radar) analysis of Sentinel-1 images that exemplifies the usefulness of the technique to recognise and monitor landslides in the Rules Reservoir (Southern Spain). The integration of DInSAR results with a comprehensive geomorphological study allowed us to understand the typology, evolution and triggering factors of three active landslides: Lorenzo-1, Rules Viaduct and El Arrecife. We could distinguish between rotational and translational landslides, and thus, we evaluated the potential hazards related to these typologies: retrogression (Lorenzo-1 and Rules Viaduct landslides) or catastrophic slope failure (El Arrecife Landslide). We also observed how changes in the water level of the reservoir influence the landslide's behaviour. Additionally, we were able to monitor the stability of the Rules Dam, as well as to detect the deformation of a highway viaduct that crosses a branch of the reservoir. Overall, we consider that other techniques must be applied to continuously monitor the movements, especially in the El Arrecife Landslide, in order to avoid future structural damages and fatalities.

Keywords

DInSAR, Sentinel-1, reservoir safety, landslides, geomorphological mapping

1. Introduction

Slope instability is a major problem in the planning, design, construction and maintenance of dams and reservoirs (Lane 1966). Until the well-known 1963 Vajont Reservoir slide in Italy, with 2000 fatalities (Kiersch 1964), experts did not fully realise the potential risk represented by unstable slopes within reservoir basins (Schuster 1979). After the Vajont case, examples worldwide have reminded us of this problem: Grand Coulee Reservoir in USA (Jones et al. 1961), Tabachaca Reservoir in Peru (Novosad et al. 1979), Geheyar Reservoir (Qi et al. 2006) and Three Gorges Reservoir (Wang et al. 2004) in China, Nechranice Reservoir in Czech Republic (Rybář 1977), Orava Reservoir in Slovakia (Spanilá et al. 2002), Wloclawek Reservoir in Poland (Spanilá et al. 2002) and Cortes (Lopez-Marinas et al. 1997) and Yesa Reservoirs (Gutiérrez et al. 2010) in Spain. These are well-documented cases, worth mentioning, in which ground instabilities within reservoirs produced threatening situations.

There are several phenomena that may produce ground instabilities and dangerous situations in reservoirs. Firstly, the water level changes play a central role in triggering landslides in reservoir slopes (Millet et al. 1992). Secondly, if dam abutments rest on moving slopes, progressive deformation of the dam could lead to its collapse and generate a subsequent catastrophic flood (Milillo et al 2016). Rapid large landslides in subaerial or submerged portions of reservoir slopes can also generate catastrophic floods due to the

creation of impulse waves of great destructive power (Gutiérrez et al. 2010). These impulse waves or landslide-related tsunamis can have devastating consequences. As in the Vajont case (Kiersch 1964), the wave can overtop or destroy the dam, and generate a massive flash flood downstream.

Monitoring dams and reservoir unstable slopes is crucial to avoid or minimise the mentioned disasters. In recent years, the use of remote sensing techniques to monitor the activity of slopes that interact with human infrastructures has significantly grown (Bozzano et al. 2011). Some of these techniques are photogrammetry (Kraus 1997), Terrestrial Laser Scanner (TLS) (Teza et al. 2007), Global Positioning Systems (GPS) (Brunner et al. 2003) and Differential Synthetic Aperture Radar Interferometry (DInSAR) satellite-based (Massonnet and Feigl 1998) and ground-based (Monserrat et al. 2014). In particular, the contribution of satellite radar interferometry is becoming one of the most useful tools for ground instability identification and monitoring (Catani et al. 2005; Herrera et al. 2009; Cigna et al. 2013; Ciampalini et al. 2015; Rocca et al. 2015; Barra et al. 2016; Crosetto et al. 2019). DInSAR monitoring has proven its effectiveness not only in detecting unstable areas on reservoir slopes but also in monitoring the stability of dams. For example, Sousa et al. (2014) discuss the potential of DInSAR technology for monitoring deformations in dams and bridges. Milillo et al. (2016), Wang et al. (2011) and Cignetti et al. (2016) also proved DInSAR effectiveness in monitoring the slopes in the Pertusillo (Italy), the Three Gorges (China) and the Beauregard (Italy) dams, respectively. Moreover, Wang et al. (2013) also validated the use of DInSAR to locate and monitor landslides in the surrounding areas of the Wudongde Reservoir (China).

The recent increase in the number of satellites with different spatial and temporal resolutions has supposed a step forward in radar techniques (Barra et al. 2017). A significant improvement is given by the new C-band sensors on-board the Sentinel-1A and Sentinel-1B satellites, launched on 2014 and 2016, respectively (Rucci et al. 2012). Sentinel-1 satellites have improved data acquisition and analysis, as its images are free-of-charge and offer wide area coverage, high temporal resolution (sampling of 6 days) and high coherent interferograms (Barra et al. 2016). These advantages make possible to monitor surface ground displacement at a high accuracy (up to 1 mm/year), that in turn, allows long-term geohazard management over local and regional areas (Tang et al. 2015).

In this paper, Sentinel-1 data combined with classical geomorphological surveys were evaluated as quick decision-support tools on critical infrastructures. We describe a study in the Rules Reservoir (Southern Spain) where unstable slopes represented a particular challenge for its design, construction and management. This study exemplifies how Sentinel-1 DInSAR allows the identification of active ground instabilities and provides support on their characterisation. Moreover, this study has been developed independently of the authorities responsible for managing the reservoir and the rest of the nearby infrastructures. Thus, the current freely available remote sensing data from European Space Agency (ESA) enabled us to make an independent and continuous assessment of critical infrastructures.

2. Background

2.1. The Rules Reservoir

The Rules Reservoir is located half-way through the Guadalfeo River course at its confluence with the Ízbor River, in the Granada Province (Southern Spain) (Figure 1). The reservoir was initially projected to have a maximum water storage of 117 hm^3 and a flooded area of 3.08 km^2 (Pérez 2004). It collects water from Sierra de Lújar, Sierra de Los Guájares and the southern slopes of the western termination of Sierra Nevada (Figure 1). The Rules Dam is a 118 m high gravity dam that is situated at the southern edge of the reservoir (Figure 1). The structure of the dam is made of vibrated concrete with a 500 m radius curved plant. The reservoir was initially projected for the following purposes: irrigation (40%), supply to residential developments on the coast (19%), energy generation (9%), flood control (30%) and environmental flow (2%) (Bergillos and Ortega-Sánchez 2017). The inauguration of the reservoir was in 2004, but neither a water irrigation system nor the hydroelectric power plant have been installed yet.

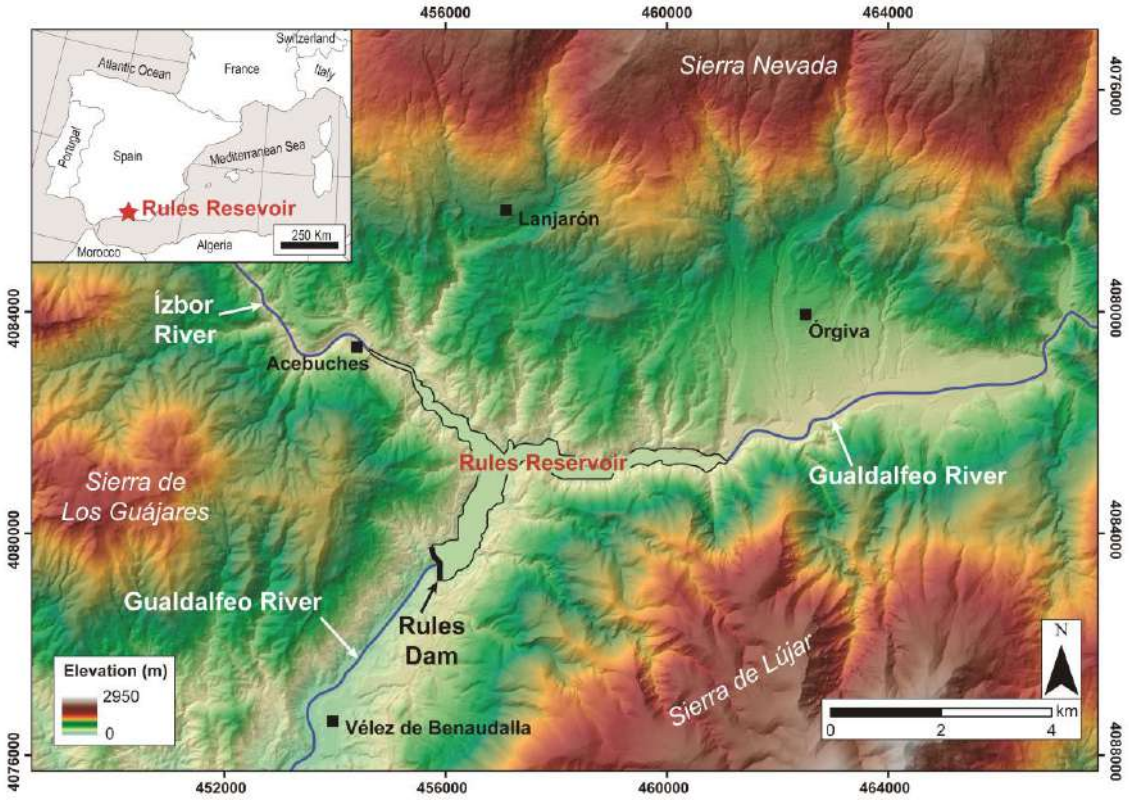

Figure 1. Location of the Rules Reservoir and the main geographical features of the area.

Two important transport infrastructures are spatially associated to the reservoir. Along its eastern slope, the A-44 Highway crosses one of the reservoir branches above a 585 m length concrete viaduct, called the Rules Viaduct. This highway runs from northern Andalusia, goes through Granada Province to the south and ends in the touristic county called 'Costa Tropical' or 'Granada Coast'. Likewise, the N-323 National Road runs through the western bank of the reservoir, having a similar route to the A-44 Highway. The N-323 road was the only connection to the Granada Coast before the A-44 construction in 2009.

2.2. Geological and geomorphological setting of the Rules Reservoir

The Rules Reservoir is located in the Internal Zones of the central Betic Cordillera, the Iberian part of the Betic-Rif orogen (Vera and Martín-Algarra 2004). The Betic Internal Zones are constituted of Mesozoic and Paleozoic rocks, usually metamorphosed and intensely deformed. Our study area is situated over the Alpujárride Complex, one of the three main units of the Internal Zones, that consists of, from bottom to top: i) dark schists ii); quartzschits; iii) phyllites and quartzites; and iv) dolomitic marbles (Simancas 2018). The Rules Reservoir lays within both the Alpujárride phyllites and dolomitic marbles (see geological map of Aldaya et al. 1979). The deformation history of the Alpujárride Complex was quite complex, resulting in highly folded and fractured rocks (see Simancas and Campos 1993; Galindo-Zaldívar et al. 1999; Martínez-Martínez et al. 2002; Sanz de Galdeano et al. 2012; Simancas 2018 for detailed geological research of the area).

From a geomorphological point of view, the Rules Reservoir is situated at 279 m above sea level in a V-shaped valley excavated by the Guadalfeo River, mainly in the Alpujárride Complex phyllites. The Sierra de Los Guájares and Sierra de Lújar ranges, reaching elevations of 1200 and 1800 m, respectively, constitute the eastern and western limits of the reservoir (Figure 1). The Sierra Nevada Range corresponds to the reservoir northern divide, reaching up to 3400 m (Figure 1). The elevation of these ranges generates high topographic gradients, as the local relief is 3000 m maximum at just 35 kilometres from the Sierra Nevada to the coastline. Such gradients have led to a deep fluvial incision that triggers abundant slope instability processes in this area (Fernández et al. 1997). Consequently, several landslide inventories have been produced along the Ízbor and Guadalfeo River basins (Fernández et al. 1997; Chacón et al. 2007). Moreover, Irigaray et al. (2000) carried out a landslide susceptibility analysis of the area, associating the highest susceptibility areas to the Alpujárride phyllites.

From the climatic point of view, the Rules Reservoir area has registered a mean annual precipitation of 340-370 mm and an average annual temperature of 12ºC. A significant part of the precipitation is recorded in winter and spring, while the drier months correspond to summer, typical of the hot-summer Mediterranean climate (Csa), according to the Köppen climate classification. Intense rainfall events and the occurrence of landslides have also been pointed out by Irigaray et al. (2000) in the area, linked to the extraordinarily heavy rains that occurred during the 1996-1997 hydrological cycle.

2.3. Slope instabilities registered in the Rules Reservoir area

After the Rules Reservoir inauguration in 2004, the northern edge of the Rules Viaduct was bent during its construction in 2006. Strengthening of the foundations of the damaged viaduct piers was carried out and the infrastructure (and thus, that A-44 Highway section) was inaugurated in 2009 (Fernández-Motril 2013a). According to the information provided by the Spanish Ministry of Public Works and Transport, this highway section required an investment of 14 million Euros per kilometre, being the most expensive highway section ever built in Spain at that time (Navarrete 2009). Just 4 years later, in August 2013, the Ministry of Public Works and Transport reported on instability problems

in the northern embankment of the viaduct and the required repaired works cost 19 million Euros (Fernández-Motril 2013b). The works consisted of the substitution of the embankment with an additional mixed steel and concrete viaduct, the construction of lateral retaining piles and an additional pile closer to the abutment. Road traffic was temporary diverted to the N-323 National Road, which also required major repairs (estimated at 3.8 million Euros) due to its deterioration (Fernández-Motril 2013c). Water level fluctuations were pointed out as the main reason for the long-term instability issues in the reservoir (Fernández-Motril 2015). Finally, the viaduct was reinaugurated in 2015 and no other problem has been reported to date.

Despite of these precedents, no information about the activity of ground instabilities in the Rules area was published until Lackezy et al. (2016). This research emphasises the potential of DInSAR for the detection of moving slopes and compiled several active landslides from different worldwide locations, including a sector of the Rules Reservoir area. The authors processed ENVISAT and Sentinel-1 images, detecting several areas with active movements, but they did not delimit any perimeter of a sliding body nor develop further research on the Rules Reservoir slopes.

3. Methodology

In order to evaluate the current ground and structure stability in the area of the Rules Reservoir, we firstly applied Differential Synthetic Aperture Radar Interferometry (DInSAR) techniques by exploiting Sentinel-1A and B images. After a comprehensive interpretation of the DInSAR results and identification of the main unstable areas, we carried out a thorough compilation of data from these areas and a detailed geomorphological field survey. We inventoried field evidences of the detected movements and produced several geomorphological maps at site-scale of the unstable areas (i.e. active landslides). In parallel, we analysed the time series of displacement in the unstable measured points. We were interested in checking the evolution of the displacements and their link to possible triggering factors, such as rainfall and water level variations in the reservoir.

3.1. SAR Interferometry

In order to derive the velocity map and the time series of displacements (TS), we applied the Persistent Scatterer Interferometry chain of the Geomatics Division (PSIG) of the Centre Tecnològic de Telecomunicacions de Catalunya (CTTC), described by Devanthéry et al. (2014). The procedure and the main parameters are resumed in the flowchart of Figure 2. After the generation of the interferograms, the first step was the estimation of the annual linear velocities over a selection of points (see Biescas et al. 2007; Crosetto et al. 2011 for more details). Then, over the same selected points, the accumulated displacement at each image date was calculated based on a two-steps phase unwrapping (see Devanthéry et al. 2014; Barra et al. 2017; Solari et al. 2020 for more details). The estimation of the annual linear velocity and the time series were both estimated along the satellite Line of Sight (LoS) direction. Therefore, the final output of the processing procedure was a surface displacement map that consisted of a set of selected points with

both the information of the estimated LoS velocity (i.e. velocity maps) and the accumulated displacement at every satellite acquisition (i.e. time series). We processed one burst of 139 Sentinel-1A and Sentinel-1B images, acquired on ascending orbits with a temporal sampling up to 6 days and covering a period from 10th March 2015 to 20th September 2018. Table 1 shows the further characteristics of the used images dataset and other processing parameters. To derive the velocity maps and the time series, we generated 6664 interferograms. In order to optimise the two processing approaches, we used long a temporal baseline observation (i.e. interferograms with a minimum temporal baseline of 150 days) to derive the annual linear velocities and a short temporal baseline observation (i.e. interferograms with a maximum temporal baseline of 60 days) to derive the accumulated displacement. This selection of the interferograms network improves the results in terms of noise and spatial coverage. The reference point to calculate the velocities was located in a small urbanised area to the south of the reservoir (N36º51'18.678"/W3º29'43.983"). According to the Barra et al. (2017) criterion, we estimated the stability range of the velocity map, and, therefore, the threshold for discriminating stable and unstable targets, as two times the standard deviation of the velocity of all the measured points. This stability range also represents the general noise of the results, i.e. the sensitivity of the velocity map. Hence, points classified as 'stable' can be truly stable as well as unstable points, with an undetectable displacement (Barra et al. 2017).

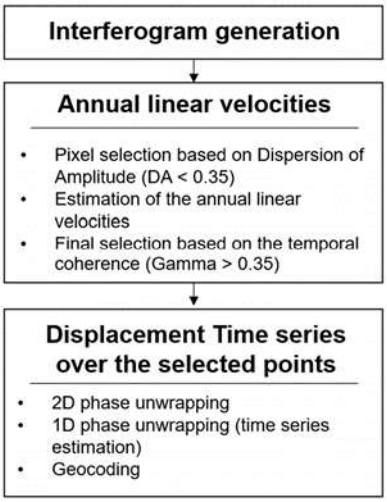

Figure 2. Flowchart resuming the main steps of the DInSAR processing.

3.2. Geomorphological investigation

After obtaining the DInSAR results, we performed a general overview of the velocity map to define unstable areas. We compiled the published scientific literature of the area, as well as historical documents, aerial photographs (1956-1957 American Flight and 2004 to 2017 from the PNOA project) and press reports until present. Once we gathered such information, we carried out a comprehensive geomorphological survey at site-scale of the areas of interest. We performed a detailed photo-interpretation and field survey combined with the exploitation of the available digital data in a GIS environment: Digital Elevation Models and derived information (e.g. hillshade and slope maps) as well as 2014 LiDAR

data. All the digital data was freely obtained from the Spanish National Geographic Institute (IGN) web page (www.ign.es). Thus, we produced a landslide inventory map of the reservoir surroundings and three geomorphological maps for each studied unstable area, after and before the construction of the reservoir, to illustrate the evolution of the slopes.

Satellite	Sentinel-1A and B
Acquisition mode	Interferometric Wide (IW) Swath
Product Type	Single Looked Complex (SLC)
Orbit	Ascending
Incidence angle	39°
Track or relative orbit number	1
Minimum revisit period (days)	6
Temporal span (years)	March 2015 – September 2018 (3.5)
Number of images	139
Wavelength (cm)	5.5
Polarisation	VV
Full resolution (azimuth/range) (m)	14/4
Number of processed swaths	1
Number of processed bursts	1

Table 1. Main characteristic of the processed satellite data.

3.3. Analysis of DInSAR times series

We analysed the time series of displacement (TS) of the unstable points within the three areas of study. Prior to this analysis, the TS of each unstable area have been referenced to a stable neighbour point. This significantly reduced the effects of residual atmospheric artefacts. The goal of the analysis was to assess the temporal behaviour of each slope and its relation to possible triggering factors. To this end, we compared the displacement time series with rainfall and reservoir water level variations. Rainfall and reservoir water level measurements were freely obtained from the public Andalusian Automatic System of Hydrologic Information (S.A.I.H. HIDROSUR, www.redhidrosurmedioambiente.es). Rainfall data correspond to the pluviometric station number 50, located within the village of Vélez de Benaudalla (Figure 1).

4. Results

4.1. DInSAR velocity map of the Rules Reservoir

We measured the velocity of 28137 points within the Rules Reservoir area (Figure 3). The obtained data allowed us to settle the stability range between 5 to -5 mm/year. According to these criteria, we identified 406 non-stable points, which represent 1.4% of the total points. As velocity is estimated along the satellite LoS direction, the points of negative values evidence points moving away from the satellite, while positive values evidence points moving towards the satellite. Taking into consideration that the SAR images were acquired in ascending orbit, positive and negative values may indicate, in addition to uplift and subsidence displacements in flat areas, westward and eastward movements in the slopes of the reservoir, respectively.

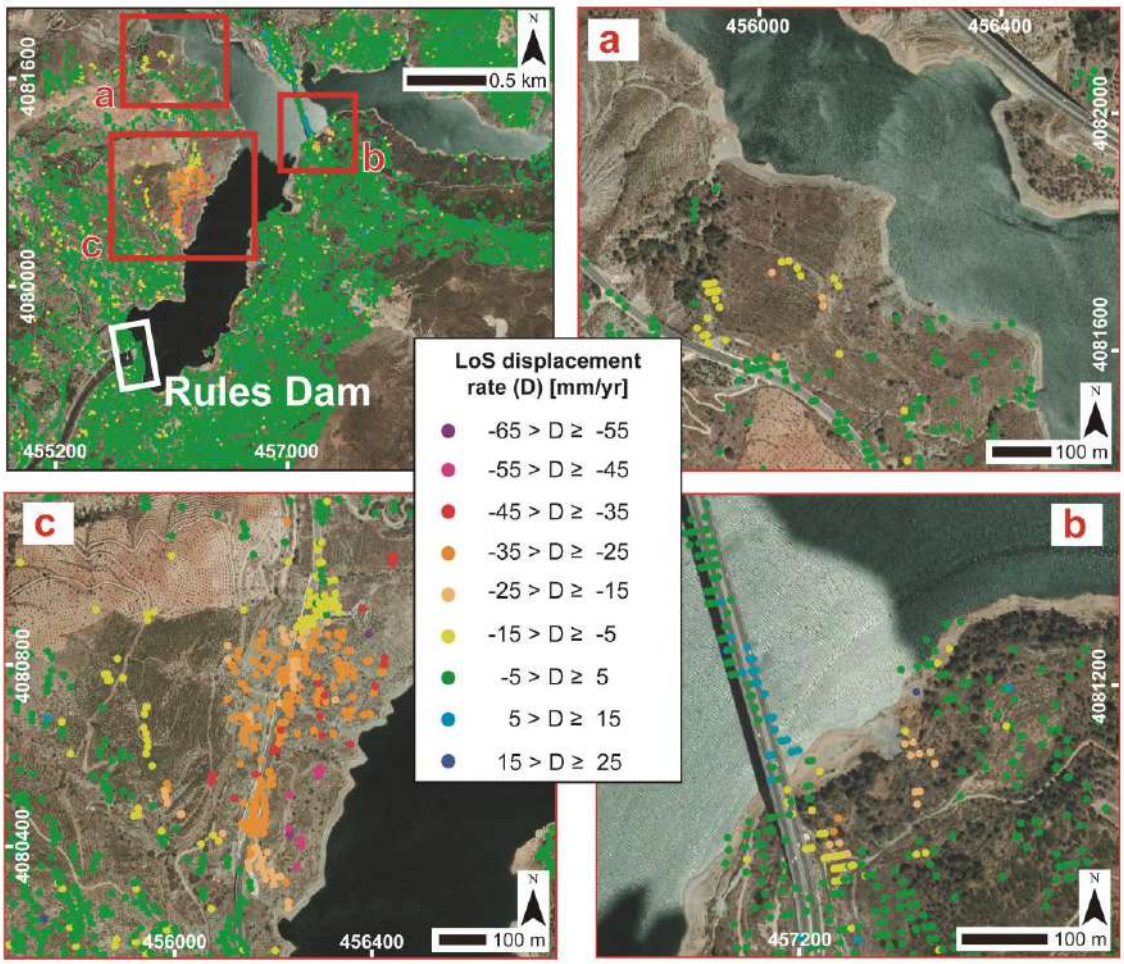

Figure 3. Surface velocity map of the Rules Reservoir area and detailed views from **(a)** the Cortijo de Lorenzo area, **(b)** the Rules Viaduct Landslide, and **(c)** the El Arrecife Landslide.

The non-stable points are concentrated mainly in three areas (Figure 3): (a) the Cortijo de Lorenzo area, along the Ízbor River branch of the reservoir, (b) the southern edge of the Rules Viaduct and (c) the El Arrecife area, along the western slope of the Rules Reservoir. The Cortijo de Lorenzo area generally presents evidence of slope instability, mainly linked to a landslide that we named as Lorenzo-1 Landslide. Velocity rates reach 20 mm/year as maximum (Figure 3a). In the southern slope of the Rules Viaduct, we detected velocities in the range of -5.5 to -24 mm/year (Figure 3b), with -15 mm/year as the mean velocity. Most of the points are settled close to the viaduct itself, while another set of points are settled 150 m away to the northeast of the viaduct (Figure 3b), located within a landslide that was inventoried by Fernández et al. (1997) and Chacón et al. (2007). We named this landslide as 'Rules Viaduct Landslide'. Lastly, in the El Arrecife area, we obtained velocities ranging from -10 to -60 mm/year and the mean velocity was -25 mm/year. Most of the points are distributed along the N-323 National Road and the lowest part of the same slope (Figure 3c). The set of points with the highest velocities (around -50 and -55 mm/year) corresponded to a small-sized landslide, also inventoried by Fernández et al. (1997) and Chacón et al. (2007). The instability of this area was also pointed out by Lackezy et al. (2016), but the spatial pattern of the velocities obtained by these authors prevents a detailed delimitation of the sliding mass. Our surface velocity

map gave us a better insight into the landslide boundaries that we named as 'El Arrecife Landslide'. Additionally, we could observe that the southern lateral limit of this landslide shows an abrupt change in terms of velocity values, while the northern limit shows a gradual velocity evolution (Figure 3c).

From our DInSAR data, we also found out that the Rules Dam and the slopes on which the structure rests showed no displacement (Figure 3). Within both slopes, Fernández et al. (1997) firstly mapped two large landslides that we named as 'Ventura Landslide', a Deep-Seated Gravitational Slope Deformation (DGSD), and 'Los Hoyos Landslide', a Rock Slope Failure (RSF) of lateral spread type (Figure 4). Moreover, other critical infrastructure in the study area seems to be affected by a slight deformation also detected through our DInSAR analysis. Along the southern edge of the Rules Viaduct, we obtained a set of points showing positive values of displacement rates between 7 and 10 mm/year (Figure 3b), which indicates a slight displacement of this viaduct segment.

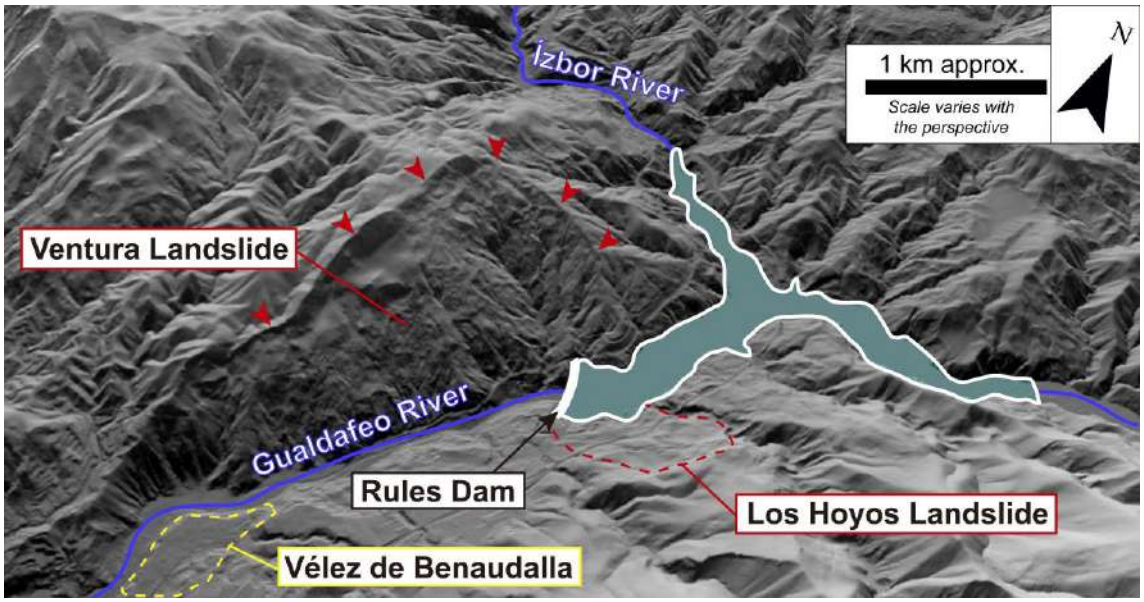

Figure 4. Oblique northwestward view of a hillshade model of the Rules Reservoir area. Red triangles point out to the main scarp of the Ventura Landslide, its most clear geomorphic feature. Note the dimensions of the Los Hoyos Landslide and Ventura Landslide at both sides of the Rules Dam. The village of Vélez de Benaudalla is also indicated downstream the reservoir.

4.2. Geomorphological study

We present an inventory of the main landslides in the Rules Reservoir area by classifying the mapped landslides into three categories (Figure 5): (1) landslides already inventoried by Fernández et al. (1997) and Chacón et al. (2007); (2) new landslides detected and delimited by using DInSAR velocity maps; and (3) landslides that were inventoried by Fernández et al. (1997) and Chacón et al. (2007), and also evidenced by our DInSAR results.

According to the first category, we included those landslides that were considered in the Fernández et al. (1997) landslide inventory and are clearly recognisable in the landscape at present time. We inventoried 12 landslides of different dimensions, two of which we

consider to be of particular relevance: 'Ventura Landslide' and 'Los Hoyos Landslide', due to its direct relationship to the Rules Dam (Figures 4, 5). As mentioned above, we did not detected displacement within both landslides. The second category includes the 'El Arrecife Landslide' (Figure 5) that we delimited in terms of the non-stable DInSAR points distribution. This landslide was not easily identifiable in the landscape as it does not show a prominent head scarp or any other landslide-related morphology within the slope. The last category includes two landslides that were inventoried by Fernández et al. (1997) and Chacón et al. (2007) and also present evidences of activity by our DInSAR results. These landslides are the 'Rules Viaduct Landslide', located next to the southern edge of the Rules Viaduct, and the 'Lorenzo-1 Landslide', located in the Cortijo de Lorenzo area, along the Ízbor River branch of the Rules Reservoir (Figure 5). Further geomorphological characteristics of each area of study are described below.

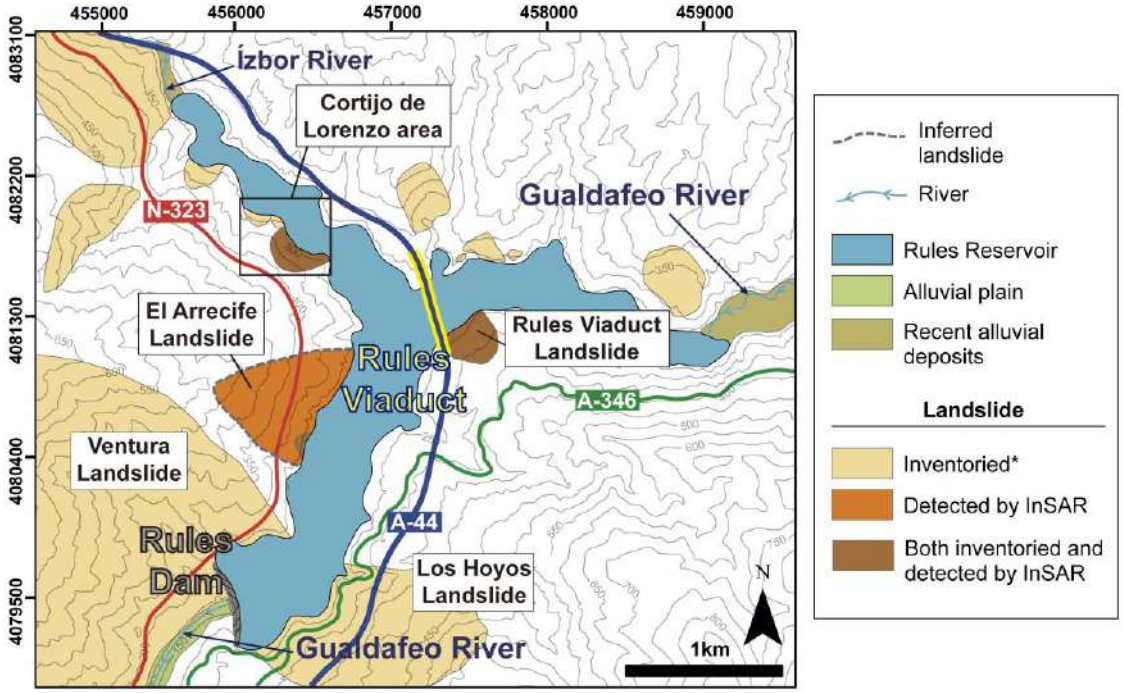

Figure 5. Landslide inventory of the most representative landslides of the Rules Reservoir area. *Landslides inventoried by Fernández et al. (1997) and Chacón et al. (2007).

4.2.1. Cortijo de Lorenzo area

The Cortijo de Lorenzo consists of an area of 0.6 km^2, located in the northwestern part of the Rules Reservoir (Figure 5) and corresponding to the Ízbor River branch of the reservoir. We mapped three landslides in this area (Figure 6): (1) Lorenzo-1 Landslide, which is the biggest one and clearly shows morphological features of a rotational landslide. It was already inventoried by Fernández et al. (1997) and Chacón et al. (2007) (Figure 5); (2) Lorenzo-2 Landslide, the smallest landslide; and (3) Lorenzo-3 Landslide, that is considerably older than the others (grey-coloured in Figure 6) as it is almost covered by vegetation and presents alluvial erosion features (Figure 7a). All of these landslides involve Alpujárride phyllites. At the present time, the reservoir water has covered a considerable part of these landslides, which is especially noticeable within Lorenzo-3 Landslide (Figure 6b).

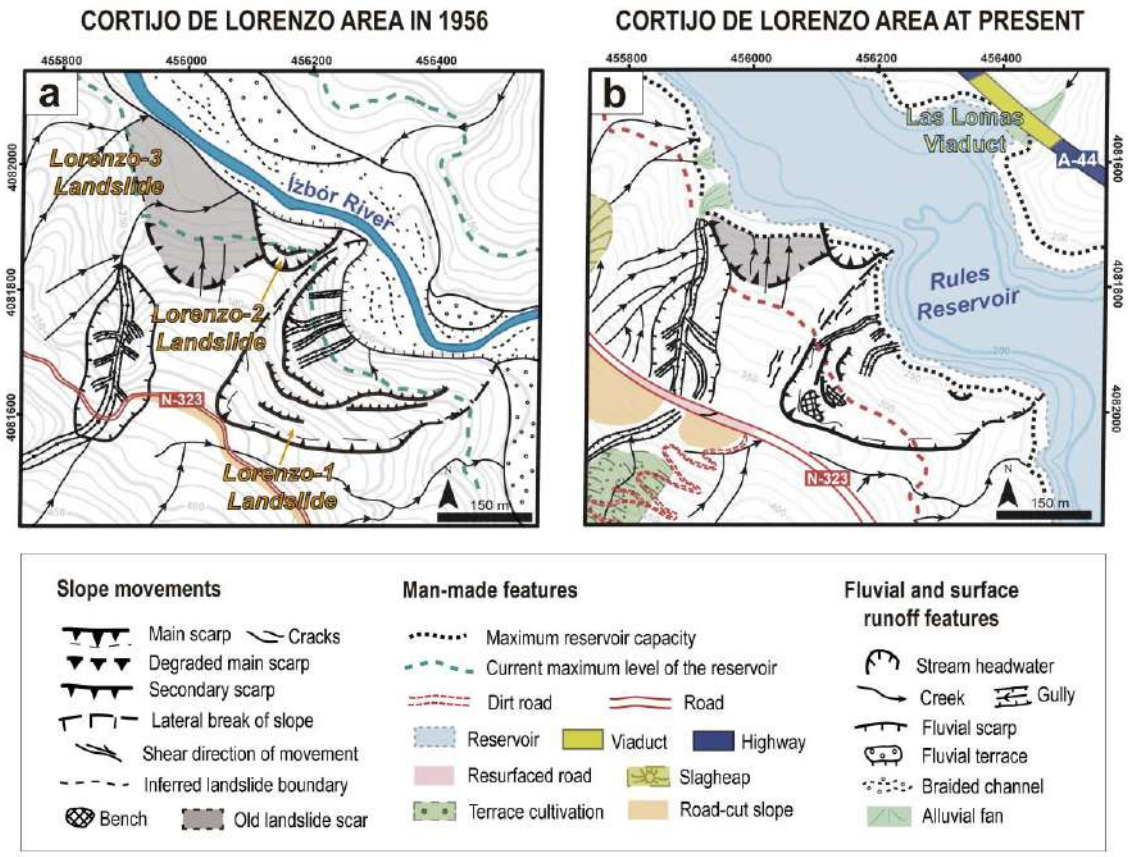

Figure 6. Geomorphological maps of the Cortijo de Lorenzo area **(a)** in 1956–1957, and **(b)** at present.

In the field, we observed several opened and fresh cracks within the landslide, what indicates its activity. We also found opened cracks and active piping away from the landslide perimeter (Figure 7b), that evidences a landslide retrogression towards the west of the slope. These field observations are corroborated by the moving points of our DInSAR velocity map (Figure 3a). The reconstruction and resettlement of the N-323 National Road has slightly modified the surface runoff dynamics along a well-incised creek (Figure 6). Part of this new trace has been recently resurfaced and it presents a large bump that crosses the road (Figure 7c), probably due to slope instability processes along the creek that have also been evidenced by our DInSAR results (Figure 3a).

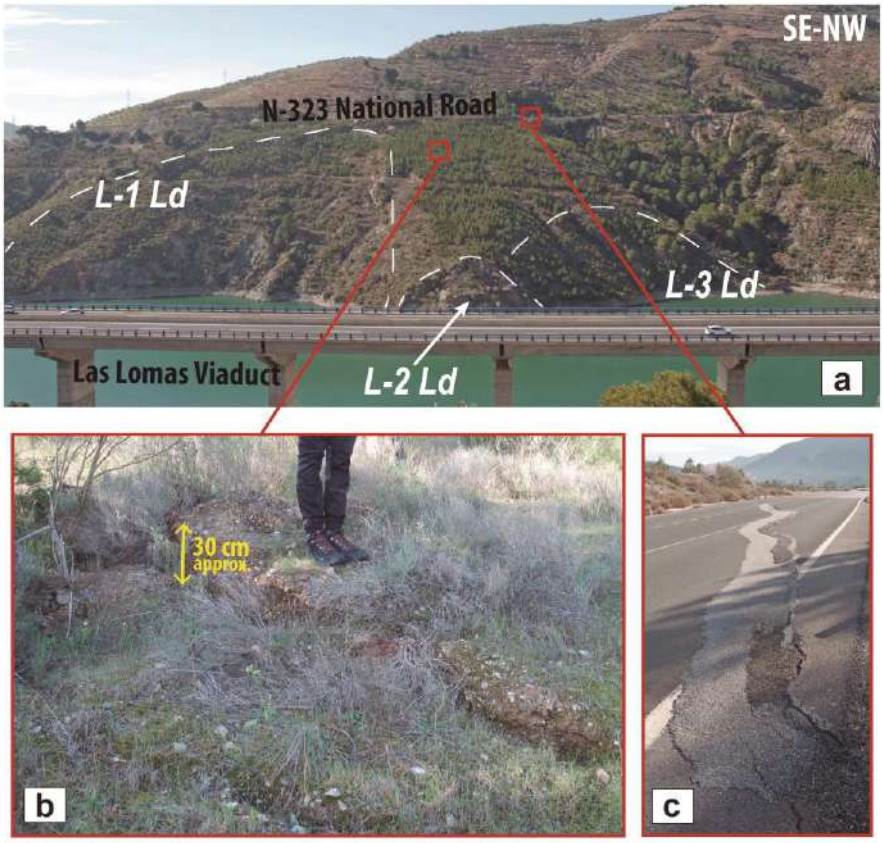

Figure 7. **(a)** Photograph of the Cortijo de Lorenzo area. The Lorenzo-1 Landslide, Lorenzo-2 Landslide and Lorenzo-3 Landslide are abbreviated as L-1 Ld, L-2 Ld and L-3 Ld, respectively. **(b)** Opened cracks next to the head scarp of the Lorenzo-1 Landslide. Notice the vertical slip of 30 cm, as maximum. **(c)** Bump across the N-323 National Road.

4.2.2. Rules Viaduct Landslide

Through the aerial photographs taken by the 1956-1957 American Flight, we were able to map several geomorphological features that had been highly modified or disappeared since the construction of the reservoir (Figure 8). The landslide had an area of 0.1 km^2 (345 m length and 330 m width) and a clear head scarp of amphitheatre shape (Figures 8, 9a). The slope morphology and the involved geomorphological features have led us to define this landslide as a retrogressive rotational type. This is evidenced by a system of secondary scarps and related benches, as well as by a big tilted block of marbles (Figure 8a). In such cases, the overlying Alpujárride marbles slide over the phyllites, as we could observe marbles in the main head scarp and also in some secondary scarps. We classified the western part of the landslide as a differentiated and active landslide, whose morphology is evidenced by separated head scarps, secondary scarps, benches and a well-defined lateral break in slope (Figure 8a). We confirmed its activity in the field, as we could observe a clear toe advance of this landslide, not observed within the presumed non-active sector (Figure 8b). Alluvial erosion and the formation of gullies also evidence no movement and stability in this part of the landslide. As previously mentioned, most of the original geomorphological features have been removed, modified or covered by man-made filling (Figure 8b). In this way, the landslide toe has been removed and covered by

the reservoir water, while the western sector (i.e., active landslide) has been replaced by an embankment for the Rules Viaduct, where one of the viaduct piers is located (Figure 8b). Almost the entire remaining landslide has been infilled with materials coming from the construction works. As a consequence, most of the secondary scarps and benches have disappeared. Part of the active landslide and the main scarps are still visible, but secondary scarps and benches have been removed or covered. We found active piping and opened, fresh cracks within the infilling material (Figures 9b, c), especially near the head scarp of the active landslide, which evidences its activity. Cracks are also found away from the landslide perimeter, also covered by infilling materials, and next to the A-44 Highway southern abutment (Figure 9b).

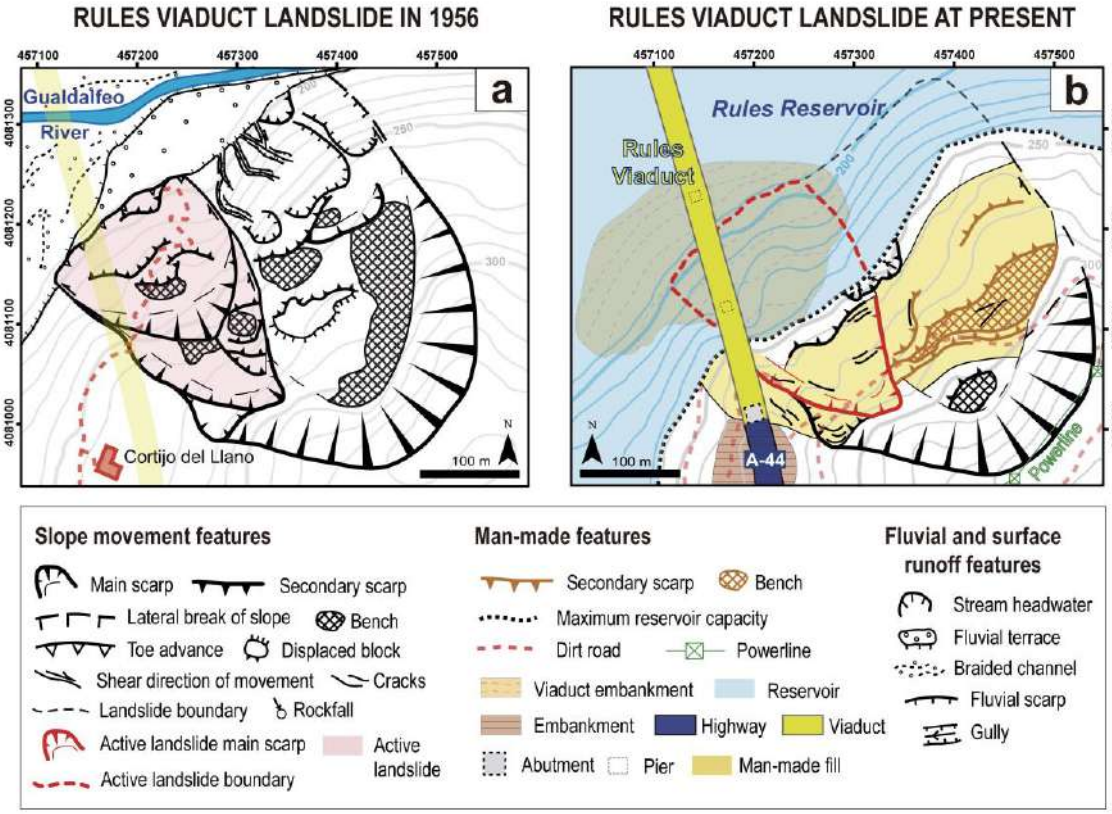

Figure 8. Geomorphological maps of the Rules Viaduct Landslide **(a)** in 1956-1957, and **(b)** at present.

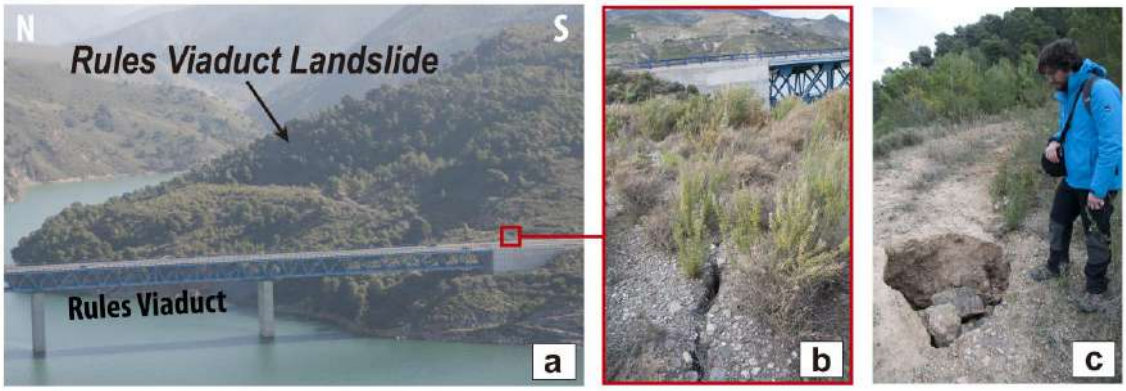

Figure 9. **(a)** Photograph of the Rules Viaduct Landslide. **(b)** Opened cracks near the southern abutment of the Rules Viaduct. **(c)** Sinkhole within the anthropic filling.

4.2.3. El Arrecife Landslide

The El Arrecife Landslide (Figures 10, 11a) had an area of 0.7 km^2, 880 m length and 750 m width. This landslide involves Alpujárride phyllites and it looks like a translational landslide due to its roughly planar slope and the absence of a well-marked head scarp (Figure 11a). In the 1956-1957 aerial photographs, the landslide shows a non-prominent head scarp and almost no secondary scarp or lateral break of slope (Figure 10a). At the landslide foot, we could recognise a small landslide, inventoried by Fernández et al. (1997) and Chacón et al. (2007). The slope, crossed by the N-323 National Road, was characterised by several incised gullies (Figure 10a) that indicate an a priori inactivity regarding gravitational processes. At present, the most remarkable features in the slope are the human modifications (Figure 10b). The main one is the road-cut slope built for a new trace of the N-323 road that was reconstructed 80 m downslope (Figure 10b). Part of the old N-323 is still visible in ruins, where we found numerous large opened cracks and pieces of pavement that have been sliced downhill (Figure 11b). The current road has been restored and resurfaced several times, probably due to the slope instability processes, which are also evidenced by recent oblique cracks, bumps (Figure 11c) and the ondulating or wavy surface of the road (Figure 11d). The surface of a slag heap that was built to accumulate some of the residual material coming from the reservoir construction works was also paved to create a viewpoint (Figure 10b), but it has been quickly cracked due to the material compaction and progressive sliding. Other man-made features of the area at present are the construction of several field tracks and a powerline network.

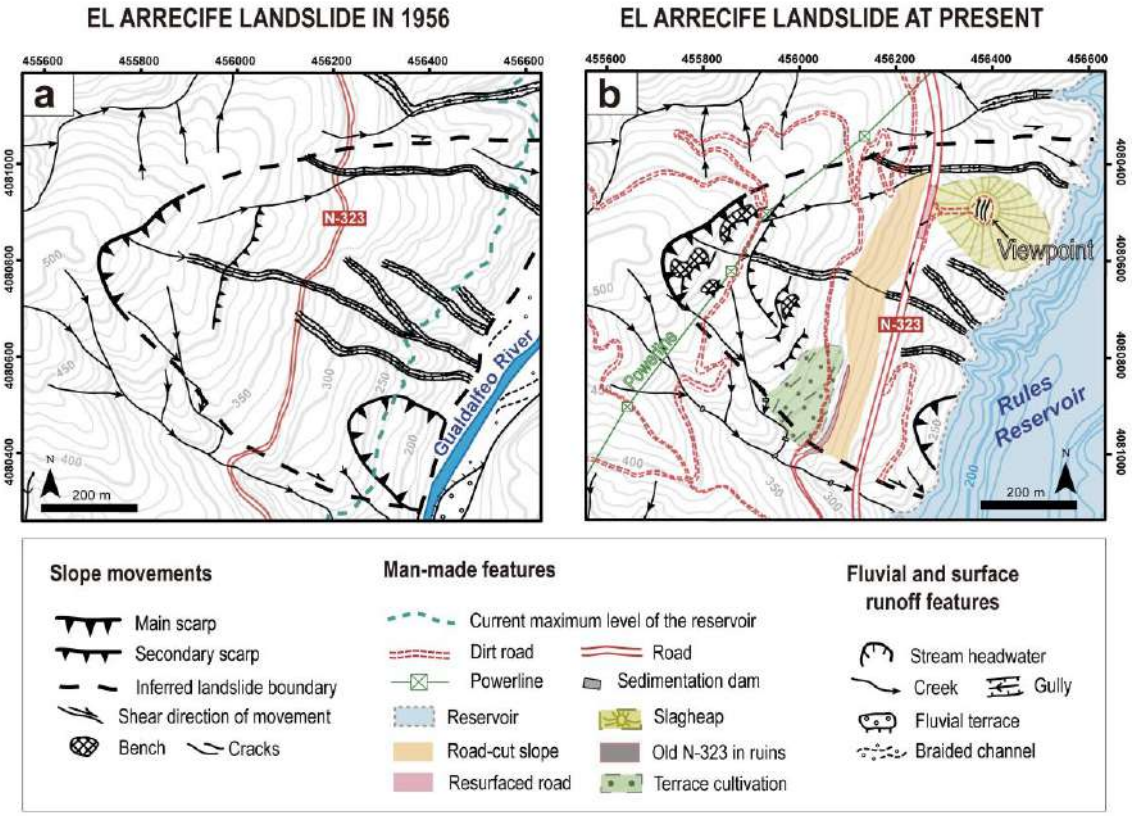

Figure 10. Geomorphological maps of the El Arrecife Landslide area **(a)** in 1956-1957, and **(b)** at present.

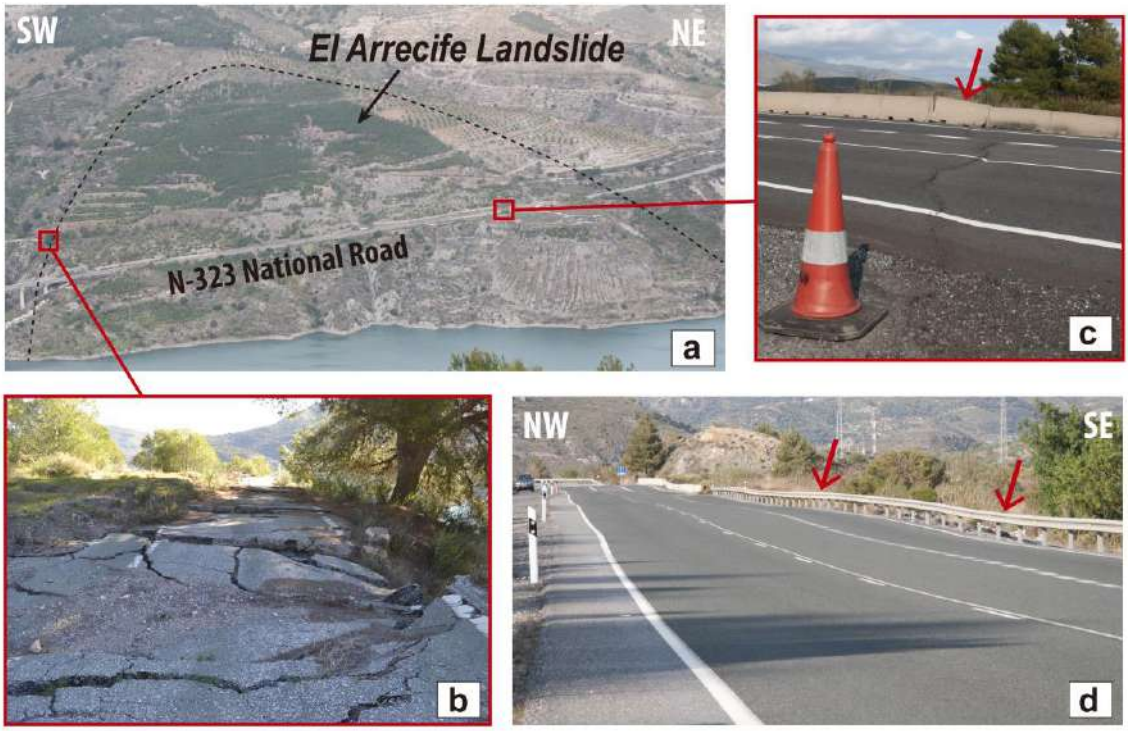

Figure 11. **(a)** Photograph of the El Arrecife Landslide. **(b)** Old N-323 National Road in ruins showing opened cracks and partial collapse of the pavement. **(c)** Bump of the N-323 National Road. **(d)** Photograph of the N-323 National Road. Notice the 'waving' of the crash barrier and the road itself.

4.3. Displacement time series of the unstable areas in the Rules Reservoir

The analysed time series of displacement (TS) are represented by the average accumulated displacement of unstable points within our areas of interest, described in Section 4.1. The El Arrecife Landslide time series shows a general linear trend (Figure 12a), while both the Rules Viaduct Landslide and Lorenzo-1 Landslide average displacement show a well-marked stepped trend (Figure 12b). The most remarkable fact that we observed was the correlation between the Rules Viaduct and the Lorenzo-1 landslides' TS, with variations in the water level of the reservoir. We identified three considerable drops of the water level that coincide with three periods of acceleration of the movement, that are evidenced by a change in the slope of the average accumulated displacement rate (Figure 12b). The first and the second periods of acceleration corresponds to autumn 2015 and summer–autumn 2016, respectively, while the third and the longest period of acceleration occurs from summer 2017 to winter 2018 (Figure 12b). On the contrary, displacement is not accelerated when water level increases, which depends directly on the amount of rainfall. The El Arrecife Landslide TS shows a slight acceleration period during autumn 2015, also correlated with a decrease in the water level reservoir (Figure 12a).

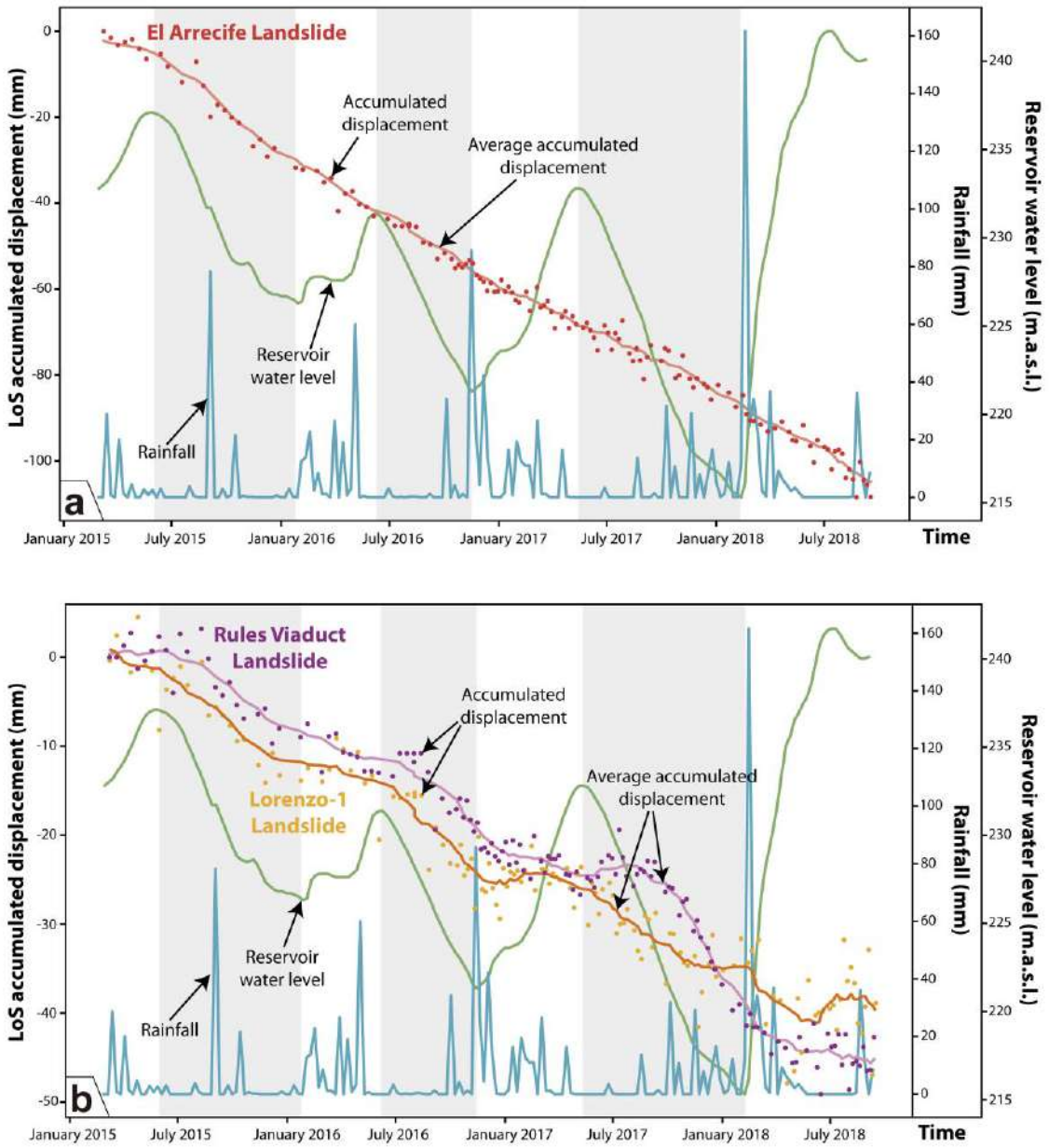

Figure 12. Time series in the Line-of-Sight (LoS) of accumulated displacement of the **(a)** El Arrecife Landslide and **(b)** both the Rules Viaduct and Lorenzo-1 landslides. 7 days cumulative rainfall and water level of the Rules Reservoir are also represented. Grey columns indicate periods of reservoir water level drawdown.

Regarding the unstable points along the Rules Viaduct, the time series shows periods of displacement coinciding with drawdowns in the water level reservoir (Figure 13). Thus, we identified three acceleration pulses during the springs of 2015, 2016 and 2017 (Figure 13).

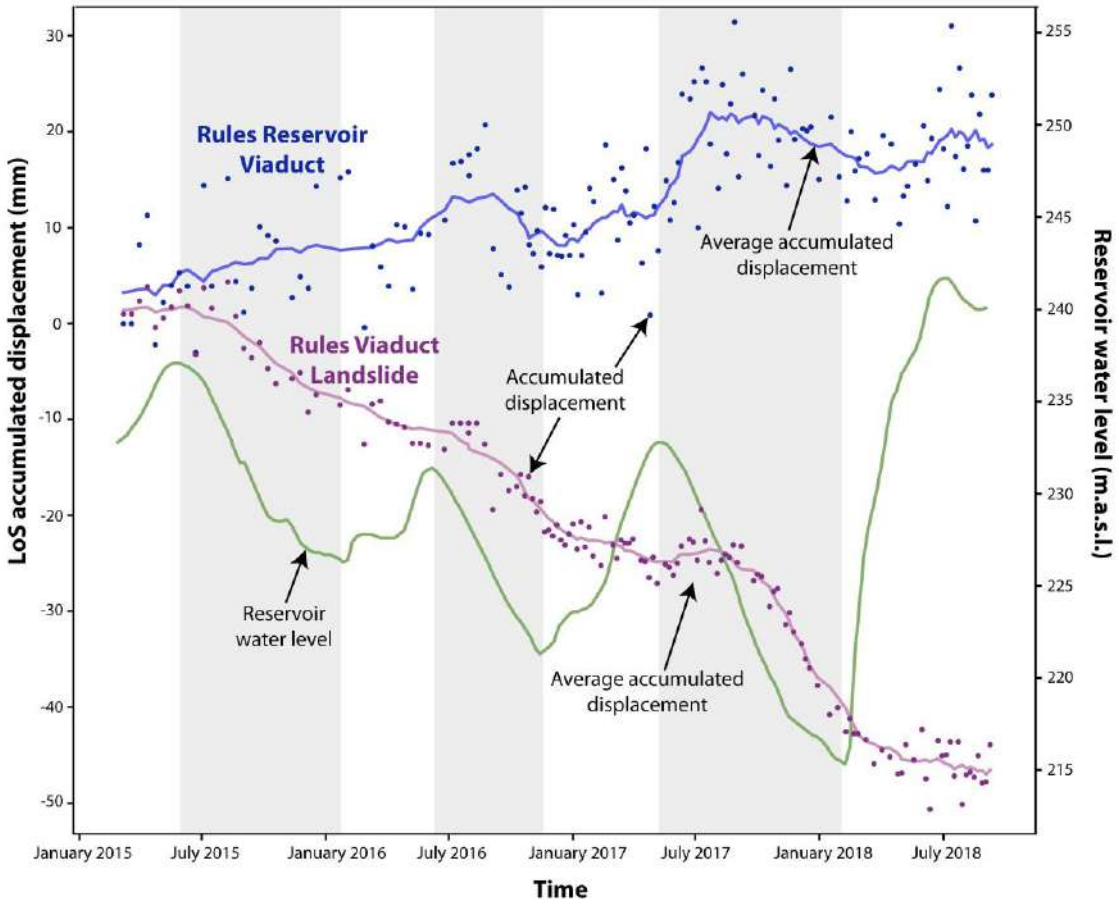

Figure 13. Time series in Line-of-Sight (LoS) of accumulated displacement of the Rules Viaduct Landslide and the Rules Viaduct. Water level of the Rules Reservoir is also represented. Grey columns indicate periods of reservoir water level drawdown. Note the noise of the Rules Viaduct TS in comparison with the Rules Viaduct Landslide TS.

5. Discussion

5.1. DInSAR as a monitoring system for the Rules Dam

Interferometry techniques have a huge potential to monitor and analyse the health of dams, as demonstrated by worldwide examples: Arjona et al. (2010); Wang et al. (2011); Di Martire et al. (2014); Milillo et al. (2016). For the case study of the Rules Reservoir, we did not register any displacement along the Rules Dam (Figure 3). Likewise, no points of movement have been obtained within the Ventura and Los Hoyos landslides, where the dam abutments are located (Figures 3, 4). Due to the magnitude of these landslides, we consider that other monitoring techniques should be applied to check the existence of ground displacement, and thus the activity of these landslides. This is necessary as the progressive movement of a sliding mass could generate a lateral pressure to the dam and cause structural damage. Therefore, detecting any slight displacement would be crucial to: (1) guarantee the security and stability of the dam; (2) reduce maintenance costs by optimising control strategies (Sousa et al. 2014); and (3) prevent failure or collapse of the dam, which would cause significant human, material and economic losses (e.g. a downstream flood would affect the village of Vélez de Benaudalla).

5.2. Triggering factors of the slope instabilities in the Rules Reservoir

In the case of both the Lorenzo-1 and Rules Viaduct landslides, there is a clear anthropic influence favouring the acceleration of the movements (i.e. anthropic triggering factor): the changes in the water level of the reservoir. As shown in Figure 12b, the three periods of acceleration in both landslides are related to periods of drawdown of the water level, while periods of no variation or increase in the water level result in stabilisation. Such a correlation has also been documented in multiple reservoirs slides as a result of either filling or drawdown of the reservoir (e.g. Jones et al. 1961; Rybář 1977; Novosad et al. 1979; Lopez-Marinas et al. 1997; Spanilá et al. 2002; Wang et al. 2004; Qi et al. 2006; Gutiérrez et al. 2010). In contrast, the sudden drawdown of a reservoir can threaten stability as a result of removing the lateral confining pressure (water) of the reservoir slopes, and the mass of soil still has a reduced shear strength (Schuster 1979). In the case of the Grand Coulee Reservoir in the USA (Jones et al. 1961), at least 150 landslides were documented, due to periods of water level drawdown. As another example, in the Three Georges Reservoir area, Liao et al. (2005) concluded that reservoir drawdowns and the descending velocity of the drawdown become major factors that affect the stability of landslides. We also regarded the inverse relationship between rainfall and acceleration of movement within the above-mentioned landslides as interesting. Rainfall usually reduces the effective shear strength of failure surfaces (Macfarlane 2009), and thus increases the potential of sliding. This fact has been evidenced by several authors (Záruba et al. 1966; De Vita et al. 1998; Polemio and Petrucci 2000; Rybář et al. 2002) that link the reactivation, acceleration or higher occurrence of landslide activity to heavy rainy periods. Contrary to this literature, both the Rules Viaduct and Lorenzo-1 landslides show a deceleration in movement related to rainfall peaks (Figure 12b). As rainfall conducts the reservoir filling, lateral confining pressure increases (as a result of a water level increase) and thus, landslide displacement decreases, what leads to a relative stabilisation of the slopes. These examples show how water level variation has a stronger influence on landslide displacement patterns than rainfall. Moreover, this paper represents the first clear detection of this behaviour using DInSAR techniques. The high temporal resolution of the Sentinel-1 images has made this possible.

5.3. Characterisation of slope stabilities and potential hazards in the Rules Reservoir

The abundance of landslides in the Rules Reservoir area was the object of detailed landslide inventories in recent years (Fernández et al. 1997; Chacón et al. 2007). In this regard, slope instability has become an important problem to deal with during the reservoir planning, design, construction, maintenance and management phases. DInSAR allowed us to determine the activity of some well-known landslides, as well as to identify, delimit and map new landslides that are not easy recognisable in the landscape. The three areas of interest of our research are affected by different kind of landslides with respect to their kinematic or size, which also lead to different problems in relation to the reservoir. In this way, DInSAR analysis together with a detailed geomorphological investigation allowed us to characterise and understand the evolution of the landslides, and thus to assess their potential hazard to the Rules Reservoir.

The observed patters in the TS of the three areas of interest, together with our morphological observations, suggest that there are two different typologies of landslides. The Rules Viaduct and Lorenzo-1 landslides show movements correlated with the variation of the reservoir water level that stops and begins again with episodes of progressive acceleration and abrupt deceleration (Figure 12b). This pattern is related to a rotational typology as, according to Turner and Schuster (1996), movement in rotational slides may stop in part after a substantial displacement. On the contrary, the El Arrecife Landslide shows an almost continuous movement with little fluctuation (Figure 12a). Whereas a rotational landslide tends to restore the displaced mass to equilibrium, a translational slide may continue unchecked if the surface of separation is sufficiently inclined (Turner and Schuster 1996). Such a continuous pattern is well-illustrated in the El Arrecife Landslide time series (Figure 12a), and thus we could confirm that it is a translational landslide.

According to the above arguments, the Lorenzo-1 and the Rules Viaduct landslides, due to their dimensions and rotational character, do not represent a significant hazard for the reservoir shorelines or the dam. An extremely rapid acceleration of these landslides and their sudden collapse into the reservoir may be possible, but is unlikely, due to their characteristics and observed behaviour, if reservoir water level management is done properly. However, the main risk associated to these landslides is their retrogressive evolution, that could potentially affect the southern abutment and piers of the Rules Viaduct (in the case of the Rules Viaduct Landslide) or the N-323 National Road (in the case of the Lorenzo-1 Landslide) in the future. Therefore, it must be a priority to keep monitoring the evolution of these landslides as well as to analyse the deformation detected along the southern sector of the Rules Viaduct (Figure 13). If the displacements are validated using other geodetic techniques, any required reinforcement works should be carried out far enough in advance to avoid severe damage to the viaduct (as happened in the last decade) in order to reduce repair costs. The origin of this deformation is still unknown, but we have hypothesised different scenarios to explain it: (1) horizontal flexural deformation due to the activity of the Rules Viaduct Landside (see Salcedo 2009 as an example). Notice the slight correlation between periods of acceleration of the viaduct and the landslide (Figure 12); or (2) thermal dilation of the viaduct (see Monserrat et al. 2011 as an example). The correlation between periods of acceleration of the viaduct (i.e. uplifting) with summer and the hottest months would supports this theory (Figure 13). In any case, our DInSAR data seems to indicate that the southern pier could be affected by a certain kind of instability that must be further investigated and monitored.

The most important result from this study is the delimitation of the El Arrecife Landslide. It has been first mapped in its entire dimensions using our DInSAR velocity map. No one mapped a landslide covering all this hillside, although several landslide inventories were made in this area. At first sight, we did not recognise any morphology or feature as an indicator to delimitate a landslide, but the distribution of the velocity points gave us a different perspective. According to the dimensions and the temporal pattern of the movement, we consider that the potential hazard of the El Arrecife Landslide is high. To date, the landslide movement shows a stationary situation with a constant, very slow,

velocity that suggests a ductile deformation of the slope (Petley et al. 2002), and the changes in the reservoir water level do not appear to influence the landslide's behaviour. However, we must not forget that the translational character of this landslide makes it possible that the sliding mass is capable of experiencing a rapid acceleration that would lead to a catastrophic slope failure. Consequently, the slide mass would collapse into the reservoir and then generate an impulse wave, as happened in Vajont (Kiersch 1964) and other events documented in Norway (Harbitz 1992) and Alaska (Fritz et al. 2001). The N-323 National Road and the power lines would be also destroyed by this catastrophic event, which would have significant implications (i.e. road accessibility and power cuts) for the nearby populations. Thus, the El Arrecife Landslide study and monitoring must be continued in order to recognise any possible pre-failure precursor (i.e. critical accelerations), as recent studies have demonstrated the effectiveness of DInSAR for such aim (see Solari et al. 2018; Dong et al. 2018; Intrieri et al. 2018 as examples).

6. Conclusions

The application of DInSAR techniques in a reservoir context makes it possible to successfully detect and monitor possible slope instabilities in such a critical infrastructure. In the case of the Rules Reservoir, the DInSAR surface velocity maps allowed us: (1) to check the stability of the Rules Dam and the potential unstable slopes where this structure rests; (2) to contribute to the delimitation of three active landslides (Lorenzo-1, Rules Viaduct and El Arrecife landslides); and (3) to monitor the activity of these landslides. The integration of DInSAR data with classical geomorphological research (i.e. field survey and mapping) helped in the definition and understanding of the kinematics and evolution of the landslides, as well as establishing their triggering factors. Thus, we distinguished that the Lorenzo-1 and Rules Viaduct landslides are of the rotational type, while the El Arrecife has a translational character. Moreover, we observed a retrogressive evolution of the rotational landslides that represents a hazard for both the N-323 National Road and the Rules Viaduct. The displacement time series (TSs) acquired through the DInSAR analysis shows that the behaviour of the Lorenzo-1 and Rules Viaduct landslides is correlated to the continuous changes in the reservoir water level (i.e. drawdowns and infillings). On the contrary, the time series obtained in the El Arrecife Landslide indicated that it was not affected by water level changes. We also detected slight displacements in the Rules Viaduct of the A-44 Highway that crosses a branch of the Rules Reservoir. These displacements may have different explanations, but the fact is that the viaduct appears to be suffering a small deformation most probably related to the adjacent landslide.

Understanding all this information was crucial to the preliminary assessment of the potential hazards of the unstable slopes in the Rules Reservoir, regarding the different problematics and implications in relation to the safety of the reservoir itself and other infrastructures related to it. Thus, this research points out that Lorenzo-1 and Rules Viaduct landslides imply a hazardous situation for the structural integrity of the N-323 and the Rules Viaduct, respectively. On the other hand, El Arrecife Landslide represents a high potential hazard of sudden slope failure. Nevertheless, to date, there is not enough

evidence to create social alarm about this topic. In this sense, DInSAR combined with other monitoring techniques must be continuously applied to detect any pre-failure precursor and any critical deformation along the Rules Viaduct to avoid irreversible damage and also to contribute to the suitable management of the reservoir.

Acknowledges and funding

A Spanish 'Sistema de Garantía Juvenil' research contract, founded by the Junta de Andalucía and the European Social Funds, supported the work of Cristina Reyes-Carmona. Spanish 'Ramón y Cajal' grant supported part of the work of Jorge Pedro Galve. This work has been partially funded by the Spanish Ministry of Economy and Competitiveness through the DEMOS project 'Deformation monitoring using Sentinel-1 data' (Ref: CGL2017-83704-P) and the LITHOSURF project 'Respuesta de la topografía y la red de drenaje a procesos litosféricos y climáticos en el sur de Iberia' (Ref: CGL2015-67130-C2-1-R). This work has been partially developed in the framework of the RISKCOAST project (Ref: SOE3/P4/E0868) funded by the Interreg SUDOE program (3rd call for proposals). Finally, we thank the editors and four anonymous reviewers for helpful comments and suggestions that improved the manuscript.

References

Aldaya F, Díaz de Federico A, García-Dueñas V, Martínez-García E, Navarro- Vilá F, Puga E (1979) Lanjarón-Geological Map of Spain 1:50000. Geological Survey of Spain, Madrid

Arjona A, Santoyo MA, Fernández J, Monells D, Prieto JF, Pallero JLG, Prieto E, Seco A, Luzón F, Mallorquí J (2010) On the Applicability of an Advanced DInSAR Techniques near Itoiz and Yesa Reservoirs, Navarra, Spain. Proceedings of the FRINGE 2009, Frascaty, Italy, pp 2-7

Barra A, Monserrat O, Mazzanti P, Esposito C, Crosetto M, Scarascia-Mugnozza G (2016) First insights on the potential of Sentinel-1 for landslides detection. Geomatics, Nat Hazards Risk 7: 1874-1883. https://doi.org/10.1080/19475705.2016.1171258

Barra A, Solari L, Béjar-Pizarro M, Monserrat O, Bianchini S, Herrera G, Crosetto M, Sarro R, González-Alonso E, Mateos RM, Ligüerzana S, López C, Moretti S (2017) A methodology to detect and update active deformation areas based on Sentinel-1 SAR images. Remote Sens 9: 1002. https://doi.org/10.3390/rs9101002

Bergillos RJ, Ortega-Sánchez M (2017) Assessing and mitigating the landscape effects of river damming on the Guadalfeo River delta, southern Spain. Landsc Urban Plan 165: 117-129. https://doi.org/10.1016/j.landurbplan.2017.05.002

Biescas E, Crosetto M, Agudo M, Monserrat O, Crippa B (2007) Two radar interferometric approaches to monitor slow and fast land deformation. J Surv Eng 133: 66-71. https://doi.org/10.1061/(ASCE)0733-9453(2007)133:2(66)

Bozzano F, Cipriani I, Mazzanti P, Prestininzi A (2011) Displacement patterns of a landslide affected by human activities: Insights from ground-based InSAR monitoring. Nat Hazards 59: 1377-1396. https://doi.org/10.1007/s11069-011-9840-6

Brunner F, Zobl F, Gassner G (2003) On the Capability of GPS for Landslide Monitoring. Felsbau 21: 51-54

Catani F, Casagli N, Ermini L, Righini G, Menduni G (2005) Landslide hazard and risk mapping at catchment scale in the Arno River basin. Landslides 2: 329-342. https://doi.org/10.1007/s10346-005-0021-0

Chacón J, Irigaray T, Fernández T (2007) Los movimientos de ladera de la provincia de Granada. In: Ferrer M (ed) Atlas Riesgos Naturales en la Provincia de Granada, 1st edn. Diputación de Granada-Geological Survey of Spain, Madrid, pp 45–82

Ciampalini A, Raspini F, Bianchini S, Frodella W, Bardi F, Lagomarsino D, Di Traglia F, Moretti S, Proietti C, Pagliara P, Onori R, Corazza A, Duro A, Basile G, Casagli N (2015) Remote sensing as tool for development of landslide databases: The case of the Messina Province (Italy) geodatabase. Geomorphology 249: 103-118. https://doi.org/10.1016/j.geomorph.2015.01.029

Cigna F, Bianchini S, Casagli N (2013) How to assess landslide activity and intensity with Persistent Scatterer Interferometry (PSI): The PSI-based matrix approach. Landslides 10: 267-283. https://doi.org/10.1007/s10346-012-0335-7

Cignetti M, Manconi A, Manunta M, Giordan D, De Luca C, Allasia P, Ardizzone F (2016) Taking advantage of the ESA G-POD service to study ground deformation processes in high mountain areas: a Valle d'Aosta case study, Northern Italy. Remote Sens 8: 852. https://doi.org/10.3390/rs8100852

Crosetto M, Devanthéry N, Cuevas-González M, Monserrat O, Barra A, Crippa B (2016) Deformation monitoring using Sentinel-1 SAR imagery. Proceedings of the Living Planet Symposium, Milan, Italy, pp 296

Crosetto M, Monserrat O, Cuevas M, Crippa B (2011) Spaceborne differential SAR interferometry: Data analysis tools for deformation measurement. Remote Sens 3: 305-318. https://doi.org/10.3390/rs3020305

De Vita P, Reichenbach P, Bathurst JC, Borga M, Crozier GM, Glade T, Guzzetti F, Hansen A, Wasowski J (1998) Rainfall-triggered landslides: A reference list. Environ. Geol 35: 219-233.

Devanthéry N, Crosetto M, Monserrat O, Cuevas-González M, Crippa B (2014) An approach to persistent scatterer interferometry. Remote Sens 6: 6662-6679. https://doi.org/10.3390/rs6076662

Di Martire D, Iglesias R, Monells D, Centolanza G, Sica S, Ramondini M, Pagano L, Mallorquí JJ, Calcaterra D (2014) Comparison between Differential SAR interferometry and ground measurements data in the displacement monitoring of the earth-dam of Conza

della Campania (Italy). Remote Sens Environ 148: 58-69. https://doi.org/10.1016/j.rse.2014.03.014

Dong J, Zhang L, Li M, Yu Y, Liao M, Gong J, Luo H (2018) Measuring precursory movements of the recent Xinmo landslide in Mao County, China with Sentinel-1 and ALOS-2 PALSAR-2 datasets. Landslides 15: 135-144. https://doi.org/10.1007/s10346-017-0914-8

Fernández T, Brabb E, Delgado F Martin-Algarra A, Irigaray C, Estévez A, Chacón-Montero J (1997) Rasgos geológicos y movimientos de ladera en el sector Ízbor-Vélez Benaudalla de la cuenca del río Guadalfeo (Granada). Proceedings of the IV Simposio Nacional Sobre Taludes y Laderas Inestables, Granada, Spain, pp 795–808

Fernández-Motril R (2013a) La A-44 se Traga en Cuatro Años Más de 80 Millones en Parches. Newspaper Granada Hoy, Granada, Spain

Fernández-Motril R (2013b) Fomento Invertirá 19 Millones en Reparar un Nuevo Fallo en el Viaducto de Rules. Newspaper Granada Hoy, Granada, Spain

Fernández-Motril R (2013c) N-323: Una Carretera Abandonada Desde 2009. Newspaper Granada Hoy, Granada, Spain

Fernández-Motril R (2015) Fomento Terminará Las Obras del Viaducto de Rules Esta Semana. Newspaper Granada Hoy, Granada, Spain

Fritz HM, Hager WH, Minor HE (2001) Lituya bay case: Rockslide impact and wave run-up. Sci Tsunami Haz 1: 3-22

Galindo-Zaldívar J, Jabaloy J, Serrano I, Morales J, González-Lodeiro F, Torcal F (1999) Recent and present-day stresses in the Granada Basin (Betic Cordilleras): Example of a late Miocene-present-day extensional basin in a convergent plate boundary. Tectonics 18: 686-702. https://doi.org/10.1029/1999TC900016

Gutiérrez F, Lucha P, Galve JP (2010) Reconstructing the geochronological evolution of large landslides by means of the trenching technique in the Yesa Reservoir (Spanish Pyrenees). Geomorphology 124: 124-136. https://doi.org/10.1016/j.geomorph.2010.04.015

Harbitz CB Model simulations of tsunamis generated by the Storegga slides (1992) Mar Geol 105: 1-21. https://doi.org/10.1016/0025-3227(92)90178-K

Herrera G, Davalillo JC, Mulas J, Cooksley G, Monserrat O, Pancioli V (2009) Mapping and monitoring geomorphological processes in mountainous areas using PSI data: Central Pyrenees case study. Nat. Hazard Earth Syst Sci 9: 1587-1598. https://doi.org/10.5194/nhess-9-1587-2009

Irigaray C, Lamas F, El Hamdouni R, Fernández T, Chacón J (2000) The importance of the precipitation and the susceptibility of the slopes for the triggering of landslides along the roads. Nat. Hazards 21: 65–81. https://doi.org/10.1023/A:1008126113789

Intrieri E, Raspini F, Fumagalli A, Lu P, Del Conte S, Farina P, Allievi J, Ferretti A, Casagli N (2018) The Maoxian landslide as seen from space: detecting precursors of failure with Sentinel-1 data. Landslides 15: 123–133. https://doi.org/10.1007/s10346-017-0915-7

Jones FO, Embody DR, Peterson WL (1961) Landslides along the Columbia River valley, Northeastern Washington. Professional Paper 367, USA Geological Survey. https://doi.org/10.3133/pp367

Kiersch GA (1694) Vaiont Reservoir disaster. Civ Eng 34: 32-40

Kraus K (1997) Photogrammetry Volume 2 Advanced methods and applications. Dümmler Verlag, Bonn

Lane KS (1996) Stability of reservoir slopes in. Proceedings of the 8th Symposium of Rock Mechanics. Minneapolis, USA, pp 321-336

Lazecky M, Authority E, Nikolaeva E, Bakon M (2016) Potential of Sentinel-1A for Nation-Wide Routine Updates of Active Landslide Maps. Proceedings of the International Archives of the Photogrammetry, Remote Sensing and Spatial Information Sciences (ISPRS), Prague, Czech Republic, pp 775-781

Liao HJ, Sheng Q, Gao SH, Xu ZP (2005) Influence of drawdown of reservoir water level on landslide stability. Chin J Rock Mech Eng 24: 3454-3458

Lopez-Marinas JM, Gazta aga JM, Cajete J (1997) Landslides in the Cortes reservoir during initial filling. Proceedings of the Transactions of the 19th International Congress on Large Dams, Florence, Italy, pp 537-550

Macfarlane DF (2009) Observations and predictions of the behaviour of large, slow-moving landslides in schist, Clyde Dam reservoir, New Zealand. Eng Geol 109: 5-15. https://doi.org/10.1016/j.enggeo.2009.02.005

Martínez-Martínez JM, Soto JI, Balanyá JC (2002) Orthogonal folding of extensional detachments: structure and origin of the Sierra Nevada Elongated Dome (Betics, SE Spain). Tectonics 21: 1-3. https://doi.org/10.1029/2001TC001283

Massonnet D, Feigl KL (1998) Radar interferometry and its application to changes in the earth's surface. Rev Geophys 36: 441-500. https://doi.org/10.1029/97RG03139

Milillo P, Perissin D, Salzer JT, Lundgren P, Lacava G, Milillo G, Serio C (2016) Monitoring dam structural health from space: Insights from novel InSAR techniques and multi-parametric modeling applied to the Pertusillo dam Basilicata, Italy. Int J Appl Earth Obs Geoinf 52: 221-229. https://doi.org/10.1016/j.jag.2016.06.013

Millet RA, Lawton GM, Repetto PC, Garga VK (1992) Stabilization of Tablachaca Dam Landslide. Proceedings of the Stability and Perfomance of Slopes and Embakments II, Berkeley, USA, pp 1365-1381

Monserrat O, Crosetto M, Cuevas M, Crippa B (2011) The thermal expansion component of persistent scatterer interferometry observations. IEEE Geosci Remote Sens Lett 8: 864-868. https://doi.org/10.1109/LGRS.2011.2119463

Monserrat O, Crosetto M, Luzi G (2014) A review of ground-based SAR interferometry for deformation measurement. ISPRS J Photogramm Remote Sens 93: 40-48. https://doi.org/10.1016/j.isprsjprs.2014.04.001

Navarrete M (2009) El Ministro de Fomento Inaugura el Tramo de Autovía Más caro de España. Newspaper Ideal, Granada Spain

Novosad S, Barvinek R, de la Torre Sabrevilla M (1979) Estudio de estabilidad del Derrumbe No. 5 en el reservorio de Tablachaca de la Central Hidroelectrica del Mantaro. Proceedings of the VI Pan-American Soil Mechanics and Foundation Engineering Congress, Lima, Perú, pp 331-344

Pérez AN (2004) La presa de Rules. Revista de Obras Públicas: Órgano Profesional de los ingenieros De caminos, canales y puertos 3441: 131-152.

Petley DN, Bulmer MH, Murphy W (2002) Patterns of movement in rotational and translational landslides. Geology 30: 719-722. https://doi.org/10.1130/0091-7613(2002)030<0719:POMIRA>2.0.CO;2

Polemio O, Petrucci O (2000) Rainfall as a Landslide Triggering Factor: an overview of recent international research. Proceedings of the 8th International Symposium on Landslides, Cardiff, UK, pp 1219-1226

Qi S, Yan F, Wang S, Xu R (2006) Characteristics, mechanism and development tendency of deformation of Maoping landslide after commission of Geheyan reservoir on the Qingjiang River, Hubei Province, China. Eng Geol 86: 37-51. https://doi.org/10.1016/j.enggeo.2006.04.004

Rocca A, Mazzanti P, Bozzano F, Perissin D (2015) Advanced characterization of a landslide-prone area by satellite a-DInSAR. In: Lollino G, Manconi A, Guzzetti F, Culshaw M, Bobrowsky PT, Luino F (eds) Engineering Geology for Society and Territory. Springer, pp 177-181

Rucci A, Ferretti A, Monti Guarnieri A, Rocca F (2012) Sentinel 1 SAR interferometry applications: The outlook for sub millimeter measurements. Remote Sens Environ 120: 156-163. https://doi.org/10.1016/j.rse.2011.09.030

Rybář J (1977) Prediction of slope failures on water reservoir banks. Bull Int Assoc Eng Geol 16: 64-67. https://doi.org/10.1007/BF02591449

Rybář J Stemberk J, Wagner P (2002) Landslides: Proceedings of the First European Conference on Landslides. CRC Press

Salcedo DA (2009) Behavior of a landslide prior to inducing a viaduct failure, Caracas-La Guaira highway, Venezuela. Eng Geol 109: 16-30. https://doi.org/10.1016/j.enggeo.2009.02.001

Sanz de Galdeano C, García Tortosa FJ, Peláez Montilla JA, Alfaro García P, Azañón JM, Galindo-Zaldívar J, López-Casado C, López-Garrido AC, Rodríguez-Fernández J, Ruano P (2012) Main active faults in the Granada and Guadix-Baza Basins (Betic Cordillera). J Iber Geol 38: 209-223.

Schuster RL (1979) Reservoir-induced landslides. Bull Int Assoc Eng Geol 20: 8-15.

Simancas JF, Campos J (1993) Compresión NNW-SSE tardía postmetamórfica y extensión subordinada en el Complejo Alpujárride (Dominio de Alborán, Orógeno Bético). Rev Soc Geol España 6: 23-35

Simancas JF (2018) A reappraisal of the Alpine structure of the Alpu- járride Complex in the Betic Cordillera: interplay of shortening and extension in the westernmost Mediterranean. J Struct Geol 115:231-242. https://doi.org/10.1016/j.jsg.2018.08.001

Solari L, Raspini F, Del Soldato M, Bianchini S, Ciampalini A, Ferrigno F, Tucci S, Casagli N (2018) Satellite radar data for back-analyzing a landslide event: the Ponzano (Central Italy) case study. Landslides 15: 773-782. https://doi.org/10.1007/s10346-018-0952-x

Solari L, Bianchini S, Franceschini R, Barra A, Monserrat O, Thuegaz P, Bertolo D, Crosetto M, Catani F (2020) Satellite interferometric data for landslide intensity evaluation in mountainous regions. Int J Appl Earth Obs 87: 102028. https://doi.org/10.1016/j.jag.2019.102028

Sousa JJ, Hlaváčová I, Bakon M, Lazecký M, Patrício G, Guimarães P, Ruiz AM, Bastos L, Sousa A, Bento R (2014) Potential of Multi-temporal InSAR Techniques for Bridges and Dams Monitoring. Procedia Technol 16: 834-841. https://doi.org/10.1016/j.protcy.2014.10.033

Spanilá T, Horsky O, Banach M (2002) Slides and sliding in the water reservoirs banks. Landslides: Proceedings of the First European Conference on Landslides. CRC Press, pp 315

Tang P, Chen F, Guo H, Tian B, Wang X, Ishwaran N (2015) Large-area landslides monitoring using advanced multi-temporal InSAR technique over the giant panda habitat, Sichuan, China. Remote Sens 7: 8925-8949. https://doi.org/10.3390/rs70708925

Teza G, Galgaro A, Zaltron N, Genevois R (2007) Terrestrial laser scanner to detect landslide displacement fields: A new approach. Int J Remote Sens 28: 3425-3446. https://doi.org/10.1080/01431160601024234

Turner AK, Schuster RL (1996) Landslides: Investigation and Mitigation. Transportation Research Board, National Academy of Sciences

Vera J, Martín-Algarra A (2004) Cordillera Bética y Baleares. Divisiones mayores y nomenclatura. In: Vera J (ed) Geología de España. Sociedad Geológica de España-Instituto Geológico y Minero de España (SGE-IGME)

Wang FW, Zhang YM, Huo ZT, Matsumoto T, Huang BL (2004) The July 14, 2003 Qianjiangping landslide, Three Gorges Reservoir, China. Landslides 1: 157-162. https://doi.org/10.1007/s10346-004-0020-6

Wang G, Xie M, Chai X, Wang L, Dong C (2013) D-InSAR-based landslide location and monitoring at Wudongde Hydropower Reservoir in China. Environ Earth Sci 69: 2763-2777. https://doi.org/10.1007/s12665-012-2097-x

Wang T, Perissin D, Rocca F, Liao MS (2011) Three Gorges Dam stability monitoring with time-series InSAR image analysis. Sci China Earth Sci 54: 720-732. https://doi.org/10.1007/s11430-010-4101-1

Záruba Q, Fencl J, Simek J, Eisenstein Z (1966) Analysis of the Dneboh Landslide. J Geol Sci 5: 141-160.

Chapter IV

Rapid characterisation of the extremely large landslide threatening the Rules Reservoir (Southern Spain)

Published on:

Landslides, 2021

Volume 18, Pages 3781-3798

DOI: 10.1007/s10346-021-01728-z

(Received: 9 April 2021, Accepted: 22 June 2021, Published: 29 September 2021)

Cristina Reyes-Carmona [1,2], Jorge Pedro Galve [1], Marcos Moreno-Sánchez [1], Adrián Riquelme [3], Patricia Ruano [1,4], Agustín Millares [5], Teresa Teixidó [4], Roberto Sarro [2], José Vicente Pérez-Peña [1,6], Anna Barra [7], Pablo Ezquerro [2,8], Juan López-Vinielles [2,8,9], Marta Béjar-Pizarro [2], José Miguel Azañón [1,4,6], Oriol Monserrat [7], Rosa María Mateos [2]

[1] Departamento de Geodinámica, Universidad de Granada, Avenida del Hospicio s/n, 18010 Granada, Spain
[2] Geohazards InSAR laboratory and Modelling group (InSARlab), Geoscience Research Department, Geological Survey of Spain (IGME), Calle de Ríos Rosas 23, 28003 Madrid, Spain
[3] Department of Civil Engineering, University of Alicante, Carrer de San Vicente del Raspeig s/n, 03690 San Vicente del Raspeig, Spain
[4] Instituto Andaluz de Geofísica, Calle del Profesor Clavera 12, 18071 Granada, Spain
[5] Instituto Interuniversitario de Investigación del Sistema Tierra en Andalucía (IISTA), Avenida del Mediterráneo s/n, 18006 Granada
[6] Instituto Andaluz de Ciencias de la Tierra (IACT-CSIC), Avenida de las Palmeras 4, 18100 Armilla, Granada, Spain
[7] Geomatics Division, Centre Tecnològic de Telecomunicacions de Catalunya (CTTC), Avinguda Carl Friedrich Gauss 7, 08860 Castelldefels, Spain
[8] Escuela Técnica Superior de Ingenieros de Caminos, Canales y Puertos, Universidad Politécnica de Madrid, Calle Profesor Aranguren s/n, 28040 Madrid, Spain
[9] HEMAV SL, Carrer d'Esteve Terrades 1, 08860 Castelldefels, Spain

Abstract

When an active landslide is first identified in an artificial reservoir, a comprehensive study has to be quickly conducted to analyse the possible hazard that it may represent to such a critical infrastructure. This paper presents the case of the El Arrecife Landslide, located in a slope of the Rules Reservoir (Southern Spain), as an example of geological and motion data integration for elaborating a preliminary hazard assessment. For this purpose, a field survey was carried out to define the kinematics of the landslide: translational in favour of a specific foliation set, and rotational at the foot of the landslide. A possible failure surface has been proposed, as well as an estimation of the volume of the landslide: 14.7 million m^3. At the same time, remote sensing and geophysical techniques were applied to obtain historical displacement rates. A mean subsidence rate of the landslide around 2 cm/year was obtained by means of Differential Synthetic Aperture Radar Interferometry (DInSAR) and Ground Penetrating Radar (GPR) data, during the last 5 and 22 years, respectively. The Structure-from-Motion (SfM) technique provided a rate up to 26 cm/year during the last 14 years of a slag heap located within the foot of the landslide, due to compaction of the anthropical deposits. All of this collected information will be valuable to optimise the planning of future monitoring surveys (i.e. differential global positioning systems, inclinometers, ground drilling, and DInSAR) that should be applied in order to prevent further damage on the reservoir and related infrastructures.

Keywords

Landslide, reservoir, quick characterisation, geological data, multi-technique monitoring, DInSAR, SfM, GPR

1. Introduction

The study of a specific landslide must start with geological and geomorphological characterisation to define its main attributes, such as dimensions, structure, geometry, or volume (Cruden and Varnes 1996). This knowledge is an essential starting point for optimising monitoring surveys and to provide a conceptual model for modelling the slope. Monitoring surveys are a key component of most landslide hazard assessments, and they typically involve obtaining surface displacement rates measured over time (Clague and Stead 2012). Additionally, the temporal displacement patterns can be analysed to detect critical accelerations that may precede a catastrophic failure of the slope (Carlà et al. 2019). Characterising and monitoring a landslide is even more important when it takes place in a reservoir, where landslides usually lead to risky situations that may result in human, material, and/or economic losses (e.g. Kiersch 1964; Schuster 1979; Spanilá et al. 2002; Wang et al. 2004; Gutiérrez et al. 2010; Reyes-Carmona et al. 2020a). Because these are such critical infrastructures, the monitoring techniques employed must use already registered information to provide quick results with which to rapidly evaluate the possible landslide impacts on the reservoir. These requirements are also important to be considered in case of an alarm situation.

Currently, there is a wide range of techniques that provide ground surface displacement data related to landslide activity: (i) remote sensing techniques, that include Differential Synthetic Aperture Radar Interferometry (DInSAR) (e.g. Massonnet and Feigl 1998), Global Positioning Systems (GPS) (e.g. Brunner et al. 2003), Terrestrial Laser Scanner (TLS) (e.g. Teza et al. 2007), and photogrammetry using aerial photographs from planes (e.g. Kraus 1997) or Remotely Piloted Aircraft Systems (RPAS) (e.g. Niethammer et al. 2012); (ii) geophysical techniques, such as Ground Penetrating Radar (GPR) (e.g. Lissak et al. 2015); or (iii) conventional geotechnical monitoring systems like inclinometers or extensometers (e.g. Corominas et al. 2000).

Only a few of these techniques can be applied to retrospectively quantify a landslide displacement rate by using already registered information: (1) DInSAR applied to archived radar satellite images, and (2) photogrammetry of historic aerial photographs. Moreover, the mentioned techniques can be used very quickly to obtain preliminary data that may guide the subsequent studies, or monitoring surveys, over a landslide. Regarding DInSAR methods, the Geohazards Exploitation Platform (GEP) of the European Space Agency (ESA) can provide Earth surface velocity maps in just 24-48 h (e.g. Manunta et al. 2016; Galve et al. 2017; Tapete and Cigna 2017; Foumelis et al. 2019; Reyes-Carmona et al. 2020b). On the other hand, Structure-from-Motion (SfM) techniques (Ullman 1979; Hartley and Zisserman 2003; Szeliski 2010; Fisher et al. 2013) allow to generate landscape 3D models to identify the evolution of landforms with historical aerial photographs, in a short period of time, by comparing at least two different Digital Elevation Models (DEMs) at different dates (Snavely et al. 2008; Westoby et al. 2012; Eltner et al. 2016; Riquelme et al. 2019). In case of a landslide, the quantified changes can be attributed to its activity, making it possible to estimate the displacement rate during a certain period of time.

Additionally, if a road crosses an active landslide, the infrastructure can also record old displacements that may have been covered by resurfacing works. In such cases, a 1-day GPR survey can be carried out to obtain cross sections along the road that can, then, be used to identify the sequence of asphalt layers. With this system, the vertical displacement rate along a road can be inferred from the evolution of the asphalt layering with time (e.g. Lissak et al. 2015).

In this paper, the methods above have been integrated in the study of the El Arrecife Landslide (Figure 1), a landslide recently recognised by DInSAR techniques (Reyes-Carmona et al. 2020a). This landslide affects the western slope of the Rules Reservoir (Southern Spain), which leads to a potential hazardous situation. For this reason, an in-depth characterisation and a multi-technique investigation of the landslide were performed, in order to evaluate its potential threat to the reservoir in the shortest possible time. Initially, a detailed geological study was conducted in order to define the structure and conditioning factors of the landslide, as well as to estimate its failure surface and volume. Subsequently, DInSAR, GPR and SfM methods were applied to obtain the historical displacement rates of the landslide. Therefore, our geological assessment will be useful to design future investigations with more precision, such as inclinometer and

Differential Global Positioning System (DGPS) monitoring, topographic surveys, or exploration drilling in an optimal manner. At the same time, the remote sensing (i.e. DInSAR and SfM) and geophysical (i.e. GPR) techniques provided displacement rates of the landslide before starting any ground monitoring action, not only in a quick and efficient approach but also by using freely available or fast acquired data. Finally, all of the produced data were integrated to perform a preliminary hazard evaluation of the El Arrecife Landslide within the Rules Reservoir context.

2. Case study

The El Arrecife Landslide is an active translational landslide located within the western slope of the Rules Reservoir, in the Granada Province (Southern Spain) (Figure 1). The El Arrecife Landslide is settled within the Permo-Triassic phyllites of the metamorphic Alpujárride Complex (Aldaya et al. 1979). The Alpujárride rocks underwent several deformational events that determined their geological complexity, which is manifested by multiple structures (i.e. foliations, lineations, folds, and faults) visible both at small and large scale, as well as through different ages (e.g. Jabaloy et al. 1993; Simancas and Campos 1993; Azañón and Goffé 1997; Martínez-Martínez et al. 2002, 2004; Simancas 2018). The most penetrative and visible structures in the study area are the S_{2A} foliation, which is usually the main foliation in the Permo-Triassic phyllites (Simancas 2018), and the F_{3A} kilometre-scale folds, widely distributed in the Alpujárride Complex, which folds the main foliation (Simancas and Campos 1993).

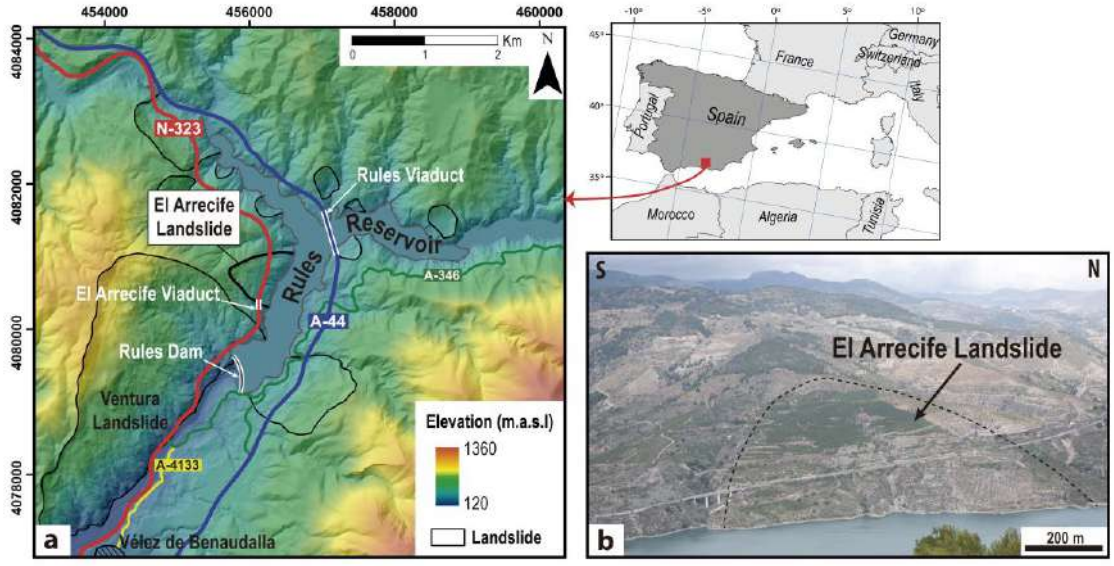

Figure 1. **(a)** Location of the El Arrecife Landslide in the Rules Reservoir, Southern Spain. The main roads (A-44, N-323, A-346, and A-4133) are marked, together with the critical infrastructures (Rules Viaduct and Rules Dam), and other relevant landslides in the surroundings of the reservoir. **(b)** Panoramic view of the El Arrecife Landslide.

The Rules Reservoir area has been affected by several slope movements during the last decades, being the subject of several landslide inventories (Fernández et al. 1997; Chacón et al. 2007). The most recent landslide inventory of the area was carried out by Reyes-Carmona et al. (2020a) where the El Arrecife Landslide was mapped for the first time.

The most noteworthy characteristic of the El Arrecife Landslide is that it does not show a prominent head scarp, or any other well-marked landslide morphology, which makes it not easily identifiable in the landscape (Reyes-Carmona et al. 2020a). These authors presented ground surface displacement data of the Rules Reservoir area, by means of Differential Interferometric Synthetic Aperture Radar (DInSAR) techniques, which revealed the actual area of the sliding body (around 0.5 km^2). Moreover, they estimated a mean surface velocity of up to -25 mm/year and an accumulated displacement of 10 cm in 3.5 years for the entire landslide body.

The activity of the El Arrecife Landslide has been also evidenced by the N-323 National Road that runs across the landslide. This road has been consistently in need of repair works due to the existence of bumps, cracks, and partial collapses of the road pavement (Fernández-Motril 2013). In 2013, the Spanish Ministry of Public Works and Transport invested a total of 3.8 million Euros to repair 8 km of the N-323 National Road, which entailed the resurfacing of the pavement and the structural restoration of the northern abutment of the El Arrecife Viaduct (Fernández-Motril 2013), located in the southern limit of the El Arrecife Landslide. In addition, Reyes-Carmona et al. (2020a) pointed out the potential hazard of the landslide, considering a rapid acceleration and a catastrophic slope failure due to its translational character. According to the authors, the collapse of a slide mass into the reservoir would have devastating consequences not only for nearby populations, in case of a downstream flash flood, but also for some infrastructures like the N-323 National Road and some power lines.

3. Methodology

Firstly, a detailed geological survey of the El Arrecife Landslide was performed, based on field observations. This step was essential to later estimate some important characteristics of the landslide, such as the surface of rupture and its volume. Subsequently, the recent displacement rate of the El Arrecife Landslide was calculated via a multi-technique approach. The techniques employed make use of already registered information, and provided quick results of variable precisions (mm/year to dm/year) at different time scales (5-20 years). This was a key information to evaluate the landslide activity during the last decades.

3.1. Geological characterisation of the landslide and volume estimation

The geological characterisation of the landslide was carried out through a structural study and a kinematic analysis of the slope that led to the estimation of its volume.

3.1.1. Structural study

A detailed field survey, which included a structural analysis, was carried out both inside and outside of the El Arrecife Landslide perimeter. Both the S_{2A} and the F_{3A} have been identified as the geological structures that most influence the slope stability conditions of the El Arrecife area, for the purposes of this paper.

3.1.2. Kinematic analysis

A kinematic analysis, by means of stereographic projection methods, can be used to easily examine the direction in which a rock slope is more likely to slide (Wyllie and Mah 2004). The first step is to identify the main sets of discontinuities of the rock slope. In order to do so, field measurements were collected and grouped into main sets of discontinuities from 5 Measurement Stations (MSs). These measurements were named MS-0*n*, where *n* is a number from '1' to '5' relating to each of the stations. Therefore, MS-02 and MS-03 are located within the El Arrecife Landslide perimeter, while MS-01, MS-04, and MS-05 are located outside of it (Figure 2). Our analysis was focused on measuring the S_{2A} foliation planes. Then, the potential for these discontinuities to result in slope failures was evaluated by using the software DIPS, following the planar failure analysis procedure (Rocscience Inc 2004). This analysis consisted in (i) plotting the poles of the foliation planes, arranging them in different sets and obtaining a mean plane for each set; (ii) plotting the average gradients of the El Arrecife Landslide slope, including the daylight envelope for each value; and (iii) creating two friction cones, using the values of 20° and 25°, which represent, respectively, the minimum and maximum internal friction angles of the involved rocks (i.e. phyllites) within the landslide (Wyllie and Mah 2004). The area of rupture is defined outside of the friction cone, where it intersects with the daylight envelope of the slope. Any poles, if plotted within the area of rupture, represent planes susceptible to planar sliding.

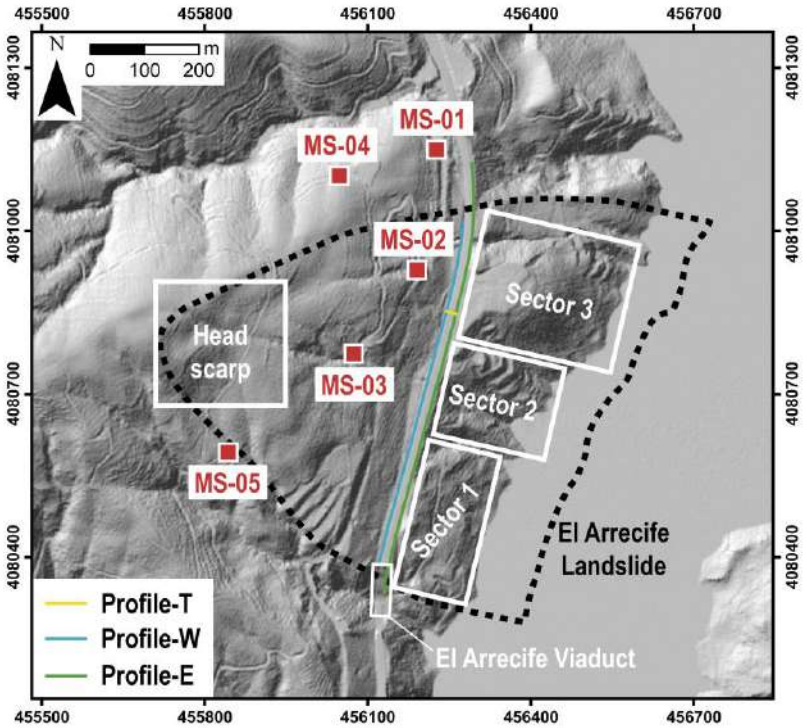

Figure 2. Location of the 5 measurement stations (MS) for the kinematic analysis of the El Arrecife Landslide area and 3 profiles, acquired from the GPR survey: 'Profile Transversal' (Profile-T), 'Profile West' (Profile-W), and 'Profile East' (Profile-E). The different areas (Head scarp, Sector 1, Sector 2, and Sector 3) selected for the DInSAR time series plots are also represented. This information is showed on a 2-m-resolution hillshade model.

Moreover, the WEDGEFAIL tool from the SAGA (Automated Geoscientific Analyses) Geographic Information System (GIS) was used to identify the terrain elements where failure on geological discontinuities is kinematically possible through the frictional feasibility criteria (Günther et al. 2012 and references therein). A 5-m resolution digital elevation model (DEM) was used to carry out four simulations of slope failure scenarios. For each simulation, a map that indicates areas of possible 'failure' or 'no failure' was obtained.

3.1.3. Volume estimation

The procedure to estimate the volume of the El Arrecife landslide initially consisted in generating a 2-m resolution DEM of the landslide area before being anthropically modified by the reservoir construction. This was carried out by extracting the contours from a 1999 topographic map. Once the DEM was obtained, six longitudinal cross sections were traced along a preferential direction of the landslide, and a possible surface of rupture was drawn within each cross section, based on the kinematic analysis, the geometry of the slope, and its main morphological features (i.e. main scarp and toe). In this case, the preferential direction to trace the cross section was the one parallel to the main dip direction of the foliation planes within the landslide perimeter. Afterwards, the contours corresponding to such failure surface were estimated in order to generate a DEM. By subtracting the landslide DEM from the failure surface DEM, a raster-type map that represented the thickness of the landslide body was obtained. The volume estimation was calculated by multiplying the average thickness value of the obtained map by the area of the landslide.

3.2. Calculation of displacement rates of the landslide

Three different techniques were applied to obtain mean annual displacement rates of the El Arrecife Landslide during the last two decades: DInSAR was useful to provide a short-term displacement rate of very slow movements (cm-mm/year), up to 5 years, while GPR and SfM techniques were used to estimate medium-term displacement rates of great magnitude (GPR >cm/year; photogrammetry >dm/year), for the last 20 years. Moreover, DInSAR supplied information about the temporal pattern of the recent displacement of the landslide by means of time series of accumulated displacement (TSs).

3.2.1. Differential Synthetic Aperture Radar Interferometry (DInSAR)

The Parallel Small Baseline Subset (P-SBAS) processing service, available at the European Space Agency (ESA)'s Geohazards Exploitation Platform (GEP), was used to derive the DInSAR data. See Casu et al. (2014) and De Luca et al. (2015) for further details of the P-SBAS algorithms and processing chain. Two different processing jobs were carried out, one in an ascending orbit and the other in a descending orbit. For the ascending orbit, 101 Sentinel-1B images covering a period from the 30th of September 2016 to the 13th of March 2020 (3.5 years), and with a temporal sampling of 12 days, were used. For the descending orbit, 241 Sentinel- 1A and Sentinel-1B images were used, which covered a period from the 22nd of December 2014 to the 19th of March 2020 (5 years), and had a temporal sampling of up to 6 days. For both processing jobs, the

coherence threshold was set at 0.85 and the reference point was established in a small structure to the south of the Rules Reservoir (Lat 36.848/Long -3.497; WGS84 projection). The main outputs of each processing job were a set of points representing the annual mean velocity and the accumulated displacement at each image date. Both the velocity and the accumulated displacement were calculated along the satellite Line of Sight (LoS) direction.

To represent the mean velocity maps in both orbits, the stability range (i.e. the threshold for discriminating stable and unstable velocity points) was estimated as two times the standard deviation of the velocity of all the measured points (Barra et al. 2017). Therefore, the stability range was set between 6 and -6 mm/year, for the ascending orbit processing job, and between 5 and -5 mm/year for the descending orbit job. The pixel size of the obtained points was 90 m. Then, the horizontal and vertical components of the mean velocity data were calculated. The procedure followed is the one described by Notti et al. (2014) and Béjar-Pizarro et al. (2017), which is applicable when both the ascending and the descending orbit data are available. Thus, assuming a small contribution of N-S horizontal motion (Notti et al. 2014), the E-W horizontal ($V_{eastward}$) and vertical ($V_{vertical}$) velocity components were calculated in a raster-type map with a resolution of 90 m.

Lastly, the TS of accumulated displacement of the unstable points from the ascending orbit processing job was plotted, in order to define the temporal behaviour of the landslide movement and its relation to the reservoir water level variations, since, according to Reyes-Carmona et al. (2020a), such a relationship is the main triggering factor of slope movement in the Rules Reservoir area. The unstable points were then assembled in different groups according to their distribution within the landslide (Figure 2): (i) the head scarp; (ii) the N-323 National Road; (iii) Sector-1, which corresponds to a smaller-sized landslide within the lower part of the El Arrecife Landslide; (iv) Sector-2, the central lower part of the landslide; and (v) Sector-3, corresponding to the slag heap area. Then, an independent TS was plotted for each of the groups of points (median value). The reservoir water level measurements were obtained for free from the public Andalusian Automatic System of Hydrologic Information (S.A.I.H. HIDROSUR, www.redhidrosurmedioambiente.es).

3.2.2. Ground penetrating radar (GPR)

A RAMAC ground penetrating radar system (Mala Geosciences) with a 400-MHz antenna was used to acquire three radar profiles (Figure 2): two of them along the N-323 National Road (i.e. ‘Profile East’ and ‘Profile West’) and the other one across the road (‘Profile Transversal’). The Profile West is 647.94-m long and runs the western side of the road while the Profile East is 820.96-m long and runs the eastern side of the road (Figure 2). The reference point (0 m) on the profiles was established in the northern abutment of the El Arrecife Viaduct (Figure 2). The Profile Transversal was acquired transversely to the road and has a length of 13.42 m (Figure 2). The radar signal could penetrate at a depth of 2-m underground, providing a profile resolution of 10 cm. The data were recorded with a sampling interval of 5 cm and a total time window of 55 ns. By means of reflected wave methods (see Conyers 2015 for further descriptions), a terrain

velocity of 9.6 cm/ns was calculated. The raw data were processed by using the GSSI RADAN 7 software (GSSI 2012). The processing chain of the raw data consisted of six steps: (i) adjusting to time 0, in this case, set at 3.9 ns; (ii) elimination of the air-ground contact; (iii) application of a gain filter to reduce the intensity on the signal; (iv) migration of the data to eliminate diffraction effects; (v) deconvolution to increase the vertical resolution, as well as cleaning the signal; and (vi) application of a vertical filter, in this case between 250 and 750 MHz, to remove background noise.

Since the El Arrecife Landside activity has caused considerable damage (i.e. cracks, potholes, sinking) along the N-323 National Road, multiple repairs of the road pavement have been carried out during recent years (State Road Demarcation 2020); and thus, a sequence of asphalt layers can be detected by the GPR. Such layers are well-evidenced by continuous and almost horizontal reflectors along the profiles. The temporal evolution of this layering can be used to infer the vertical displacement rate along the road (Lissak et al. 2015). The latter can then be used to extrapolate the displacement rate of the landslide. Thus, the displacement rate can be estimated by dividing the thickness of the whole sequence of asphalt layers by the total period of time of the road paving.

3.2.3. Structure-from-Motion (SfM)

The methodology described by Riquelme et al. (2019) was applied to detect ground movements in the Rules Reservoir from its construction (2004) to present time. For this purpose, two different surfaces from the years 2000 and 2014 were compared. The 2014 DEM was generated by using Airborne Laser Scanner (ALS) data, freely obtained from the PNOA project (https://pnoa.ign.es/). The 2000 DEM was generated by exploiting aerial photos and using the SfM technique. To apply this technique, it was necessary to insert ground control points (GCP) into the photos. For each photo, several distinctive features were identified in the 2014 DEM (ALS-DEM). The coordinates of those points were extracted to generate the 2000 DEM dense cloud, which was then finally compared with the ALS-DEM.

4. Results

4.1. Geological structure of the El Arrecife Landslide

The Alpujárride Complex phyllites are the predominant lithology within the El Arrecife Landslide area, whose boundary is indicated by a black dashed line (Figure 3). Within the landslide perimeter, phyllites outcrops appear considerably fractured and partially covered by debris or soil and colluvium deposits (Figure 4a). By contrast, outcrops are better preserved outside of the landslide perimeter, and phyllites show a noteworthy level of tectonisation (Figure 4b). The most recognisable tectonic fabric of the Alpujárride phyllites is the S_{2A} foliation with NE-SW to E-W trend, dipping 25º (median value) to SE (Figure 3). A less prevalent NW dipping NE-SW trend is also present. Both foliation trends evidence the existence of centimetre- to metre-scale minor folds (Figure 4b), with fold axes plunging 20º to 245º approximately (see stereographic projection in Figure 3), and showing a NW vergence. These minor folds are associated with the existence of a major fold, interpreted as a F_{3A} fold. The cross section in Figure 3 illustrates this foliation

pattern, mainly dipping towards SE, while the NW dipping trend forms the short limbs of F_{3A} minor folds.

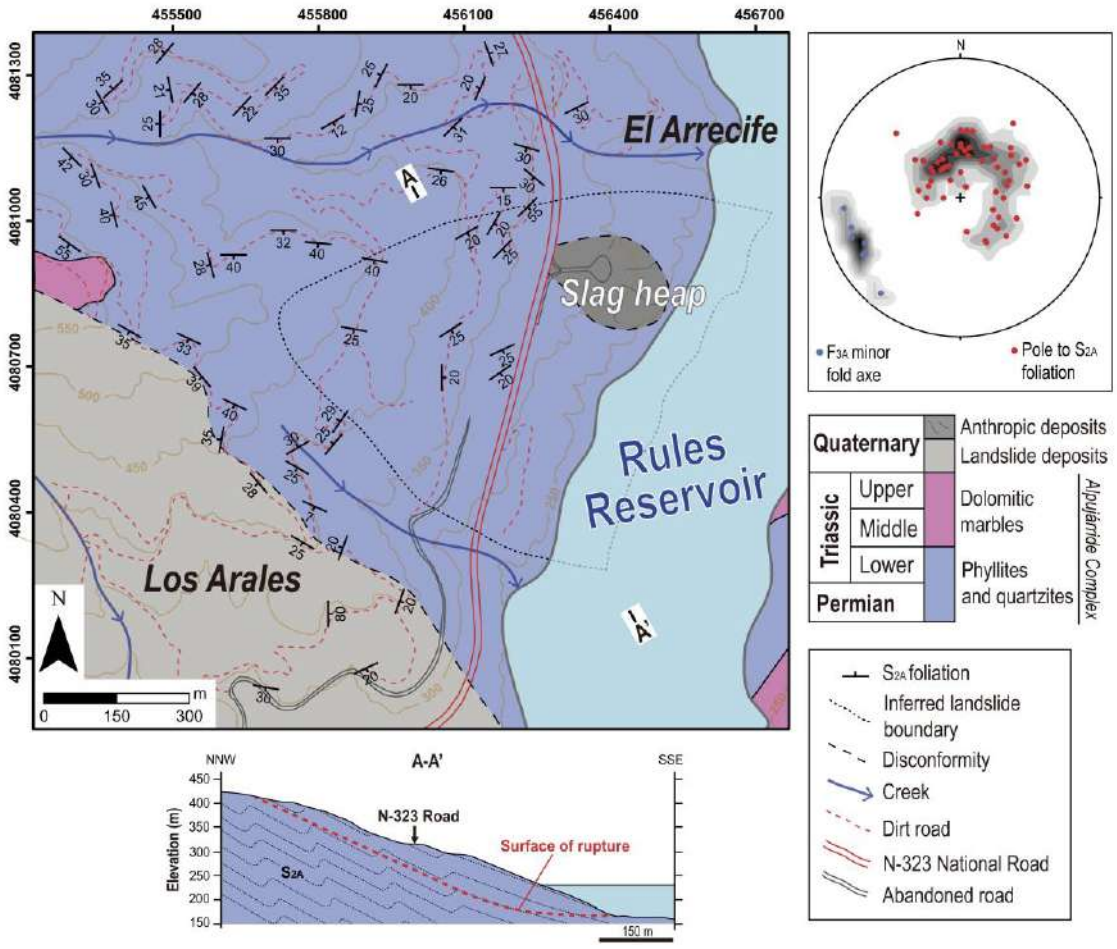

Figure 3. Geological map and cross section of the El Arrecife Landslide area. Poles to S_{2A} foliation and F_{3A} minor fold axes are plotted in stereographic projection (lower hemisphere, equal area).

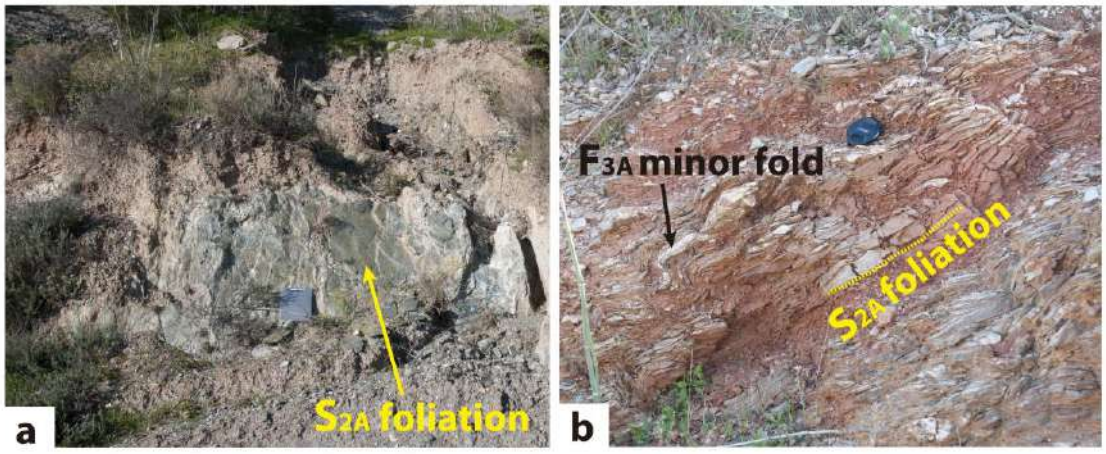

Figure 4. Field photos of the Alpujárride phyllites in the El Arrecife Landslide area. **(a)** An outcrop showing the main foliation S_{2A} almost covered by colluvial deposits within the landslide perimeter. **(b)** An outcrop covered by red-coloured soil deposits located out of the landslide perimeter, where F_{3A} minor folds and the S_{2A} foliation can be observed.

The surface of rupture of the El Arrecife Landslide was drawn according to the plane 21/120 (dip/dip direction) that is parallel both to a foliation plane set and to the median gradient of the slope. Such assumption would imply a movement of the landslide body towards N120ºE, that is parallel to the mean orientation of the slope (Figure 5a). Despite the fact that the whole mass may be sliding downhill through a planar surface of rupture (i.e. translational landslide), the lower part of the landslide is affected by smaller-sized rotational movements, evidenced by several secondary scarps (Figure 5a). These movements are progressively eroding the El Arrecife Landslide foot, clearly influenced by the reservoir water level fluctuations. Moreover, above the N-323 National Road, active piping phenomena were identified (Figure 5b), along with several opened cracks with vertical steps up to 0.5 m (Figure 5c). These findings are clear signals of the El Arrecife Landslide's activity.

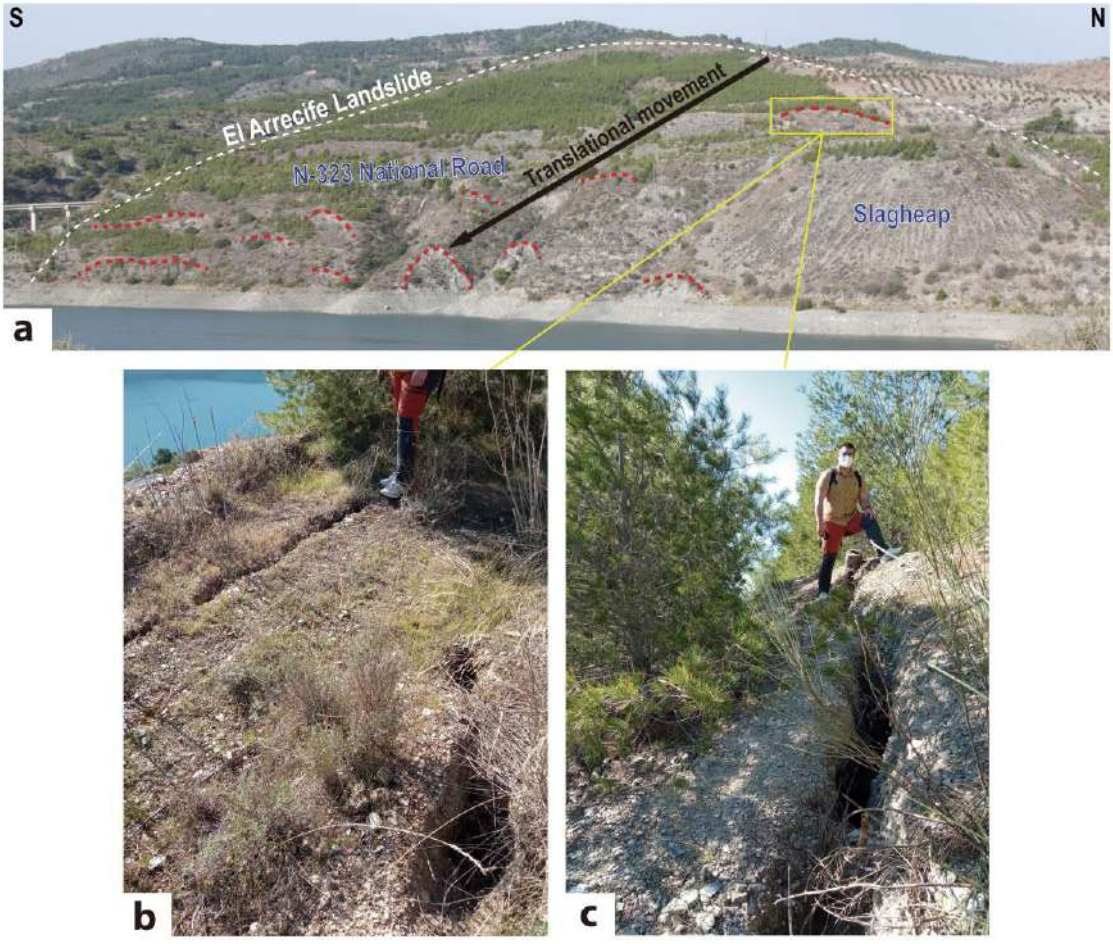

Figure 5. **(a)** Panoramic view of the El Arrecife Landslide. Rotational secondary scarps are indicated by red dashed lines. The translational direction of movement is also indicated by a black arrow. **(b)** Photograph of the piping phenomena within the El Arrecife Landslide perimeter. **(c)** Photograph of a crack with a superficial vertical step of 0.5 m and 1.5 m depth in the El Arrecife Landslide perimeter

4.2. Kinematic analysis of the El Arrecife Landslide

The kinematic analysis is shown in two different stereographic projections, relative to inside and outside of the El Arrecife Landslide perimeter. For both cases, the area of rupture is defined by the intersection of the daylight envelope of the slope with the 20º friction cone (Figure 6). In a first approach, three foliation trends are clearly noticed: (i) a NE-SW trend, corresponding to the measurement stations within the landslide (i.e. MS-02 and MS-03); (ii) a E-W trend, corresponding to stations located outside of the landslide and close to its northern limit (i.e. MS-01 and MS-04); and (iii) a NW-SE trend, corresponding to MS-05, located outside of the landslide perimeter and close to its southern limit (Figure 2). Within the landslide, almost all of the poles can be assembled in one set (Set-1), which is defined by the mean plane 34/140 (dip/dip direction). Only one of these poles is plotted within the area of rupture, which corresponds to the plane 21/120 (dip/dip direction), being the most likely surface to generate the planar failure along the El Arrecife slope. This pole and its related plane were named 'critical pole' and 'critical plane', respectively. Outside of the landslide perimeter, the distribution of poles is clearly arranged into two groups of poles, named Set-2 and Set-3, that are defined by the mean planes of 30/188 and 28/306, respectively. None of these poles is plotted within or near the area of rupture.

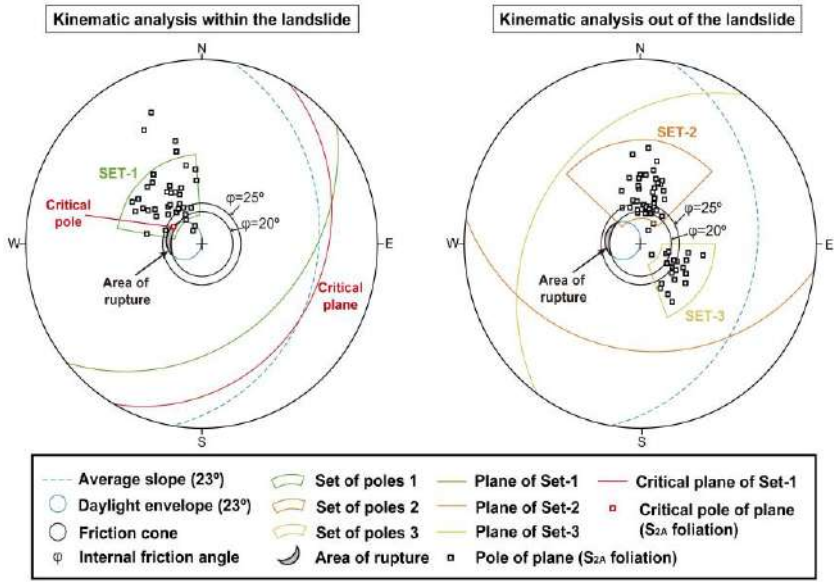

Figure 6. Kinematic analysis of the El Arrecife Landslide, inside and outside of the landslide perimeter. The main discontinuity sets of the area and their mean planes are shown.

The previous statements are also confirmed by the analysis done by means of SAGA-GIS (Figure 7). The critical plane of Set-1 defines an extensive area where failure is likely to occur, especially within the El Arrecife Landslide area. This is not the case for Sets-1, Set-2, and Set-3, as almost any slope failure areas are estimated within the landslide perimeter. These results led us to confirm that planes with orientations close to 21/120 (dip/dip direction) can potentially generate slope failures in the area; and thus, it is reasonable to assume such plane as the possible surface of rupture of the El Arrecife Landslide.

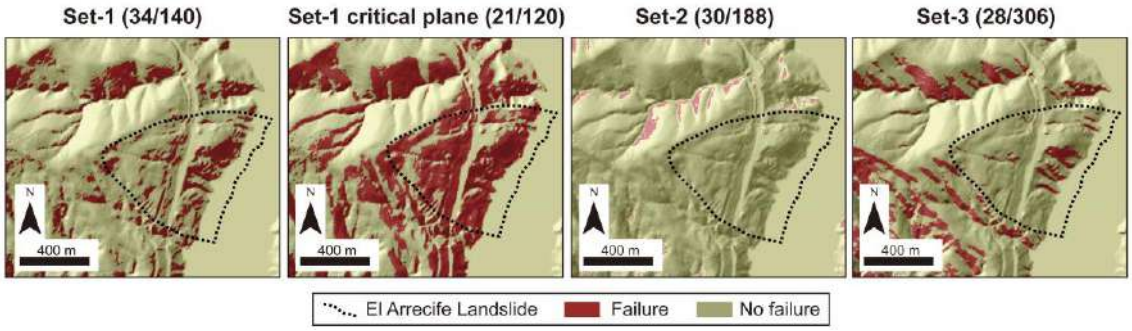

Figure 7. Areas where slope failure is kinematically possible through each of the main discontinuity sets of the El Arrecife Landslide area.

4.3. Volume of the landslide

Assuming the critical plane as the surface of rupture, six longitudinal cross sections were traced across the landslide according to the critical plane dip direction (N120ºE). In the same way, the surface of rupture was established as a flat plane dipping 21º (dip of the critical plane) for each cross section. The resultant map of the landslide body thickness is shown in Figure 8. The maximum thickness is 72.6 m, estimated in the lower southern part of the landslide. Thickness values near zero meters clearly define the head scarp, especially along the northern edge of the landslide and in contrast to the southern limit. Notice that thickness values in the slag heap area include natural and anthropical materials. Knowing that the mean thickness value of the landslide body is 31.1 m, and that the landslide area is 473107 m^2, a volume of 14.7 million m^3 was estimated. According to Fell's (1994) classification, this one can be considered as an 'extremely large' landslide.

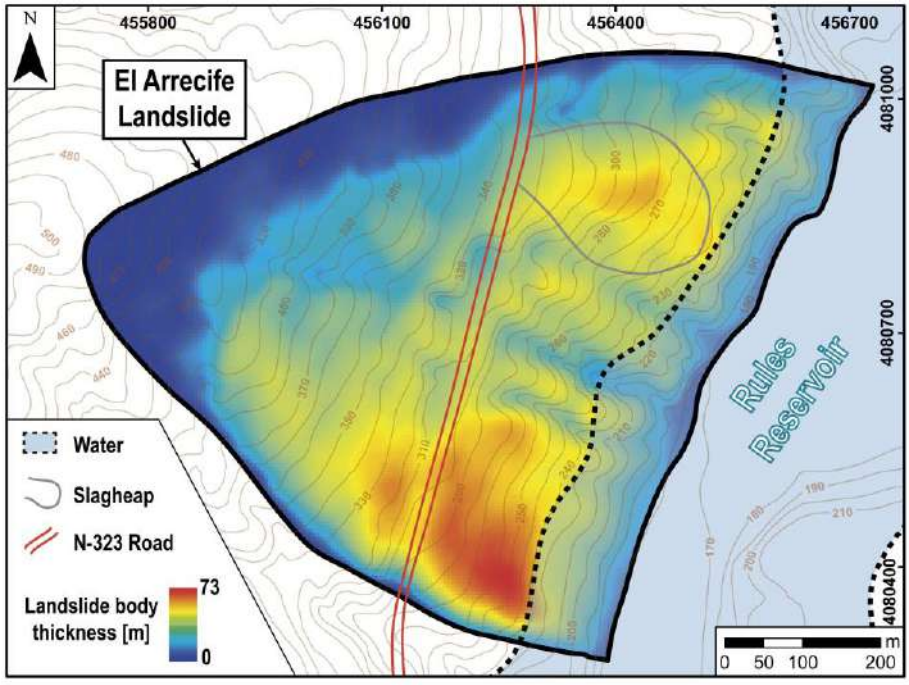

Figure 8. Map of thickness of the El Arrecife Landslide. Other elements of interest such as the N-323 National Road and the slag heap are also indicated.

4.4. DInSAR results

4.4.1. Velocity maps

Unstable points were detected in both ascending and descending geometries within the El Arrecife Landslide perimeter, mostly in the lower part of the slope (Figure 9). Since the velocity was estimated along the satellite LoS direction, negative values indicate that points move away from the satellite, while positive values refer to points moving towards the satellite. For the ascending processing, negative values indicate an eastward movement along the El Arrecife Landslide slope, in addition to subsidence in flat areas. On the contrary, for the descending processing, the eastward movement of the landslide is indicated by positive values. The point coverage is higher in the ascending processing, from which unstable points showing a displacement of up to -31 mm/year, in the southern lower part of the landslide, were obtained (Figure 9). This area corresponds to a small-sized landside, mapped by Fernández et al. (1997) and Chacón et al. (2007), and its activity was confirmed by the DInSAR data presented in Reyes-Carmona et al. (2020a). Along the N-323 National Road, displacement rates fluctuate around -20 mm/year, with the highest rate obtained in the slag heap area, showing a value of -39 mm/year. By contrast, the descending processing shows a worse quality of point coverage, but it can be confirmed that the lower parts of the El Arrecife Landslide and the N-323 National Road are moving down (Figure 9).

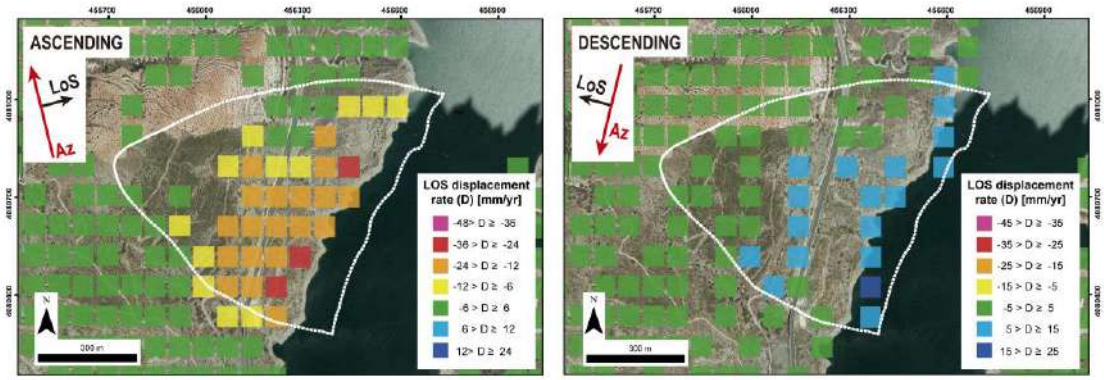

Figure 9. Surface velocity maps in ascending and descending geometries of the El Arrecife Landslide area. Red arrows indicate satellite flight direction or azimuth (Az) and black arrows indicate the Line of Sight (LoS) direction.

Figure 10 shows eastward and vertical components of the surface displacement data, obtained by the ascending and descending orbits P-SBAS processing. Positive and negative values indicate eastward and downward movements, respectively. Eastward displacement reaches values of 4.5 cm/year along the lower part of the landslide, which is consistent with a mass movement downhill of the slope. Negative vertical displacement (subsidence) is registered almost in the entire landslide area, except from the head scarp. Thus, the mean vertical velocity is around -1.5 cm/year, while the highest value (-2 cm/year) is registered within the slag heap area.

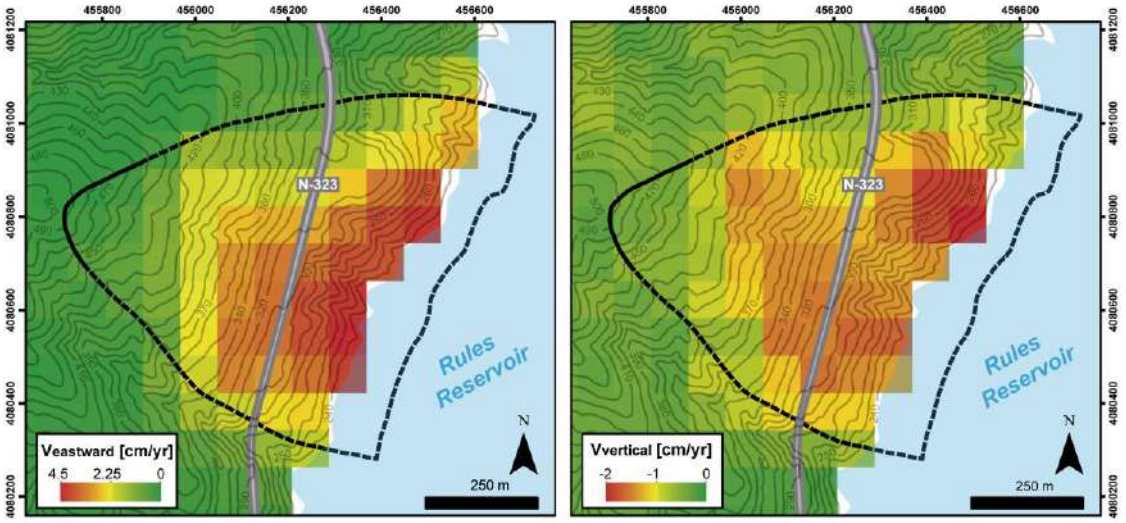

Figure 10. Surface displacement velocity in the eastward and vertical directions in the El Arrecife Landslide. The landslide boundary is marked by a black dashed line.

4.4.2. Analysis of the time series of accumulated displacement

Figure 11 shows the TS of the five groups (Figure 2) of points within the El Arrecife Landslide area together with the Rules Reservoir water level variations. The TSs of the head scarp and the N-323 National Road, as well as the mean TS of all the points within the landslide perimeter, are plotted in Figure 11a, while the TS of Sectors 1, 2, and 3 are plotted in Figure 11b. Such distinction refers to the difference in the TS displacement patterns: almost linear in the El Arrecife Landslide, its head scarp and the N-323 Road (Figure 11a), as opposed to the steeped trend of Sectors 1, 2, and 3 TSs (Figure 11b). The steep trend of Sectors 1, 2, and 3 is evidenced by two acceleration periods (i.e. change to a steeper slope of the line trend) that fit well with two periods of reservoir water level decline: (i) during the second decline, from autumn 2017 to spring 2018, and (ii) during the third decline, from summer 2019 to autumn 2019 (Figure 11b). These acceleration periods are not observable in the main scarp TS, which does not show a significant displacement, in the El Arrecife Landslide, or in the N-323 National Road TSs.

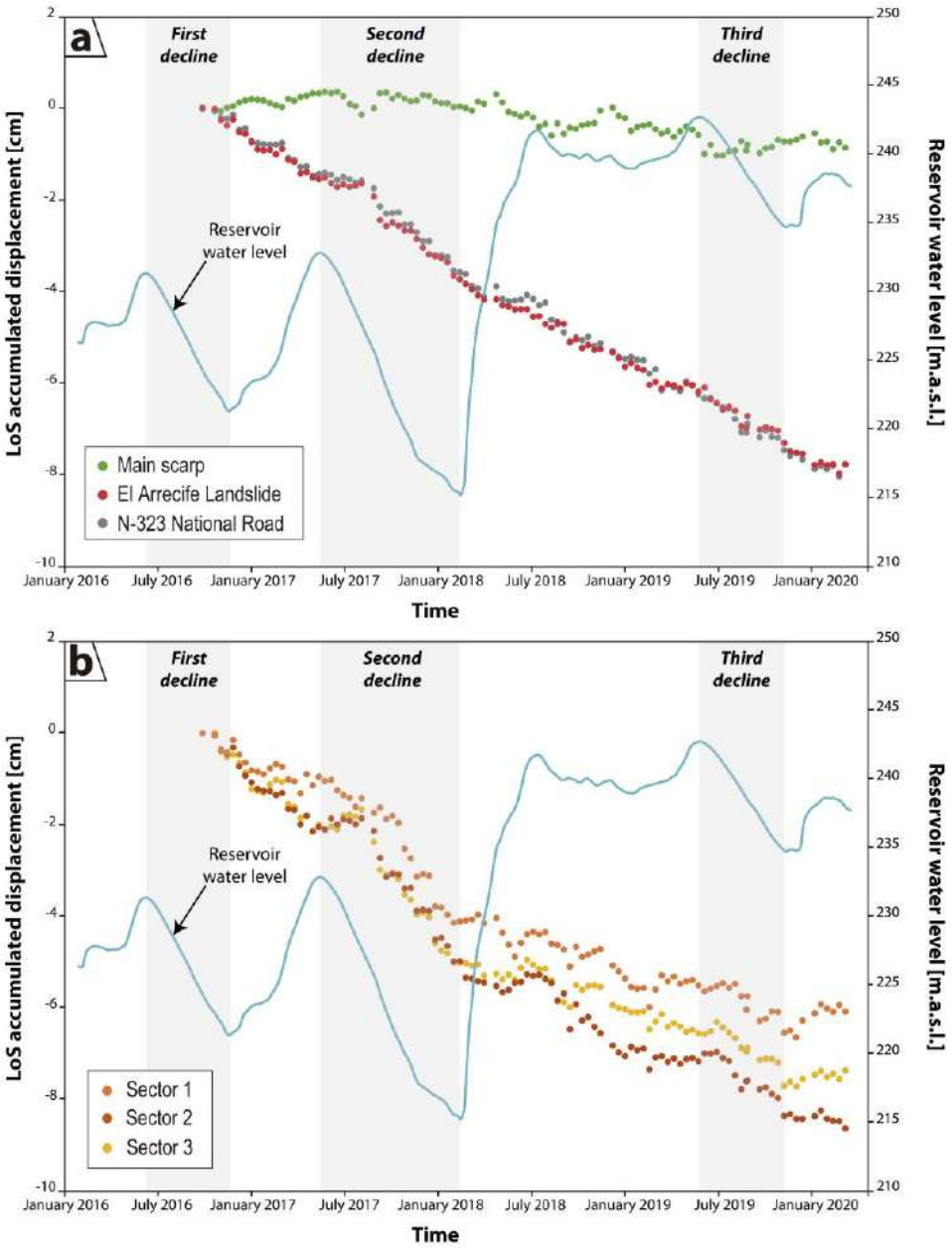

Figure 11. Time series (TS) in Line-of-Sight (LoS) direction of accumulated displacement of **(a)** the El Arrecife Landslide, the landslide main scarp, and the N-323 National Road, and **(b)** TSs of the Sectors 1, 2, and 3. The related sectors for each TS are indicated in Figure 2. Water level variations of the Rules Reservoir are also plotted as a blue line. Grey columns indicate three periods of decrease of the reservoir water level, from March 2015 to March 2020.

4.5. Estimated medium-term displacement rates

4.5.1. SfM

The difference between the two DEMs obtained (Figures 12a, b) within the Rules Reservoir area is shown in Figure 12c. A zoom view of the slag heap area and its estimated elevation change is also presented for a better appreciation (Figures 12d, e, f). Negative values are indicated in red colours and correspond to subsiding areas, while green colours correspond to stable areas. In order to quantify the difference between the DEMs, taking

into account the error of this technique, a histogram that shows the distribution of the elevation changes was produced, where two Gaussian distributions seem to be present (Figure 12g). The two Gaussian distributions were fitted, and the R-squared value obtained was 0.993, showing a good fit. The mean (μ) of the first distribution ($Dist_1$) is -4.27 m, which is approximately close to the technique error, according to Riquelme et al. (2019). However, the centre of the second distribution ($Dist_2$) is located at -7.94 m. These values correspond to those located within the slag heap area. The maximum registered displacement in the slag heap area was 10 m: 5 m when removing the technique error. As the difference in time between both models is 14 years, an annual subsidence rate of up to 35.7 cm/year was estimated within the slag heap area.

No other changes of enough magnitude to be detected by this technique (> 4-5 m) have been recorded in the area. Therefore, the movements represented by several scarps, observed within the foot of the El Arrecife Landslide, could not be dated. Apart from the subsidence in the slag heap area that could not be related to the landslide activity, no rapid movement occurred during the analysed period (2000-2014).

4.5.2. GPR

The full extent of the GPR Profiles East and West are shown in Appendix, together with a top view scheme of the N-323 National Road damages, based on field observations. Figure 13 show the same top view scheme (Figure 13d) and a few field photographs of the main damaged areas found along the road (Figures 13a, b, f, g), as well as two extracts from the Profile East (from 0 to 115 m) (Figure 13c) and the Profile West (from 390 to 515 m) (Figure 13e). In both GPR profiles, several asphalt layers were identified. These have been progressively superimposed since the construction of the N-323 road, in 1997 (State Road Demarcation 2020), until the acquisition date of the profiles in March 2020. The minimum thickness of the asphalt layers sequence within the landslide body is around 0.7 m in both profiles, while the maximum thickness is up to 1 m in the Profile West, and up to 1.2 m in the Profile East. Such increase in thickness towards to east of the road is coherent with the El Arrecife Landslide's downhill movement. The minimum thickness of the asphalt layering outside of the landslide perimeter is also around 0.7 m (Figure 14a). Therefore, there is an extra asphalt thickness of up to 0.3 m and 0.5 m in the Profiles West and East, respectively, as a result of the additional resurfacing work done on the road across the landslide. Knowing that the last layer of asphalt was settled in 2019 and the total registered time in GPR profiles is 22 years, a mean annual subsidence rate of the road from 1.4 to 2.3 cm/year was estimated.

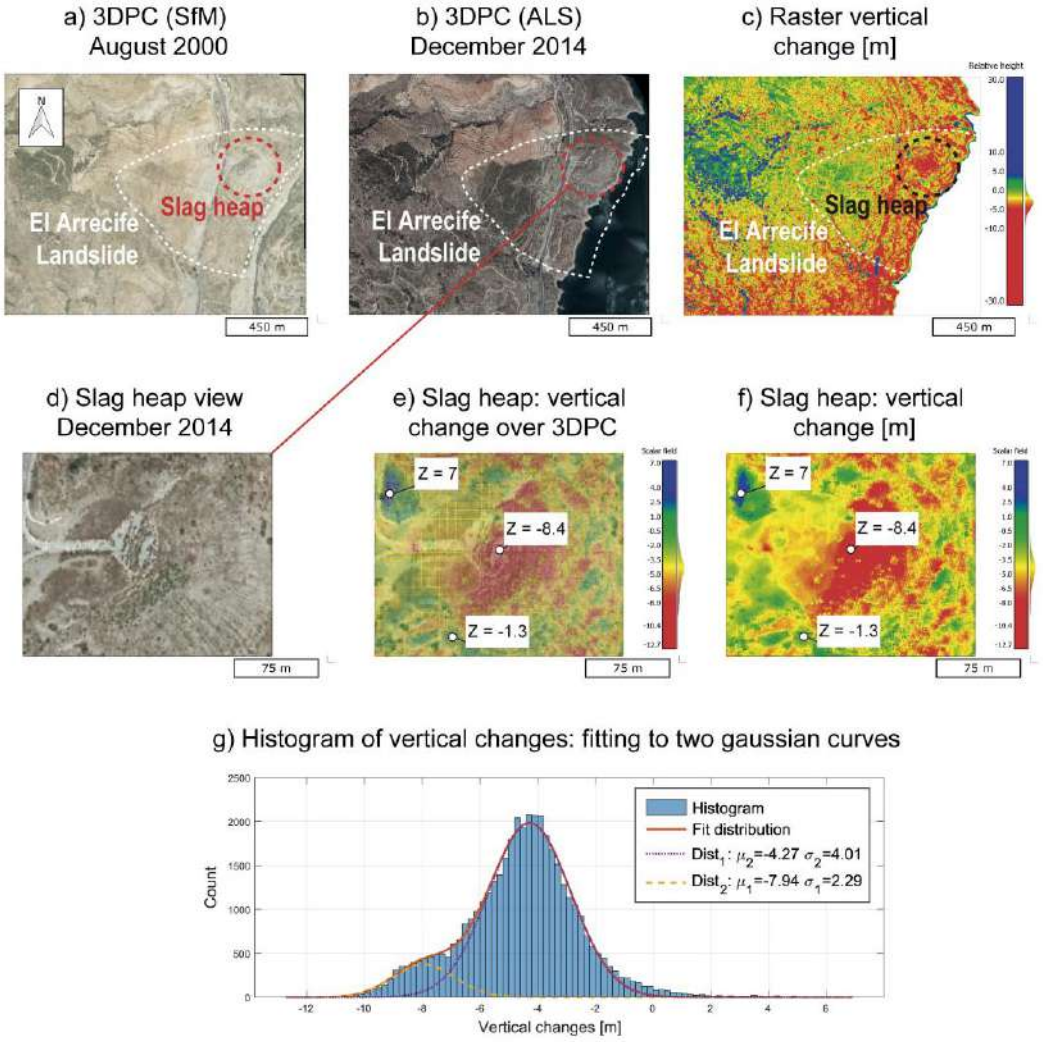

Figure 12. Results from the Structure-from-Motion (SfM) technique within the Rules Reservoir. **(a)** 3-Dimention points cloud (3DPC) obtained from SfM procedure using aerial photos from August 2000. **(b)** 3DPC obtained from the Airborne Laser Scanner (ALS) data from December 2014. **(c)** Vertical change in metres, calculated from the comparison of the 2000 and 2014 models. **(d)** Zoom view of the slag heap area, from the 2014 3DPC. **(e)** Vertical change in metres of the slag heap area, shown over the 2014 3DPC. **(f)** Vertical change in metres of the slag heap area. **(g)** Histogram of the elevation changes distributions. Notice the two different Gaussian distributions $Dist_1$ and $Dist_2$.

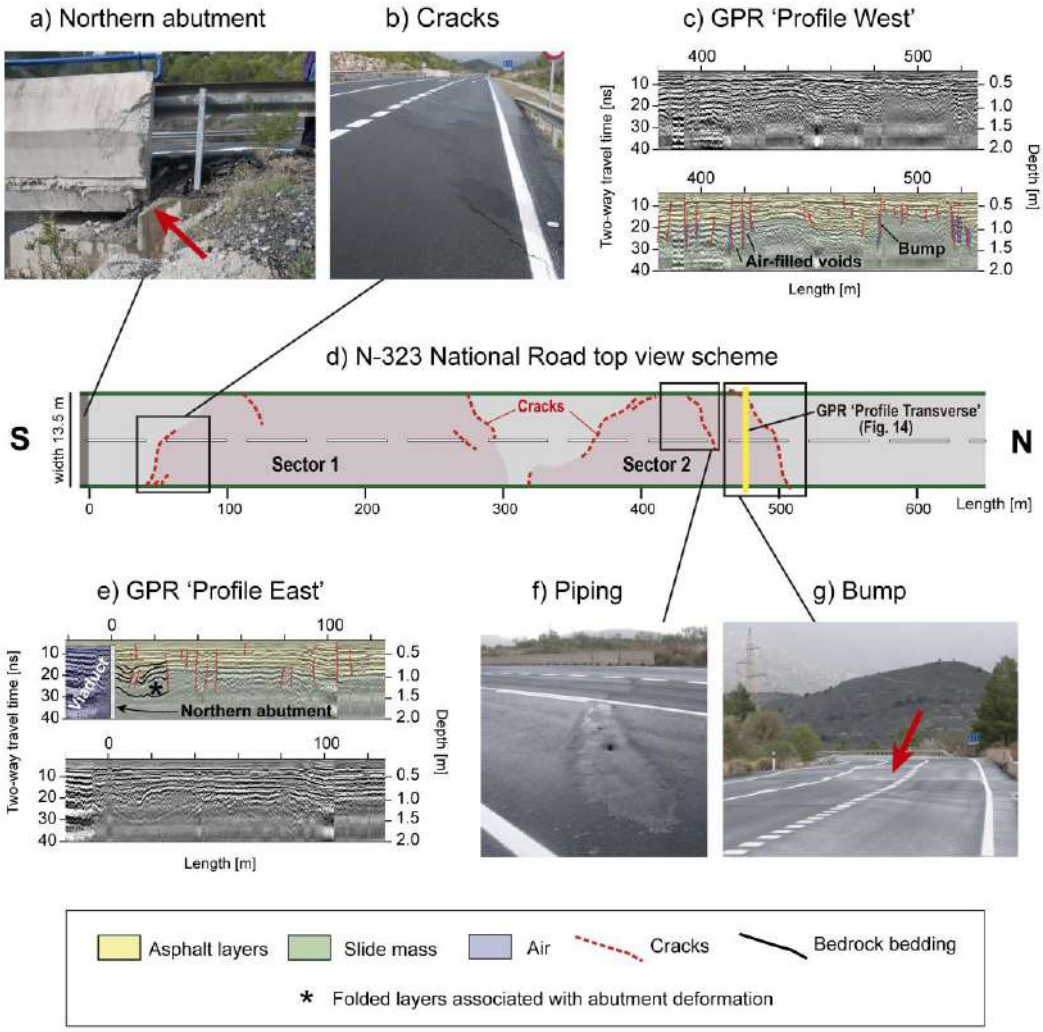

Figure 13. **(a)** Photograph of the northern abutment of the El Arrecife Viaduct. Notice the broken corner marked with a red arrow. **(b)** Cracks on the N-323 National Road surface. **(c)** Extract of the GPR 'Profile West' (length from 390 to 515 m). **(d)** Top view scheme of the N-323 National Road that shows the main damaged areas observed. **(e)** Extract of the GPR 'Profiles East' (length from 0 to 115 m). **(f)** Photograph of a crack with associated piping phenomena. **(g)** Bump on the N-323 National Road, marked with a red arrow.

A large number of vertical cracks were identified within both GPR profiles, which are evidenced by cuts in the continuity of the reflectors (Figures 13c, e). Associated to some of these cracks, several 'air-filled voids' were identified, which are related to opened tensional cracks as a result of piping phenomena. The majority of these cracks do not affect the most superficial asphalt layers and just a few of them are visible on the N-323 National Road surface (Figures 13b, f). Along the road, several cracks that delimited two sectors (Sectors 1 and 2) were mapped, and found to be affected by smaller-scale rotational slides within the whole landslide body (Figure 13d). Close to Sector 1, some damage can be observed within the northern abutment of the El Arrecife Viaduct (Figure 13a), attributed to the pushing of the viaduct into the abutment, which required repair works in 2014 (State Road Demarcation 2020). Folded bedding and asphalt layers can be appreciated within the Profile East (Figure 13e), probably associated with the abutment deformation. Moreover, several NW-SE incipient cracks were found at the southern

boundary of the Sector 1 (Figure 13b). Within Sector 2, a NE-SW crack with associated piping was found (Figure 13f), as well as a prominent NE-SW bump (Figure 13g) that defines the northern boundary of this sector. All of these findings are indicators of the El Arrecife Landslide recent activity, at least during the last two decades. Moreover, a possible northern boundary of the El Arrecife Landslide can be inferred at 625 m within the Profile East (Figure 14a). Such limit clearly separates the slide mass, which is characterised by the absence of reflectors along the profile, from the in situ bedrock that shows a well-marked bedding from 625 to 730 m.

Additionally, the Profile Transverse (Figure 14b) reveals other morphologies typically related to landslide activity. The asphalt layers define a cumulative wedge-out, that is the result of a progressive rotational movement (Gutiérrez et al. 2010) and subsequent deformation of the road. This finding clearly indicates a rotational kinematic for the lower part of the El Arrecife Landslide.

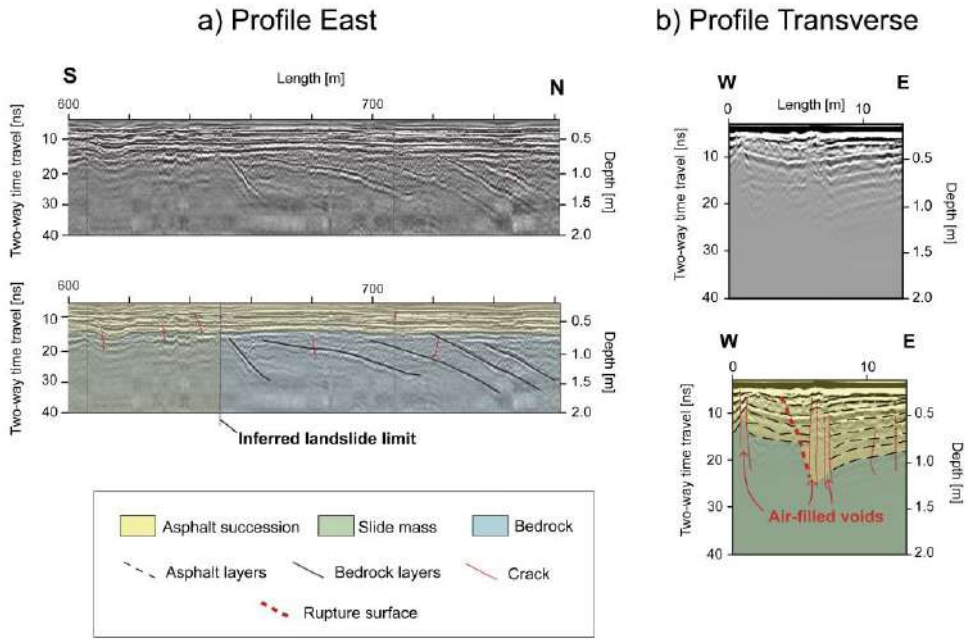

Figure 14. **(a)** Extract of the GPR 'Profile East' (length from 600 to 760 m). **(b)** GPR 'Profile Transverse'. The location of the profile trace across the N-323 National Road is indicated in Figure 13d.

5. Discussion

5.1. Conditioning factors of the El Arrecife Landslide

The understanding of the El Arrecife Landslide was possible by the detailed analysis of the geological and structural settings, given that the geomorphology of the slope does not offer clear signs of the landslide type and characteristics. The great importance of the geological conditions, such as lithology or geological structure, in the El Arrecife Landslide generation has been demonstrated through this work. The slope is made up of phyllites, which represents the main conditioning factor for the landslides in the region, since around 40% of the area where the Alpujárride Complex rocks are exposed is

affected by landslides (El Hamdouni 2001; Chacón et al. 2007). Moreover, from the mechanical point of view, slopes formed by phyllites usually have a great potential to become unstable, due to the phyllites being coarse-grained rocks with a high mica content and a low friction angle (20-27º) (Roopnarine et al. 2013).

The El Arrecife Landslide is also clearly conditioned by the regional structure and the penetrative planar fabric of the phyllite rocks of the Alpujárride Complex. Due to the deformation of these rocks (Simancas 2018 and references therein), changes in orientation of main foliation are expected. Such orientation variability leads to different kinematic scenarios that may, or may not, be conducive to sliding off a slope. For the El Arrecife Landslide case, a favourable planar failure scenario is defined within the landslide perimeter for the Set-1 critical plane orientation, in contrast to other plane orientations (i.e. Set-2 and Set-3) outside of the landslide perimeter. Nevertheless, the presence of a neo-formation surface, not related to foliation planes, cannot be dismissed.

5.2. Estimated displacement rates of the El Arrecife Landslide

The integration of multi-technique results has proved to be an effective procedure for a comprehensive view of the geometry and kinematics of slope movements, as evidenced by recent works (e.g. Janeras et al. 2017; Peduto et al. 2021; Cenni et al. 2021). For our case of study, the selected techniques provided valuable information on the El Arrecife Landslide displacement rate at very different time scales. While DInSAR methods were used to obtain a short-term rate for a time scale of up to 5 years, the GPR technique made a medium-term rate estimation of 22 years possible. The SfM technique did not allow characterising the landslide movement in the last 14 years as the registered movement of the slag heap is not considered as necessarily connected to that of the landslide. One of the main advantages of applying DInSAR and SfM techniques is that they both take advantage of freely available images and follow automated procedures that can produce results in a few days. Moreover, all of these techniques can be applied and interpreted by different teams 100% dedicated to this task, in a matter of about 2 weeks. By using the provided information, a quick evaluation of the slope kinematics that affected a time span of a few decades could be performed.

The multi-technique study that was carried out within the El Arrecife Landslide made it possible to correlate all of the obtained rates to, then, complement and maximise the information provided by each method. Along the N-323 National Road, the subsidence rate obtained by the P-SBAS DInSAR service (1.5-2 cm/year) can be almost correlated with the estimated rate from the GPR data (1.4-2.3 cm/year). On the contrary, the subsidence rate of up to 36 cm/year, estimated from the SfM procedure, significantly differs from the DInSAR and GPR rates. Such difference can be well explained by assuming that the slag heap could have been rapidly sliding during the first years after its construction, due to the initial typical compaction and overall shrinkage of the anthropic filling deposits (Barnes 2016). Our DInSAR results show a mean velocity of 3.6 cm/year in ascending orbit geometry in the slag heap area (Figure 9), in contrast to a highest displacement rate of up to 5 cm/ year, presented by Reyes-Carmona et al. (2020a). Such underestimation of the displacement may be related to the difference in the spatial

resolution (i.e. pixel size) between both data: 14x4 m (Reyes-Carmona et al. 2020a) versus the 90x90 m obtained by the GEP DInSAR service.

5.3. Potential hazard of the El Arrecife Landslide

Once a landslide is identified in a reservoir context, it is essential to discuss about the possibility of a rapid landslide acceleration, or reactivation, and a subsequent collapse of the slide mass into the reservoir. The most dangerous hazard is the generation of an impulse water wave (Gutiérrez et al. 2015). If the impulse wave overtops the reservoir dam, a massive flash flood could be generated downstream from the reservoir, as well as other devastating consequences, such as human and material damage in nearby towns, roads, or power lines among others. The acceleration of landslides is a complex topic under discussion within the scientific community, probably due to the large number of factors that determine the potential of acceleration: (i) the volume of the landslide, (ii) its velocity, (iii) the shear strength of the failure surface, or (iv) the resistance opposed by the reservoir water (Pinyol et al. 2012), among others. Even when considering just one influence factor, there is no agreement. As an example, with respect to the dip angle of failure, Gutiérrez et al. (2015) suggested the existence of a natural threshold around 20º for the development of extremely rapid rockslides, capable of generating impulse water waves. By contrast, Glastonbury and Fell (2010) concluded that the inclination of the basal rupture surface could be as low as 5º. According to the volume of the landslide, it is also difficult to establish a well-proven link with a critical acceleration possibility: the 1000 million m^3 Mayunmaca rockslide in Peru (Kojan and Hutchinson 1978) and the 15 million m^3 Guinsaugon rockslide in the Philippines (Evans et al. 2007) both reached the same velocity, around 35 m/s. Under these uncertainties, the El Arrecife Landslide that presents a surface of rupture dipping 21º and a volume of 14.7 million m^3 could be considered a potential landslide for a fast sliding.

Despite the fact that there are no indicators of a catastrophic failure of the El Arrecife Landslide at present time, this does not imply that a rapid acceleration could not happen in the future (Pinyol et al. 2016). The aforementioned authors referenced several landslides with a relatively slow motion along pre-existing shearing surfaces prior to a sudden failure: the Grijalva landslide in Mexico (Alcántara-Ayala and Domínguez-Morales 2008), the Qianjiangping landslides in China (Wang et al. 2004; Dai et al. 2004), the Val Pola landslide (Govi et al. 2002), and the Sale Mountain landslide (Zhang et al. 2002). The El Arrecife Landslide TS reveals a slow and constant movement of the slope with no indicators of a critical acceleration (Figure 11), although, according to Reyes-Carmona et al. (2020a), an acceleration of the whole landslide body is possible due to its translational character. Despite that, in our opinion, the smaller-scale rotational landslides, located at the foot of the El Arrecife Landslide, are more likely to generate damage in the short term. These rotational landslides have been disrupting the N-323 National Road during the past two decades, at least, as evidenced by GPR findings and field studies, resulting in a constant subsidence of the road and its deterioration. Moreover, the DInSAR TSs revealed higher displacement rates within the El Arrecife Landslide's foot (i.e. Sectors 1, 2, and 3), as well as a correlation between the acceleration

of the movement and periods of decline of the reservoir water level (Figure 11). These findings will serve to develop the importance of a proper management of the Rules Reservoir water level, especially during water discharge operations. Additionally, one should keep in mind that this reservoir is in an active seismic region, with a peak ground acceleration (PGA) of up to 0.2 g (IGN-UPM 2015), which means that earthquakes could reach intensities of up to VIII, according to the European Macroseismic scale (IGN-UPM 2002). These accelerations in unstable slopes could provoke their failure, as evidenced by other worldwide examples of earthquake-triggered landslides: e.g. Rodriguez et al. (1999); Khazai and Sitar (2004); Gorum et al. (2011). For this reason, the catastrophic failures of the whole landslide, or of one of its sectors, are possible scenarios that must be taken into consideration. Regarding the latter scenario, detecting rapid accelerations that may be pre-failure precursors of a landslide is still a challenging task for the research community. Some recent studies demonstrate that DInSAR is a suitable displacement monitoring technique for the recognition of such accelerations (Solari et al. 2018; Dong et al. 2018). Moreover, in case of critical acceleration, it is possible to forecast the time of slope failure by using the Inverse Velocity Method (IVM), developed by Fukuzono (1985). The IVM has been effectively applied to several landslides (e.g. Segalini et al. 2019) and it has also provided satisfactory forecasting results when using DInSAR data (Casagli et al. 2017; Carlà et al. 2017, 2019; Moretto et al. 2017; Intrieri et al. 2018). For the correct implementation of the IVM to identify possible accelerations, the monitoring activity should be constant in time and continued for as long as possible (Valletta et al. 2020). In this sense, the Geohazards Exploitation Platform (GEP) offers the chance to obtain daily DInSAR results, and it could be a promising tool for the continuous monitoring of the El Arrecife Landslide's activity. However, we consider that other DInSAR procedures should also be applied to confirm the GEP applicability. Also, it is our recommendation that in situ measurement techniques, such as inclinometers or GPS, among others, must be applied. These conventional methods provide relevant information not only for validating remotely obtained displacement data but also for their use as an early warning system (Chae et al. 2017). As a paradigmatic example, the Las Torres del Irazú Landslide (Costa Rica) proved the effectiveness of the application of GPS real-time monitoring to successfully forecast the time of failure (August 2020) by using the IVM (Muller et al. 2021).

Lastly, it is our opinion that an inclinometer survey should be carried out to confirm and precisely define the depth of the surface of rupture of the El Arrecife Landslide, and also to monitor its movement. This information is necessary for a more precise estimation of its volume, an essential determining factor to correctly assess the landslide-related hazard (e.g. modelling of an impulse wave in case of landslide collapse). Our study will help in decisions related to where and how deep to drill.

6. Conclusions

The geological and motion data presented in this study highlight the relevance of the El Arrecife Landslide, an extremely large landslide located in an artificial reservoir context. The compiled geological data indicates an estimated possible surface of failure dipping

21º, and a landslide volume of 14.7 million m^3. Furthermore, the lithology and the geological structures have been established as being the main conditioning factors. Moreover, the landslide kinematics have been defined as an overall translational movement, together with a rotational movement within the landslide foot. The translational character could imply a potential hazard of fast sliding and collapse of the whole landslide within the reservoir, which would have devastating consequences. Despite this, the rotational movement within the landslide foot is more likely to generate damage in the short term, especially along the N-323 National Road.

The multi-technique monitoring employed revealed that the El Arrecife Landslide has been active at least since the last two decades: DInSAR provided information for a period up to the last 5 years, while SfM and GPR registered information during 14 and 22 years, respectively. The vertical subsidence of the landslide obtained from DInSAR techniques (1.5-2 cm/year), and estimated from GPR data (1.4-2.3 cm/year), can be almost correlated. SfM provided a higher subsidence rate of 26 cm/year in a small sector of the landslide foot, due to the existence of a slag heap. The main advantage of these techniques is that results can be provided in a quick and easy way by using already registered information, which is essential to evaluate the landslide hazard in case of an alarm situation. Moreover, combining different methods is key to complement the information obtained by each technique, improving confidence in the estimated values.

Finally, it is our recommendation to apply other remote and in situ techniques for a continuous monitoring of the El Arrecife Landslide. DInSAR and GPS are suitable methods for real-time monitoring and also for predicting a possible time of failure, in case of a rapid acceleration of the landslide. On the other hand, other in situ methods should be carried out, such as inclinometers or drilling surveys, to confirm the depth of the failure surface and the volume of the landslide. These attributes are essential for further modelling of the slope, as well as for an accurate landslide hazard assessment. For such purpose, our geological study offers a preliminary characterisation of the landslide that may guide and optimise the planning of future surveys.

Acknowledges and funding

This work was mainly supported by the European Regional Development Fund (ERDF) through the project RISKCOAST (SOE3/P4/E0868) of the Interreg SUDOE Programme. The work of Jorge Pedro Galve, Marcos Moreno-Sánchez, Patricia Ruano and José Miguel Azañón was also supported by the 'Ramón y Cajal' Programme (RYC-2017-23335) of the Spanish Ministry of Science; the project MORPHOMED/PID2019-107138RB-I00 SRA (State Research Agency) and the project RADANDALUS (P18-RT-3632) and B-RNM-305-UGR1818 of the FEDER/Junta de Andalucía-Consejería de Transformación Económica, Industria, Conocimiento y Universidades. The access to the Geohazard Exploitation Platform (GEP) of the European Space Agency (ESA) was provided by the NoR Projects Sponsorship (Project ID: 63737). The authors wish to thank the Road State Demarcation for providing valuable information and testimonies. The authors are grateful to Cristina Accotto and Alejandro Ruiz-Fuentes for the assistance on

the structural geology interpretations. The authors also thank two anonymous reviewers for their comments and Lorenzo Valetti for the language revision.

References

Alcántara-Ayala I, Domínguez-Morales L (2008) The San Juan de Grijalva catastrophic landslide, Chiapas, Mexico: lessons learnt. In: Casagli N, Fanti R, Tofani V (eds) Web Proceedings of the First World Landslide Forum. Tokyo, Japan, pp 96-99

Aldaya F, Díaz de Federico A, García-Dueñas V, Martínez-García E, Navarro- Vilá F, Puga E (1979) Lanjarón-Geological Map of Spain 1:50000. Geological Survey of Spain, Madrid

Azañón JM, Goffé B (1997) Ferro- and magnesiocarpholite assemblages as record of high-P, low-T metamorphism in the central Alpujárrides, Betic Cordillera (SE Spain). Eur J Mineral 9: 1035-1051

Barnes G (2016) Soil mechanics: principles and practice. Macmillan International Higher Education, London

Barra A, Solari L, Béjar-Pizarro M, Monserrat O, Bianchini S, Herrera G, Crosetto M, Sarro R, González-Alonso E, Mateos RM, Ligüerzana S, López C, Moretti S (2017) A methodology to detect and update active deformation areas based on Sentinel-1 SAR images. Remote Sens 9: 1002. https://doi.org/10.3390/rs9101002

Béjar-Pizarro M, Notti D, Mateos RM, Ezquerro P, Centolanza G, Herrera G, Bru G, Sanabria M, Solari L, Duro J, Fernández J (2017) Mapping vulnerable urban areas affected by slow-moving landslides using Sentinel-1 InSAR Data. Remote Sens 9:876. https://doi.org/10.3390/rs9090876

Brunner F, Zobl F, Gassner G (2003) On the capability of GPS for landslide monitoring. Felsbau 21: 51-54

Carlà T, Farina P, Intrieri E, Botsialas K, Casagli N (2017) On the monitoring and early-warning of brittle slope failures in hard rock masses: examples from an open-pit mine. Eng Geol 228:71–81. https://doi.org/10.1016/j.enggeo.2017.08.007

Carlà T, Intrieri E, Raspini F, Bardi F, Farina P, Ferretti A, Colombo D, Novali F, Casagli N (2019) Perspectives on the prediction of catastrophic slope failures from satellite InSAR. Sci Rep 9: 1-9. https://doi.org/10.1038/s41598-019-50792-y

Casagli N, Frodella W, Morelli S, Tofani V, Ciampalini A, Intrieri E, Raspini F, Rossi G, Tanteri L, Lu P (2017) Spaceborne, UAV and ground-based remote sensing techniques for landslide mapping, monitoring and early warning. Geoenviron Disasters 4:1–23. https://doi.org/10.1186/s40677-017-0073-1

Casu F, Elefante E, Imperatore P, Zinno I, Manunta M, De Luca C, Lanari R (2014) SBAS-DInSAR parallel processing for deformation time series computation. IEEE J Sel Top Appl Earth Obs Remote Sen 7: 3285–3296. https://doi.org/10.1109/JSTARS.2014.2322671

Cenni N, Fiaschi S, Fabris M (2021) Integrated use of archival aerial photogrammetry, GNSS, and InSAR data for the monitoring of the Patigno landslide (Northern Apennines, Italy). Landslides. https://doi.org/10.1007/s10346-021-01635-3

Chacón J, Irigaray T, Fernández T (2007) Los movimientos de ladera de la provincia de Granada. In: Ferrer M (ed) Atlas Riesgos Naturales en la Provincia de Granada, 1st edn. Diputación de Granada-Geological Survey of Spain, Madrid, pp 45-82

Chae BG, Park HJ, Catani F, Simoni A, Berti M (2017) Landslide prediction, monitoring and early warning: a concise review of state-of-the-art. Geosci J 21: 1033–1070. https://doi.org/10.1007/s12303-017-0034-4

Clague JJ, Stead D (2012) Landslides: types, mechanisms and modelling. Cambridge University Press

Conyers LB (2015) Analysis and interpretation of GPR datasets for integrated archaeological mapping. Near Surf Geophys 13: 645-651

Corominas J, Moya J, Lloret A, Gili JA, Angeli MG, Pasuto A, Silvano S (2000) Measurement of landslide displacements using a wire extesometer. Eng Geol 55: 149-166. https://doi.org/10.1016/S0013-7952(99)00086-1

Cruden DM, Varnes DJ (1996) Landslide types and processes. In: Turner AK, Schuster RL (eds) Landslides investigation and mitigation. Transportation Research Board, National Academy of Sciences, pp 36-75

Dai FC, Deng JH, Tham LG, Law KT, Lee CF (2004) A large landslide in Zigui County, Three Gorges area. Can Geotech J 41: 1233-1240

De Luca C, Cuccu R, Elefante S, Zinno I, Manunta M, Casola V, Rivolta G, Lanari R, Casu F (2015) An on-demand Web tool for the unsupervised retrieval of earth's surface deformation from SAR Data: the P-SBAS Service within the ESA G-POD Environment. Remote Sens 7: 15630-15650. https://doi.org/10.3390/rs71115630

Dong J, Zhang L, Li M, Yu Y, Liao M, Gong J, Luo H (2018) Measuring precursory movements of the recent Xinmo landslide in Mao County, China with Sentinel-1 and ALOS-2 PALSAR-2 datasets. Landslides 15: 135-144. https://doi.org/10.1007/s10346-017-0914-8

El Hamdouni R (2001) Estudio de Movimientos de Ladera en la Cuenca del Río Ízbor mediante un SIG: Contribución al Conocimiento de la Relación entre Tectónica Activa e Inestabilidad de Vertientes. Doctoral Thesis, University of Granada

Eltner A, Kaiser A, Castillo C, Rock G, Neugirg F, Abellán A (2016) Image-based surface reconstruction in geomorphometry, merits, limits and developments. Earth Surf Dyn 4: 359–389. https://doi.org/10.5194/esurf-4-359-2016

Evans SG, Guthrie RH, Roberts NJ, Bishop NF (2007) The disastrous 17 February 2006 rockslide-debris avalanche on Leyte Island, Philippines: a catastrophic landslide in

tropical mountain terrain. Nat Hazards Earth Syst Sci 7: 89-101. https://doi.org/10.5194/nhess-7-89-200

Fell R (1994) Landslide risk assessment and acceptable risk. Can Geotech J 31: 261-272. https://doi.org/10.1139/t94-031

Fernández-Motril R (2013) N-323: Una Carretera Abandonada Desde 2009. Newspaper Granada Hoy, Granada, Spain

Fernández T, Brabb E, Delgado F, Martin-Algarra A, Irigaray C. Estévez A, Chacón-Montero J (1997) Rasgos geológicos y movimientos de ladera en el sector Ízbor-Vélez Benaudalla de la cuenca del río Guadalfeo (Granada). Proceedings of the IV Simposio Nacional Sobre Taludes y Laderas Inestables, Granada, pp 795-808

Fisher RB, Breckon TP, Dawson-Howe K, Fitzgibbon A, Robertson C, Trucco E, Williams CKI (2013) Dictionary of computer vision and image processing. John Wiley & Sons

Foumelis M, Papadopoulou T, Bally P, Pacini F, Provost F, Patruno J (2019) Monitoring geohazards using on-demand and systematic services on ESA's geohazards exploitation platform. IGARSS 2019–2019 IEEE Inter- national Geoscience and Remote Sensing Symposium, Yokohama, pp 5457–5460. https://doi.org/10.1109/igarss.2019.8898304

Fukuzono T (1985) A new method for predicting the failure time of a slope. Proceedings of the fourth international conference and field workshop on landslides, Tokyo, Japan, pp 145-150

Galve JP, Pérez-Peña JV, Azañón JM, Closson D, Caló F, Reyes-Carmona C, Jabaloy A, Ruano P, Mateos RM, Notti D, Herrera G, Béjar-Pizarro M, Monserrat O, Bally P (2017) Evaluation of the SBAS InSAR Service of the European Space Agency's Geohazard Exploitation Platform (GEP) Remote Sens 9 1291 https://doi.org/10.3390/rs9121291

GSSI (2012) RADAN 7 (Software)

Glastonbury J, Fell R (2010) Geotechnical characteristics of large rapid rock slides. Can Geotech J 47: 116-132

Gorum T, Fan X, van Westen CJ, Huang RQ, Xu Q, Tang C, Wang G (2011) Distribution pattern of earthquake-induced landslides triggered by the 12 May 2008 Wenchuan earthquake. Geomorphology 133:152– 167. https://doi.org/10.1016/j.geomorph.2010.12.030

Govi M, Gullà G, Nicoletti PG (2002) Val Pola rock avalanche of July 28, 1987, in Valtellina (Central Italian Alps). Rev Eng Geol 15: 71-89. https://doi.org/10.1130/REG15-p71

Gullà G, Peduto D, Borrelli L, Antronico L, Fornaro G (2017) Geometric and kinematic characterization of landslides affecting urban areas: the Lungro case study (Calabria, Southern Italy). Landslides 14: 171-188. https://doi.org/10.1007/s10346-015-0676-0

Günther A, Wienhöfer J, Konietzky H (2012) Automated mapping of rock slope geometry, kinematics and stability with RSS-GIS. Nat Hazards 61: 29-49. https://doi.org/10.1007/s11069-011-9771-2

Gutiérrez F, Lucha P, Galve JP (2010) Reconstructing the geochronologi- cal evolution of large landslides by means of the trenching technique in the Yesa Reservoir (Spanish Pyrenees). Geomorphology 124: 124-136. https://doi.org/10.1016/j.geomorph.2010.04.015

Gutiérrez F, Linares R, Roqué C, Zarroca M, Carbonel D, Rosell J, Gutiérrez M (2015) Large landslides associated with a diapiric fold in Canelles Reservoir (Spanish Pyrenees): detailed geological–geomorphological mapping, trenching and electrical resistivity imaging. Geomorphology 241: 224-242. https://doi.org/10.1016/j.geomorph.2015.04.016

Hartley R, Zisserman A (2003) Multiple view geometry in computer vision. Cambridge University Press, Cambridge

IGN-UPM, (2002) Actualización de Mapas de Peligrosidad Sísmica de España 2002 (en valores de intensidad, escala EMS-98). Centro Nacional de Información Geográfica, Madrid

IGN-UPM, (2015) Actualización de Mapas de Peligrosidad Sísmica de España 2012. Centro Nacional de Información Geográfica, Madrid

Intrieri E, Raspini F, Fumagalli A, Lu P, Del Conte S, Farina P, Allievi J, Ferretti A, Casagli N (2018) The Maoxian landslide as seen from space: detect- ing precursors of failure with Sentinel-1 data. Landslides 15: 123-133. https://doi.org/10.1007/s10346-017-0915-7

Jabaloy A, Galindo-Zaldívar J, González-Lodeiro F (1993) The Alpujárride- Nevado-Filábride extensional shear zone, Betic Cordillera, SE Spain. J Struct Geol 15:555–569

Janeras M, Jara JA, Royan MJ, Vilaplana JM, Aguasca A, Fàbregas X, Gili JA, Buxó P (2017) Multi-technique approach to rockfall monitoring in the Montserrat massif (Catalonia, NE Spain). Eng Geol 219: 4-20. https://doi.org/10.1016/j.enggeo.2016.12.010

Jol HM (2008) Ground penetrating radar theory and applications. Elsevier

Khazai B, Sitar N (2004) Evaluation of factors controlling earthquake- induced landslides caused by Chi-Chi earthquake and comparison with the Northridge and Loma Prieta events. Eng Geol 71:79–95. https://doi.org/10.1016/S0013-7952(03)00127-3

Kiersch GA (1964) Vaiont Reservoir disaster. Civ Eng 34: 32-40

Kojan E, Hutchinson JD (1978) Mayunmarca rockslide and debris flow, Peru. In: Voight B (ed) Developments in geotechnical engineering. Elsevier, pp 315-353

Kraus K (1997) Photogrammetry Volume 2 Advanced methods and applications. Dümmler Verlag, Bonn

Lissak C, Maquaire O, Malet JP, Lavigne F, Virmoux C, Gomez C, Davidson R (2015) Ground-penetrating radar observations for estimating the vertical displacement of rotational landslides. Nat Hazards Earth Syst Sci 15: 1399-1406. https://doi.org/10.5194/nhess-15-1399-2015

Manunta M, Bonano M, Buonanno S, Casu F, De Luca C, Fusco A, Lanari R, Manzo M, Ojha, C, Pepe A, Zinno I (2016) Unsupervised parallel SBAS- DInSAR chain for massive and systematic Sentinel-1 data processing. Proceedings of the 2016 IEEE International Geosci Remote Sens Symposium, Beijing, China, pp 3890-3893. https://doi.org/10.1109/igarss.2016.7730010

Martínez-Martínez JM, Soto JI, Balanyá JC (2002) Orthogonal folding of exten- sional detachments: structure and origin of the Sierra Nevada Elongated Dome (Betics, SE Spain). Tectonics 21: 1-3. https://doi.org/10.1029/2001T C001283

Martínez-Martínez JM, Soto JI, Balanyá JC (2004) Elongated domes in extended orogens: a mode of mountain uplift in the Betics (Southeast Spain). Geol Soc A Spec Pap 380: 243-266

Massonnet D, Feigl KL (1998) Radar interferometry and its application to changes in the earth's surface. Rev Geophys 36: 441-500. https://doi.org/10.1029/97RG03139

Moretto S, Bozzano F, Esposito C, Mazzanti P, Rocca A (2017) Assessment of landslide pre-failure monitoring and forecasting using satellite SAR interferometry. Geosciences 7: 36. https://doi.org/10.3390/geoscience s7020036

Muller C, Pacheco J, Angarita M, Alvarado GE, Sánchez B, Avard G (2021) El deslizamiento de las Torres del Irazú del 2020 (Costa Rica): antecedentes, colapso y situación actual. Universidad Nacional de Costa Rica/Observatorio Vulcanológico y Sismológico de Costa Rica/Comisión Nacional de Emergencias. Technical Report, pp. 34

Niethammer U, James MR, Rothmund S, Travelletti J, Joswig M (2012) UAV-based remote sensing of the Super-Sauze landslide: evaluation and results. Eng Geol 128: 2-11. https://doi.org/10.1016/j.enggeo. 2011.03.012

Notti D, Herrera G, Bianchini S, Meisina C, García-Davalillo JC, Zucca F (2014) A methodology for improving landslide PSI data analysis. Int J Remote Sens 35: 2186-2214. https://doi.org/10.1080/01431161. 2014.889864

Pathak S, Nilsen B (2004) Probabilistic rock slope stability analysis for Himalayan conditions. Bull Eng Geol Environ 63: 25-32. https://doi.org/10.1007/s10064-003-0226-1

Peduto D, Santoro M, Aceto L, Borrelli L, Gullà G (2021) Full integration of geomorphological, geotechnical, A-DInSAR and damage data for detailed geometric-kinematic features of a slow-moving landslide in urban area. Landslides 18: 807–825. https://doi.org/10.1007/s10346-020-01541-0

Pinyol NM, Alonso EE, Corominas J, Moya J (2012) Canelles landslide: modelling rapid drawdown and fast potential sliding. Landslides 9: 33-51. https://doi.org/10.1007/s10346-011-0264-x

Pinyol NM, Alonso EE, Corominas J, Moya J (2016) Discussion on 'Large landslides associated with a diapiric fold in Canelles reservoir (Spanish Pyrenees): detailed geological–geomorphological mapping, trenching and electrical resistivity imaging' by Gutiérrez et al. (2015). Geomorphology 263: 170-174. https://doi.org/10.1016/j.geomorph.2015.11.016

Poisel R, Angerer H, Pöllinger M, Kalcher T, Kittl H (2009) Mechanics and velocity of the Lärchberg-Galgenwald landslide (Austria). Eng Geol 109: 57-66. https://doi.org/10.1016/j.enggeo.2009.01.002

Regmi AD, Yoshida K, Nagata H, Pradhan AMS, Pradhan B, Pourghasemi HR (2013) The relationship between geology and rock weathering on the rock instability along Mugling-Narayanghat road corridor, Central Nepal Himalaya. Nat Hazards 66: 501-532. https://doi.org/10.1007/s11069-012-0497-6

Reyes-Carmona C, Barra A, Galve JP, Monserrat O, Pérez-Peña JV, Mateos RM, Notti D, Ruano P, Millares A, López-Vinielles J, Azañón JM (2020a) Sentinel-1 DInSAR for monitoring active landslides in critical infrastructures: the case of the Rules Reservoir (Southern Spain). Remote Sens 12: 809. https://doi.org/10.3390/rs12050809

Reyes-Carmona C, Galve JP, Barra A, Monserrat O, Mateos RM, Azañón JM, Pérez-Peña JV, Ruano P (2020b) The Sentinel-1 CNR-IREA SBAS ser- vice of the European Space Agency's Geohazard Exploitation Platform (GEP) as a powerful tool for landslide activity detection and monitoring. EGU General Assembly Conference Abstracts, pp 19410. https://doi.org/10.5194/egusphere-egu2020-19410

Riquelme A, Del Soldato M, Tomás R, Cano M, Bordehore LJ, Moretti S (2019) Digital landform reconstruction using old and recent open access digital aerial photos. Geomorphology 329: 206-223. https://doi.org/10.1016/j.geomorph.2019.01.003

Rocscience Inc (2004) DIPS (Software)

Rodriguez CE, Bommer JJ, Chandler RJ (1999) Earthquake-induced landslides: 1980–1997. Soil Dyn Earthq Eng 18: 325-346. https://doi.org/10.1016/S0267-7261(99)00012-3

Roopnarine R, Eudoxie G, Opadeyi J (2013) Soil friction angle as an instability factor in landslide susceptibility modelling. Soil Dyn Earthq Eng 3: 55-71

Schuster RL (1979) Reservoir-induced landslides. Bull. Int. Assoc. Eng Geol Bull L'assoc Int Géologie L'ingénieur 20: 8-15. https://doi.org/10.1007/BF02591233

Segalini A, Carri A, Valletta A, Martino M (2019) Innovative monitoring tools and early warning systems for risk management: a case study. Geosciences 9: 62. https://doi.org/10.3390/geosciences9020062

Simancas JF (2018) A reappraisal of the Alpine structure of the Alpujárride Complex in the Betic Cordillera: interplay of shortening and extension in the westernmost Mediterranean. J Struct Geol 115: 231-242. https://doi.org/10.1016/j.jsg.2018.08.001

Simancas JF, Campos J (1993) Compresión NNW-SSE tardi a postmeta- mórfica y extensión subordinada en el Complejo Alpujárride (Dominio de Alborán, Orógeno Bético). Rev Soc Geol España 6: 23-35

Snavely N, Seitz SM, Szeliski R (2008) Modeling the world from internet photo collections. Int J Comput vis 80: 189-210

Solari L, Barra A, Herrera G, Bianchini S, Monserrat O, Béjar-Pizarro M, Crosetto M, Sarro R, Moretti S (2018) Fast detection of ground motions on vulnerable elements using Sentinel-1 InSAR data. Geomatics Nat Hazards Risk 9: 152-174. https://doi.org/10.1080/19475705.2017.1413013

Spanilá T, Horsky O, Banach M (2002) Slides and sliding in the water reservoirs banks. In: Rybár J, Stemberk J, Wagner P (eds) Landslides: Proceedings of the First European Conference on Landslides. Boca Ratón, USA, pp 315

Szeliski R (2010) Computer vision: algorithms and applications. Springer

Tapete D, Cigna F (2017) InSAR data for geohazard assessment in UNE- SCO World Heritage sites: state-of-the-art and perspectives in the Copernicus era. Int J Appl Earth Obs Geoinf 63: 24-32. https://doi.org/10.1016/j.jag.2017.07.007

Teza G, Galgaro A, Zaltron N, Genevois R (2007) Terrestrial laser scanner to detect landslide displacement fields: a new approach. Int J Remote Sens 28: 3425-3446. https://doi.org/10.1080/01431160601024234

Ullman S (1979) The interpretation of visual motion. Massachusetts Institute of Technology

Valletta A, Segalini A, Carri A (2020) Application of a generalized criterion: time-of-failure forecast and alert thresholds assessment for landslides. In: De Mario M, Tiwari AK (eds) Applied geology. Springer, pp 283-298. https://doi.org/10.1007/978-3-030-43953-8_17

Wang FW, Zhang YM, Huo AT, Matsumoto T, Huang BT (2004) The July 14, 2003 Qianjiangping landslide, Three Gorges Reservoir, China. Landslides 1: 157-162. https://doi.org/10.1007/s10346-004-0020-6

Westoby MJJ, Brasington J, Glasser NFF, Hambrey MJJ, Reynolds JMM (2012) Structure-from-motion photogrammetry: a low-cost, effective tool for geoscience applications. Geomorphology 179: 300-314. https://doi.org/10.1016/j.geomorph.2012.08.021

Wyllie DC, Mah C (2004) Rock slope engineering. CRC Press

Chapter V

General discussion and conclusions

1. General discussion

Chapters II, III and IV collect the results of the three study cases of this Ph.D. Thesis. The discussion in each chapter provides new insights into the potential of satellite differential interferometry combined with geological methods for landslide detection, and contributes to the further understanding of the landslides' characteristics and hazard. Nevertheless, a summarised integration of the most important topics of these three chapters is also required. The current section offers a broad discussion of such topics, along with some additional ideas that arose from the research presented in this thesis.

1.1. Applicability of satellite interferometry for landslide research

The value of satellite differential interferometry (DInSAR) for detecting and analysing ground displacements due to landslides has been extensively demonstrated by numerous investigations worldwide. In the last decades, efforts have been focused on the development and optimisation of the processing methods (Ferretti et al. 2001; Berardino et al. 2002; Hooper 2008; Hu et al. 2014; Lee and Shirzaei 2023) and especially, on the applicability of DInSAR to detect and monitor landslides (Colesanti and Wasowski 2006; Herrera et al. 2013; Barra et al. 2016; Bozzano et al. 2017; Solari et al. 2020). This technique has already demonstrated a successful application at different geographical environments, such as coastal areas (Cuervas-Mons et al. 2021), mountainous regions (Bekaert et al. 2020), or urban settlements (Notti et al. 2015). These studies include different scales, ranging from local (Bardi et al. 2014) to regional (Rosi et al. 2018) or national (Dehls et al. 2019; Festa et al. 2022). As a result, DInSAR is already considered a consolidated remote sensing technique for the landslide research community.

The use of DInSAR in this thesis confirms its well-known potential for detecting and mapping new landslides at different contexts and scales. In the Sierra Nevada Range (Chapter II), DInSAR revealed activity in 25 landslides, what facilitated the elaboration of a new landslide inventory at regional-scale. Similarly, DInSAR data allowed performing a local analysis in a strategical infrastructure: the Rules Reservoir, where activity was detected in three landslides and the largest one (El Arrecife) was delimited, for the first time, after being revealed by DInSAR data (Chapter III).

Because of the increasing availability of satellite data, new online platforms are coming to light, such as those supported by European agencies. The Geohazard Exploitation Platform (GEP, https://geohazards-tep.eu/) is a good example. The GEP is an initiative, created by the European Space Agency (ESA), which was set up in October 2016, and provides automated and unsupervised processing chains to derive independent DInSAR data. Recent works already showed satisfactory results for landslide detection by using the GEP services (Galve et al. 2017; Gaidi et al. 2021; Cigna and Tapete 2021) and this

thesis confirms its usefulness in two different locations: the Sierra Nevada range (Chapter II) and the El Arrecife Landslide (Chapter IV). More recently, in May 2022, the European Ground Motion Service (EGMS, https://egms.land.copernicus.eu/) was launched, a very ambitious and unprecedented initiative of the European Copernicus programme. The EGMS offers downloadable DInSAR displacement data, derived from Sentinel-1 images, with a millimetric precision and annual updating from almost all the European countries. These online platforms are very valuable for many sectors, such as academia, industry or public institutions, as they offer the opportunity to work with freely available DInSAR data for non-experts in data processing. However, such supply of data can also be a risky bet, as it provides complex and potentially sensitive information to the general public who may misunderstand or misinterpret it.

The growing availability and dissemination of these free platforms is also increasing the development of new methodologies to semi-automatically extract, simplify and interpret DInSAR data for all kinds of users. For example, Navarro et al. (2020) developed the 'ADAtools', that are tools of great interest for being implemented in a free-of-charge and user-friendly plugin (based on a Geographic Information System, GIS) which can simplify a large amount of DInSAR-derived information. The ADAtools can detect the areas with the highest ground displacement rates (i.e. the Active Deformation Areas, ADAs), as well as inferring the geological or anthropical origin of the displacement: landslide, subsidence or settlements. Other recent research lines of post-processing development are focused on deriving operational products from the raw DInSAR data, with an especial focus on landslide risk assessment. For example, Barra et al. (2022) proposes a semi-automated methodology to derive potential damage maps by calculating velocity gradients from the DInSAR displacement points. Through these maps, it is possible to identify not only buildings prone to damage, but also critical ground unstable areas where urban development could be restricted. Another emerging research field is the integration of DInSAR data into machine learning algorithms for landslide hazard and risk mapping (Novellino et al. 2021), as well as for detecting new landslides (Zhang et al. 2022) or predicting landslide displacement (Wang et al. 2022).

Under this context of high accessibility of free data and automatic tools, erroneous interpretations of the DInSAR data can occur when no expert criteria are applied. It is necessary a solid geological and geomorphological background to correctly interpret the data and the associated processes (e.g. Schlögel et al. 2015). In the case of landslides, a good quality landslide database is crucial. As an example, a landslide inventory has to be integrated with DInSAR data to perform the classification process in the ADAtools (Navarro et al. 2020). Similarly, a thorough geological and geomorphological investigation based on field surveys, sub-surface data from boreholes, aerial photographs and LiDAR data was essential to generate the required inputs for training machine learning algorithms (Novellino et al. 2021). Therefore, it is desirable to generate as much geomorphological information on landslides as possible, since the more complete the landslide database is, the more reliable the results and interpretations derived from DInSAR will be.

1.2. The key role of geology and geomorphology in landslide research

Whether it is to ensure a proper interpretation of the raw DInSAR data or to obtain accurate inputs from semi-automatic tools, a geomorphological investigation for landslide research should be implemented. This thesis aims to emphasise that, despite DInSAR data was useful to first spotlight unstable slopes in both the study areas, an in-depth geomorphological investigation was the decisive procedure to accurately delimit and map the existing landslides. The recognition of surface morphologies such as scarps, cracks, benches and slide masses were useful not only to identify a landslide but also to determine its typology. The geomorphological investigation of this thesis was based on photo-interpretation of aerial photographs and fieldwork, that have been traditionally the main strategy for the study of landslides (Sowers and Royster 1978). The recent availability of very high-resolution DEMs obtained by airborne laser profilers or LiDAR sensors has provided unprecedented opportunities to detect and map landslides (Jaboyedoff et al. 2012). In this sense, the visual inspection DEM-derived products (e.g. maps of contours, shades, slope, aspect, curvature or roughness) has also been an essential procedure for identifying landslide morphologies. In the Sierra Nevada (Chapter II), the geomorphological survey was essential to identify the boundaries of the landslides, as well as to distinguish the typologies: DGSD or rockslide. For the Rules Reservoir area (Chapter III), the geomorphological examination of the slopes, especially through archived aerial photographs (prior and during the reservoir construction) was essential to recognise landslide-related morphologies, and then distinguishing between translational or rotational landslides. The El Arrecife Landslide case (Chapter IV) shows that a standard geological investigation (e.g. collection of field measurements) can also support the estimation of the failure surface geometry, as well as the volume of the landslide.

Geomorphological information is undoubtedly useful, but it is not always included in other fields or investigations. This may be due to a variety of reasons, including a lack of awareness of the potential benefits, limited resources, or competing priorities. For example, Griffiths (2016) expresses concern that geomorphology is not widely implemented in engineering investigations, which usually result in adverse consequences. In this regard, Hearn (2019) presents a case study of landslides on the road network of Ethiopia where in situ geomorphological and geological assessment not only assisted in understanding ground conditions, but also helped in planning sub-surface investigations. This author also proposes an optimal framework for the geo-assessment and modelling of dynamic terrains that fully recognises geomorphology, based on field mapping and supplemented by remote sensing and in situ measurements. On another note, Guzzetti et al. (2012) points out that the number of experienced image interpreters is rapidly decreasing, what is a serious obstacle to produce good quality landslide maps, and thus complicates the validation of new methods for landslide mapping. This fact could lead to a progressive de-emphasis on the rigorousness of landslide investigations and a consequent generation of inaccurate or erroneous maps. Therefore, it is still necessary to emphasise the relevance of geomorphological and geological data for developing a comprehensive understanding of landslides and their hazard. At any case, this task has been greatly facilitated by the application of remote sensing technologies (e.g. DInSAR),

as well as by the combination of many conventional and innovative methods embodied in a multi-disciplinary approach.

1.3. The convenience of a geological multi-technique approach to understand landslides

Apart from the effectiveness of DInSAR techniques and the importance of the geomorphological knowledge, this thesis also shows how other geological methods can enhance the detection, characterisation and mapping of landslides. Several recent works have already demonstrated the potential of multi-technique approaches for landslide research, that usually integrates DInSAR with geological, geomorphological and geotechnical data (Gullà et al 2017; Del Soldato et al. 2018; Peduto et al. 2021), as well as with data derived from photogrammetric techniques (Casagli et al. 2017; Mateos et al. 2017); Global Navigation Satellite Systems (GNSS) (Carlà et al. 2019a; Cenni et al. 2021) or Automated Tracking Total Stations (ATTS) (Vecchiotti et al. 2022). Geophysical methods, such as Electrical Resistivity Tomography (ERT) or Ground-Penetrating Radar (GPR), were also applied to support the characterisation of landslides, often in combination with other geophysical, geomorphological and geotechnical data (Boon et al. 2015; Lissak et al. 2015; Tomás et al. 2018). Nevertheless, geophysical methods and DInSAR are not commonly applied together for the purpose of landslide investigation. For example, DInSAR and GPR data were integrated to monitor the health of infrastructures like bridges (Alani et al. 2020) or railways (Bianchini Ciampoli et al. 2020), as well as to characterise and quantify ground subsidence phenomena (Gutiérrez et al. 2011; Carbonel et al. 2015). Regarding landslides, Cook et al. (2022) investigated an urban landslide by using DInSAR and GPR techniques to identify internal structures of the landslide. In the El Arrecife Landslide case, the integration of DInSAR and GPR data was used, for the first time, to estimate the displacement rate of the landslide at different time-scales (Chapter IV). Other novel combination of techniques in this thesis was the application in the Sierra Nevada Range (Chapter II) of DInSAR techniques and Landscape Analysis based on river gradient-related indexes to identify active landslides. Few investigations integrate the analysis of geomorphic indexes with data derived from other techniques such as geophysics (Nath et al. 2019) or DInSAR (Qureshi and Khan 2020), both cases to assess active tectonics in the Frontal Himalayas. In this sense, this thesis presents the first study case in which DInSAR and a gradient-related index (the k_{snn}) were applied with the purpose of detecting landslides (Chapter II).

Therefore, the multi-disciplinary approach carried out in this thesis proves to have been a good option landslide mapping and characterisation in the three study cases. In the Sierra Nevada Range (Chapter II), the integration of DInSAR data, k_{snn} index anomalies and geomorphological observations made it possible to reveal the presence of large landslides, their activity at different time scales and their typology (DGSDs and rockslides). In the case of the Rules Reservoir (Chapter III), DInSAR data and geomorphological observations allowed detecting and characterising three active landslides: two of rotational retrogressive type (the Lorenzo-1 and Rules Viaduct landslides) and one of translational type (the El Arrecife Landslide). In Chapter IV, a

comprehensive characterisation of the Arrecife Landslide was possible by the combination of data derived from structural fieldwork, kinematic analysis, DInSAR, GPR and SfM methods. It is important to remark that these techniques not only generated accurate information, but also produced prompt results by using already registered and freely available data.

The combination of different DInSAR processing chains in this thesis also gives some insights about their utility and potential. The El Arrecife Landslide was analysed through both, the PSIG (Chapter III) and P-SBAS (Chapter IV), and shows that both chains are feasible enough to spotlight this unstable slope, although results of different resolutions were provided. The PSIG results are of a better spatial resolution (14x4m), what means a higher accuracy of the obtained displacement rates. In contrast, the P-SBAS results are of lower spatial resolution (90x90m) and the detected displacements are also lower. By comparing the displacement rates obtained from different chains, the SBAS underestimated the movement around 1.5 cm/year with respect to the PSIG. This underestimation can be compensated by the temporal operability of the P-SBAS chain, as it can be used automatically and unsupervised through the GEP to obtain rapid results (24-48 h). This fast-processing also allows to obtain results in both orbits and easily execute post-processing calculations (e.g. horizontal and vertical displacement) (Chapter IV). Although the PSIG chain provides more accurately results, its application in this thesis was much more laborious (around, 2 months of work). Therefore, the PSIG chain is more appropriate to rigorously quantify ground movements, while the P-SBAS may be the best choice for spotlighting unstable slopes.

1.4. Landslide hazard in the Sierra Nevada Range and the Rules Reservoir: a new perspective

The geological and geomorphological knowledge of landslides generated through the many methodologies applied offer new insights about the landslide-hazard in both areas of this thesis. The preliminary hazard scenarios depend primarily on (1) the geographical context: a high-relief mountain range vs. an artificial water reservoir, and (2) the types of landslides: DGSD/rockslide in the Sierra Nevada vs. translational/rotational slides in the Rules Reservoir.

In the case of the Sierra Nevada Range, where DGSDs are prevalent, even their slow movement can threaten critical infrastructures, such as the hydroelectric plant of Pampaneira (Alonso et al. 2021). Although the temporal movement pattern of DGSDs is usually a constant (i.e. slope creeping), it can be disturbed by rapid accelerations and lead to more risky scenarios (Pánek and Klimeš 2016). Therefore, the main hazard of DGSDs is the possibility of evolving to faster and more destructive secondary movements, such as rotational/translational slides or rock/debris avalanches. Rock avalanches and rockslides would be the most hazardous scenarios in localised areas within DGSDs, resulting in catastrophic events (Pedrazzini et al. 2013). Such faster movements are usually triggered by earthquakes, intense or cumulative precipitation or snowmelt (e.g. Crosta and Agliardi 2002; Moro et al. 2009; Chigira 2009; Nie et al. 2017). DGSDs are easily overlooked, and they are not usually contemplated on landslide inventory maps

(Ambrosi and Crosta 2006), as they are huge old landslides with very diffuse boundaries. For this reason, it is essential to focus not only on the smaller and more visible nested movements, but also on the full dimensions of the DGSDs to properly evaluate hazard scenarios, monitoring surveys and stabilisation measurements (Soldati et al. 2013). The understanding of the internal geological structure, the spatial distribution of DGSDs in the region and their role in the landscape evolution can provide important information to assess hazard (e.g. Agliardi et al. 2013; Tsou et al. 2015). In this sense, a preliminary step toward landslide hazard and risk assessment is to produce a landslide inventory map (Guzzetti et al. 2006; Van Westen et al. 2006). These authors also point out about the tediousness of the inventory procedure over time. Usually, universities and research centres produce detailed inventory maps, but they use to be only in specific areas in the framework of research projects with limited duration. This fact complicates the production and updating of a wide landslide database. Greater efforts are done in Spain to complete and improve the existing landslide database from the Geological and Mining Institute of Spain, IGME-CSIC (the BD-MOVES, https://info.igme.es/BDMOVES/), as made in the case of Sierra Nevada (Chapter II). New works, like the present thesis, can contribute to the enrichment previous landslide databases by including some types of landslides not commonly identified, such as DGSDs. In the case of Spain, DGSDs have been only described in the Pyrenees (Gutiérrez et al. 2005; Herrera et al. 2013; Troiani et al. 2014). Therefore, the priority in the Sierra Nevada for a proper hazard assessment should be not only to continue detecting and mapping new landslides of this type (through conventional and innovative methods), but also to perform detailed investigations about the internal segmentation and kinematics of the already known DGSDs.

The case of the Rules Reservoir (Chapters III and IV) presents a different hazardous situation. The landslides are of the type rotational and translational and their activity is related to the position of the reservoir water level. The rotational landslides evidence a retrogressive evolution that impact on numerous infrastructures: the Lorenzo-1 Landslide has been generating damages along the N-323 National Road, while the Rules Viaduct Landslide could generate future damages to the southern abutment and southern pier of the Rules Viaduct. Such damage to the viaduct may be already occurring at present, as DInSAR also registered a small displacement along the viaduct that could be related to this landslide (Chapter III). The rotational landslides of the El Arrecife Landslide' foot have been also generating damages to the N-323 National Road during the last two decades. This is the most current hazard derived from El Arrecife Landslide, although the possibility of a partial or total collapse of the landslide cannot be excluded. Because of the translational character of the El Arrecife Landslide, a rapid acceleration of the whole landslide body should not be discarded. The variations of the water level of a reservoir often trigger changes in the movement of landslides, for which it is essential to control the velocity of drawdowns of the water level (e.g. Zhou et al. 2020; Xu et al. 2021). In the Rules reservoir, the drawdown velocity of summer-autumn 2016 and spring 2017-winter 2018 was 6.4 cm/day. At first glance, this velocity seems not to be enough to generate a rapid acceleration or collapse of a landslide, in comparison to documented velocities in other reservoirs. For example, drawdown velocities from 50 to 120 cm/day

reactivated a large translational landslide in the Canelles Reservoir, Spain (Pinyol et al. 2012). These authors also estimated a secure drawdown velocity of 15 cm/day to ensure the stability of this slope. The DInSAR TSs indicated that the previously mentioned drawdowns in the Rules Reservoir were not rapid enough to cause an acceleration of the El Arrecife Landslide. (Chapter III). On the contrary, these drawdowns triggered slight accelerations in both the Lorenzo-1 and the Rules Viaduct rotational landslides (Chapter III). Similarly, the drawdown of spring 2017-winter 2018 caused a slight acceleration of the rotational landslides located at the foot of the El Arrecife Landslide (Chapter IV). During this drawdown period, the Rules Viaduct Landslide and the lower part of El Arrecife Landslide achieve very low velocities: 0.09 mm/day and 0.18 mm/day, respectively. These velocities are negligible in comparison to those that led to catastrophic failures or risky situations in other cases. A well-known example is the Vajont Landslide (Italy), that collapsed in 1963 into a reservoir with devastating consequences, and reached pre-failure velocities from 5 mm/day to 20 cm/day (Carlà et al. 2017). Other example in a reservoir context is the Shuping Landslide in China, that was reactivated in 2013 and reached velocities up to 18.4 mm/day during water level drawdowns (Song et al. 2018). Therefore, the low accelerations of the rotational landslides in the Rules Reservoir, together with the fact that they tend to re-establish their equilibrium when the water level rises, means that they are not significantly hazardous for the reservoir shorelines at present. Similarly, the El Arrecife Landslide does not pose an imminent hazard of rapid and catastrophic slope failure, at least under the current drawdown velocities of the reservoir. However, it is important to consider that the El Arrecife Landslide remains a potential candidate for rapid movements in the future due to several factors, that includes its continuous activity (for at least the last 22 years), large volume (14.7×10^6 m^3), dipping of the surface of rupture (21º), and overall translational kinematics. Rapid accelerations could be triggered by abnormal factors, such as extremely high drawdown velocities, a long period of intense rainfall, an earthquake or a combination of many of these factors (Pinyol et al. 2012; Song et al. 2018; Handwerger et al. 2019). As an example, the Xinmo Landslide in China (2017) was a catastrophic slope failure mainly triggered by prolonged rainfall, but the rock mass would have already been progressively weakened by strong earthquakes (M_w 7.2-7.9) since 1933 (Fan et al. 2017). When considering the significance of a critical infrastructure, such as a reservoir, continuous monitoring of its slopes is strongly recommended. For detecting possible pre-failure precursors, hazard assessment in the Rules Reservoir should be focused on developing a real-time monitoring strategy for the identified active landslides, by the combination of DInSAR techniques (Carlà et al. 2019b; Moretto et al. 2021) and in situ methods, such as GPS or boreholes inclinometers (Liu et al. 2019).

Finally, it is important to remind that both, the Sierra Nevada range and the Rules Reservoir are located in an active seismic region (the highest of the Iberian Peninsula). Seismic activity is concentrated along the western and southern borders of the Sierra Nevada, including the extensional system of the Granada Basin (Madarieta-Txurruka et al. 2022). Many of the active faults of this system are potential seismic sources of earthquakes with moment magnitudes (M_w) larger than 6.0 (Sanz de Galdeano et al.

2003). It is important to highlight that the region has already experienced significant earthquakes ranging from M_w 4.9 to 6.5, which triggered slope failures (Morales et al. 1996; Rodríguez-Peces et al. 2011, 2014). Moreover, despite the semi-arid climate of the region, periods of extreme precipitation are expected. In the well-known 1996-1997 and 2009-2010 hydrological years, the average annual precipitation was more than doubled (Jiménez-Perálvarez et al. 2017) and numerous landslides were triggered (Palenzuela et al. 2016), that resulted in severe damage to some of the villages of 'La Alpujarra' (southern side of the Sierra Nevada range) (Chacón et al. 2007; Jiménez-Perálvarez 2012). Although there is no immediate cause for social alarm regarding landslide hazard in the analysed areas of this thesis, it is crucial to consider the influence of possible extraordinary events, such as the previously described earthquakes or extreme precipitation. These occurrences could potentially lead to hazardous scenarios related to the studied landslides in both the Sierra Nevada and the Rules Reservoir areas. Therefore, it is still necessary to conduct further investigations to better understand and manage potential risks associated with these landslides.

2. Conclusions

This Ph.D. Thesis demonstrates the potential of a multi-technique approach that integrates Differential Satellite Interferometry (DInSAR) with geological methods to successfully detect and characterise landslides in two different geographical contexts: a high-relief mountain range and an artificial water reservoir. The geomorphological investigation was crucial, based on in situ field surveys, exploration of high-resolution Digital Elevation Models (DEMs), and photo-interpretation of aerial images. One of the objectives of this thesis is to highlight the importance of the geomorphological methods in the procedure of landslide mapping. The other used methods include (1) geomorphic analysis of the landscape, through the normalised steepness index (k_{sn}) of river channels; (2) geophysical techniques, by using the Ground Penetrating Radar (GPR); (3) photogrammetric techniques, through the Structure-for-Motion (SfM) method; and (4) structural and kinematic analysis, through fieldwork and basic tools on a Geographic Information System (GIS) environment. These techniques and procedures were applied in one or more of the selected study cases: the Sierra Nevada Range (Chapter II), the Rules Reservoir (Chapter III) and the El Arrecife Landslide (Chapter IV). The scale of the final products varies from a regional landslide inventory map, in the case of Sierra Nevada, to detailed geomorphological maps of independent landslides, in the case of the Rules Reservoir. The El Arrecife Landslide, located in the western slope of the Rules Reservoir, is the case where a detailed geological analysis regarding its internal structure, kinematics and displacement patterns was performed. In this way, the specific results of this thesis have been addressed with the following conclusions related to each of the three study cases:

- **Sierra Nevada**. The integration of DInSAR and Landscape Analysis techniques enhanced the detection and mapping of large landslides in the southwestern sector of Sierra Nevada. The Landscape Analysis was based on the double normalised steepness index (k_{snn}), a novel variant derived from the conventional k_{sn} index to reduce the effect of tectonics in the Sierra Nevada. The combination of both

techniques allowed overcoming some of their individual limitations and offered two distinct temporal perspectives of the landslides: DInSAR revealed their short-term activity (5 years), while k_{snn} anomalies suggested their long-term movement (centuries or millennia). The visualisation of the unstable areas revealed by DInSAR and the k_{snn} anomalies along rivers enabled the production of an updated inventory map of 28 new landslides in this range. Such mapping indicates a significant increase in the area affected by landslides, from 14.5% (database of the Geological Institute of Spain, IGME-CSIC) to 33.5% in this study. For the first time, 8 rockslides and 17 large Deep-seated Gravitational Slope Deformations (DGSDs) were identified in the Sierra Nevada Range. Mapping the DGSDs was an arduous task due to their large size, poorly-defined boundaries, uniform lithology (mainly schists), and the presence of glacial landforms in the area. The assessment of DGSDs hazard should be enhanced in further investigation of their internal structure to evaluate the possibility of evolving to faster destructive secondary movements, such as rockslides or rock avalanches, which could be triggered by exceptional events like earthquakes or intense precipitation.

- **Rules Reservoir**. The combination of DInSAR and classical geomorphological research (photo-interpretation and fieldwork) allowed to detect three active landslides in the Rules Reservoir's slopes, as well as to understand the general kinematic and triggering factors of their displacement. The Lorenzo-1 and the Rules Viaduct landslides are retrogressive rotational landslides, with an average displacement along the satellite Line-of-Sight (LoS) of around -15 mm/yr. The most significant finding regarding these landslides is the acceleration of their movement in correlation with drawdowns of the reservoir water level. These landslides do not represent a significant hazard to the reservoir shorelines due to their dimensions and typology, what makes it improbable a rapid acceleration of their movement if the reservoir water level is properly managed. However, their risk is associated to their affection to other infrastructures: the Lorenzo-1 Landslide is damaging the N-323 National Road, and the Rules Viaduct Landslide may be threatening the integrity of the southern sector of the Rules Viaduct. The application of DInSAR techniques in this reservoir also proves that the Rules Dam is stable, and that the southern part of the Rules Viaduct (A-44 Highway) is suffering a slight deformation, probably related to the adjacent landslide.
- **El Arrecife Landslide**. This landslide was not easily identifiable in the landscape and it was first mapped in this thesis. A detailed and rapid characterisation of this landslide was carried out by incorporating geological, geophysical (based on GPR) and remote sensing techniques, that includes DInSAR and photogrammetry (SfM). Made of very deformed phyllites, it is a translational landslide with a mean LoS displacement rate around -25 mm/yr, and a linear displacement pattern that is not overall affected by the reservoir water level variations. The in situ geological data was used to define the most likely orientation for a planar slope failure (21/120), which was proposed as the possible surface of rupture of the El Arrecife Landslide and led to a volume estimation of 14.7 million m^3. Although

the entire landslide body has a translational kinematic, the landslide's foot is affected by numerous smaller-sized rotational slides. The DInSAR times series (TSs) showed that these rotational slides are accelerated in correlation with reservoir water level drawdowns. The combination of ascending and descending images data allowed to decompose the vertical velocity of the landslide (-15 mm/yr), which could be almost correlated with the vertical subsidence rate inferred from the GPR data (around 20 mm/yr). Both techniques also offered two distinct temporal perspectives of the landslide activity: short-term by DInSAR (5 years) and medium-term by GPR (22 years). Furthermore, no rapid shallow failures have been detected through the SfM method within the landslide body in the last 14 years. The characteristics of this landslide (translational kinematics and large volume) does not allow to rule out major dangers like the occurrence of a rapid and critical acceleration of the entire landslide body, particularly in response to exceptional events, such as drastic reservoir water level drawdowns, heavy rainfall or an earthquake. Nevertheless, the greatest hazard of the El Arrecife Landslide is related to the rotational slides at the landslide's foot, that have been damaging the N-323 National Road for the last decades and will surely continue.

3. Future research

The results of this Ph.D. Thesis represent an important contribution for landslide mapping and characterisation of the analysed areas, as well as for demonstrating the applicability of several techniques in combination. However, some issues remain open for future research, some of which have already been mentioned in the previous sections and chapters. The most significant open issues and possible approaches to address them are stated below:

- Other techniques should be applied for a real-time continuous monitoring of the active landslides in the Rules Reservoir, with an especial focus on the El Arrecife Landslide. Not only remote sensing methods (DInSAR and GPS), but also in situ conventional measurement techniques (boreholes inclinometers and extensometers) are suitable enough to detect possible pre-failure accelerations of a landslide (e.g. Crosta et al. 2017; Song et al. 2018). In situ measurement such as GPS, GNSS or Total Stations could be also valuable to monitor the movement of DGSDs in the Sierra Nevada, as usually performed to investigate DGSDs in other locations (e.g. Crippa et al. 2020).
- Both drilling and inclinometer surveys would be also essential to precisely define the depth of the failure surface of the El Arrecife Landslide. A more precise definition of the geometry and calculation of the landslide volume is needed.
- Drilling and geotechnical surveys would be also necessary to obtain the mechanical parameters of the rocks (e.g. Corominas et al. 2005) in both study areas: phyllites of the Alpujárride Complex and the schists of the Nevado-Filábride Complex. These data could provide valuable information for many purposes, such for numerical modelling of the slope failures (e.g. Pinyol et al. 2012; López-Vinielles et al. 2021), in special for the El Arrecife Landslide case.

The lithological influence as a conditioning factor on the DGSDs and rockslides generation could be relevant. It would be necessary to prove considerable mechanical differences between the graphitic schists of the La Ragua Unit and the graphitic mica-schists of the Calar-Alto Unit. In such case, the lithological contact could be the failure surface of these deep slope movements. The provided information would be also valuable to further understand the active slope instability processes in the same region where these rocks outcrop.

- A dendrochronological analysis could be also performed to further understand the evolution and activity of the landslides. This analysis could be well-integrated with DInSAR and geomorphological data (e.g. Bozzano et al. 2020). This dating technique could be applied in the El Arrecife Landslide as well as in some DGSDs in the Sierra Nevada, where some pine trees have already been sighted as good candidates.
- Detailed investigations, such as those made by Agliardi et al. (2001), to describe the morphological and structural features of the DGSDs and rockslides are still necessary for a comprehensive understanding of this phenomena. This study should be focused on defining the influence of foliation orientation and/or brittle structures on these large landslides' generation. This information is also necessary to perform geomechanical simulations about the evolution of these large landslides. Moreover, it would be interesting to investigate about the interplays between different processes (e.g. tectonic exhumation, fluvial incision, landslides), that control the long-term evolution of the orogenic landscape in the Sierra Nevada Range. Some previous works in the Southern Alps of New Zealand (Korup 2005), in the European Alps (Agliardi et al. 2013) and in the Central Range of Taiwan (Tsou et al. 2015) can inspire this line.

References

Agliardi F, Crosta G, Zanchi A (2001) Structural constraints on deep-seated slope deformation kinematics. Eng Geol 59: 83-102. https://doi.org/10.1016/S0013-7952(00)00066-1

Agliardi F, Crosta GB, Frattini P, Malusà MG (2013) Giant non-catastrophic landslides and the long-term exhumation of the European Alps. Earth Planet Sci Lett 365: 263-274. https://doi.org/10.1016/j.epsl.2013.01.030

Alani AM, Tosti F, Ciampoli LB, Gagliardi V, Benedetto A (2020) An integrated investigative approach in health monitoring of masonry arch bridges using GPR and InSAR technologies. NDT E Int 115: 102288. https://doi.org/10.1016/j.ndteint.2020.102288

Alonso EE, Sondon M, Alvarado M (2021) Landslides and hydraulic structures. Eng Geol 292: 106264. https://doi.org/10.1016/j.enggeo.2021.106264

Ambrosi C, Crosta GB (2006) Large sackung along major tectonic features in the Central Italian Alps. Eng Geol 83:183-200. https://doi.org/10.1016/j.enggeo.2005.06.031

Bardi F, Frodella W, Ciampalini A, Bianchini S, Del Ventisette C, Gigli G, Fanti R, Moretti S, Basile G, Casagli N (2014) Integration between ground based and satellite SAR data in landslide mapping: The San Fratello case study. Geomorphology 223: 45-60. https://doi.org/10.1016/j.geomorph.2014.06.025

Barra A, Monserrat O, Mazzanti P, Esposito C, Crosetto M, Scarascia-Mugnozza G (2016) First insights on the potential of Sentinel-1 for landslides detection. Geomatics, Nat Hazards Risk 7: 1874-1883. https://doi.org/10.1080/19475705.2016.1171258

Barra A, Reyes-Carmona C, Herrera G, Galve JP, Solari L, Mateos RM, Azañón JM, Béjar-Pizarro M, López-Vinielles J, Palamà R, Crosetto M, Sarro R, -Mons J, Monserrat O (2022) From satellite interferometry displacements to potential damage maps: A tool for risk reduction and urban planning. Remote Sens Environ 282: 113294. https://doi.org/10.1016/j.rse.2022.113294

Bekaert DP, Handwerger AL, Agram P, Kirschbaum DB (2020) InSAR-based detection method for mapping and monitoring slow-moving landslides in remote regions with steep and mountainous terrain: An application to Nepal. Remote Sens Environ 249:111983. https://doi.org/10.1016/j.rse.2020.111983

Berardino P, Fornaro G, Lanari R, Sansosti E (2002) A new algorithm for surface deformation monitoring based on small baseline differential SAR interferograms. IEEE Trans Geosci Remote Sens 40: 2375-2383. https://doi.org/10.1109/TGRS.2002.803792

Bianchini Ciampoli L, Gagliardi V, Clementini C, Latini D, Del Frate F, Benedetto A (2020) Transport infrastructure monitoring by InSAR and GPR data fusion. Sur Geophys 41: 371-394. https://doi.org/10.1007/s10712-019-09563-7

Boon DP, Chambers JE, Hobbs PR, Kirkham M, Merritt AJ, Dashwood C, Pennington C, Wilby PR (2015) A combined geomorphological and geophysical approach to characterising relict landslide hazard on the Jurassic Escarpments of Great Britain. Geomorphology 248: 296-310. https://doi.org/10.1016/j.geomorph.2015.07.005

Bozzano F, Mazzanti P, Perissin D, Rocca A, De Pari P, Discenza ME (2017) Basin scale assessment of landslides geomorphological setting by advanced InSAR analysis. Remote Sens 9: 267. https://doi.org/10.3390/rs9030267

Bozzano F, Carabella C, De Pari P, Discenza ME, Fantucci R, Mazzanti P, Miccadei E, Rocca A, Romanco S, Sciarra N (2020) Geological and geomorphological analysis of a complex landslides system: The case of San Martino sulla Marruccina (Abruzzo, Central Italy). J Maps 16: 126-136. https://doi.org/10.1080/17445647.2019.1702596

Carbonel D, Rodríguez-Tribaldos V, Gutiérrez F, Galve JP, Guerrero J, Zarroca M, Roqué C, Linares R, McCalpin JP, Acosta E (2015) Investigating a damaging buried sinkhole cluster in an urban area (Zaragoza city, NE Spain) integrating multiple techniques: Geomorphological surveys, DInSAR, DEMs, GPR, ERT, and trenching. Geomorphology 229: 3-16. https://doi.org/10.1016/j.geomorph.2014.02.007

Carlà T, Intrieri E, Di Traglia F, Nolesini T, Gigli G, Casagli N (2017) Guidelines on the use of inverse velocity method as a tool for setting alarm thresholds and forecasting landslides and structure collapses. Landslides 14: 517-534. https://doi.org/10.1007/s10346-016-0731-5

Carlà T, Tofani V, Lombardi L, Raspini F, Bianchini S, Bertolo D, Thuegaz P, Casagli N (2019a) Combination of GNSS, satellite InSAR, and GBInSAR remote sensing monitoring to improve the understanding of a large landslide in high alpine environment. Geomorphology: 335, 62-75. https://doi.org/10.1016/j.geomorph.2019.03.014

Carlà T, Intrieri E, Raspini F, Bardi F, Farina P, Ferretti A, Colombo D, Novali F, Casagli N (2019b) Perspectives on the prediction of catastrophic slope failures from satellite InSAR. Sci Rep 9: 14137. https://doi.org/10.1038/s41598-019-50792-y

Casagli N, Frodella W, Morelli S, Tofani V, Ciampalini A, Intrieri E, Raspini F, Rossi G, Tanteri L, Lu P (2017) Spaceborne, UAV and ground-based remote sensing techniques for landslide mapping, monitoring and early warning. Geoenvironmental Disasters 4: 1-23. https://doi.org/10.1186/s40677-017-0073-1

Cenni N, Fiaschi S, Fabris M (2021) Integrated use of archival aerial photogrammetry, GNSS, and InSAR data for the monitoring of the Patigno landslide (Northern Apennines, Italy). Landslides 18: 2247-2263. https://doi.org/10.1007/s10346-021-01635-3

Chacón J, Irigaray T, Fernández T (2007) Los movimientos de ladera de la provincia de Granada. In: Ferrer M (ed) Atlas Riesgos Naturales en la Provincia de Granada, 1st edn. Diputación de Granada-Geological Survey of Spain, Madrid, pp 45–82

Chigira M (2009) September 2005 rain-induced catastrophic rockslides on slopes affected by deep-seated gravitational deformations, Kyushu, southern Japan. Eng Geol 108: 1-15. https://doi.org/10.1016/j.enggeo.2009.03.005

Cigna F, Tapete D (2021) Sentinel-1 big data processing with P-SBAS InSAR in the geohazards exploitation platform: An experiment on coastal land subsidence and landslides in Italy. Remote Sens 13:885. https://doi.org/10.3390/rs13050885

Colesanti C, Wasowski J (2006) Investigating landslides with space-borne Synthetic Aperture Radar (SAR) interferometry. Eng Geol 88: 173-199. https://doi.org/10.1016/j.enggeo.2006.09.013

Coo ME, Brook MS, Hamling IJ, Cave M, Tunnicliffe JF, Holley R, Alama DJ (2022) Engineering geomorphological and InSAR investigation of an urban landslide, Gisborne, New Zealand. Landslides 19: 2423-2437. https://doi.org/10.1007/s10346-022-01938-z

Corominas J, Moya J, Ledesma A, Lloret A, Gili JA (2005) Prediction of ground displacements and velocities from groundwater level changes at the Vallcebre landslide (Eastern Pyrenees, Spain). Landslides 2: 83-96. https://doi.org/10.1007/s10346-005-0049-1

Crippa C, Franzosi F, Zonca M, Manconi A, Crosta GB, Dei Cas L, Agliardi F (2020) Unraveling spatial and temporal heterogeneities of very slow rock-slope deformations with targeted DInSAR analyses. Remote Sens 12: 1329. https://doi.org/10.3390/rs12081329

Crosta GB, Agliardi F (2002) How to obtain alert velocity thresholds for large rockslides. Phys Chem Earth 27: 1557-1565. https://doi.org/10.1016/S1474-7065(02)00177-8

Crosta GB, Agliardi F, Rivolta C, Alberti S, Dei Cas L (2017) Long-term evolution and early warning strategies for complex rockslides by real-time monitoring. Landslides, 14, 1615-1632. https://doi.org/10.1007/s10346-017-0817-8

Cuervas-Mons J, Domínguez-Cuesta MJ, Mateos Redondo F, Barra A, Monserrat O, Valenzuela P, Jiménez-Sánchez M (2021) Sentinel-1 data processing for detecting and monitoring of ground instabilities in the rocky coast of central Asturias (N Spain). Remote Sens 13: 3076. https://doi.org/10.3390/rs13163076

Dehls JF, Larsen Y, Marinkovic P, Lauknes TR, Stødle D, Moldestad DA (2019) INSAR. No: A national insar deformation mapping/monitoring service in Norway--From concept to operations. Proceedings of the IGARSS-IEEE International Geoscience and Remote Sensing Symposium, Yokohama, Japan, pp 5461-5464. https://doi.org/10.1109/IGARSS.2019.8898614

Del Soldato M, Riquelme A, Bianchini S, Tomás R, Di Martire D, De Vita P, Moretti S, Calcaterra D (2018) Multisource data integration to investigate one century of evolution for the Agnone landslide (Molise, southern Italy). Landslides 15: 2113-2128. https://doi.org/10.1007/s10346-018-1015-z

Fan X, Xu Q, Scaringi G, Dai L, Li W, Dong X, Zhu X, Pei X, Dai K, Havenith HB (2017) Failure mechanism and kinematics of the deadly June 24th 2017 Xinmo landslide, Maoxian, Sichuan, China. Landslides 14: 2129-2146. https://doi.org/10.1007/s10346-017-0907-7

Ferretti A, Prati C, Rocca F (2001) Permanent scatterers in SAR interferometry. IEEE Trans Geosci Remote Sens 39: 8-20. https://doi.org/10.1109/36.898661

Festa D, Bonano M, Casagli N, Confuorto P, De Luca C, Del Soldato M, Lanari R, Lu P, Manunta M, Manzo M, Onorato G, Raspini F, Zinno I, Casu F (2022) Nation-wide mapping and classification of ground deformation phenomena through the spatial clustering of P-SBAS InSAR measurements: Italy case study. J Photogramm Remote Sens 189: 1-22. https://doi.org/10.1016/j.isprsjprs.2022.04.022

Gaidi S, Galve, JP, Melki F, Ruano, Reyes-Carmona C, Marzougui W, Devoto S, Pérez-Peña JV, Azañón JM, Chouaieb H, Zargouni F Booth-Rea G (2021) Analysis of the geological controls and kinematics of the chgega landslide (Mateur, Tunisia) exploiting photogrammetry and InSAR technologies. Remote Sens 13: 4048. https://doi.org/10.3390/rs13204048

Galve JP, Pérez-Peña JV, Azañón JM, Closson D, Caló F, Reyes-Carmona C, Jabaloy A, Ruano P, Mateos RM, Notti D, Herrera G, Béjar-Pizarro M, Monserrat O, Bally P (2017) Evaluation of the SBAS InSAR Service of the European Space Agency's Geohazard Exploitation Platform (GEP) Remote Sens 9: 1291. https://doi.org/10.3390/rs9121291

Gullà G, Peduto D, Borrelli L, Antronico L, Fornaro G (2017) Geometric and kinematic characterization of landslides affecting urban areas: the Lungro case study (Calabria, Southern Italy). Landslides 14: 171-188. https://doi.org/10.1007/s10346-015-0676-0

Griffiths JS (2016) Incorporating geomorphology in engineering geological ground models. Geol Soc Lond Eng Geol Spec Publ 27: 159. https://doi.org/10.1144/EGSP27.14

Gutiérrez F, Galve JP, Lucha P, Castañeda C, Bonachea J, Guerrero J (2011) Integrating geomorphological mapping, trenching, InSAR and GPR for the identification and characterization of sinkholes: A review and application in the mantled evaporite karst of the Ebro Valley (NE Spain). Geomorphology 134: 144-156. https://doi.org/10.1016/j.geomorph.2011.01.018

Gutiérrez-Santolalla F, Acosta E, Ríos S, Guerrero J, Lucha P (2005) Geomorphology and geochronology of sackung features (uphill-facing scarps) in the Central Spanish Pyrenees. Geomorphology 69: 298-314. https://doi.org/10.1016/j.geomorph.2005.01.012

Guzzetti F, Reichenbach P, Ardizzone F, Cardinali M, Galli M (2006) Estimating the quality of landslide susceptibility models. Geomorphology 81: 166-184. https://doi.org/10.1016/j.geomorph.2006.04.007

Guzzetti F, Mondini AC, Cardinali M, Fiorucci F, Santangelo M, Chang KT (2012) Landslide inventory maps: New tools for an old problem. Earth-Sci Rev 112: 42-66. https://doi.org/10.1016/j.earscirev.2012.02.001

Handwerger AL, Fielding EJ, Huang MH, Bennett GL, Liang C, Schulz WH (2019) Widespread initiation, reactivation, and acceleration of landslides in the northern California Coast Ranges due to extreme rainfall. J Geophys Res Earth Surf 124: 1782-1797. https://doi.org/10.1029/2019JF005035

Hearn GJ (2019) Geomorphology in engineering geological mapping and modelling. Bull Eng Geol Environ 78: 723-742. https://doi.org/10.1007/s10064-017-1166-5

Herrera G, Gutiérrez F, García-Davalillo JC, Guerrero J, Notti D, Galve JP, Fernández-Merodo JA, Cooksley G (2013) Multi-sensor advanced DInSAR monitoring of very slow landslides: The Tena Valley case study (Central Spanish Pyrenees). Remote Sens Environ 128: 31-43. https://doi.org/10.1016/j.rse.2012.09.020

Hooper A (2008) A multi-temporal InSAR method incorporating both persistent scatterer and small baseline approaches. Geophys Res Lett 35: L16302. https://doi.org/10.1029/2008GL034654

Hu J, Li ZW, Ding XL, Zhu JJ, Zhang L, Sun Q (2014) Resolving three-dimensional surface displacements from InSAR measurements: A review. Earth-Sci Rev 133:1-17. https://doi.org/10.1016/j.earscirev.2014.02.005

Jaboyedoff M, Oppikofer T, Abellán A, Derron MH, Loye A, Metzger R, Pedrazzini A (2012) Use of LIDAR in landslide investigations: a review. Nat Hazards 61: 5-28. https://doi.org/10.1007/s11069-010-9634-2

Jiménez-Perálvarez JD (2012) Movimientos de ladera en la vertiente meridional de Sierra Nevada (Granada, España): identificación, análisis y cartografía de susceptibilidad y peligrosidad mediante SIG. Doctoral Thesis, University of Granada

Jiménez-Perálvarez JD, El Hamdouni R, Palenzuela JA, Irigaray C, Chacón J (2017) Landslide-hazard mapping through multi-technique activity assessment: an example from the Betic Cordillera (southern Spain). Landslides 14: 1975-1991. https://doi.org/10.1007/s10346-017-0851-6

Korup O (2005) Distribution of landslides in southwest New Zealand. Landslides 2: 43-51. https://doi.org/10.1007/s10346-004-0042-0

Lee JC, Shirzaei M (2023) Novel algorithms for pair and pixel selection and atmospheric error correction in multitemporal InSAR. Remote Sens of Environ 286: 113447. https://doi.org/10.1016/j.rse.2022.113447

Liao HJ, Sheng Q, Gao SH, Xu ZP (2005) Influence of drawdown of reservoir water level on landslide stability. Chin J Rock Mech Eng 24: 3454–3458

Lissak C, Maquaire O, Malet JP, Lavigne F, Virmoux C, Gomez C, Davidson R (2015) Ground-penetrating radar observations for estimating the vertical displacement of rotational landslides. Nat Hazards Earth Syst Sci 15: 1399–1406. https://doi.org/10.5194/nhess-15-1399-2015

Liu C, Shao X, Li W (2019) Multi-sensor observation fusion scheme based on 3D variational assimilation for landslide monitoring. Geomat Nat Hazards Risk 10: 151-167. https://doi.org/10.1080/19475705.2018.1513871

López-Vinielles J, Fernández-Merodo JA, Ezquerro P, García-Davalillo JC, Sarro R, Reyes-Carmona C, Barra A, Navarro JA, Krishnakumar V, Alvioli M, Herrera G (2021) Combining satellite insar, slope units and finite element modeling for stability analysis in mining waste disposal areas. Remote Sens 13: 2008. https://doi.org/10.3390/rs13102008

Madarieta-Txurruka A, González-Castillo L, Peláez JA, Catalán M, Henares J, Gil AJ, Lamas-Fernández F, Galindo-Zaldívar J (2022) The role of faults as barriers in confined seismic sequences: 2021 seismicity in the Granada Basin (Betic Cordillera). Tectonics 41: e2022TC007481. https://doi.org/10.1029/2022TC007481

Mateos RM, Azañón JM, Roldán FJ, Notti D, Pérez-Peña V, Galve JP, Pérez-García JL, Colomo CM, Gómez-López JM, Montserrat O, Devantèry N, Lamas-Fernández F, Fernández-Chacón F (2017) The combined use of PSInSAR and UAV photogrammetry

techniques for the analysis of the kinematics of a coastal landslide affecting an urban area (SE Spain). Landslides 14: 743-754. https://doi.org/10.1007/s10346-016-0723-5

Morales J, Singh SK, Ordaz M (1996) Analysis of the Granada (Spain) earthquake of 24 June, 1984 (M= 5) with emphasis on seismic hazard in the Granada Basin. Tectonophysics 257: 253-263. https://doi.org/10.1016/0040-1951(95)00188-3

Moretto S, Bozzano F, Mazzanti P (2021) The role of satellite InSAR for landslide forecasting: Limitations and openings. Remote Sens 13: 3735. https://doi.org/10.3390/rs13183735

Moro M, Saroli M, Tolomei C, Salvi S (2009) Insights on the kinematics of deep-seated gravitational slope deformations along the 1915 Avezzano earthquake fault (Central Italy), from time-series DInSAR. Geomorphology 112: 261-276. https://doi.org/10.1016/j.geomorph.2009.06.011

Nath S, Chatterjee R, Mohanty, SP, Gaurav S (2019) Comparative evaluation of active tectonics in parts of the frontal region of NW Himalaya, India by geomorphic analysis and geophysical investigation. J Geol Soc India 94: 197-205. https://doi.org/10.1007/s12594-019-1289-3

Navarro JA, Tomás R, Barra A, Pagán JI, Reyes-Carmona C, Solari L, López-Vinielles J, Falco S, Crosetto M (2020) ADAtools: Automatic detection and classification of active deformation areas from PSI displacement maps. ISPRS Int J Geo-Inf 9: 584. https://doi.org/10.3390/ijgi9100584

Nie W, Krautblatter M, Leith K, Thuro K, Festl J (2017) A modified tank model including snowmelt and infiltration time lags for deep-seated landslides in alpine environments (Aggenalm, Germany). Hazards Earth Syst Sci 17: 1595-1610. https://doi.org/10.5194/nhess-17-1595-2017

Notti D, Galve JP, Mateos RM, Monserrat O, Lamas-Fernández F, Fernández-Chacón F, Roldán-García FJ, Pérez-Peña JV, Crosetto M, Azañón JM (2015) Human-induced coastal landslide reactivation. Monitoring by PSInSAR techniques and urban damage survey (SE Spain). Landslides 12: 1007-1014. https://doi.org/10.1007/s10346-015-0612-3

Novellino A, Cesarano M, Cappelletti P, Di Martire D, Di Napoli M, Ramondini M, Sowter A, Calcaterra D (2021) Slow-moving landslide risk assessment combining Machine Learning and InSAR techniques. Catena 203: 105317. https://doi.org/10.1016/j.catena.2021.105317

Palenzuela JA, Jiménez-Perálvarez JD, Chacón J, Irigaray C (2016) Assessing critical rainfall thresholds for landslide triggering by generating additional information from a reduced database: an approach with examples from the Betic Cordillera (Spain) Nat Hazards 84: 185-212. https://doi.org/10.1007/s11069-016-2416-8

Pánek T, Klimeš J (2016) Temporal behavior of deep-seated gravitational slope deformations: A review. Earth-Sci Rev 156: 14-38. https://doi.org/10.1016/j.earscirev.2016.02.007

Pedrazzini A, Jaboyedoff M, Loye A, Derron MH (2013) From deep seated slope deformation to rock avalanche: destabilization and transportation models of the Sierre landslide (Switzerland). Tectonophysics 605: 149-168. https://doi.org/10.1016/j.tecto.2013.04.016

Peduto D, Santoro M, Aceto L, Borrelli L, Gullà G (2021) Full integration of geomorphological, geotechnical, A-DInSAR and damage data for detailed geometric-kinematic features of a slow-moving landslide in urban area. Landslides 18: 807-825. https://doi.org/10.1007/s10346-020-01541-0

Pinyol NM, Alonso EE, Corominas J, Moya J (2012) Canelles landslide: modelling rapid drawdown and fast potential sliding. Landslides 9: 33-51. https://doi.org/10.1007/s10346-011-0264-x

Qureshi KA, Khan SD (2020) Active tectonics of the frontal himalayas: An example from the manzai ranges in the recess setting, western pakistan. Remote Sens 12: 3362. https://doi.org/10.3390/rs12203362

Raspini F, Bianchini S, Ciampalini A, Del Soldato M, Montalti R, Solari L, Tofani V, Casagli N (2019) Persistent Scatterers continuous streaming for landslide monitoring and mapping: The case of the Tuscany region (Italy). Landslides 16: 2033-2044. https://doi.org/10.1007/s10346-019-01249-w

Rodríguez-Peces MJ, García-Mayordomo J, Azañón JM, Insua-Arévalo JM, Jiménez-Pintor J (2011) Constraining pre-instrumental earthquake parameters from slope stability back-analysis: Palaeoseismic reconstruction of the Güevéjar landslide during the 1st November 1755 Lisbon and 25th December 1884 Arenas del Rey earthquakes. Quat Int 242: 76-89. https://doi.org/10.1016/j.quaint.2010.11.027

Rodríguez-Peces MJ, García-Mayordomo J, Martínez-Díaz JJ (2014) Slope instabilities triggered by the 11th May 2011 Lorca earthquake (Murcia, Spain): comparison to previous hazard assessments and proposition of a new hazard map and probability of failure equation. Bull Earthq Eng 12: 1961-1976. https://doi.org/10.1007/s10518-013-9509-5

Rosi A, Tofani V, Tanteri L, Tacconi Stefanelli C, Agostini A, Catani F, Casagli N (2018) The new landslide inventory of Tuscany (Italy) updated with PS-InSAR: geomorphological features and landslide distribution. Landslides 15: 5-19. https://doi.org/10.1007/s10346-017-0861-4

Sanz de Galdeano C, Peláez Montilla JA, López Casado C (2003) Seismic potential of the main active faults in the Granada Basin (southern Spain). Pure Appl Geophys 160: 1537-1556. https://doi.org/10.1007/s00024-003-2359-3

Schlögel R, Doubre C, Malet JP, Masson F (2015) Landslide deformation monitoring with ALOS/PALSAR imagery: A D-InSAR geomorphological interpretation method. Geomorphology 231: 314-330. https://doi.org/10.1016/j.geomorph.2014.11.031

Solari L, Del Soldato M, Raspini F, Barra A, Bianchini S, Confuorto P, Casagli N, Crosetto M (2020). Review of satellite interferometry for landslide detection in Italy. Remote Sens 12: 1351. https://doi.org/10.3390/rs12081351

Soldati M (2013) Deep-seated gravitational slope deformation. In: Bobrowsky PT (ed) Encyclopedia of natural hazards. Springer, pp 151-155

Song K, Wang F, Yi Q, Lu S (2018) Landslide deformation behavior influenced by water level fluctuations of the Three Gorges Reservoir (China). Eng Geol 247: 58-68. https://doi.org/10.1016/j.enggeo.2018.10.020

Sowers GF, Royster (1978) Field Investigation, in Landslide Analysis and Control. In: Schuster RL, Krizek RJ (eds) National Academy of Sciences, pp 81-111

Tomás R, Abellán A, Cano M, Riquelme A, Tenza-Abril AJ, Baeza-Brotons F, Saval JM, Jaboyedoff M (2018) A multidisciplinary approach for the investigation of a rock spreading on an urban slope. Landslides 15: 199-217. https://doi.org/10.1007/s10346-017-0865-0

Troiani F, Galve JP, Piacentini, Della Seta M, Guerrero J (2014) Spatial analysis of stream length-gradient (SL) index for detecting hillslope processes: a case of the Gállego River headwaters (Central Pyrenees, Spain). Geomorphology, 214, 183-197. https://doi.org/10.1016/j.geomorph.2014.02.004

Tsou CY, Chigira M, Matsushi Y, Chen SC (2015) Deep-seated gravitational deformation of mountain slopes caused by river incision in the Central Range, Taiwan: Spatial distribution and geological characteristics. Eng Geol 196:126-138. https://doi.org/10.1016/j.enggeo.2015.07.005

Van Westen CJ, Van Asch TW, Soeters R (2006) Landslide hazard and risk zonation—why is it still so difficult?. Bull Eng Geol Environ 65: 167-184. https://doi.org/10.1007/s10064-005-0023-0

Vecchiotti F, Amabile AS, Clemente S, Ostermann M, Nicodemo G, Peduto D (2022) Kinematic and geometric characterization of the Vögelsberg Rockslide (Tyrol, Austria) by Means of MT-InSAR data. Geosciences 12: 256. https://doi.org/10.3390/geosciences12070256

Wang Y, Tang H, Huang J, Wen T, Ma J, Zhang J (2022) A comparative study of different machine learning methods for reservoir landslide displacement prediction. Eng Geol 298: 106544. https://doi.org/10.1016/j.enggeo.2022.106544

Xu WJ, Wang YJ, Dong XY (2021) Influence of reservoir water level variations on slope stability and evaluation of landslide tsunami. Bull Eng Geol Environ 80: 4891-4907. https://doi.org/10.1007/s10064-021-02218-1

Zhang T, Zhang W, Cao D, Yi Y, Wu X (2022 A New Deep Learning Neural Network Model for the Identification of InSAR Anomalous Deformation Areas. Remote Sens 14: 2690. https://doi.org/10.3390/rs14112690

Zhou C, Cao Y, Yin K, Wang Y, Shi X, Catani F, Ahmed B (2020) Landslide characterization applying sentinel-1 images and InSAR technique: The Muyubao Landslide in the three Gorges Reservoir Area, China. Remote Sens,12: 3385. https://doi.org/10.3390/rs12203385

Appendix

Supplementary information of Chapter IV

The present appendix includes the supplementary information of Chapter IV. This information consists of the entire GPR profiles ‘East’ and ‘West’, in spatial correlation with a top view scheme of the N-323 National Road. The damages observed in the field along the road, as well as the damages and other features of the GPR profiles are also illustrated in the figure. It is clarifying to show the complete extent of the GPR profiles and the top view scheme of the N-323 National Road as only some extracts of them are shown in Chapter IV (Figures 13 and 14).

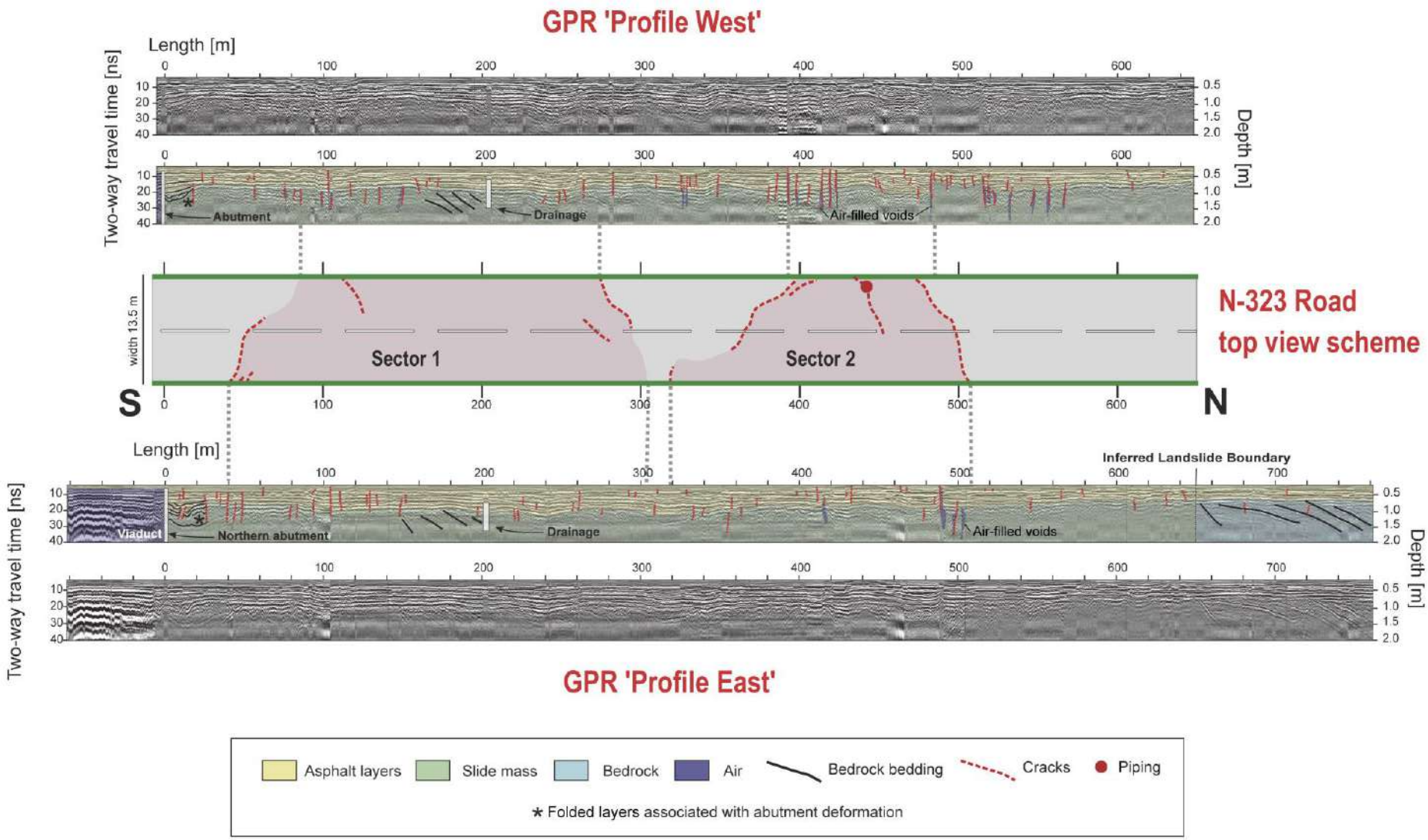
GPR 'Profile West'
Length [m]
Two-way travel time [ns]
Depth [m]
Abutment
Drainage
Air-filled voids
width 13.5 m
Sector 1
Sector 2
S
N
N-323 Road
top view scheme
Inferred Landslide Boundary
Viaduct
Northern abutment
GPR 'Profile East'
Asphalt layers
Slide mass
Bedrock
Air
Bedrock bedding
Cracks
Piping
★ Folded layers associated with abutment deformation

Sunset from Sierra Nevada summits